Title
Computational network models of neocortical seizures

Permalink
https://escholarship.org/uc/item/8948d8tx

Author
Frohlich, Flavio

Publication Date
2007

Peer reviewed|Thesis/dissertation

UNIVERSITY OF CALIFORNIA, SAN DIEGO

Computational Network Models of Neocortical Seizures

A Dissertation submitted in partial satisfaction of the
Requirements for the degree Doctor of Philosophy

in

Biology / Specialization in Computational Neurobiology

by

Flavio Frohlich

Committee in charge:

Terrence J. Sejnowski, Chair
Henry D. I. Abarbanel
Maxim V. Bazhenov
Gert Cauwenberghs
Vicente J. Iragui-Madoz
Massimo Scanziani

2007

The Dissertation of Flavio Frohlich is approved, and it is acceptable in quality and form for publication on microfilm:

Chair

University of California, San Diego

2007

DEDICATION

To my wife Anita,

In infinite and eternal love.

TABLE OF CONTENTS

Signature Page iii

Dedication iv

Table of Contents v

List of Figures vi

Acknowledgements ix

Vita xiv

Abstract xv

Introduction 1

1 Pathological Cortical Network Reorganization 5

  1-1 Pathological Effect of Homeostatic Synaptic Scaling on Network Dynamics in Diseases of the Cortex. 6

  1-2 Interictal Discharges Originate at the Border between Intact and Deafferented Cortex 39

2 Potassium Dynamics in the Cortex and Epilepsy 53

  2-1 New Insights on an Old Topic 54

  2-2 Extracellular Potassium Mediates Transitions between Physiological and Pathological Cortical Network Dynamics 80

  2-3 Slow State Transitions of Sustained Neural Oscillations by Activity-Dependent Modulation of Intrinsic Excitability 97

  2-4 Coexistence of Tonic Firing and Bursting in Cortical Neurons 144

  2-5 Maintenance and Termination of Neocortical Oscillations by Dynamic Modulation of Intrinsic and Synaptic Excitability 169

3 Conclusions 192

4 Appendix 192

  Extracellular Single-Unit Recordings of Spontaneous and Evoked Population Activity in the Acute Cortical Slice Preparation 194

5 References 220

LIST OF FIGURES

Figure 1-1 Network reorganization after partial deafferentation 16

Figure 1-2 Network activity after deafferentation.. 17

Figure 1-3 Rastergrams for PYs after homeostatic scaling in response to different deafferentation degrees.. 19

Figure 1-4 Firing rates as a function of time for 80 PYs.. 21

Figure 1-5 Recovery time-course of firing rates as a function of their input.............. 24

Figure 1-6 Distribution of firing rates as a function of time for different deafferentation degrees.. 26

Figure 1-7 Average PY network firing rate as a function of time.............................. 28

Figure 1-8 Spike-triggered conductances.. 32

Figure 1-9 Increased activity in intact subpopulation and irregular network discharges in deafferented subpopulation after homeostatic scaling 44

Figure 1-10 Posttraumatic network reorganization as a function of fraction of deafferented cells (lesion size) 46

Figure 1-11 Two sample rastergrams of partially deafferented (D = 80%) networks in case of weaker deafferentation. 49

Figure 2-1 Potassium accumulation hypothesis 61

Figure 2-2 Slow state transitions in cortical network model....................................... 73

Figure 2-3 “Open-loop” method... 77

Figure 2-4 Physiological activity in network with $[K^+]_o$ dynamics............................. 86

Figure 2-5 Transition from “physiological” to “pathological” activity........................ 88

Figure 2-6 Average $[K^+]_o$ traces for perturbations 91

Figure 2-7 Termination of seizure-like activity by inducing switch back to physiological state 93

Figure 2-8 Single PY neuron 110

Figure 2-9 Membrane voltage traces for depolarizing current step injection 111

Figure 2-10 Time courses of membrane voltage Vm 112

Figure 2-11 Bifurcation analysis of PY cell dynamics 113

Figure 2-12 Robustness analysis to variation of intrinsic conductances 117

Figure 2-13 Time course of membrane voltage 118

Figure 2-14 Globally connected network with five PY cells and one IN. 122

Figure 2-15 Transition from slow bursting to fast run 123

Figure 2-16 Controlling inactivation. 124

Figure 2-17 Quantification of periodic slow transitions 127

Figure 2-18 Effect of synaptic coupling.. 128

Figure 2-19 Time course of burst and underlying synaptic currents 130

Figure 2-20 Large network (60 PY cells and 15 INs) 133

Figure 2-21 Sample trace of electrographic seizure 135

Figure 2-22 Single unit activity for $[K^+]_o$ = 2.5 mM and $[K^+]_o$ = 6.5 mM 152

Figure 2-23 Poincare cross-sections 155

Figure 2-24 Bifurcation diagram for $[K^+]_o$ = 5.9 mM. 156

Figure 2-25 Three-dimensional bifurcation diagram for $[K^+]_o$ = 5.5 mM. 160

Figure 2-26 Bifurcation diagram for $[K^+]_o$ = 9.0 mM 162

Figure 2-27 Cortical network oscillation patterned into alternating epochs of slow bursting and fast run following stimulation of PYs 176

Figure 2-28 Time-course of membrane voltage before termination of oscillations shows slow bursting. 180

Figure 2-29 Patterned oscillatory firing for slow synaptic depression 182

Figure 2-30 Patterned cortical network oscillations of finite length for dynamically updated intracellular chloride concentration. 184

Figure 2-31 Spontaneous firing patterns of regular-spiking and fast-spiking cortical neurons during electrographic seizure *in vivo*. 187

Figure 4-1 Spike sorting *in vitro* 204

Figure 4-2 Intracellular and extracellular waveforms 206

Figure 4-3 Pyramidal cells and fast-spiking interneurons have different extracellular action potential waveforms 208

Figure 4-4 Spontaneous activity in hippocampus CA3 210

Figure 4-5 Input-output map in the hippocampal CA3 – CA1 circuit 213

Figure 4-6 Input discrimination ability of a small population of neurons in hippocampus CA1 215

ACKNOWLEDGEMENTS

I would like to take this opportunity to express my gratitude for all the help, support, encouragement, and constructive criticism that have shaped me and my graduate work over the past four years. Of course, any shortcomings of my work remain my own sole responsibility.

I am greatly indebted to my advisor Dr. Terry Sejnowski. As his graduate student, I had the chance to develop my own scientific ideas and ideals under his supportive and encouraging guidance. Through his mentorship, I had the chance to learn and live the truly interdisciplinary spirit of neuroscience. In Terry's lab, I had the great fortune to work with Dr. Maxim Bazhenov who taught me the nuts and bolts of computational modeling in neuroscience. More importantly, Maxim has generously provided me with freedom, opportunities, and a collegial environment tailored to my scientific enthusiasm. As a result, I am gratefully looking back at years of very productive scientific collaboration and friendship.

I would like to acknowledge Dr. Massimo Scanziani for accepting me as a graduate student in his lab and for introducing me to *in vitro* neurophysiology. While the idea of a PhD in two different laboratories was certainly quite an adventure for both of us, I have tremendously benefited from the exposure and practical experience I gained through my work his laboratory. I am very impressed by his strong focus on scientific excellence and clarity.

Also, I would like to thank my scientific collaborators outside the two laboratories in which I have performed my graduate research. Dr. Igor Timofeev and the late Dr. Mircea Steriade have both provided me with many important experimental data and insights that were guiding my modeling work on cortical oscillations and epileptic seizures. My collaboration with Dragos Nita in Igor's laboratory has been a pleasure and he has greatly contributed to my understanding of *in vivo* recordings of electrographic seizures.

The material presented in this dissertation is based on a series of manuscripts, some of them are published and others are either under review or in their final stage before submission. I was the primary investigator and author of all these manuscripts. Chapter 1-1, in full, is a reprint of the material as it was submitted to the Journal of Neuroscience, 2007 (accepted for publication pending revisions), Frohlich Flavio, Bazhenov Maxim, Sejnowski Terrence. Chapter 1-2, in full, is a manuscript in preparation for submission, Frohlich Flavio, Bazhenov Maxim, Nita Dragos, Timofeev Igor, Sejnowski Terrence. Chapter 2-1, in full, is a manuscript in preparation for submission, Frohlich Flavio, Bazhenov Maxim, Iragui-Madoz Vicente, Sejnowski Terrence. Chapter 2-2, in full, is a manuscript in preparation for submission, Frohlich Flavio, Terrence Sejnowski, Bazhenov Maxim. Chapter 2-3, in full, is an exact reprint as it appeared in the Journal of Neuroscience, 2006, Frohlich Flavio, Bazhenov Maxim, Timofeev Igor, Steriade Mircea, Sejnowski Terrence. Chapter 2-4, in full, is an exact reprint as it appeared in Physical Review E, 2006, Frohlich Flavio, Bazhenov

Maxim. Chapter 2-5, in full, is an exact reprint as it appeared in Thalamus and Related Systems, 2007, Frohlich Flavio, Bazhenov Maxim, Timofeev Igor, Sejnowski Terrence. Chapter 3-1, in full, is a manuscript in preparation for submission, Frohlich Flavio, Scanziani Massimo.

I would like to thank my thesis committee for the continued dedication to my dissertation research and my academic growth: Dr. Terrence Sejnowski (chair), Dr. Henry Abarbanel, Dr. Maxim Bazhenov, Dr. Gert Cauwenberghs, Dr. Vicente Iragui-Madoz, and Dr. Massimo Scanziani (in alphabetical order). Henry has provided support and encouragement throughout my time as a graduate student at UCSD. Also, thanks to him, I was able to visit the Bernstein Centers for Computational Neuroscience in Germany. I would like to thank Vicente for his interest in my work. I am very grateful for the essential insights on the clinical aspects of epilepsy he has provided me with. I share the passion for engineering with Gert who has joined my thesis committee at a crucial time. His steady support has helped my research tremendously.

Since I consider it impossible to list all the people who contributed to my research over the past four years, I would like to collectively thank everyone for the great discussions and inputs. I would like to acknowledge my fellow lab members in the Sejnowski and Scanziani laboratories. Also, I am indebted to Dr. E.J. Chichilnisky, Dr. Dan Feldman, Dr. Marla Feller, Dr. Anirvan Ghosh, Dr. Jeff Isaacson, Dr. David

Kleinfeld, Dr. Rich Krauzlis, Dr. Bill Kristan, Dr. Pam Reinagel, Dr. Nick Spitzer, and Dr. Jochen Triesch and their respective laboratories as they all have provided great help in one or the other form throughout my graduate work.

Also, I would like to thank my mentors at previous institutions. They have played a tremendous role in preparing me for the challenge of a PhD at UCSD. Dr. Walter Schaufelberger at the Swiss Federal Institute of Technology (ETH), Zurich (Switzerland), has provided me with excellent guidance and advice throughout my time at ETH. Dr. Igor Aleksander at Imperial College, London (UK), has been a great mentor and he deserves the credit for encouraging me to go to graduate school in the United States. Dr. Rodney Douglas at the Institute for Neuroinformatics, University of Zurich (Switzerland), introduced me to the world of interdisciplinary neuroscience research and provided strong support and encouragement for my research. Dr. Saso Jezernik at ETH thoroughly prepared me for my graduate work by teaching me many applied skills related to the scientific process. Dr. Tobias Mueller at Heidelberger Druckmaschinen has provided me with encouragement and inspiration at critical points on my way into the academic world and it is with him that I published my very first article. Dr. Ruediger Wehner at the University of Zurich is a fantastic mentor who deserves the credit for encouraging me to do my PhD in Terry’s laboratory.

I thank my friends for all their great support and help, in particular, Justin and Joy, Kate and Jonathan, Shantanu, Will, Hiro and Akiko, Joachim, Luca and Toni.

This PhD would not have been possible without the all encompassing support by my family, in particular by my wife Anita, my parents Enrico and Claudia and my sister Carla. By far, my wife Anita has carried the greatest weight during my time as a graduate student. Her infinite love and support are the basis of all my achievements. I have no words to describe my deep gratitude and love to her.

Flavio Frohlich, December 2007

VITA

2001	International Diploma, Imperial College, London, United Kingdom
2003	Dipl. El.-Ing. ETH, Swiss Federal Institute of Technology, Zurich, Switzerland
2007	Doctor of Philosophy, University of California, San Diego

PUBLICATIONS

D. Nita, C. Youssouf, F. Frohlich and I. Timofeev. *Cortical and thalamic components of neocortical kindling-induced epileptogenesis in behaving cats*. Experimental Neurology, 2007, submitted.

F. Frohlich, M. Bazhenov, and T.J. Sejnowski. *Pathological effect of homeostatic synaptic scaling on network dynamics in diseases of the cortex*. J Neurosci, 2007, accepted pending revisions.

F. Frohlich, I. Timofeev, T.J. Sejnowski and M. Bazhenov. *Extracellular potassium dynamics and epileptogenesis*. In: Computational Neuroscience in Epilepsy, Editors: Ivan Soltesz and Kevin Staley (2007), in press.

F. Frohlich, M. Bazhenov, I. Timofeev and T.J. Sejnowski. *Maintenance and termination of neocortical oscillations by dynamic modulation of intrinsic and synaptic excitability.* Thalamus & Related Systems, 2007. Memorial Issue Mircea Steriade.

F. Frohlich and M. Bazhenov. *Coexistence of tonic firing and bursting in cortical neurons.* Physical Review E, 2006 Sept 28; Vol. 74, No. 3.

F. Frohlich, M. Bazhenov, I. Timofeev, M. Steriade, and T.J. Sejnowski. *Slow state transitions of sustained neural oscillations by activity-dependent modulation of intrinsic excitability.* J Neurosci, June 7, 2006, 26(23):6153-6162.

F. Frohlich and S. Jezernik. *Feedback control of Hodgkin–Huxley nerve cell dynamics.* Control Engineering Practice. 2005, Sept;13(9):1195-1206

F. Frohlich and S. Jezernik. *Annihilation of single cell neural oscillations by feedforward and feedback control.* J Comput Neurosci. 2004, 17(2):165-78.

T. Müller and F. Frohlich. *Maschine hört mit. Akustische Messungen am Papierlauf von Bogendruckmaschinen.* Sensor Report, 5/2002.

FIELDS OF STUDY

Major Field: Biology

Studies in Computational Neuroscience
Terrence J. Sejnowski and Maxim Bazhenov

Studies in Neurophysiology
Massimo Scanziani

ABSTRACT OF THE DISSERTATION

Computational Network Models of Neocortical Seizures

by

Flavio Frohlich
Doctor in Philosophy in Biology / Specialization in Computational Neurobiology
University of California, San Diego, 2007
Professor Terrence J. Sejnowski, Chair

Epilepsy is a common neurological disorder that is characterized by bouts of synchronized hyperactivation of neuronal networks. The development of new treatment modalities is highly desirable but unfortunately hindered by our limited understanding of the pathophysiology of epileptic seizures. The complexity of neuronal dynamics make computational models an important tool in the research aimed at unraveling the mechanisms underlying epileptogenesis and epileptic seizures. In this dissertation, computational network models were used to study the dynamics of (1) pathological cortical network reorganization and (2) cortical seizures. We found that changes in synaptic properties by homeostatic plasticity after partial deafferentation can explain clinical electroencephalographic observations associated with diffuse and focal central nervous system pathologies. We then show that initiation, maintenance, and termination of cortical seizures can be explained by the dynamic interaction between neural activity and extracellular potassium concentration. Together, this dissertation provides a comprehensive set of specific hypotheses that can now be tested in experiments to further our understanding of neural pathophysiology.

INTRODUCTION

This dissertation describes our computational modeling studies aimed at contributing to an improved understanding of the pathophysiology of cortical neurological disorders. Computational models do not replace animal models and clinical studies of epilepsy but rather complement them by providing powerful tools for the study of the underlying pathological dynamics. We focus on general mechanisms that may apply to epileptogenesis and seizure dynamics in many different clinical manifestations of aberrant synchronous cortical network activity.

Chapter 1 describes our studies on pathological reorganization that may make cortical networks seizure-prone. Specifically, we investigated the role that homeostatic plasticity may play in response to loss of afferent input. In case of activity decrease by deafferentation, we found that homeostatic scaling of recurrent excitatory synapses recovered target activity levels but caused the occurrence of qualitatively different network dynamics. In Section 1-1, we present the network dynamics shaped by homeostatic synaptic scaling in response to deafferentation of a random subpopulation of neurons. In these models, we found a threshold for network reorganization in terms of the relative fraction of cells deafferented for which aberrant synchronized network dynamics occurred after synaptic scaling. This pathological network reorganization was characterized by periodic network-wide activation with bursts in individual cells and impaired information transmission capabilities. These results led us to suggest that periodic electroencephalographic (EEG) complexes in a broad range of central nervous system (CNS) may have homeostatic plasticity in response to the decrease in afferent input as a shared underlying mechanism. In Section 1-2, we introduce “structured deafferentation” where we removed the afferent input to a contiguous subpopulation of neurons to model cortical undercut that is commonly used to study posttraumatic epileptogenesis. In agreement with experimental data (e.g. Nita et al., 2006), we found that homeostatic plasticity introduced synchronous periodic activation of the intact subpopulation and aperiodic network-wide activation that originated at the border between intact and deafferented subnetworks. We suggest that these network-wide discharges may correspond to interictal discharges during posttraumatic epileptogenesis. In summary, the first part of this dissertation shows that homeostatic synaptic scaling may be the underlying mechanisms for several clinically ubiquitous EEG phenomena that have so far lacked an explanation.

Importantly, however, the findings presented in Chapter 1 do not explain cortical seizures but rather explain how networks reorganize and may become seizure-prone. Chapter 2 then addresses the dynamics and underlying mechanisms of cortical seizures. In Section 2-1 we discuss in depth the merits of a historic hypothesis concerning seizures, the so-called “potassium accumulation hypothesis” (e.g. Fertziger and Ranck, 1970). This hypothesis puts positive feedback interaction between neural activity and extracellular potassium concentration $[K^+]_o$ in the limelight as an explanation for seizure initiation, propagation, and termination. This hypothesis has failed to gain widespread support until few years ago when new studies on animal models of epilepsy and human tissue began to implicate aberration of the $[K^+]_o$ homeostasis apparatus in cortical epilepsies. Initial computational models of single cells that included ion concentration homeostasis mechanism (Kager et al., 2002, 2000) further contributed to a revived interest in the role of $[K^+]_o$ dynamics in epilepsy. In our own work, we studied the more complex scenario of a cortical network that included $[K^+]_o$ dynamics (Frohlich et al., 2007b). Based on our results, we propose a more subtle but similarly comprehensive role of $[K^+]_o$ in cortical epilepsies. In Section 2-2, we then recast the common dynamic model of cortical seizures as instabilities by providing evidence for our hypothesis that the occurrence of seizures in fact is the result of the switching to an additional stable network state. Interestingly, this stable seizure state only occurred in models that included the $[K^+]_o$ regulation apparatus. Section 2-3 is concerned with the evolution of seizures, in particular of neocortical seizures that are characterized by slowly alternating epochs of spike-wave (bursting) activity and fast runs (tonic firing). We show that a bistability between bursting and tonic firing for intermediate levels of $[K^+]_o$ in pyramidal cell models is the underlying mechanism that causes these slow state transitions to occur. In Section 2-4, we provide more detailed mathematical insight into both the intrinsic burst mechanism in our models and the bifurcation landscape that mediates this bistability between tonic firing and bursting. Finally, in Section 2-5, we show how activity-dependent changes in synaptic properties can mediate seizure termination in our potassium model of cortical seizures. In summary, we here present a comprehensive model of cortical seizures that are mediated by the dynamic interaction between neural activity and $[K^+]_o$.

In the appendix, we present experimental work unrelated to the study of epilepsy. We developed a novel recording technique based on multisite extracellular recording electrodes to monitor the action potential firing of a population of neurons with single-unit resolution in the acute hippocampal slice preparation. This method may serve as the important link between more traditional *in vitro* studies concerned with single-cell dynamics and population-oriented *in vivo* physiology.

It is our hope that the computational modeling work presented in this dissertation further motivates an increased and rejuvenated effort to better understand the pathophysiological dynamics of both epileptogenesis and seizures. Throughout this dissertation, we try to clearly state the predictions derived from our modeling work and to what extent they have already been confirmed by previous experiments and to what extent new experiments are required for further probing of the dynamic mechanisms we propose. Tightly integrated into the broader field of epilepsy research, we hope to eventually contribute with our work to the development and application of new treatment modalities for the prevention, treatment, and cure of the epileptic condition.

1 Pathological Cortical Network Reorganization

In this first part, we used cortical deafferentation as a model system to investigate cortical network reorganization that may lead to pathological firing patterns in CNS disease. Our key hypothesis was that homeostatic plasticity - in response to deafferentation - induces changes in the network structure that lead to pathological synchronized discharges by a shift from afferent to recurrent excitation. In the first section of this chapter, we investigate how homeostatic plasticity after deafferentation of a random subset of cortical cells can lead to periodic discharges similar to the periodic EEG discharges observed in a multitude of CNS disorders associated with diffuse cell loss. In the second section of this chapter, we then study deafferentation of a contiguous subset of neurons as a model of partial deafferentation by cortical undercut. After recovery of the target activity level by homeostatic plasticity, the network exhibited periodic activation in the intact subnetwork and aperiodic network-wide bursts of activity that originated at the border between intact and deafferented cortex and that qualitatively resembled interictal spikes. In summary, the work in this chapter suggests that homeostatic plasticity may play a key role in pathological cortical network reorganization and may explain several EEG phenomena associated with CNS disorders that have so far lacked a mechanistic explanation.

1.1 Pathological Effect of Homeostatic Synaptic Scaling on Network Dynamics in Diseases of the Cortex

Slow periodic EEG discharges are common in central nervous system (CNS) disorders. The pathophysiology of this aberrant rhythmic activity is poorly understood. We used a computational model of a neocortical network with a dynamic homeostatic scaling rule to show that loss of input (partial deafferentation) can trigger network reorganization that result in pathological periodic discharges. Decrease in average firing rate in the network by deafferentation was compensated by homeostatic synaptic scaling of recurrent excitation among pyramidal cells. Synaptic scaling succeeded in recovering the network target firing rate for all degrees of deafferentation (fraction of deafferented cells), but there was a critical degree of deafferentation for pathological network reorganization. For deafferentation degrees below this value, homeostatic upregulation of recurrent excitation had minimal effect on the macroscopic network dynamics. For deafferentation above this threshold, however, slow periodic oscillation appeared, patterns of activity were less sparse, and bursting occurred in individual neurons. Also, comparison of spike-triggered afferent and recurrent conductances revealed that information transmission was strongly impaired. These results suggest that homeostatic plasticity can lead to secondary functional impairment in case of cortical disorders associated with cell loss.

INTRODUCTION

Repetitive low frequency discharges is the most common electroencephalographic (EEG) abnormality in a broad spectrum of diseases with central nervous system (CNS) manifestation (e.g. encephalitis, tumors) (Bauer and Pieber, 1974; Niedermeyer, 2005). These periodic EEG patterns at low frequencies occur over prolonged epochs, in contrast to epileptic seizures that are usually transient and evolving (Kuroiwa and Celesia, 1980). Although periodic complexes are a typical clinical finding in encephalopathies associated with structural cerebral damage (Fisch, 1999), the underlying pathophysiology remains unknown (Brenner and Schaul, 1990; Niedermeyer, 2005). Understanding the cellular and network basis of this aberrant EEG state may facilitate the development of clinical intervention approaches to reduce disruption of neuronal function during cortical disease.

The cortex is endowed with feedback control mechanisms (i.e. homeostatic plasticity) that maintain activity levels of neurons and neural circuits (Davis, 2006). In particular, fast excitatory synaptic transmission is enhanced by synaptic scaling in response to prolonged activity blockage (Desai, 2003; Rich and Wenner, 2007; Turrigiano, 2007). We here used computational modeling to investigate how homeostatic plasticity reorganizes network dynamics in response to decrease in afferent input caused by transient or irreversible loss of presynaptic neurons. In our model, global homeostatic plasticity upregulates the recurrent excitatory synaptic conductances to compensate for deafferentation of a random subset of neurons (partial deafferentation). We hypothesized (1) that the average firing rate of the network is recovered, and (2) that the distribution of firing rates across cells and the fine temporal structure of the spike patterns in individual cells differ from before deafferentation. According to our hypothesis, these changes in network dynamics are due to the shift in balance between afferent and recurrent excitatory inputs caused by partial deafferentation (reduced afferent excitation) and synaptic scaling (increased recurrent excitation, Houweling et al. 2004). Of particular interest is the interaction between deafferented and intact cells during this homeostatic reorganization process. Our hypothesis is motivated (1) by recent studies of homeostatic plasticity *in vivo* (Mrisc-Flogel, 2007; Goeal et al. 2007; Desai et al. 2002) and (2) by observation of gradual recovery of activity levels over weeks with altered EEG patterns in response to cortical deafferentation (Nita et al., 2006, 2007; Topolnik et al., 2003a, b).

In our simulations, we found a critical degree of partial deafferentation (fraction of neurons deafferented) that determined the final outcome of homeostatic network reorganization. For deafferentation degrees below this threshold, network dynamics recovered without any qualitative reorganization that would predict macroscopic EEG aberrations. At the critical deafferentation degree, however, a relative abrupt change in network dynamic reorganization occurred with the following key characteristics that were absent in the intact and moderately deafferented network: (1) prominent periodic network activation, (2) decreased sparseness, (3) bursts of action potentials in individual cells, and (4) strongly nonlinear recovery time-course of average firing rate. On the basis of these results, we suggest that the clinically ubiquitous periodic complexes in CNS disorders with cortical manifestation may be caused by a paradoxical inability of homeostatic plasticity to maintain sparse, asynchronous network activity in case of change in input structure by partial deafferentation.

METHODS

We used two-compartment conductance-based neuron models (Mainen and Sejnowski, 1996) as previously described in detail elsewhere (Frohlich and Bazhenov, 2006; Frohlich et al., 2006) Briefly, neurons consisted of two electrically coupled compartments, the dendritic and axo-somatic compartment. The coupling strength of these two compartments determined the firing pattern of the cells in response to a depolarizing current injection (regular spiking for pyramidal cells, PYs, and fast-spiking for inhibitory interneurons, INs). Each compartment was endowed with a set of ionic conductances to model a specific complement of ion channels. The axo-somatic compartment contained transient voltage-gated sodium and delayed-rectifying potassium channels for spike generation (G_{Na} = 3000 mS/cm^2, G_{Kv} = 200 mS/cm^2), persistent sodium channels (G_{NaP} = 4.0 mS/cm^2) and voltage-independent potassium leak channels (G_{Kl} = 0.1 mS/cm^2). The dendritic compartment included high-threshold calcium, calcium-activated potassium, slowly-activating potassium, persistent sodium, hyperpolarization-activated depolarizing mixed cationic, potassium leak, and mixed cationic leak ion channels (G_{HVA} = 0.016 mS/cm^2, G_{KCa} = 3.5 mS/cm^2, G_{Km} = 0.01

mS/cm^2, G_{NaP} = 4.0 mS/cm^2, G_{h} = 0.05 mS/cm^2, G_{Kl} = 0.01 mS/cm^2, G_{L} = 0.033 mS/cm^2). INs had a similar ion channel complement (different values for: G_{Na} = 2500 mS/cm^2, G_{NaP} = 0.0 mS/cm^2 in both compartments, dendritic leak conductance G_{Kl} = 0.005 mS/cm^2, G_{HVA} = 0.01 mS/cm^2, G_{KCa} = 0.3 mS/cm^2, G_{Km} = 0.0 mS/cm^2). Equations and parameters for these ion channels and intracellular calcium dynamics were previously described in detail (Frohlich and Bazhenov, 2006). Network heterogeneity was introduced by drawing random values for the potassium leak conductance from a normal distribution (mean 0.01 mS/cm^2, STD 0.001 mS/cm^2 for PYs; mean 0.005 mS/cm^2, STD 0.0005 mS/cm^2 for INs).

The cortical network model consisted of 80 PYs and 20 INs. Similar to previously studied network configurations (Bazhenov et al., 2002; Frohlich et al., 2006), synaptic connectivity in the model was local such that each PY projected to five neighboring PYs on each side (both AMPA and NMDA receptor channels). Also, each PY targeted three neighboring INs (both AMPA and NMDA receptor channels) that in turn backprojected to eleven neighboring PYs ($\mathrm{GABA_A}$ receptor channels). In addition, all PYs and INs received independent afferent input that was modeled by a 100 Hz Poisson process. Postsynaptic receptor channels were modeled with a simplified first-order kinetic scheme of binding and unbinding of neurotransmitter described by instantaneous rise and exponential decay of synaptic conductances (Destexhe et al., 1994). To increase computational efficiency, each cell had a single synaptic conductance that was updated by the according change in conductance each time a spike in one of the presynaptic cells occurred. Maximal total synaptic conductances per cell were chosen such that (1) both afferent input and network input contributed to the firing before deafferentation and (2) average cross-correlogram was flat before deafferentation. Synaptic conductances for connections within the network were $g_{\mathrm{AMPA(PY\text{-}PY)}} = 3.2$ nS, $g_{\mathrm{NMDA(PY\text{-}PY)}} = 0.32$ nS, $g_{\mathrm{AMPA(PY\text{-}IN)}} = 3.0$ nS, $g_{\mathrm{NMDA(PY\text{-}IN)}} = 0.30$ nS, $g_{\mathrm{GABA(IN\text{-}PY)}} = 4.0$ nS. These maximal synaptic conductances were divided by the number of synapses targeting a given cell to determine the unitary conductances. AMPAergic synapses between PYs included short-term depression with use constant $U = 7\%$ per action potential and exponential recovery with time-constant $\tau = 700$ msec (Tsodyks and Markram, 1997). Afferent AMPAergic input conductances were set to $g_{\mathrm{PY}} = 0.5$ nS and $g_{\mathrm{IN}} = 1.0$ nS for PYs and INs, respectively.

We modeled neuronal dysfunction with partial deafferentation. In case of deafferentation, the frequency of the afferent excitatory Poisson input was reduced from 100 Hz to 5 Hz. Afferent input was simultaneously reduced for all deafferented cells. We simulated networks with different fractions of neurons subject to deafferentation as a model of disease severity (deafferentation degree D with values between 10% and 100%). For example, a deafferentation degree $D = 40\%$ indicated that a random 40% of both PYs and INs were subject to reduced afferent excitatory synaptic input. The subset of deafferented cells was random. We simulated four different random deafferentation patterns for each deafferentation degree. Firing rate analysis was based on the average of these four simulations. In all simulations, firing rate of the network was computed every four seconds by averaging over all PY spikes in the preceding four second interval. AMPA conductances G between PYs were then updated at these checkpoints by adding

$$\Delta G = \varepsilon (f^* - f) G,$$

where ε is the scaling rate (here $\varepsilon = 0.05$), f^* is the target firing rate (5 Hz), and f is the current average firing rate. This homeostatic scaling rule ensured multiplicative scaling of the synapses. In the limit where the activity mismatch f^*-f is small, our homeostatic plasticity rule represents a discrete time implementation of a first-order exponential recovery scheme. If not stated otherwise, time-points in the figures correspond to the checkpoints where the firing rate was computed and the synaptic conductances were updated based on this homeostatic scaling rule. The choice of the nature of this updating rule was motivated by (1) the computational impossibility to implement the biological time-scale for homeostatic scaling in such a model (hours to days) and (2) the fact that homeostatic regulation of synaptic conductances is sufficiently slower than the effect of a change in conductance on the firing behavior. We therefore separated the two time-scales and approximated the slow synaptic regulation with a discrete-time update scheme. Intervals between update time-points can therefore be considered of arbitrary length in time and are only meaningful in comparison to other simulations with the same update rule (e.g. different deafferentation degrees).

Simulated local field potential (lfp) was computed by averaging PY spike trains smoothed with a Gaussian kernel (STD 20 msec). For presentation purposes, the lfp trace was filtered with a fifth order Butterworth bandpass filter (0.5 Hz, 400 Hz). The spectrogram of the lfp trace was determined by the Matlab (The MathWorks, Natick, MA) function specgram with five second window size and two second overlap between windows. Spectrogram was smoothed by ten-fold oversampling and two-dimensional linear interpolation. Averaged cross-correlograms were calculated by computing the cross-correlation between all possible pairs of 40 randomly selected PY smoothed spike trains. Mean cross-correlograms are shown in black and the corresponding SEM in gray. Burst index quantifies the relative fraction of interspike intervals (ISIs) shorter than 50 msec in all PYs for a given four second interval. If not noted otherwise, figures show mean values (error bars: SEM) that were determined by pooling the four simulations with different random deafferentation patterns for a given degree of deafferentation. All analysis was performed with custom written Matlab (The MathWorks, Natick, MA) routines.

RESULTS

Homeostatic plasticity of excitatory synapses may control overall activity levels in neural circuits. Decrease in activity level caused by partial loss of excitatory input can be compensated by synaptic scaling of the remaining excitatory synapses. We studied how a dynamic homeostatic scaling rule for recurrent excitatory synapses reorganizes network dynamics in case of input loss by partial deafferentation. In our computational model of a cortical circuit, homeostatic synaptic scaling succeeded in recovering target average frequency of pyramidal cells for all deafferentation degrees tested (*D* = 10% to 100%). We found, however, substantial reorganization of fine temporal structure of spike trains, network synchronization, and firing rate distributions as a function of deafferentation degree. The interplay between cells with intact input and deafferented cells shaped the dynamics of the recovery from deafferentation. While in reality homeostatic plasticity occurs on the time-scale of many hours to days, we had to artificially warp time in our model (i.e. recovery of target firing rate occurs faster than in reality) due to technical constraints. The underlying approximation of separation of time-scales is well justified by the fact that the effect of changes in synaptic conductances on firing rates is immediate while homeostatic scaling triggered by changes in activity levels occurs on a much slower time-scale (see also Methods section).

Severe deafferentation (*D* = 90%) of a cortical network model composed of pyramidal cells (PYs) and fast-spiking inhibitory interneuron (INs) caused an initial drop in activity level (Figure 1-1, arrow head) with subsequent recovery of activity by upregulation of recurrent synaptic excitation (Membrane voltages of PYs and INs color-coded in Figure 1-1A, local field potential (lfp) in 1-1B, smoothed time-dependent frequency decomposition in 1-1C). Before deafferentation, the network exhibited asynchronous firing (low amplitude lfp, mean firing rate of PYs 5.03 Hz, STD 3.77 Hz) in response to independent Poisson input to all PYs and INs (frequency:

100 Hz). After deafferentation, as recovery of activity level by synaptic scaling progressed, slow periodic activation of the network occurred (oscillations in lfp in Fig. 1-1B and red band around 1 Hz in spectrogram of lfp in Fig. 1-1C). Eventually, average PY firing rate recovered to 5.02 Hz (STD 2.83 Hz). In contrast to before deafferentation, individual PYs fired bursts of action potentials (Figure 1-2: zoom in of network activity after scaling from Fig. 1-1A, sample membrane voltage trace in Figure 1-2B, dominant peak for small interspike intervals in Figure 1-2D "after scaling"). The different temporal fine-structure of the network activity before deafferentation and after synaptic scaling is reflected in the averaged cross-correlograms (Figure 1-2C, average in black, gray lines delimit SEM). Before deafferentation, network activity was asynchronous (flat trace). After synaptic scaling, the cross-correlogram revealed periodic modulation of firing activity with an approximate period of 950 msec (measured from central peak to first sideband peak, oscillatory cross-correlogram). Synaptic scaling changed not only the spiking patterns but also the distribution of firing rates across PYs. Before deafferentation, the distribution of resting potentials defined a decaying distribution of firing rates with a peak for cells with firing rate below 1 Hz (Figure 1-2E left). After scaling, the peak in distribution of firing rates was shifted to higher rates (Figure 1-2E right).

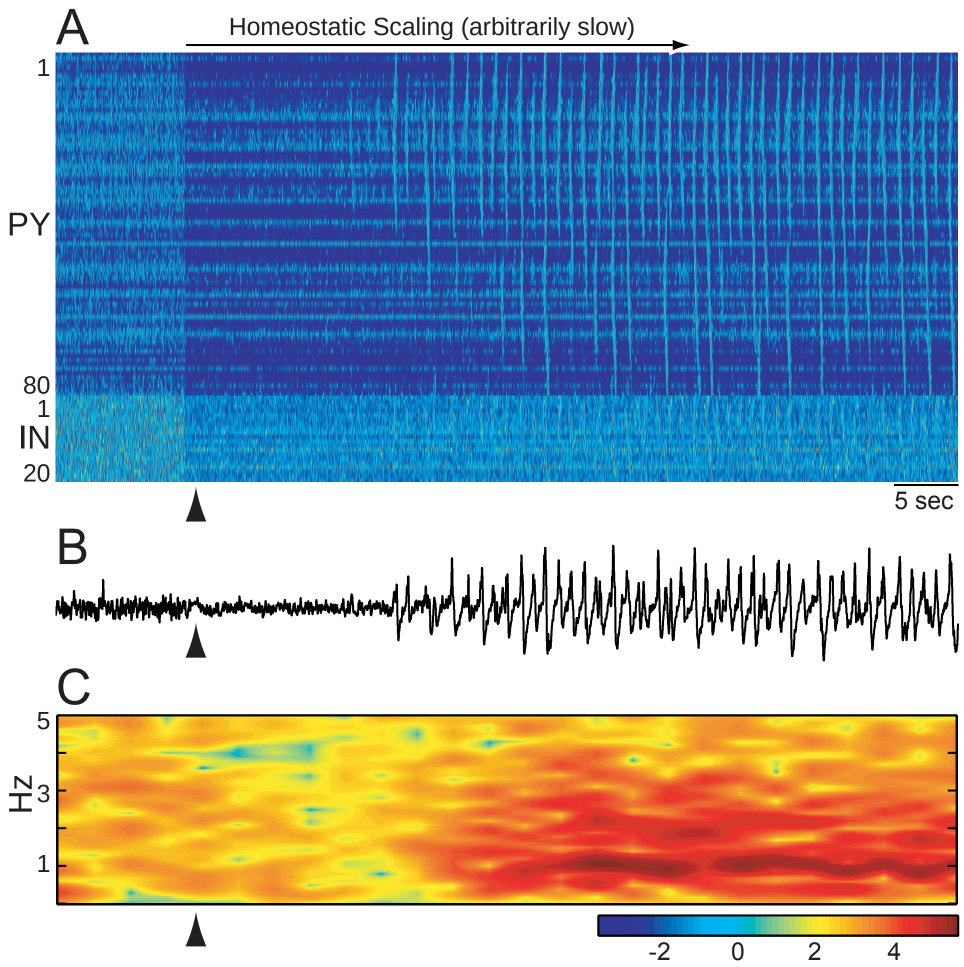

Figure 1-1 Network reorganization after partial deafferentation (deafferentation degree $D = 90\%$). (A) Activity map of all 80 PYs (top) and 20 INs (bottom). Cool and hot colors indicate hyperpolarization and depolarization, respectively. Deafferentation with consecutive drop in network activity (arrow head). Recovery of target firing rate by homeostatic scaling. Prominent periodic network activation. (B) Simulated local field potential (lfp). Same time-scale as in (A). High-frequency activity with low amplitude before deafferentation. Drop in lfp level after deafferentation (arrowhead). Recovery of activity level is characterized by slow high-amplitude lfp oscillations. (C) Spectrogram of lfp. Same time-scale as in (A). Cool and hot colors indicate low and high power on arbitrary logarithmic scale, respectively. Drop in power after deafferentation (arrowhead). Prominent peak in power around 1 Hz after homeostatic scaling (dark red band).

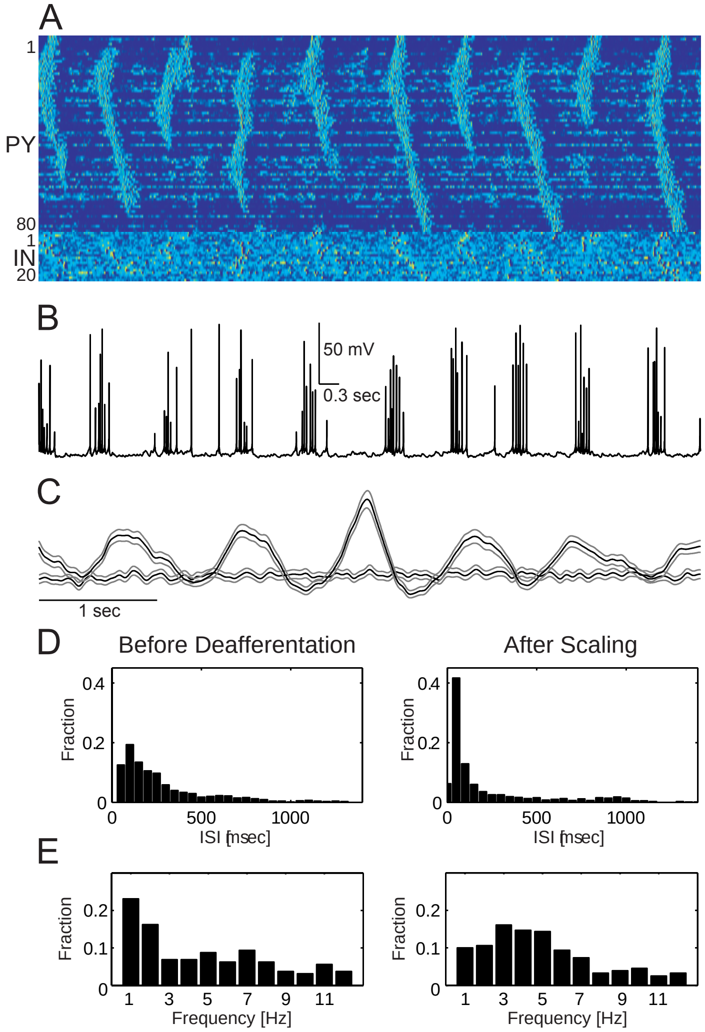

Figure 1-2 Network activity after deafferentation (D = 90%) and homeostatic synaptic scaling (zoom in of Fig. 1-1A, after synaptic scaling). Average firing frequency across network matched target rate f^* = 5 Hz. (A) Strong periodic activation of entire PY population (bands of lighter color). (B) Sample membrane voltage trace exhibits low frequency bursting. Some action potentials are truncated due to finite sampling of membrane voltage. Same time-scale in (A) and (B). (C) Average cross-correlogram for PY activity before deafferentation (flat line) and after homeostatic scaling triggered by deafferentation (oscillatory trace). (D) Histogram of interspike intervals (ISIs) before deafferentation (left) and after homeostatic scaling in response to deafferentation (right). Dominant peak for short ISI after scaling indicates bursting in individual cells. (E) Firing rate distribution across the network. Peak for very low firing rate before deafferentation (left) is shifted to higher frequencies and less prominent after synaptic scaling (right).

We expected the steady-state network dynamics after synaptic scaling to depend on the deafferentation degree. Therefore, we simulated the same network for different deafferentation degrees (Figure 1-3A rastergrams, Figure 1-3B average cross-correlograms; network dynamics after synaptic scaling). For weak deafferentation (D = 20%, top row), we found no oscillatory firing (flat average cross-correlogram). Very mild oscillatory modulation of instantaneous firing rates occurred for moderate deafferentation (D = 40% and D = 60%, middle rows). For strong deafferentation (D = 80% and D = 100%, bottom rows), however, we observed pronounced synchronized periodic network activation. In summary, cross-correlograms progressively showed more oscillatory structure with growing period for increasing deafferentation degree (Figure 1-3B, from top to bottom). Thus, the more severe the deafferentation, the slower and the more pronounced the periodic activation patterns of the network became. Interestingly, the oscillatory structure of the cross-correlograms did not increase linearly with deafferentation degree. Instead, we observed a rather abrupt transition between D = 60% (low amplitude cross-correlogram) and D = 80% (high amplitude cross-correlogram).

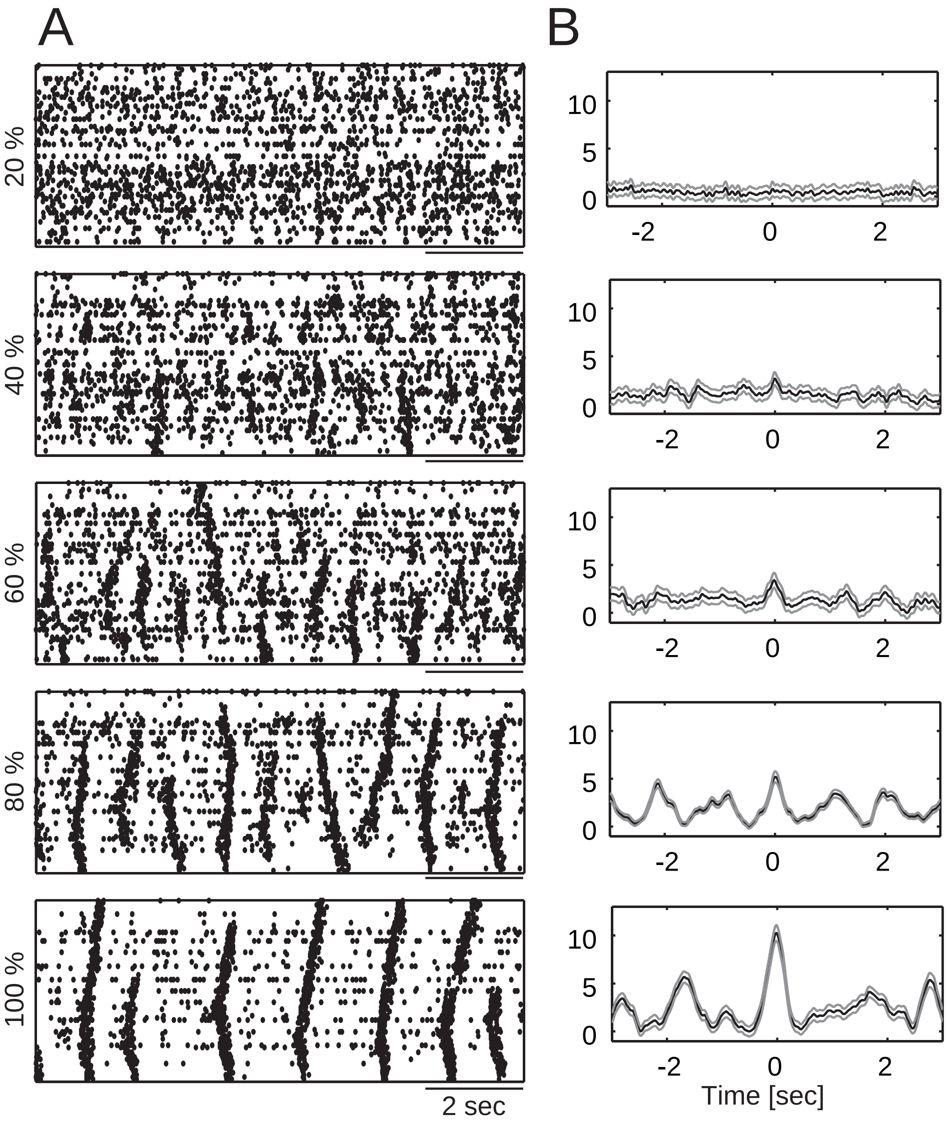

Figure 1-3 (A) Rastergrams for PYs after homeostatic scaling in response to different deafferentation degrees (*D* = 20% to *D* = 100% from top to bottom). (B) Average cross-correlograms show very little oscillatory activity up to *D* = 60%, however for *D* = 80% and *D* = 100% strong pronounced oscillations occurred. Oscillation frequency decreased for increasing degree of deafferentation.

So far, we have discussed the “steady-state” network dynamics after recovery of the target firing rate by synaptic scaling. Now, we consider the temporal evolution of activity during synaptic scaling (Figure 1-4). The following key observations become evident: (1) Firing rates as a function of time for increasing degrees of deafferentation (color coded in Figure 1-4A, $D = 20\%$ to $D = 100\%$ panels from left to right) show that recovery of overall activity levels by synaptic scaling is shaped by cells with high firing rate before deafferentation (continuous horizontal bands of hot colors in Figure 1-4A). After synaptic scaling, non-zero firing rates occurred preferentially in cells in close proximity to these highly excitable cells. (2) For strong degrees of deafferentation ($D = 80\%$ and $D = 100\%$), network-wide activation occurred and cells that were silent before deafferentation became active (decreased sparseness in comparison to before deafferentation).The observed reorganization of global network dynamics in response to partial deafferentation by homeostatic synaptic scaling is a result of interplay between excitability of deafferented and intact PYs cells. We therefore compared the initial firing rates α before deafferentation (measure of excitability because all cells received the same amount of afferent input), firing rates β immediately after deafferentation, and firing rates γ after recovery of target activity level by synaptic scaling.

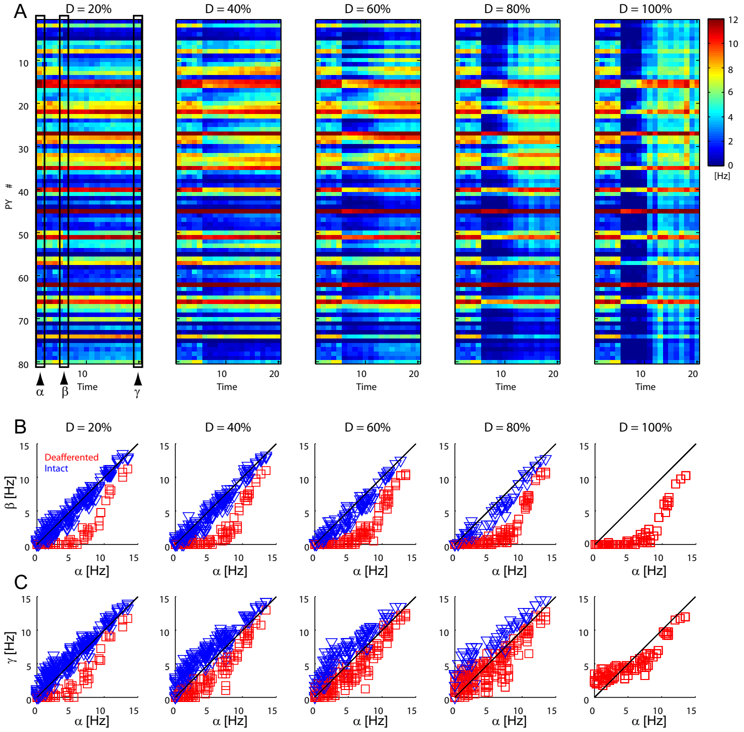

Figure 1-4 (A) Firing rates as a function of time for 80 PYs (panels correspond to increasing degrees of deafferentation from left to right). Hot colors indicate high firing rates; cool colors indicate low firing rates. For severe deafferentation, network-wide activation occurred (*D* = 80% and *D* = 100%). Arrow heads indicate three time points considered in panels (B) and (C): firing rates *α* before deafferentation, firing rates β shortly after deafferentation and firing rates *γ* after homeostatic scaling in response to deafferentation. (B) Scatter plots with firing rates *β* immediately after deafferentation as a function of firing rates *α* before deafferentation. Red squares represent firing rates of deafferented cells, blue triangles indicate intact cells (not subject to deafferentation). Black lines denote identity lines (no change in firing rate caused by deafferentation). Intact cells showed increasing decreases in firing rate for progressively more severe degrees of deafferentation (from left to right) as indicated by blue triangles falling below identity line. Deafferented cells fell silent if they exhibited low firing rate before deafferentation (red squares on abscissa). (C) Same representation as in (B) but with firing rates *γ* after synaptic scaling on ordinate. Intact cells show recovery and overcompensation (blue triangles above unit line). Deafferented cells partially recovered their prior firing rate α before deafferentation (red squares closer to unity line than in (B). For severe degrees of deafferentation, however, less excitable cells with low firing rates before deafferentation showed overcompensation (red squares above unity line for *D* = 80% and 100%).

We next established the relative contributions of deafferented and intact cells to the recovery of the target firing rate as function of their excitability. In theory, it is conceivable that reorganization is mediated by (1) intact cells increasing their firing rate, (2) deafferented cells recovering their firing rate, or (3) a combination of the latter two mechanisms in any temporal order. To test which hypothesis is correct, we separated intact (blue triangles) from deafferented cells (red squares) and plotted firing rate β (immediately after deafferentation) and firing rate γ (after synaptic scaling), respectively, as a function of initial firing rate α (before deafferentation) (from left to right in Figure 1-4B and C, from 20% to 100% deafferentation; β as a function of α in Figure 1-4B, γ as a function of α in Figure 1-4C). Intact cells (blue) suffered little loss of activity for mild to moderate deafferentation (firing rates β crowded along the diagonal). For stronger deafferentation, however, rates of PYs with intact input fell consistently below the diagonal (e.g. Figure 1-4B, D = 80%). Quite in contrast, the drop in firing rate for deafferented cells (shown in red) depended on their intrinsic excitability (i.e. firing rate α before deafferentation). Specifically, PYs with low α turned silent in response to deafferentation and thus clustered on the x-axis. Other PYs (i.e. those with relatively high firing rate α before deafferentation) also suffered from a decrease in firing rate, but stayed active after deafferentation. After homeostatic scaling (Figure 1-4C), PYs with intact afferent input assumed firing rates γ above initial firing rates α for all degrees of deafferentation (blue triangles above diagonal). For deafferented PYs, we found two distinct patterns of behavior depending on the degree of deafferentation. Relatively little increase in firing rates caused by synaptic scaling occurred in case of weak to moderate deafferentation (by comparison of Panels B and C). In case of strong deafferentation, however, we observed complete recovery of initial firing rates for some fraction of deafferented cells (red squares on and above diagonal for $D = 80\%$ and $D = 100\%$).

Next, we quantified the temporal dynamics of the activity levels of intact and deafferented cells. Specifically, we considered the case of 80% deafferentation in more details in order to determine the time-course and relative order of changes in firing frequency in (1) intact cells, (2) deafferented cells with initial firing frequency below target rate ($\alpha < f^*$), and (3) deafferented cells with initial firing frequency above target firing rate ($\alpha > f^*$). We computed the frequency shift for each cell by subtracting α from β and γ, respectively (histograms of frequency shifts in Figure 1-5A). As expected, the peaks of these distributions shift towards more positive values as time progressed (by comparison of top to bottom row in Panel A). Time-courses of mean values determined from frequency shift histogram fits exhibited sigmoid shapes for all three subpopulations (Figure 1-5B). Half-maximum frequency shift occurred almost simultaneously for cells with intact input (blue triangles) and deafferented cells with $\alpha > f^*$ (red diamonds). Only with a marked delay, however, deafferented cells with $\alpha < f^*$ increased their firing rates (red squares in 5B). Thus, the more excitable deafferented cells ($\alpha > f^*$) contributed to the early increase in activity levels after deafferentation and the less excitable cells ($\alpha < f^*$) mostly mediated the later increase

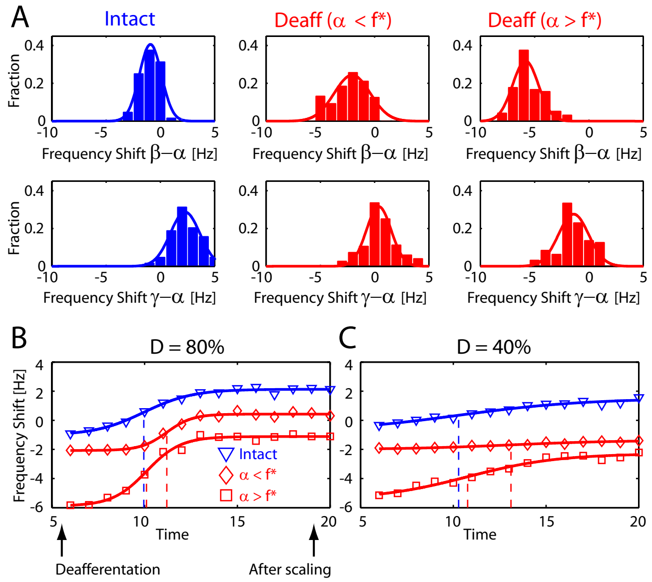

Figure 1-5 Recovery time-course of firing rates as a function of their input (intact in blue, deafferented in red) and of their excitability (low excitability with initial firing rate α below target firing rate f^*, high excitability with initial firing rate α above target firing rate f^*). Frequency shift represents the arithmetic difference between firing rate at a given time-point and the firing rate α before deafferentation (negative and positive values indicate undercompensation and overcompensation, respectively). (A) Distribution of frequency shifts β-α after deafferentation (top row) and frequency shifts γ - α after scaling (bottom row). Lines indicate Gaussian distribution fits. Both intact (left) and less excitable deafferented cells (middle) showed overcompensation (peak in distribution for positive frequency shifts). (B) Same analysis as in (A) for all time-points from deafferentation (time-point 6) to steady-state after homeostatic scaling (time-point 20). Plots show mean frequency shifts determined by Gaussian distribution fits as in (A). Vertical dashed lines indicate 50% of maximal shift determined from logistic functions fits. Both intact (blue triangles) and more excitable cells (red squares) reached 50% recovery at very similar time points. However, less excitable deafferented cells (red diamonds) reached 50% recovery at a later time-point (D = 80%, left). In case of D = 40% (right panel), however, less excitable cells contributed very little to recovery of the target firing (flat line for red diamonds).

in activity levels. In contrast, for D = 40% (Figure 1-5C), recovery of target activity level was almost exclusively mediated by intact PYs and deafferented PYs with $\alpha > f^*$. In summary, instead of further upregulating the firing rate of the more excitable cells in more deafferented networks (e.g. D = 80%), the scaling process recruited PYs that were silent or displayed only low activity level before deafferentation. We therefore found that reorganization of cortical network dynamics by synaptic scaling consists of several distinct processes occurring in a well-defined sequence as a function of the severity of partial deafferentation.

So far, we have established that recruitment of less excitable deafferented cells constituted a major difference between moderate and severe deafferentation by comparison of the time-courses of the respective mean firing rates for different deafferentation degrees. We therefore expected different firing rate distributions after synaptic scaling as a function of deafferentation degree. Specifically, our previous analysis suggests that strong deafferentation degree will reduce the fraction of silent cells (decreased sparseness). We quantified the time-course of firing rates on a cell-by-cell basis by plotting the time-dependent frequency histograms for D = 20% to 100% (Figure 1-6A, panels from left to right, black boxes indicates date re-plotted in Panels B and C). We had chosen the initial distribution of PY membrane voltages such that for intact afferent input a limited fraction of cells remained silent (hot colored patches in top left corners of panels in Figure 1-6A).

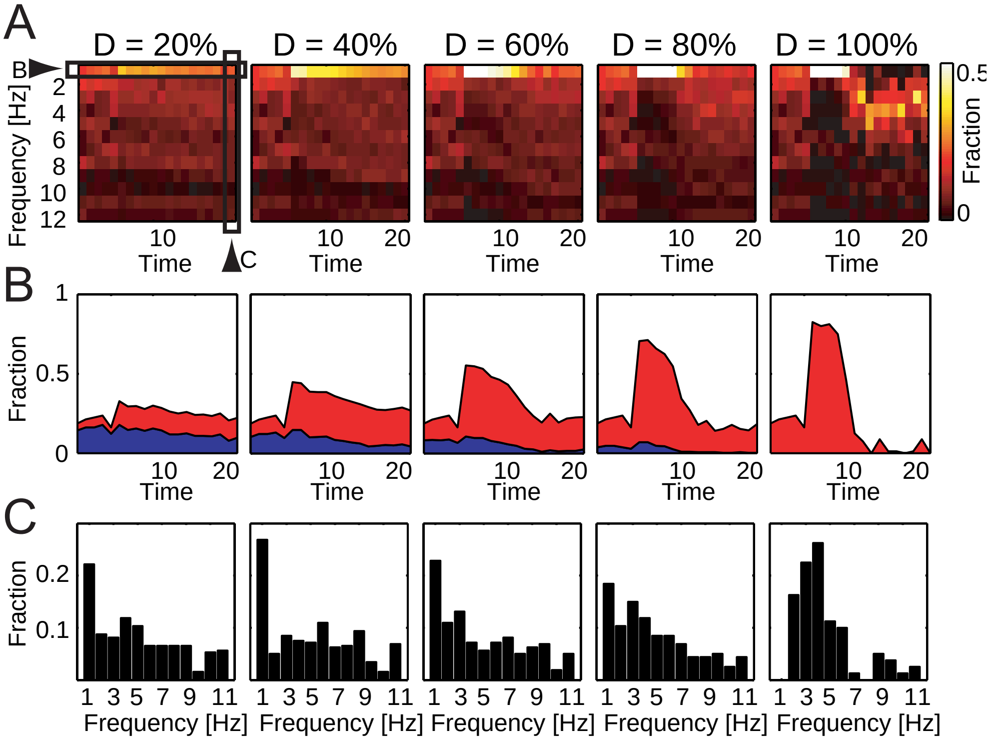

Figure 1-6 (A) Distribution of firing rates as a function of time for different deafferentation degrees (from 20% to 100%, from left to right). Black boxes indicate data that are replotted in (B) and (C). (B) Fraction of silent cells (firing rate below 1 Hz) as a function of time (intact cells in blue, deafferented cells in red). (C) Firing rate histograms after recovery of target firing rate by synaptic scaling.

Deafferentation transiently increased the number of silent cells. Indeed, while for mild to moderate deafferentation the fraction of silent cells recovered (in fact, in some cases to values higher than before deafferentation), more severe deafferentation qualitatively changed the firing rate distribution of the network such that all cells were active, resulting in a shift of the peak of the firing rate distribution as a function of time (Figure 1-6A, right most panel). We next considered the time-course of silent cells (split into two subpopulations, cells with intact input and deafferented cells, in blue and red, respectively, Figure 1-6B). In case of mild deafferentation, we observed a quite linear decrease in silent cells during synaptic scaling, mostly mediated by intact cells (blue band becomes narrower and red band assumes constant width as time progresses). This indicates that the network recovered its target activity level in part by activating cells with intact input that were silent right after deafferentation. Yet, for more severe deafferentation, we found a strongly nonlinear time-course of fraction of silent cell. In particular, the fraction of silent cells (average firing rate below 1 Hz) sharply increased after deafferentation, but then decreased to values lower than before deafferentation (vertical slice in Figure 1-6A, time-courses in Figure 1-6B). Thus, most of the silent cells, including the deafferented ones, became active during recovery of target activity level. Accordingly, frequency histograms after synaptic scaling exhibited a decrease in fraction of silent cells and a sharpening of the distribution (Figure 1-6C) in case of severe deafferentation.

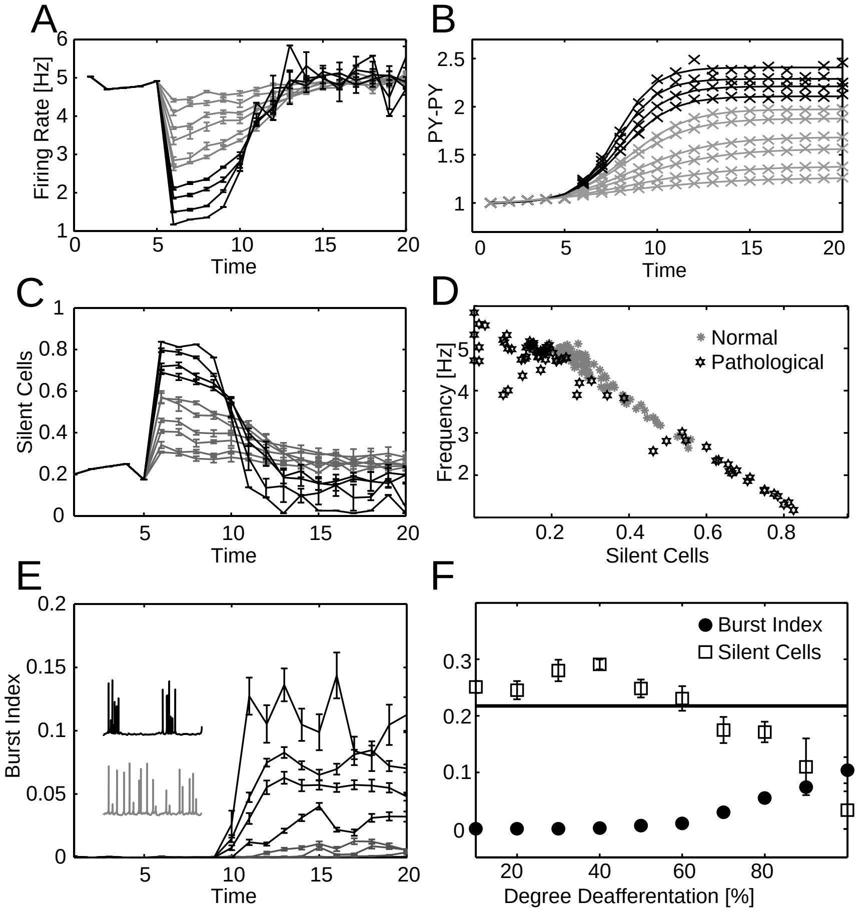

Figure 1-7 (A) Average PY network firing rate as a function of time. Each line corresponds to a deafferentation degree from *D* = 10% to *D* = 100%. The higher *D*, the stronger the initial drop of activity after deafferentation at time-point 5. Linear recovery time-course in gray, nonlinear recovery time-course in black. (B) Time-course of normalized PY-PY coupling (crosses: data, lines: logistic function fits) for *D* = 10% to *D* = 100%. Gray and black shading as in (A). More severe deafferentation causes more rapid scaling of recurrent excitatory synapses. (C) Time-course of fraction of silent cells for *D* = 10% to *D* = 100%. Gray and black shading as in (A). Similar clustering into linear and nonlinear time-course as in (A). (D) Average network frequency as a function of fraction of silent cells. Scatter plot of all time-points in (A) and (C). (E) Burst index (fraction of ISIs smaller 50 msec) as a function of time for *D* = 10% to *D* = 100%. Sample membrane voltage traces for *D* = 10% (single spikes) and *D* = 100% (bursts of spikes), respectively (2 sec). (F) Steady-state value of burst index (dark filled circles) and fraction of silent cells (open squares) as a function of *D*.

The average firing rate of the network as a function of time (Figure 1-7A) permitted a similar classification into more linear and more nonlinear time-courses (shown in gray and black, respectively). Specifically, for deafferentation degrees up to 60% (curves in gray), the network firing rate recovered with approximately even rate with only modest fluctuations in slope. In case of more severe deafferentation (*D* = 70% and higher), however, an initially relative flat time-course is followed by an epoch of high slope recovery (curves in black). In other words, we found linear firing rate time-course for weak to moderate deafferentation and nonlinear firing rate time-course for strong deafferentation. The deafferentation degrees for which this strong nonlinearity occurred corresponded to the values of deafferentation for which we found pronounced network oscillations after synaptic scaling (Figure 1-3). These two distinct recovery modes were not a simple consequence of how the PY-PY coupling was scaled by the dynamics of the homeostatic plasticity rule. Time-courses of the recurrent AMPA conductance on PYs were well fitted with sigmoids for all degrees of deafferentation (Figure 1-7B) independent from whether the firing rate time-course was linear or not. Therefore, the scaling rule itself was not the direct source of the non-linear recovery behavior for severe deafferentation. Rather, the time-course of the fraction of silent cells (Figure 1-7C, summary plot from data in Figure 1-6B, for *D* = 10% to 100%), exhibited strong similarity to the time-courses of the average network firing rate (Figure 1-7A). A scatter plot of average network firing rates and fraction of silent cells indeed exhibited tight correlation (Figure 1-7D). Thus, the two different network behaviors for mild/moderate and severe deafferentation, respectively, are driven by the differential recruitment of additional cells that resulted in decreased fraction of silent cells (i.e. sparseness) after severe deafferentation.

We then determined how this finding related to the observed bursting for strong deafferentation (Figure 1-2) by computing the relative fraction of interspike intervals smaller than 50 ms (burst index) as a function of time after deafferentation for D = 10% to 100%. Similar in time-course to the fraction of silent cells, burst index strongly increased for $D > 60$ % (Figure 1-7E). A comparison of steady-state values of fraction of silent cells and burst index after recovery of target firing rate as a function of deafferentation shows that, as the fraction of silent cells falls below the value before deafferentation, cells in the network fire bursts of action potentials (Figure 1-7F). We therefore found a transition point that determines whether the network recovered with limited pathological consequences (no bursting, sparseness maintained, no pronounced oscillation with synchrony) or not. In our case, this transition point occurred between D = 60% and 70%.

We expected pathological reorganization by homeostatic plasticity after severe deafferentation to have a negative impact on the network ability to respond to afferent input. We quantified and compared the impact of afferent and recurrent excitatory input on spiking in PYs by calculating the spike-triggered average afferent and recurrent excitatory conductance. This measure allows for a direct quantitative comparison of the role of afferent and recurrent excitation in driving spiking of postsynaptic cells. For example, if recurrent excitation is sufficiently weak that the afferent input alone determines when a postsynaptic cell spikes, we would expect in average a flat, low-amplitude spike-triggered conductance for recurrent excitation and a pronounced transient increase in spike-triggered afferent conductance. In other words, a comparison of the peak values of the spike-triggered conductances serves as a measure for the relative importance of afferent and recurrent excitation in determining the network dynamics. Here, afferent excitation was dominant before deafferentation (Figure 1-8A, left; total excitatory conductance in black, afferent excitatory conductance in red, recurrent excitatory conductance in blue) and after synaptic scaling in response to deafferentation for moderate degrees of deafferentation (Figure 1-8A, middle, D = 40%). Recurrent excitation, however, dominated after synaptic scaling in case of more severe deafferentation (Figure 1-8A, right, D = 80%). Integrated spike-triggered total excitatory conductances for different degrees of deafferentation were fairly constant (Figure 1-8B, black line) The more deafferented the network was, however, the stronger the integrated recurrent excitatory conductance was (Figure 1-8B, blue line). A comparison of the peak values further emphasized the critical degree of deafferentation between 60% and 70% (Figure 1-8C). At this point, the peak recurrent excitation exceeded the peak afferent excitation. Thus, pathological network reorganization was mediated by a shift between afferent and recurrent excitation that resulted in poor information transmission in case of severe deafferentation since the influence of the afferent input on spiking was very limited (low amplitude spike-triggered conductance). This shift, therefore, may explain deficiency of normal cortical function as a result of brain disorders associated with cell loss.

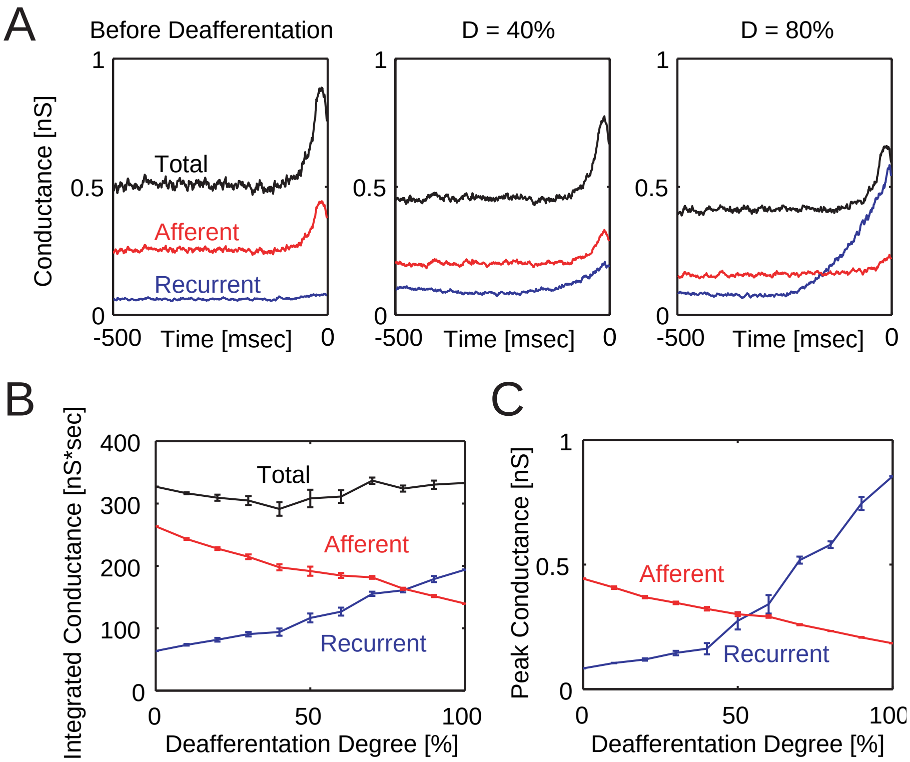

Figure 1-8 Spike-triggered conductances. (A) Afferent excitatory (red), recurrent excitatory (blue), and total (black) spike-triggered synaptic conductance for PYs (left: before deafferentation; middle: D = 40%; right: D = 80%). (B) Integrated spike-triggered afferent (red), recurrent (blue), and total (black) excitatory conductance. (C) Peak values of spike-triggered afferent (red) and recurrent (blue) excitatory conductance.

DISCUSSION

Homeostatic plasticity describes the regulation of synapses and intrinsic properties to counteract changes in activity levels and to maintain overall stability of synaptic strength (Turrigiano, 2007; Turrigiano et al., 1998; Turrigiano and Nelson, 2004). Here, we studied homeostatic plasticity as a putative mechanism for cortical network reorganization that occurs during CNS disorders associated with neural dysfunction. We assumed (1) that the loss of inputs that occurs in cortical disorders with structural damage is random, (2) that a homeostatic rule scales the recurrent excitatory synapses on PYs to match the average firing rate of the network before disease onset, and (3) that disease severity can be modeled by varying fractions of deafferented cells. On the basis of these assumptions, we simulated cortical network models subject to different deafferentation degrees and found a critical threshold for pathological network reorganization. For deafferentation more severe than this critical value, we observed periodic network-wide discharges with bursts of action potentials in individual cells after homeostatic scaling of recurrent excitatory synapses. Our findings therefore represent an unexpected and seemingly paradoxical effect of homeostatic plasticity. In fact, the target frequency of the whole network was indeed recovered in our model but the spike timing was substantially altered such that there were periods of high activity interleaved with epochs of relative quiescence in case of severe deafferentation (periodic EEG complexes). As a result of this pathological network reorganization, representation of afferent input in the spiking of the network was severely diminished since the network dynamics were dominated by recurrent excitation (Figure 1-8).

Computational network models of homeostatic plasticity have almost uniquely focused on the role of synaptic scaling in regulating and stabilizing overall synaptic excitability in presence of Hebbian learning (Lazar et al., 2007; Rabinowitch and Segev, 2006a, b; Toyoizumi et al., 2007; Triesch, 2007). Computational models of tinnitus suggested involvement of homeostatic plasticity (Dominguez et al., 2006; Schaette and Kempter, 2006), but there has been little work that examines the role of homeostatic plasticity in more realistic, conductance-based models of cortical networks. In a previous computational modeling study (Houweling et al., 2004), cortical deafferentation was simulated to examine homeostatic plasticity as a potential cause of posttraumatic epilepsy. A recent study with cultured hippocampal slices provided further support for this hypothesis (Trasande and Ramirez, 2007). In contrast to this previous modeling work, we have now studied the time-course of network reorganization after partial deafferentation in order to understand the specific roles of intact and deafferented cells as function of time after disease onset. Since we here studied disorders of the cortex that incapacitate a presumably random fraction of neurons, the partial deafferentation scheme is different from the one previously used to investigate posttraumatic epilepsy (Houweling et al., 2004) where all cells in the network were subject to the same degree of reduction in input.

A priori, the heterogeneity of input levels introduced by partial deafferentation permits two orthogonal strategies of recovering target network activity levels. In the first scenario, intact cells carry the burden of recovering target activity levels by increasing their firing rate above their initial activity level before partial deafferentation. In the second scenario, deafferented cells recover their firing rate. In our simulations, we found the two scenarios to occur in a well-defined temporal sequence. In case of mild to moderate deafferentation, we only observed concurrent upregulation of firing rates of both intact cells and more depolarized deafferented cells. Only in case of severe deafferentation, less excitable deafferented cells also became active. Thus, network reorganization in response to partial deafferentation is not a linear process. Rather, we found a non-linear regime that essentially mediated a threshold for pathological reorganization in case of more severe deafferentation.

The goal of our work is to provide hypotheses to experimentalists and clinicians about the underlying mechanism of aberrant brain activity in response to CNS disorders. As for any computer simulation, the conclusions drawn are inherently limited by the accurateness and sophistication of our model. We purposefully did not attempt to closely match any specific experimental data set in order to keep the model as general as possible. Rather, we used a modified version of a standard cortical network model that consisted of locally connected, conductance-based pyramidal cells and inhibitory interneurons. Nevertheless, two novel aspects of our model deserve closer scrutiny. First novelty in our model was the choice of homeostatic scaling rule.

Most likely, homeostatic plasticity describes a range of different phenomena at different spatial scales and with different expression loci (Turrigiano, 2007). Activity levels could be sensed and regulated at the synapse, cell, or network level. We modeled homeostatic plasticity at the network level [e.g. mediated by a diffusible factor as in (Stellwagen and Malenka, 2006)] by designing a simple rule that prescribed incremental scaling of synaptic conductances proportional to their size and to the mismatch between target and current average frequency. Exploratory simulations indicated that more local homeostatic rules are likely to result in different patterns of network reorganization after partial deafferentation. *In vitro* studies of neural cultures exposed to activity blockage showed concurrent upregulation of AMPA synapses and downregulation of $GABA_A$ synapses (Kilman et al., 2002; Mody, 2005; Turrigiano et al., 1998). Little is known, however, about homeostatic scaling of inhibition *in vivo* (Echegoyen et al., 2007; Mody, 2005) and we therefore did not include such a mechanism in our model. Second novel design choice was the random pattern of partial deafferentation as a model of the effect of cortical disease on neural firing. This choice is based on the phenomenological approximation that a broad class of CNS disorders cause diffuse random cell loss and thus partial deafferentation of postsynaptic circuits. Although our model certainly represents a simplification of the underlying processes, it is sufficiently refined and accurate to provide new hypotheses and insights about the pathophysiology of slow periodic discharges in a broad range CNS disorders affecting cortex.

There is little *in vivo* data available on the dynamics of cortical circuits in CNS disease at the cellular and synaptic level. The findings from our modeling work therefore represent predictions that require comprehensive experimental testing. However, there exists ample literature on EEG patterns in patients with CNS disorders [reviewed in (Niedermeyer, 2005)] that we used to qualitatively assess our model simulation results. Our model predicts the following EEG characteristics: (1) slow periodic discharges in severely deafferented networks (Figure 1-1 and 1-2), (2) decrease in frequency of periodic discharges during disease progression (Figure 1-3), and (3) delayed onset of network reorganization in comparison to disease progression (Figure 1-7). The clinical EEG literature confirms all three predictions. Periodic discharges at low frequencies are a hallmark of many types of CNS disorders associated with transient and permanent cell loss (Niedermeyer, 2005). Delayed onset and recovery of EEG during recovery from CNS disease has been observed for example in case of herpes simplex infections (Illis and Taylor, 1972; Upton and Gumpert, 1970).

Little progress has been made in the debate about the nature of periodic discharge types and mechanisms (Chong and Hirsch, 2005; Hirsch et al., 2005; Jirsch and Hirsch, 2007). The variety of structural damages has hindered the development of a unifying theory about the pathophysiology (Gurer et al., 2004; Kalamangalam et al., 2007; Yemisci et al., 2003). We found that homeostatic plasticity is a very likely candidate mechanism underlying pathological reorganization of cortical network dynamics in CNS disease. Hopefully, our findings on reorganization dynamics and critical value of disease progression for occurrence of pathological macroscopic oscillations will serve as a starting point for the development of early intervention approaches to prevent secondary cortical dysfunction caused by homeostatic plasticity.

ACKNOWLEDGEMENTS

Section 1.1, in full, is a reprint of the material as it was submitted to the Journal of Neuroscience, 2007, Frohlich, Flavio; Bazhenov, Maxim; Sejnowski, Terrence. The dissertation author was the prime investigator and author of this paper.

1.2 Interictal Discharges Originate at the Border between Intact and Deafferented Cortex

INTRODUCTION

Traumatic brain injury (TBI) is a common cause of epilepsy. Although certain risk factors for posttraumatic epilepsy (PTE) have been identified, the pathophysiology of PTE remains unknown (D'Ambrosio and Perucca, 2004; Garga and Lowenstein, 2006). Interestingly, interictal discharges start to occur early after TBI but spontaneous seizures with clinical manifestation usually appear only significantly later (Staley and Dudek, 2006). Interictal discharges represent synchronous bursts of action potentials (paroxysmal depolarizing shift) by neurons in epileptic cortical networks and have served as clinical EEG marker for many decades. The possible role of interictal discharges in epileptogenesis after TBI remains unclear.

Deafferentation by cortical undercut is used to study cortical network reorganization in response to a substantial decrease in afferent input by injury (Bazhenov et al., 2007). Surgically isolated cortical slabs (“islands”) developed paroxysmal bursting over the time-course of hours to days (Echlin and Battista, 1963; Sharpless and Halpern, 1962). Slices from deafferented cortex (Hoffman et al., 1994) revealed changes in both intrinsic properties (Prince and Tseng, 1993) and excitatory synaptic transmission (Li and Prince, 2002) (formation of new excitatory circuits by axonal sprouting (Jin et al., 2006; Salin et al., 1995) and enhanced release probability (Li et al., 2005)). Recently, in *vivo* recordings over several weeks after partial deafferentation in chronically implanted animals showed an increase in spontaneous seizure occurrence (Nita et al., 2006, 2007). The possible confounder that spontaneous seizures also occur in absence of cortical undercut in case of ketamine-xylazine anesthesia was eliminated by recordings in the unanaesthetized head-fixed animal (Nita et al., 2007).

Despite these advances in the development of animal models of TBI and PTE, the mechanisms that turn a network silenced by (partial) deafferentation into a network that exhibits hypersynchronous paroxysmal activity have remained unclear. Based on a computational model of an isolated cortical slab, we previously suggested that homeostatic plasticity (Rich and Wenner, 2007; Turrigiano, 2007) may be a key player in posttraumatic epileptogenesis (Houweling et al., 2005). This counter-intuitive pathological effect of homeostatic plasticity resulted from the upregulation of recurrent excitatory synapses to compensate for the loss in afferent excitatory input by simulated axotomy. As a consequence of this shift from afferent to recurrent excitation, paroxysmal periodic network activation occurred for uniform deafferentation of the entire cortical network (Houweling et al., 2005). More recently, we found similar periodic activity after deafferentation of a random subpopulation of cells (Chapter 1.1). So far, these computational models have not taken into account the geometry of partial deafferentation in experimental cortical undercuts.

We here studied the effect of homeostatic plasticity on the border zone between intact and deafferented cortex in a computational network model with local synaptic connectivity. We found two distinct types of posttraumatic network dynamics after homeostatic scaling. In cases of mild to moderate lesion sizes, the deafferented cortex remained quiet and the intact cortex compensated for the loss in activity. For larger lesions, we additionally found irregular network-wide bursts that qualitatively resemble interictal spikes. These discharges were initiated at the border to the injured cortex and propagated through the deafferented cortex.

METHODS

The computational model used in this study has been previously described in details elsewhere (Frohlich and Bazhenov, 2006; Frohlich et al., 2006; Mainen and Sejnowski, 1996). Briefly, the network consisted of two-compartment conductance based models of pyramidal cells (PYs) and fast-spiking inhibitory interneurons (INs). The axo-somatic compartment of both PYs and INs included a voltage-gated sodium (PY: $G_{\mathrm{Na}} = 3000$ mS/cm^2, IN: $G_{\mathrm{Na}} = 2500$ mS/cm^2), a delayed-rectifier potassium ($G_{\mathrm{Kv}} = 200$ mS/cm^2), and a leak conductance ($G_{\mathrm{Kl}} = 0.1$ mS/cm^2). The dendritic compartment was endowed with high-threshold calcium, calcium-activated potassium, slowly-activating potassium, persistent sodium, hyperpolarization-activated depolarizing mixed cationic, potassium leak, and mixed cationic leak conductances (PY: $G_{\mathrm{HVA}} = 0.016$ mS/cm^2, IN: $G_{\mathrm{HVA}} = 0.01$ mS/cm^2; PY: $G_{\mathrm{KCa}} = 3.5$ mS/cm^2, IN: $G_{\mathrm{KCa}} = 0.3$ mS/cm^2; PY: $G_{\mathrm{Km}} = 0.01$ mS/cm^2, IN: $G_{\mathrm{Km}} = 0.0$ mS/cm^2; PY: $G_{\mathrm{NaP}} = 4.0$

mS/cm^2, IN: G_{NaP} = 0.0 mS/cm^2; G_{h} = 0.05 mS/cm^2; PY: G_{Kl} = 0.01 mS/cm^2, IN: G_{Kl} = 0.005 mS/cm^2; G_{L} = 0.033 mS/cm^2). Synaptic transmission was modeled with a simplified first-order kinetic scheme with immediate rise and exponential decay of synaptic conductances. All excitatory connections had a fast AMPA and a slow voltage-dependent NMDA component (total conductances: $g_{\mathrm{AMPA(PY\text{-}PY)}}$ = 3.2 nS, $g_{\mathrm{NMDA(PY\text{-}PY)}}$ = 0.32 nS, $g_{\mathrm{AMPA(PY\text{-}IN)}}$ = 3.0 nS, $g_{\mathrm{NMDA(PY\text{-}IN)}}$ = 0.30 nS). Inhibition was mediated by fast GABA$_{\mathrm{A}}$ synaptic conductances ($g_{\mathrm{GABA(IN\text{-}PY)}}$ = 4.0 nS). Synaptic connectivity was local (footprint radii: PY-PY: 5; PY-IN: 1; IN-PY: 5). AMPA synapses were endowed with short-term depression (7% use constant; 700 msec recovery time-constant).

Both PYs and INs received random afferent input (Poisson process with rate 100 Hz; conductances: g_{PY} = 0.5 nS and g_{IN} = 1.0 nS). At deafferentation, input frequency of a contiguous block of both PYs and INs was reduced to 10 Hz. A simple homeostatic scaling rule scaled $G_{\mathrm{PY\text{-}PY}}$ such that the average firing rate of all PYs in the network eventually matched the target frequency f^* = 5 Hz. Here, we only discuss the steady-state network dynamics after f^* was recovered.

RESULTS

We used a one-dimensional network of 80 PYs and 20 INs to study "posttraumatic network reorganization" mediated by homeostatic scaling of recurrent excitatory PY-PY synapses after partial deafferentation. In our model, a contiguous block of cells were deafferented (lesion size measured in fraction of deafferented cells D). Synaptic coupling strengths were set such that both the random afferent input and the recurrent connections within the cortical network contributed to the random firing behavior before deafferentation (average firing rate $f = 5$ Hz).

In response to deafferentation of 80% of all PYs and INs ($D = 80\%$), the average firing rate of the network dropped to 1.4 Hz (not shown). The homeostatic plasticity rule then scaled the excitatory PY-PY synapses (AMPA-type) such that the average target firing rate $f^* = 5$Hz was eventually recovered. Although the average network firing rate was the same after homeostatic scaling as before deafferentation, we found substantial reorganization of network dynamics (Fig. 1-9A). Specifically, the firing behavior of intact (i.e. "non-deafferented") and deafferented cells strongly differed (Fig. 1-9B). Intact cells fired rhythmic bursts of action potentials with a frequency of about 2 Hz (average cross-correlogram in Fig.1-9C, bottom panel). The deafferented subpopulation, however, was essentially silent with the occasional exception of massive network-wide burst discharges that occurred in irregular intervals (Fig. 1-9C, top panel). All of these bursts ("interictal spikes") originated at the border between intact and deafferented cortex and invaded the deafferented cortex (cross-correlograms in Fig. 1-9D).

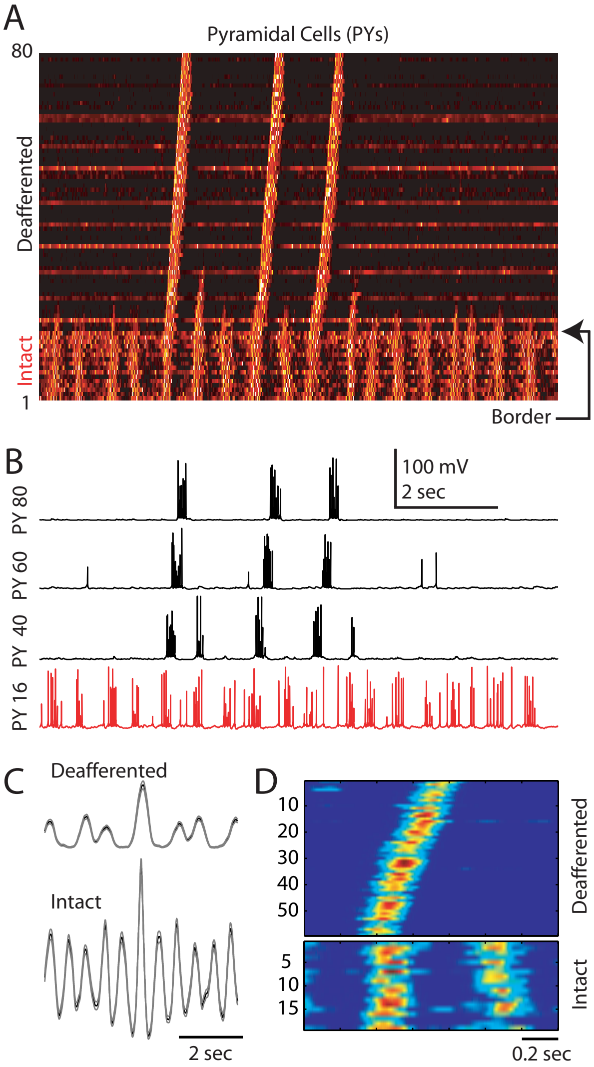

Figure 1-9 Increased activity in intact subpopulation and irregular network discharges in deafferented subpopulation after homeostatic scaling in response to partial deafferentation. (A) Activity map of 80 PYs (dark and hot colors correspond to hyperpolarized and depolarized membrane voltages, respectively); Top 80% PYs were subject to deafferentation; inputs to bottom 20% PYs remained intact. (B) Sample membrane voltage traces of PYs for same time interval (cell 16 with intact input, cells 40, 60, and 80 were deafferented). (C) Average cross-correlograms for deafferented (top) and intact (bottom) subpopulation. S.E.M. shown in gray. (D) Cross-correlation of cell 16 at border between intact and deafferented cells with all deafferented (top) and intact (bottom) cells.

The appearance of these network-wide discharges depended on the relative fraction of deafferented cells *D* (i.e. lesion size). We found either of two distinct "posttraumatic" network-behavior types after homeostatic synaptic scaling. For D ≤ 50%, homeostatic scaling recovered the target network firing rate without any significant suprathreshold activation of the cells silenced by deafferentation (Fig. 1-10A, top panel, *D* = 50%). The intact cells exhibited synchronized periodic activation due to the increased excitatory PY-PY coupling. Thus, the injured cortex remained permanently quiet while the intact cortex compensated for the loss of activity caused by partial deafferentation. We call this outcome *Type I Post-Traumatic Network Dynamics* (rhythmic hyperactivity in intact subpopulation, silence in deafferented subpopulation). For deafferentation fraction D ≥ 60%, we found not only rhythmic bursts in intact cortex but also irregular network-wide bursts that propagated through the injured cortex (*Type II Post-Traumatic Network Dynamics;* Fig. 1-10A, middle panel, *D* = 60 %). For even larger lesions (e.g. D = 70% in Fig. 1-10A, bottom panel), the occurrence of these network-wide bursts remained irregular but increased in frequency.

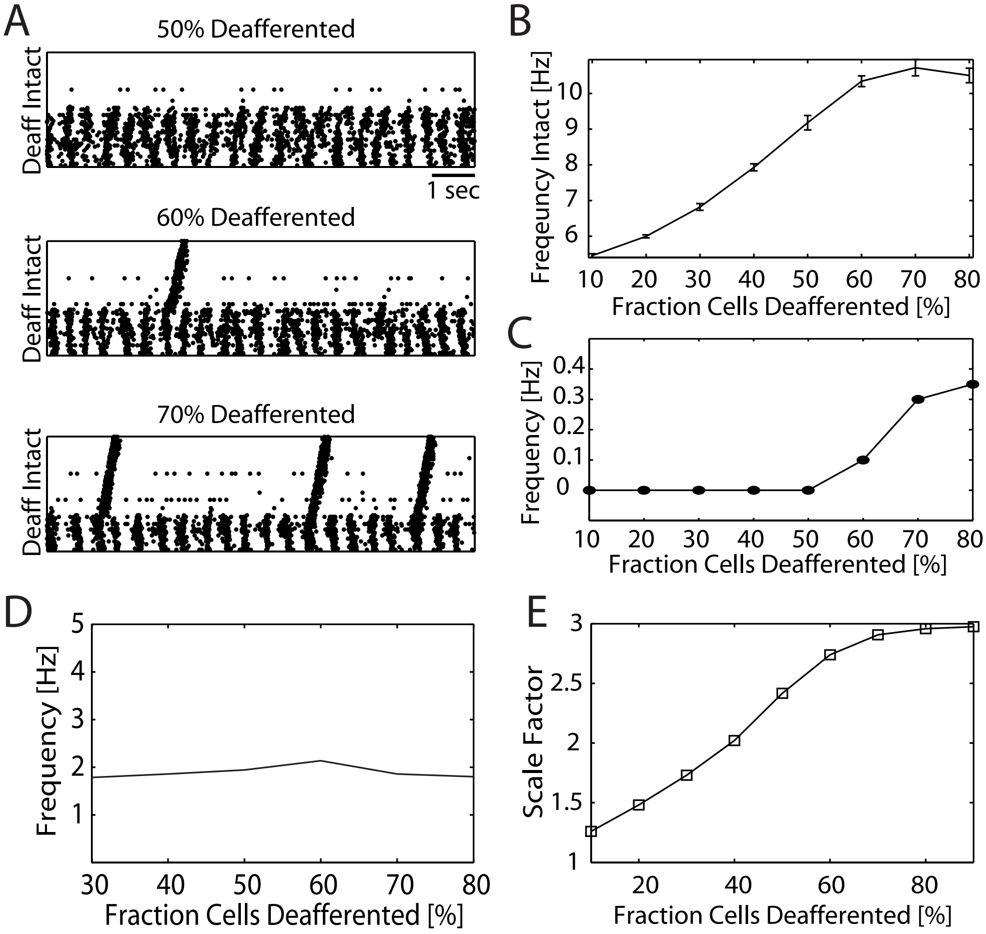

Figure 1-10 Posttraumatic network reorganization as a function of fraction of deafferented cells (lesion size). (A) Raster plots of 80 PYs after homeostatic scaling in response to partial deafferentation. Top Panel: Top half of network is deafferented (intermediate lesion size, D = 50%). Recovery of target firing rate is almost exclusively mediated by intact cells. Middle Panel: Occasional burst of activity in deafferented subpopulation (“interictal discharge”) for D = 60%. Bottom Panel: Increased frequency of network-wide discharges (D = 70%) for larger lesions. (B) Average frequency of intact PY subpopulation. (C) Frequency of irregular discharges in deafferented network (determined over 10 sec window). (D) Average burst frequency in intact subpopulation. Determined from average cross-correlogram. (E) Scaling factor of recurrent AMPA-type PY-PY synaptic conductance $G_{\text{PY-PY}}$.

We next quantified the firing behavior of the intact and deafferented subpopulations for relative deafferentation fractions $D = 10\%$ to $D = 90\%$. Average firing rate of the intact subpopulation (Fig. 1-10B) increased with growing deafferentation fraction D as long as long as no network-wide bursts occurred (Type I, $D \leq 50\%$, Fig. 1-10C). The increased average firing frequency was not accompanied by a substantial increase in burst frequency in the intact subpopulation (Fig. 1-10D) but was rather mediated by activation of less excitable intact cells. For deafferentation fractions D that resulted in Type II network dynamics, however, intact firing rate grew very little for increasing deafferentation fractions D. In summary, network-wide bursts only occurred in case of large lesions for which the intact sub-network was incapable of fully recovering the target firings rate.

These two different types of reorganization outcomes were also reflected in the amount of $G_{\mathrm{PY\text{-}PY}}$ scaling that was required for recovering the target firing rate (Fig. 1-10E). The slope of $G_{\mathrm{PY\text{-}PY}}$ as a function of deafferentation fraction D was higher for Type I than for Type II. Thus, for excitatory synaptic conductances that were sufficiently strong to mediate network-wide bursts, minor additional scaling was sufficient to increase the frequency of network-wide bursts and recover the target network average.

Importantly, we did not find the above discussed reorganization of a partially deafferented cortical network in case of weaker deafferentation where more of the afferent input per deafferented cell was maintained (input frequency reduced to 50 Hz instead of 10 Hz). In the case of such weaker deafferentation, different network activity patterns emerged depending on the specific distribution of intrinsic excitabilities in a given simulation (two different cases, i.e. “Network 1” and “Network 2”shown in Figure 1-11). The average cross-correlograms of the spike trains of the deafferented cells exhibited different frequencies for the two networks (Figure 1-11, Panel B). Despite these differences in reorganization outcome, we have never found consistent emergence of activity bursts that would have originated in the border zone and propagated through the deafferented subnetwork. Therefore, the model suggests that milder deafferentation may not have as devastating consequences as more severe deafferentation does.

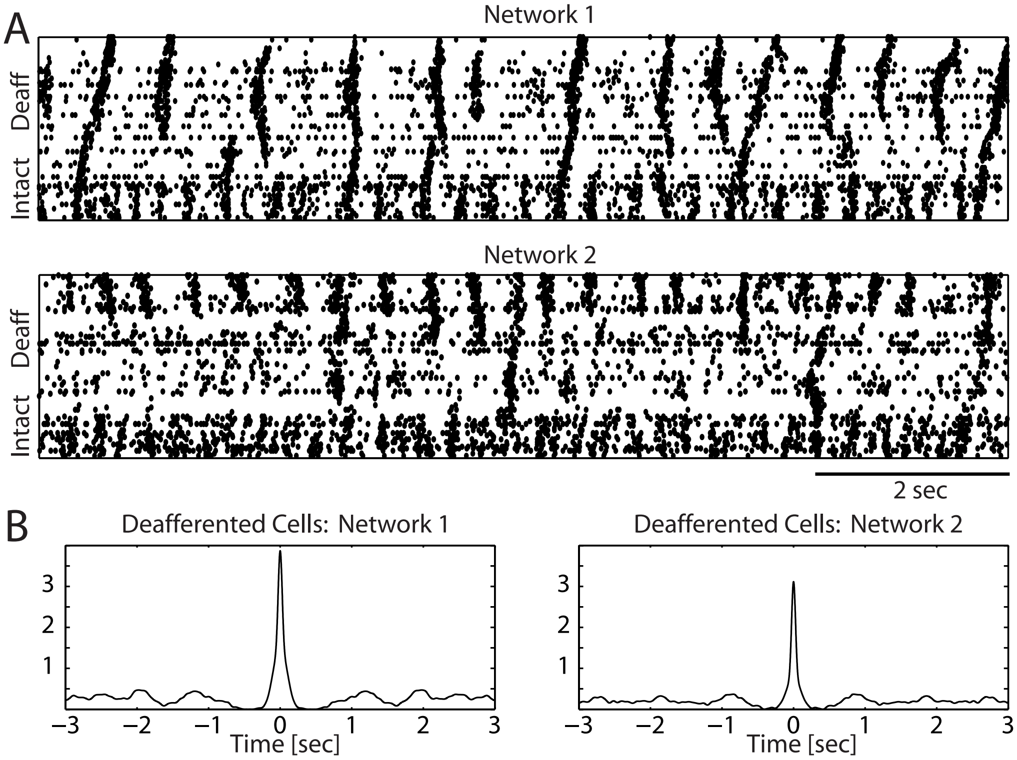

Figure 1-11 (A) Two sample rastergrams of partially deafferented (*D* = 80%) networks in case of weaker deafferentation (i.e. more afferent input retained). Network dynamics differed from simulation to simulation depending on the specific random distribution of intrinsic excitability. Importantly, no consistent network-wide bursts emerged at the border between intact and deafferented subnetworks. (B) Average cross-correlograms for deafferented cells. Note the different oscillation frequencies.

DISCUSSION

Although the development of PTE appears to be a relatively slow process since first seizures may occur weeks to years after TBI, no successful clinical intervention has yet been found to hinder epileptogenesis after TBI. In particular, the prolonged prophylactic prescription of anti-epileptic drugs has mostly proven unsuccessful. The exact reasons for this disappointing finding remain unknown (D'Ambrosio and Perucca, 2004).

Cortical undercut is a model of cortical deafferentation by TBI. We previously suggested homeostatic plasticity as a candidate mechanism for the development of paroxysmal rhythmic discharges in deafferented cortical networks. Computational models of uniformly deafferented cortex showed that homeostatic plasticity increased the excitatory recurrent synapses between PYs such that periodic network bursts occurred for severe deafferentation (Houweling et al., 2005). Recent experiments *in vivo* investigated the activity at the border between intact and deafferented cortex in a partially deafferented cortical gyrus (Nita et al., 2006, 2007). We here used a computational network model to study the spatio-temporal network dynamics at this border zone. We found two distinct types of posttraumatic network dynamics depending on the relative size of the deafferented population. The main difference between these two types of network dynamics was the occurrence of irregular bursts (interictal discharges) in the deafferented network for larger lesions.

Importantly, the direct comparison between experiment and computational model is hindered by the fact that our model does not replicate different natural oscillatory states (e.g. slow sleep oscillations). Nevertheless, two key qualitative features of the model are in agreement with the findings in the chronic deafferentation preparation (Nita et al., 2006, 2007): (1) development of enhanced activity in the relatively intact cortex next to the injury site and (2) activity propagation from the border between intact and deafferented cortex into the undercut gyrus. As for any computational model, the predictive power of our model is limited by the accurateness and level of details included. Although our model neglects many details about cortical fine structure, we are confident that the mechanism studied here is sufficiently general to be applicable *in vivo*.

If homeostatic plasticity indeed plays a role in PTE it comes as little surprise that anti-epileptic drugs that reduce activity levels cannot prevent the development of PTE (Bazhenov et al., 2007). Rather, interventions that prevent homeostatic plasticity seem to deserve closer scrutiny as possible preventive measurements. In theory, both pharmacological interventions and electrical stimulation of deafferented networks may serve this purpose. Computational modeling as in this current study may become an important tool on the path towards a better understanding of PTE and the eventual development of effective prophylactic modalities.

ACKNOWLEDGEMENT

Section 1.2, in full, is a final draft of the material as it will be submitted for publication, Frohlich, Flavio; Bazhenov, Maxim; Nita, Dragos; Timofeev, Igor; Sejnowski, Terrence. The dissertation author was the prime investigator and author of this paper.

2 Potassium dynamics in the cortex and epilepsy

In this chapter, we present our studies on the role of extracellular potassium concentration $[K^+]_o$ in cortical seizures. The first section provides a comprehensive review of the literature on the role of $[K^+]_o$ seizure dynamics and links previous studies with more recent insights based on experiments and computational models. It concludes with a proposed research program to address a series of key unanswered questions. The remaining sections then present our original work on the topic. The second section focuses on seizure initiation and introduces a novel conceptual framework for seizure dynamics. The third section investigates tonic-clonic like transitions during cortical seizures. The fourth section describes the underlying dynamics of a pyramidal cell in elevated $[K^+]_o$. The fifth and last section contains material on a relevant but often ignored topic - seizure cessation.

2.1 New Insights on an Old Topic

Although ion concentrations in the central nervous system are perturbed in a broad range of neurological disorders, the role of extracellular potassium concentration $[K^+]_o$ in epilepsy has remained unclear. Historically, it was hypothesized that $[K^+]_o$ is the causal factor for epileptic seizures. This so-called potassium accumulation hypothesis had initially been subject to substantial debate but has subsequently failed to find wide acceptance. However, recent studies on the pathophysiology of tissue from epileptic human patients and animal epilepsy models revealed aberrations in the $[K^+]_o$ regulation apparatus. Computational models of cortical circuits that include ion concentration dynamics have acted as a catalyst for a renewed interest in the role of $[K^+]_o$ in epilepsy. We here connect classical and more recent insights on $[K^+]_o$ dynamics in cortex with the goal of providing starting points for a next generation of $[K^+]_o$ research. Such research may ultimately lead to an entirely new class of anti-epileptic drugs that act on the $[K^+]_o$ regulation system.

Gradients between intracellular and extracellular ion concentrations are the basis for electrical signaling in the nervous system by means of transmembrane ion currents (Hille, 2001; Somjen, 2002). Since ion currents reflect net ion flux across the cell membrane, these concentration gradients would rapidly degrade in the absence of mechanisms to maintain intra- and extracellular ion concentrations. Although the central nervous system is endowed with powerful ion concentration homeostasis mechanisms, ion concentrations do not assume constant values in the living brain.

Rather, they change over time in an activity-dependent manner and therefore are dynamic variables. Aberrant ion concentration homeostasis has been linked to variety of severe neurological conditions that include epilepsy, stroke, hypoxic encephalopathy, and migraines (Hille, 2001; Somjen, 2002).

As even minor fluctuations result in a measurable change in the K^+ equilibrium potential and therefore K^+ currents (Box 1), we here focus on extracellular potassium concentration $[K^+]_o$. Since K^+-currents play an essential role in controlling neuronal excitability, it was initially hypothesized that $[K^+]_o$ elevations are the cause of epileptiform activity (Fertziger and Ranck, 1970; Green, 1964). Measurements of $[K^+]_o$ with K^+ sensitive microelectrodes (KSMs, see Box 2) indeed showed increases in $[K^+]_o$ of several millimolars during experimental seizures. These recordings, however, appeared not to meet criteria for a causal role of $[K^+]_o$ in seizure initiation and termination since $[K^+]_o$ increases seemed delayed relative to the seizure onset and $[K^+]_o$ did not reach values where neurons would have been to depolarized to fire action potentials [see below, also e.g. (Somjen, 1979)]. As a consequence, interest in $[K^+]_o$ dynamics and their role in epilepsy had mostly waned.

Box 1

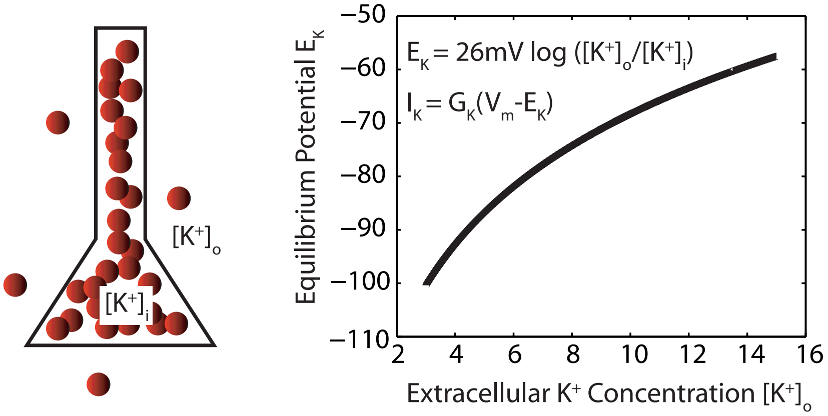

Intracellular potassium concentration $[K^+]_i$ is high (ca. 130 mM) in comparison to the extracellular concentration $[K^+]_o$, which is typically around 3 mM in cortex. This concentration gradient defines the equilibrium potential E_K (Nernst equation, top) for all potassium currents I_K (bottom equation, G_K is the conductance, V_m is the membrane potential). Changes in $[K^+]_i$ have limited effect on the equilibrium potential (not shown) whereas changes in $[K^+]_o$ can substantially depolarize the K^+ reversal potential (right panel).

Box 2: Measuring $[K^+]_o$

Typically, $[K^+]_o$ is measured with potassium-ion selective microelectrodes (KSMs) (Neher and Lux, 1973; Vyskocil and Kriz, 1972; Walker, 1971). KSMs are usually double-barrelled glass electrodes. One barrel is filled with a column of potassium-selective ion exchanger and backfilled with KCl. The other barrel is filled with NaCl. The K^+ dependent potential is determined by differential amplification of the signals from the two barrels. Half-max rise-time constants were measured to be smaller than 20 msec for a K^+ source 10 µm away from the KSM (Lux and Neher, 1973). The tip of the KSM creates an unnatural deadspace in neural tissue and therefore the measured $[K^+]_o$ values represent underestimates of the true values that would occur in the unperturbed case. Also, typically used K^+ ion exchangers are sensitive to various neurotransmitters even in very low concentrations (Kuramoto and Haber, 1981). Recently, K^+-selective fluorescent probes have been developed and applied to measure $[K^+]_o$ dynamics during experimental spreading depression (Padmawar et al., 2005). Optical imaging represents an exciting new opportunity for non-invasive measurements of $[K^+]_o$ signals.

Recently, however, an increasing number of studies on the pathophysiology of tissue from both animal epilepsy models and human epileptic patients have strongly pointed toward impairment of $[K^+]_o$ homeostasis apparatus in a variety of epilepsies with different etiologies. These more recent results thus are in apparent conflict with the previous conclusion that denied $[K^+]_o$ a significant role in cortical seizures. While many different explanations for these discrepancies are imaginable, we here argue that in-depth consideration of the interaction between $[K^+]_o$ and neural activity demonstrates a crucial role of $[K^+]_o$ in seizure dynamics. Indeed, computational models of cortical circuits that include ion concentration dynamics have provided novel insights in the complex interaction between neural activity and $[K^+]_o$.

We structured the remainder of this review as follows. First, we briefly highlight some of the classical findings on $[K^+]_o$ in cortex. We then review recent experimental and computational modeling findings on the role of $[K^+]_o$ dynamics in epilepsy. The scope of this article is purposefully limited to hippocampal and neocortical networks since $[K^+]_o$ dynamics in other preparations appear sufficiently distinct to deserve separate consideration. We conclude by proposing an integrated research approach to further clarify the role of $[K^+]_o$ dynamics in epilepsy.

$[K^+]_o$ MEASUREMENTS *IN VIVO*

Initial studies on $[K^+]_o$ were mostly performed in the anesthetized *in vivo* preparation (Lux and Neher, 1973; Moody et al., 1974; Prince et al., 1973). $[K^+]_o$ increased in cortex in response to physiological stimuli. These findings indicated that $[K^+]_o$ is not a parameter with a fixed value but rather a dynamic variable (Connors et al., 1979; Singer and Lux, 1975). Substantial $[K^+]_o$ fluctuations were also found in cat suprasylvian cortex during slow oscillations under ketamine-xylazine anesthesia (Amzica and Steriade, 2000). Very few $[K^+]_o$ recordings in the waking animal are reported in the literature. One group found surprisingly strong $[K^+]_o$ transients in response to behaviorally relevant stimuli (Skinner and Molnar, 1983). The interpretation of these results, however, is hampered by the fact that KSMs are sensitive to even very low concentrations of neurotransmitters and neuromodulators (Kuramoto and Haber, 1981). Neurochemical changes in the awake animal in response to the stimuli used in that study (e.g. presentation of food or foot shocks) may have tainted the $[K^+]_o$ recordings. During electrically or pharmacologically induced paroxysmal activity, $[K^+]_o$ changed more substantially but never rose above a “ceiling value” of about 12 mM in the absence of spreading depression in the adult animal (Heinemann and Lux, 1977).

According to the so-called “potassium accumulation hypothesis” (Fertziger and Ranck, 1970; Green, 1964), an initial $[K^+]_o$ increase above a certain threshold triggers a positive feedback cycle that mutually boosts $[K^+]_o$ and neural activity until

$[K^+]_o$ reaches a value for which neurons are too depolarized to fire (Figure 2-1). However, the initial predications derived from this potassium accumulation hypothesis mostly eluded experimental verification. In fact, little evidence was found for the expected (1) $[K^+]_o$ threshold for seizure initiation (but see Sypert and Ward, 1974), (2) monotonic increase in $[K^+]_o$ during seizures, and (3) depolarization block of neurons at seizure cessation (Heinemann and Lux, 1977; Moody et al., 1974; Sypert and Ward, 1974). Rather, dynamic changes in $[K^+]_o$ appeared to be delayed in comparison to changes in neural activity. This delayed rise in $[K^+]_o$ was interpreted as evidence for that increased $[K^+]_o$ is result and not cause of cortical seizures. Also, $[K^+]_o$ increased during tonic firing phases and decreased during clonic bursting phases of the electrographic seizure (Moody et al., 1974; Sypert and Ward, 1974) as shown Fig. 1C. Recently, the interpretation of these findings and the rejection of $[K^+]_o$ as an important factor in seizure generation have been reconsidered in the light of methodological concerns and novel insights from computational models (Frohlich et al., 2007b; Somjen, 2004).

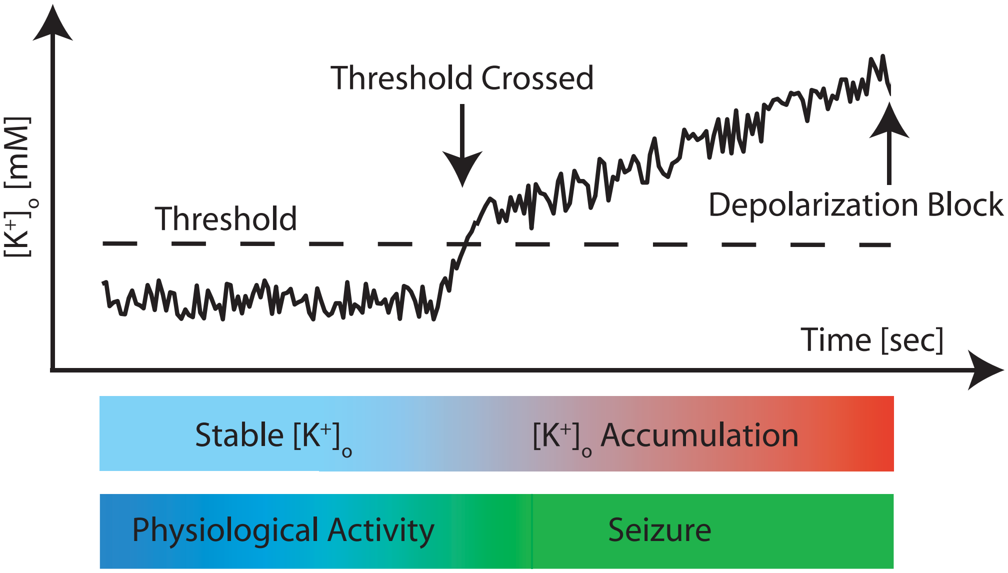

Figure 2-1 According to the potassium accumulation hypothesis, $[K^+]_o$ fluctuates around a stable baseline (typically 3 mM) during physiological activity levels. A transient increase triggers the occurrence of a seizure during which $[K^+]_o$ further accumulates. As a result, neurons become even more depolarized, fire more action potentials, and release even more K^+ ions into the extracellular space. Eventually, these run-away dynamics (positive feedback) come to an end when the neurons are so depolarized that they can no longer spike due to sodium channel inactivation. At this point, the seizure terminates. Although the potassium accumulation hypothesis had originally been rejected, more recent computational studies of ion concentrations during seizures have provided more refined models that are partially based on such positive feedback dynamics. See also text.

IONIC MODELS OF EPILEPSY *IN VITRO*

With the advent of the *in vitro* preparation, brain slices perfused with artificial cerebrospinal fluid (ACSF) mimicking the ionic composition as measured *in vivo* during seizures have become an important model system for the study of hypersynchronous activation ("ionic models"). While observations of *in vitro* "interictal" and "ictal" activity in ionic models do not represent a proof for a causal role of ionic disbalance in epileptogenesis, they show that changes of the extracellular ionic microenvironment are *sufficient* for network hyperactivation. Specifically, elevation of K^+ concentration in the ACSF to 7.5 or 8.5 mM was sufficient to trigger both periodic network activation ("interictal spikes") and in some cases events resembling electrographic seizures with a "tonic" firing and "clonic" bursting phase in hippocampus (Jensen and Yaari, 1997; Korn et al., 1987; Traynelis and Dingledine, 1988). Furthermore, seizure-like events occurred in an all-or-none fashion depending on the degree of $[K^+]_o$ increase evoked by extracellular electrical stimulation or focal potassium injection in a high $[K^+]_o$ and low $[Ca^{2+}]_o$ model (Konnerth et al., 1986; Yaari et al., 1986). These findings contrast with the presumed absence of a $[K^+]_o$ threshold for seizure initiation *in vivo*. Also, brief $[K^+]_o$ transients of 0.2 – 2.0 mM by focal K^+ injection were sufficient to trigger fast network oscillations that lasted several seconds (LeBeau et al., 2002).

Together, these ionic models illustrate that elevated $[K^+]_o$ is clearly sufficient to trigger synchronized oscillatory activity at various frequencies in the hippocampal networks *in vitro*. Nevertheless, it has remained mostly unclear how the observed epileptiform dynamics correspond to the *in vivo* situation. This limitation is of heightened concern when the activity-dependent changes of ion concentrations are studied since it is unknown how the presence of a practically infinite K^+ source/sink in the form of the perfused ACSF affects the ion concentration dynamics. Clearly, ion concentrations are not tightly controlled by the perfusion as activity-dependent $[K^+]_o$ fluctuations are routinely measured *in vitro*. Therefore, the interpretation of the above described findings as absolute levels of ionic concentrations required for initiation of epileptiform activity are difficult to justify in their direct application to the *in vivo* situation. While elevated $[K^+]_o$ and decreased $[Ca^{2+}]_o$ are most certainly useful models of the ionic microenvironment during epileptic seizures, manipulations such as the omission of magnesium in the ACSF or the pharmacological blockade of inhibition are more difficult to interpret in terms of their applicability *in vivo*.

EFFECTS OF $[K^+]_o$ ON NEURAL ACTIVITY

The slice preparation provides a relatively controlled environment to study the dependence of intrinsic and synaptic properties on $[K^+]_o$. While we are far from having a complete picture of how the parameters of neurons and synapses depend on $[K^+]_o$, it is well established that a $[K^+]_o$ increase in the range observed *in vivo* during electrographic seizures depolarizes neurons, decreases input resistance, and - importantly - can activate latent intrinsic bursting mechanisms in cortical pyramidal neurons. The changes in intrinsic firing properties have been best studied in hippocampus where pyramidal cells in both CA1 and CA3 (Frohlich and Bazhenov, 2006; Jensen et al., 1994) but not stratum oriens inhibitory interneurons (McBain, 1994) can burst in the presence of elevated $[K^+]_o$. Further regional and cell-type specific variations can be expected but have not been explored. Elevated $[K^+]_o$ also affects action potential propagation (Hablitz and Lundervold, 1981; Meeks and Mennerick, 2004; Poolos et al., 1987). For example, activity-dependent increases in $[K^+]_o$ from postsynaptic cell firing modulates fiber recruitment and action potential propagation in the presynaptic Schaffer collaterals in hippocampus CA1 (Poolos et al., 1987). This effect was first described in the cerebellum (Kocsis et al., 1983; Malenka et al., 1981). Interestingly, elevated $[K^+]_o$ affects action potential propagation and thus transmitter release differently in glutamatergic and GABAergic axons in hippocampus (Meeks and Mennerick, 2004).

Increases in $[K^+]_o$ also directly affect synaptic inhibition. The reversal potential of GABA(A)-type inhibitory synapses depolarizes in elevated $[K^+]_o$ (Jensen et al., 1993; Thompson and Gahwiler, 1989) due to the reduced electrochemical driving force for the KCC2 co-transporter that extrudes chloride from the cytoplasm at low levels of $[K^+]_o$ (DeFazio et al., 2000; Payne et al., 2003). However, in the case of low intracellular chloride concentration $[Cl^-]_i$ and elevated $[K^+]_o$, KCC2 switches transport direction and aids $[K^+]_o$ homeostasis by transporting K^+ ions back into cells at the price of intracellular Cl^- accumulation (DeFazio et al., 2000; Jarolimek et al., 1999; Payne, 1997; Staley and Proctor, 1999). In addition to the KCC2-mediated change in equilibrium potential, depolarization of postsynaptic cells by elevated $[K^+]_o$ increased the GABAergic conductance due to inward rectification of the GABA(A) receptor channels (Jensen et al., 1993).

Since KCC2 provides a key link between $[K^+]_o$ and fast synaptic inhibition, it is particularly interesting that deficient KCC2 expression has been related to different types of cortical hyperactivity. For example, Depolarizing GABA(A) currents were found in human epileptic tissue from the subiculum (Cohen et al., 2002) and associated with reduced or absent KCC2 expression in subicular pyramidal cells (Huberfeld et al., 2007; Munoz et al., 2007; Palma et al., 2006). Also, impaired KCC2-dependent Cl^- extrusion ability was found in epileptic tissue in a model of injury induced epileptogenesis (Jin et al., 2005). Sustained activity in hippocampal slices downregulated KCC2 expression level by endogenous brain-derived neurotrophic factor (BDNF) action on tyrosine receptor kinase B (TrkB) (Rivera et al., 2004). Although the exact impact of KCC2 downregulation on $[K^+]_o$ dynamics is not clear, the above findings implicate $[K^+]_o$ in changes of fast inhibitory synaptic transmission.

REGULATION OF $[K^+]_o$

Mechanisms that contribute to $[K^+]_o$ homeostasis under physiological conditions have been recently reviewed in detail (Kofuji and Newman, 2004). While the relative individual contributions are not fully known for cortex, it is clear that transporters (Na^+/K^+ ATPase, KCC2, and NKCC) on both neurons and astrocytes

(Kofuji and Newman, 2004), passive uptake through inward-rectifying potassium (Kir) channels on astrocytes (Butt and Kalsi, 2006), and diffusion in the extracellular space (Fisher et al., 1976; Lux and Neher, 1973; Nicholson et al., 2000) contribute to extracellular potassium homeostasis. The question whether $[K^+]_o$ is regulated locally (K^+ uptake) or whether K^+ is moved to sites of low $[K^+]_o$ by K^+-currents through the glial syncytium (spatial buffering) is one of considerable debate and may depend on brain region (Kofuji and Newman, 2004). Simultaneous dual glial recordings combined with KSM measurements suggest the presence of spatial buffering in cortex *in vivo* during slow sleep oscillations and electrographic paroxysmal activity (Amzica et al., 2002). Such nonlocal K^+ transport by glial cells may contribute to the spatial propagation of synchronized neural activity (Steriade, 2003b). The dissection of $[K^+]_o$ homeostasis into its individual components has been hampered by the fact that activity levels are usually not controlled for, by the lack of specificity of the applied pharmacology, and by the technical pitfalls concerning selectivity of KSMs.

Despite the experimental difficulties listed above, alterations of the potassium homeostasis apparatus represent an appealing hypothesis for explaining the pathophysiology of epilepsy given the role of $[K^+]_o$ in regulating excitability (Pollen and Trachtenberg, 1970). While early measurements in artificially induced glial scarring remained inconclusive (Heinemann and Dietzel, 1984), there is now accumulating evidence for glial dysfunction in epileptic tissue from patients with temporal lobe epilepsies (Binder and Steinhauser, 2006). Density and inward rectification of potassium current through glial Kir channel are reduced in patients with temporal lobe epilepsy accompanied by Ammon's horn sclerosis (Hinterkeuser et al., 2000; Schroder et al., 2000). This finding is in agreement with previous, less direct studies that showed that barium, a Kir channel antagonist, had a reduced effect on $[K^+]_o$ dynamics in slices from pilocarpine-treated rats and epileptic patients with sclerosis (Gabriel et al., 1998; Jauch et al., 2002; Kivi et al., 2000).

The *Tsc1*$^{\mathrm{GFAP}}$CKO mouse model of tuberous sclerosis complex (TSC), a genetic disorder associated with multiple seizure types, was found to exhibit reduced Kir channel expression and accordingly decreased Kir current amplitudes in astrocytes (Jansen et al., 2005). Decreased glial Kir channel expression and reduced potassium buffering capacity were also found in an animal model of blood-brain barrier disruption (Ivens et al., 2007). A link between altered $[K^+]_o$ homeostasis mediated by changes in Kir channels on astrocytes and posttraumatic epilepsy has also been suggested (D'Ambrosio et al., 1999), although this study has been questioned by some on methodological grounds (Santhakumar et al., 2003). Na^+/K^+ ATPase also contributes to $[K^+]_o$ clearance. Ouabain application hindered clearance of stimulation induced $[K^+]_o$ increases in olfactory cortex (Ballanyi et al., 1987) and hippocampus (D'Ambrosio et al., 2002). Although the exact roles of Na^+/K^+ ATPase with neuronal and glial location has not yet been fully determined, differential affinity for K^+ suggest that mostly glial Na^+/K^+-ATPase is responsible for clearance of activity dependent changes in $[K^+]_o$. In samples from human epileptic patients, overall activity of Na^+/K^+-

ATPase was reduced and K^+ sensitivity of glial Na^+/K^+-ATPase was lost (Grisar et al., 1992). Loss of function mutations of the ATP1A2 gene that codes for the alpha 2 subunit of the Na^+/K^+ ATPase were found in families with familial hemiplegic migraine and benign familial infantile convulsions (Vanmolkot et al., 2003). Recent evidence suggest that the glial water channel aquaporin-4, AQP4, (Amiry-Moghaddam and Ottersen, 2003) may also play a role in $[K^+]_o$ homeostasis. Clearance of elevated $[K^+]_o$ after orthodromic stimulation was slower and hyperthermia-induced epileptic seizures were of higher intensity in alpha-syntrophin knockout mice that exhibited disrupted AQP4 localization (Amiry-Moghaddam et al., 2003). Similarly, prolonged seizure duration and extended $[K^+]_o$ transients during seizures (Padmawar et al., 2005) and spreading depression (Binder et al., 2006; Padmawar et al., 2005) were observed in AQP4 -/- knockout mice. Measurements of changes in extracellular volume fraction in neocortical slices by intrinsic imaging combined with KSM measurements (Niermann et al., 2001) further support the link between water transport and $[K^+]_o$ clearance.

In summary, there is an increasing number of studies suggesting an important link between aberrant $[K^+]_o$ regulation and epileptogenesis in a broad variety of human epilepsies and animal models. While it is unclear whether the observed alterations are a cause or an effect of epileptiform activity, there is little doubt that the further study of $[K^+]_o$ may be key to a better understanding of epileptogenesis.

UNDERSTANDING THE DYNAMICS

The original consideration of $[K^+]_o$ as a key element in epileptogenesis was mostly based on the question of whether increases in $[K^+]_o$ are a cause or an effect of epileptiform activity. This conceptual framework seems ill posed as neural activity and $[K^+]_o$ are intimately linked through complex feedback loops. Unfortunately, however, feedback dynamics are notoriously hard to study in experimental set-ups. Computational models, however, have recently played a central role in the analysis of such feedback interactions. We here review some of the main modeling results to illustrate the power of computational models in studying the role of $[K^+]_o$ dynamics in epileptic seizures.

Historically, computational models mostly served the study of $[K^+]_o$ dynamics by focusing on mechanisms of extracellular K^+ clearance. These initial models did not consider the effect of activity-dependent $[K^+]_o$ increases on neural activity (but see Whisler and Johnston, 1978 for a pioneering exception) and therefore avoided the complexity of feedback dynamics (e.g. Dietzel et al., 1989; Gardner-Medwin, 1983; Odette and Newman, 1988; Vern et al., 1977). Although the conclusions in these studies were not uniform, these models contributed to the important insight that mechanisms different from diffusion must also be involved in $[K^+]_o$ regulation (see discussion above). Nevertheless, the exact role of K^+ diffusion is not yet fully clear. For example, *in vitro* experiments suggest that K^+ diffusion can synchronize otherwise unconnected neural populations (e.g. Lian et al., 2001). Models of neuronal coupling via K^+ transients in the absence of synaptic transmission (Lebovitz, 1996; Park and Durand, 2006) support the relevance of extracellular spatial structure. Compartmentalization of the extracellular space and inhomogeneity of potassium channel localization may require more detailed modeling of microenvironments with explicit consideration of electrodiffusion (Qian and Sejnowski, 1990).

More recent models include the feedback between neural activity and $[K^+]_o$ (Bazhenov et al., 2004; Frohlich and Bazhenov, 2006; Frohlich et al., 2006; Kager et al., 2002, 2000). In these models, individual neurons are endowed with ion channels described by the commonly used conductance-based formalism (Hodgkin and Huxley, 1952). This modeling approach allows the detailed quantification of K^+ ions entering the extracellular space via ion channels. Additionally, each cell is surrounded by an extracellular compartment that includes a $[K^+]_o$ regulation apparatus (Na^+/K^+-ATPase and glial buffer). Ion concentrations are dynamically updated and the corresponding equilibrium potentials computed. The first single-cell models with ion concentration dynamics (Kager et al., 2002, 2000) included detailed neuronal morphology but a limited number of ion-channel types (reviewed in Somjen, 2002). In response to stimulation, these model neurons exhibited sustained afterdischarges (bursting) in the case of weakened Na^+/K^+-ATPase capacity. The authors focused on different recovery time-constants of $[K^+]_o$ and $[Na^+]_i$ at the time-scale of individual burst as the underlying mechanism of these self-sustained "clonic" discharges since the model did not include ion channels mediating intrinsic bursting. In the case of enhanced inward currents in the dendrites, self-sustained prolonged depolarization ("spreading-depression-like") occurred after a critical $[K^+]_o$ level ("ignition point") was reached. The key insight from this model was that the interaction dynamics between ion concentrations and neural activity can lead to self-sustained pathological neural activation even in the case of an isolated cell (in this case "clonic" bursting and "spreading-depression"). From a dynamic system viewpoint, the bursting represents a stable oscillatory state since it lasted infinitely. The spreading-depression-like episode, however, is the result of an unstable positive feedback loop, similar in nature to the original $[K^+]_o$ accumulation hypothesis. The main limitations of these models are (1) the absence of a more realistic ion channel composition and (2) the lack of network interaction.

These points were addressed by the incorporation of $[K^+]_o$ regulation mechanisms in standard models of cortical pyramidal cells, PYs, and fast-spiking inhibitory interneurons, INs (Bazhenov et al., 2004). In comparison to the models discussed above, these PY and IN models were of simplified morphology but had a more comprehensive set of ion channels (Bazhenov et al., 2004; Frohlich and Bazhenov, 2006) such that intrinsic bursting occurred for elevated $[K^+]_o$ in agreement with the experimental literature. Specifically, persistent sodium and high-threshold calcium ion channels were critical for the depolarization at the burst onset. This depolarization then caused a burst of action potentials before Ca^{2+}-activated potassium current was sufficiently activated to mediate burst termination (Bazhenov et al., 2004;

Frohlich and Bazhenov, 2006). In this model, prolonged intense stimulation caused $[K^+]_o$ to increase. After termination of stimulation, a single PY exhibited a transient after-discharge that was structured into two distinct consecutive phases, i.e. bursting and tonic firing (Bazhenov et al., 2004; Frohlich et al., 2006). Yet, in contrast to the single-cell model, a network of PYs and INs exhibited slow state transitions between bursting and tonic firing (Fig. 2-2A-C) that qualitatively resembled sequences of tonic-clonic discharges during seizures (Frohlich et al., 2006). $[K^+]_o$ increased during tonic firing and decreased during bursting in agreement with the classic *in vivo* recordings (Moody et al., 1974; Sypert and Ward, 1974) and more recent *in vitro* ionic models of tonic-clonic seizures (Jensen and Yaari, 1997). Different firing rates and thus different loads on the $[K^+]_o$ regulation apparatus for these two firing modes explain the different signs of the $[K^+]_o$ gradient.

The identification and eventual abstraction of dynamic principles of epileptic seizures carries the promise that the broad range of clinical manifestations associated with seizures can eventually be reduced to a few key pathophysiological mechanisms.

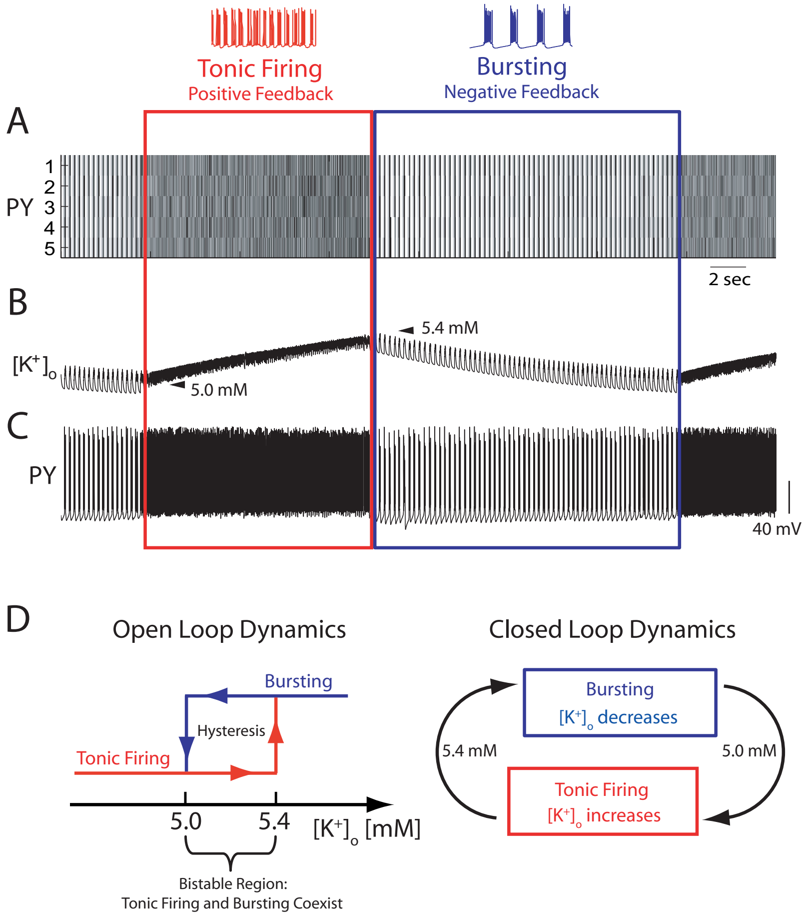

Figure 2-2 Slow state transitions in cortical network model. (A) The activity of five PYs is structured into alternating epochs of tonic firing and bursting. (B) $[K^+]_o$ increases during tonic firing (positive feedback) but decreases during bursting (negative feedback). (C) Sample PY membrane voltage trace. Panels A-C adapted from (Frohlich et al., 2006). (D) Open loop analysis shows bistability between tonic firing and bursting for $[K^+]_o$ between 5.0 and 5.4 mM (left). This bistability with hysteresis explains the slow state transitions in the closed-loop system. (right).

The differing time-scales of action-potential firing and changes in $[K^+]_o$ (neglecting small amplitude transients following individual action potentials) provide the means to study $[K^+]_o$ dynamics in computational models by opening the feedback loop (so-called "open loop" dynamics, see Figure 2-3). In practical terms, the behavior of the neuron is determined as a function of $[K^+]_o$ that is treated as a constant parameter (Frohlich and Bazhenov, 2006; Frohlich et al., 2006; Hahn and Durand, 2001). Application of this open-loop analysis (also called bifurcation theory) on the above discussed single-cell PY model revealed (1) the existence of four distinct activity patterns as a function of $[K^+]_o$, i.e. silence, tonic firing, bursting, and depolarization block, and (2) a bistability with hysteresis between tonic firing and bursting for elevated $[K^+]_o$ levels (Frohlich and Bazhenov, 2006; Frohlich et al., 2006). This bistability found by open-loop analysis explains the occurrence of transitions between tonic firing and bursting (Fig. 2-2D). Specifically, neurons remained in tonic-firing mode while $[K^+]_o$ increased up to the level where they were forced to switch to bursting mode (upper endpoint of hysteresis). Conversely, neurons remained in bursting mode while $[K^+]_o$ decreased until the lower endpoint of the hysteresis was reached where they were forced to switch back to tonic-firing mode and the next cycle began. In other words, although it was originally assumed that only positive feedback between $[K^+]_o$ and neural activity occurred during seizures, these modeling results show the alternating occurrence of positive (tonic firing) and negative (bursting) feedback. Thus, these slow transitions were essentially the result of slow alternations between two meta-stable states, tonic firing and bursting. The existence of this bistability and therefore the occurrence of slow state transitions were robust to changes in model parameters but depended on the high-threshold Ca^{2+} conductance.

Thus, the relatively detailed nature of the model permitted novel insights into the possible involvement of specific ion channel types in mediating tonic-clonic seizure dynamics. Also of note is the fact that even if a different mechanism were to provide such a bistability with hysteresis between tonic firing and burst mode, we would expect the same slow patterning of the epileptiform activity.

The different responses of the single cell and the network to a potassium transient (transient after-discharge versus sustained tonic-clonic sequences) showed that the nature of the paroxysmal-like activity crucially depended on the network interaction. This finding further emphasizes the importance of network simulations to investigate the role of $[K^+]_o$ in cortical dynamics. The model predicts *in vivo* neural dynamics during tonic-clonic seizures that have previously lacked an explanation. Also, the $[K^+]_o$ time-course is in qualitative agreement with the original $[K^+]_o$ recordings *in vivo* (Moody et al., 1974; Sypert and Ward, 1974). Slow state transitions as discovered in the network model resemble electrographic neocortical seizures that are patterned into epochs of “fast runs” (tonic discharge) and “slow bursting” (Frohlich et al., 2006).

WAYS FORWARD

Aberrant $[K^+]_o$ regulation has recently begun to resurface as a potential player in epileptogenesis. Most studies on epileptic tissue cannot entirely exclude that reduced $[K^+]_o$ homeostasis capabilities are rather a consequence than the primary cause of repetitive seizures. Nevertheless, the accumulating evidence for disturbances in the $[K^+]_o$ regulation apparatus discussed here warrants renewed research efforts to unravel the role of $[K^+]_o$ dynamics in physiological brain activity and epileptogenesis. We therefore conclude by outlining an integrated research approach based on recent methodological developments that should render it possible to overcome the limitations of previous generations of $[K^+]_o$ studies. Specifically, we propose the use of non-invasive optical techniques to control and measure activity of neural populations combined with fluorometric and KSM-based $[K^+]_o$ measurements to dissect the interaction between neural activity and $[K^+]_o$. In conjunction, advanced patch-clamp recording techniques combined with genetic labeling can be used to obtain more specific information about how $[K^+]_o$ modulates synaptic and intrinsic properties of individual cell types. Below, we outline how *in vivo*, *in vitro*, and computational modeling methods can be combined to tackle the challenge of understanding the role of $[K^+]_o$ in cortical dynamics.

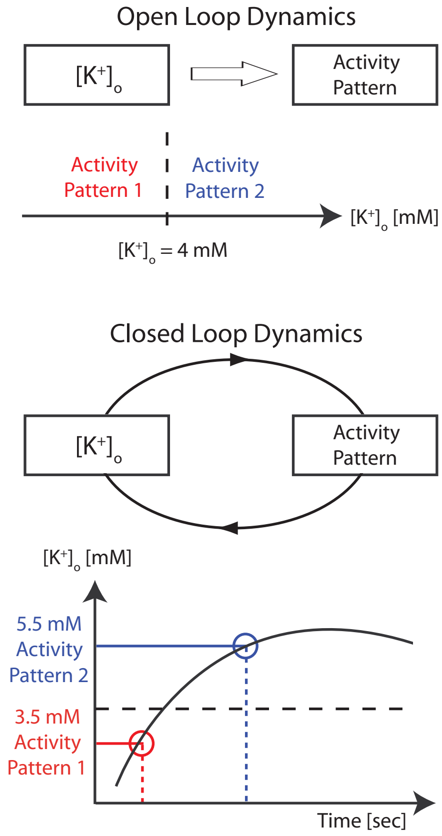

Figure 2-3 In computational models, feedback interaction between $[K^+]_o$ and neural activity can be studied by treating $[K^+]_o$ as a parameter. With this "open-loop" method, the modulation of $[K^+]_o$ by neural activity is artificially removed and therefore the feedback removed (top). By choosing different values for $[K^+]_o$, the corresponding activity patterns for each value of $[K^+]_o$ can be determined ("open loop" dynamics). The behavior of the entire system with feedback ("closed loop" dynamics) is then predicted by stringing together the activity patterns as determined by open loop analysis (bottom). This approximation is valid since (1) the macroscopic time-course of $[K^+]_o$ is slow in comparison to the time-scale of action potential firing and (2) most effects of changes in $[K^+]_o$ on neural dynamics are instantaneous.

While $[K^+]_o$ time-courses during cortical seizures in the anesthetized preparation have been thoroughly documented in the early *in vivo* studies, we know very little about $[K^+]_o$ dynamics in the awake and naturally sleeping animal. For example, active cortical states and synchronized sleep oscillations may be associated with significant fluctuations in $[K^+]_o$. Crucially, $[K^+]_o$ recordings *in vivo* need to be accompanied by simultaneous quantification of neural activity ideally with single unit resolution (Heinemann and Lux, 1975; Sykova et al., 1974). Such quantification of physiological $[K^+]_o$ fluctuations will provide an important baseline for the eventual design of therapeutic interventions that enhance the power of the $[K^+]_o$ regulation apparatus. Since the uncoupling of the feedback loop between $[K^+]_o$ and neural activity will remain a challenge *in vivo*, the *in vitro* preparation remains the model system of choice to study the effects of $[K^+]_o$ levels on intrinsic and synaptic properties. So far, most studies of that kind in cortical preparations have focused on the effect of strong $[K^+]_o$ elevations on hippocampal fields CA3 and CA1. Since substantial $[K^+]_o$ fluctuation were also found in neocortex *in vivo*, it is essential to understand the resulting modulation of neural behavior independent from whether epileptiform activity can be elicited by elevated $[K^+]_o$ in neocortical slice. Moreover, since most studies have been restricted to studying intrinsic excitability and synaptic transmission by extracting average pre- and postsynaptic behavior from field recordings, we know very little about how different cell types are affected by changes in $[K^+]_o$. Therefore, patch-clamp recordings from dendrites, somata, and axon terminals of identified cells and synaptically coupled neuron pairs will provide crucial new insight into specific effects of different levels of $[K^+]_o$.

Recent computational models of neuronal networks with incorporated ion concentration dynamics were successful at providing new insights and predictions concerning cortical seizure dynamics. Therefore, we propose that such models can serve as the essential and so far neglected link between *in vitro* results on specific properties and *in vivo* results on global network dynamics. In fact, the complexity of $[K^+]_o$ dynamics is best tackled with tools derived from systems theory and computational neuroscience that have begin seeing widespread application in many other subfields of neuroscience. We thus hope that this combined approach of experiments and computational models will eventually lead to the development of a new generation of antiepileptic drugs that specifically target the $[K^+]_o$ regulation system and therefore might be free from the current limitations of pharmacotherapy for epilepsy (Duncan et al., 2006).

ACKNOWLEDGEMENT

Section 2.1, in full, is a final draft of the material as it will be submitted for publication, Frohlich, Flavio; Bazhenov, Maxim; Iragui-Madoz, Vicente; Sejnowski, Terrence. The dissertation author was the prime investigator and author of this paper.

2.2 Extracellular potassium mediates transitions between physiological and pathological cortical network dynamics

Epileptic seizures are commonly considered unstable runaway dynamics of neuronal networks. Specifically, it has been suggested that positive feedback interaction between extracellular potassium concentration $[K^+]_o$ and neural activity mediates cortical seizures. This potassium accumulation hypothesis has been initially rejected but recently reconsidered. We here used a computational model of a cortical circuit with afferent input to investigate the role of $[K^+]_o$ in seizure dynamics. In our model, sparse physiological and synchronous pathological activity occurred for the same input level. Perturbations in the afferent input switched the network between these two stable states. Therefore, epileptic seizures may be the manifestation of an additional stable network state co-existing with the normal physiological state instead of a network instability.

INTRODUCTION

Epilepsy is a common, disabling neurological disorder that is characterized by recurring bouts of synchronous neuronal hyperactivity. Currently available pharmacotherapy represents no perfect solution to this problem (Duncan et al., 2006) since (1) a substantial fraction of patients fails to achieve seizure control even with multidrug therapy and (2) several first-line treatment options are associated with severe side-effects. The development of novel pharmacological agents with different modes of action is hampered by the fact that relatively little is known about the underlying pathophysiology of epileptic seizures. We here revisit the question whether extracellular potassium concentration $[K^+]_o$ dynamics play a relevant role in the pathophysiology of cortical seizures.

Historically, it was hypothesized that cortical seizures are mediated by increases in $[K^+]_o$ (Fertziger and Ranck, 1970; Green, 1964). According to this so-called potassium accumulation hypothesis, an elevation in $[K^+]_o$ depolarizes neurons and therefore increases their activity level. As a result, further accumulation of $[K^+]_o$ occurs. Based on this positive-feedback model, it was hypothesized (1) that there is critical value of $[K^+]_o$ for which seizures are triggered, (2) that $[K^+]_o$ monotonically increases during seizures, and (3) that seizures terminate when $[K^+]_o$ is sufficiently elevated to induce depolarization block. *In vivo* measurements of $[K^+]_o$ during electrographic seizures with K^+ selective ion microelectrodes, however, failed to provide convincing evidence in support of these hypotheses (Somjen, 1979)

Recently, we found seizure-like discharge patterns in computational models implementing $[K^+]_o$ dynamics (Bazhenov et al., 2004; Frohlich et al., 2006). Also, there is accruing evidence for aberrations in the potassium regulation apparatus in tissue from human patients with epilepsy (Binder and Steinhauser, 2006; Hinterkeuser et al., 2000; Schroder et al., 2000) and animal models of epilepsies with different etiologies (Grisar et al., 1992; Ivens et al., 2007; Jansen et al., 2005). Considered together, this new evidence suggests a need to reconsider the role of $[K^+]_o$ in cortical epileptic seizures.

The complexity of the interaction between neural activity and $[K^+]_o$ makes computational models a valuable tool for studying the resulting network dynamics. We here introduce a large cortical network model with $[K^+]_o$ dynamics and afferent input to test the original predictions derived from the potassium accumulation hypothesis. While our simulations support the key role of $[K^+]_o$ in cortical seizures, we found that a substantial revision of the conceptual framework of seizure dynamics may be required.

METHODS

The computational models used in this study were similar to the ones previously described in detail elsewhere (Frohlich and Bazhenov, 2006; Frohlich et al., 2006). Briefly, both pyramidal cells (PYs) and fast-spiking inhibitory interneurons (INs) were modeled as two-compartment, conductance-based neurons. The axo-somatic compartment was endowed with a voltage-gated sodium (PY: G_{Na} = 3000 mS/cm^2, IN: G_{Na} = 2500 mS/cm^2), a delayed-rectifier potassium (G_{Kv} = 200 mS/cm^2), and a leak conductance (G_{Kl} = 0.1 mS/cm^2). The dendritic compartment had high-threshold calcium, calcium-activated potassium, slowly-activating potassium, persistent sodium, hyperpolarization-activated depolarizing mixed cationic, potassium leak, and mixed cationic leak conductances (PY: G_{HVA} = 0.016 mS/cm^2, IN:

$G_{\mathrm{HVA}} = 0.01$ mS/cm^2; PY: $G_{\mathrm{KCa}} = 3.5$ mS/cm^2, IN: $G_{\mathrm{KCa}} = 0.3$ mS/cm^2; PY: $G_{\mathrm{Km}} = 0.01$ mS/cm^2, IN: $G_{\mathrm{Km}} = 0.0$ mS/cm^2; PY: $G_{\mathrm{NaP}} = 4.0$ mS/cm^2, IN: $G_{\mathrm{NaP}} = 0.0$ mS/cm^2; $G_{\mathrm{h}} = 0.05$ mS/cm^2; PY: $G_{\mathrm{Kl}} = 0.01$ mS/cm^2, IN: $G_{\mathrm{Kl}} = 0.005$ mS/cm^2; $G_{\mathrm{L}} = 0.033$ mS/cm^2). The network used in this study consisted of 200 PYs and 40 INs. Synaptic connectivity was random (connection probability p =0.1) with doubled value of p within local footprint (radii: PY-PY: 5; PY-IN: 1; IN-PY: 5). All excitatory connections had a fast AMPA and a slow voltage-dependent NMDA component (total conductances: $g_{\mathrm{AMPA(PY\text{-}PY)}} = 9.6$ nS, $g_{\mathrm{NMDA(PY\text{-}PY)}} = 0.96$ nS, $g_{\mathrm{AMPA(PY\text{-}IN)}} = 3.0$ nS, $g_{\mathrm{NMDA(PY\text{-}IN)}} = 0.30$ nS). Inhibition was mediated by fast GABA$_{\mathrm{A}}$ synaptic conductances ($g_{\mathrm{GABA(IN\text{-}PY)}} = 9.6$ nS). Afferent excitatory input ($G_{\mathrm{PY}} = 0.9$ nS, $G_{\mathrm{IN}} = 0.9$ nS) was modeled with a Poisson process with frequency $f = 140$ Hz for both PYs and INs. Perturbations to switch between network states were modeled with a transient increase of the PY afferent input to $f = 150$ Hz.

Each cell was surrounded by an extracellular compartment that modeled the $[K^+]_o$ dynamics in the interstitial space (Bazhenov et al., 2004; Kager et al., 2000). $[K^+]_o$ was determined by the interaction of he neuronal potassium currents $I_{\Sigma K}$, Na$^+$/K$^+$ ATPase activity ($I_{\mathrm{KPump}} = I_{\max} /(1+([K^+]_{o(eq)}/[K^+]_o))^2$; $[K^+]_{o(eq)} = 3.5$ mM; dendrites: $I_{\max} = 5$mA/cm^2, soma: $I_{\max} = 40$ mA/cm^2), K$^+$ buffering G (d[B]/dt = $k_1([B]_{\max}-[B])-k_2 [K^+]_o [B]$, $G = k_1([B]_{\max}-[B])/k_{1N}-k_2 [K^+]_o [B]$; $k_1 = 0.008$; $k_2 = k_1/(1+\exp(([K^+]_o-[K^+]_{o(th)})/-1.15))$; soma: $[K^+]_{o(th)} = 15$ mM; dendrites: 9 mM; $k_{1N} = 1.1$), and lateral diffusion between neighboring compartments ($D = \delta \Delta x([\mathrm{K}^+]_{o1}\text{-}2[\mathrm{K}^+]_{o2} + [\mathrm{K}^+]_{o3})$, $\delta = 4\ 10^{-6}\ \mathrm{cm}^2/\mathrm{sec}$; $\Delta x = 100\mu\mathrm{m}$):

$d[\mathrm{K}^+]_o/dt = (k/Fd)\ (I_{\Sigma\mathrm{K}} + I_{\mathrm{KPump}}) + G + D$,

where $k = 10$ denoted a conversion factor, $F = 96489$ C/mol was the Faraday constant, and d determined the ratio of the volume of the extracellular compartment to the surface area. Equilibrium potentials were continuously updated under the assumption that diffusion-drift equilibrium was reached immediately and that all other ion concentrations remained constant ($\mathrm{Na}^+]_o$ = 130 mM, $[\mathrm{Na}^+]_i$ = 20 mM, $[\mathrm{Cl}^-]_o$ = 130 mM, $[\mathrm{Cl}^-]_i$ = 8 mM):

$E_\mathrm{K} = 26.64\ \mathrm{mV}\ \ln([\mathrm{K}^+]_o/[\mathrm{K}^+]_i)$.

$E_\mathrm{h} = 26.64\ \mathrm{mV}\ \ln([\mathrm{K}^+]_o + 0.2\ [\mathrm{Na}^+]_o)/(\ [\mathrm{K}^+]_i + 0.2\ [\mathrm{Na}^+]_i)$

$E_\mathrm{L} = 26.64\ \mathrm{mV}\ \ln([\mathrm{K}^+]_o + 0.085\ [\mathrm{Na}^+]_o + 0.1\ [\mathrm{Cl}^-]_i)/([\mathrm{K}^+]_i + 0.085\ [\mathrm{Na}^+]_i + 0.1\ [\mathrm{Cl}^-]_o)$.

RESULTS

A comprehensive description of cortical seizure pathophysiology requires understanding of how seizures are initiated, how pathological hyperactivity evolves during seizures, and how seizures terminate. In a previous study, we showed that computational models of cortical networks consisting of few neurons without afferent input robustly reproduced tonic-clonic activity patterns when $[\mathrm{K}^+]_o$ dynamics were included (Frohlich et al., 2006). The underlying dynamics were described in (Frohlich and Bazhenov, 2006). Here, we now present a network model with afferent input (200

PYs and 40 INs) that exhibited both asynchronous, sparse ("physiological") activity and seizure-like ("pathological") hyperactivity.

For the baseline afferent input used in this study, the model exhibited asynchronous firing with low average firing rate accompanied by minor $[K^+]_o$ fluctuations initiated by action potential firing (activity map in Fig. 2-4A, $[K^+]_o$ map in Fig. 2-4B). Throughout the simulations, the network activity remained stable with average frequencies of 1.18 Hz and 9.96 Hz for PYs and INs, respectively (firing frequency distribution histograms in Fig. 2-4C). The $[K^+]_o$ fluctuations in the extracellular compartment surrounding a given cell (e.g. PY2 in Fig. 2-4D) were primarily determined by the action potential firing of the corresponding cell but action potentials in neighboring cells also contributed by K^+ diffusion. With these simulations we established the model's capability to exhibit stable physiological activity in presence of $[K^+]_o$ dynamics. We next studied the stability of this physiological state in response to transient increases in afferent input.

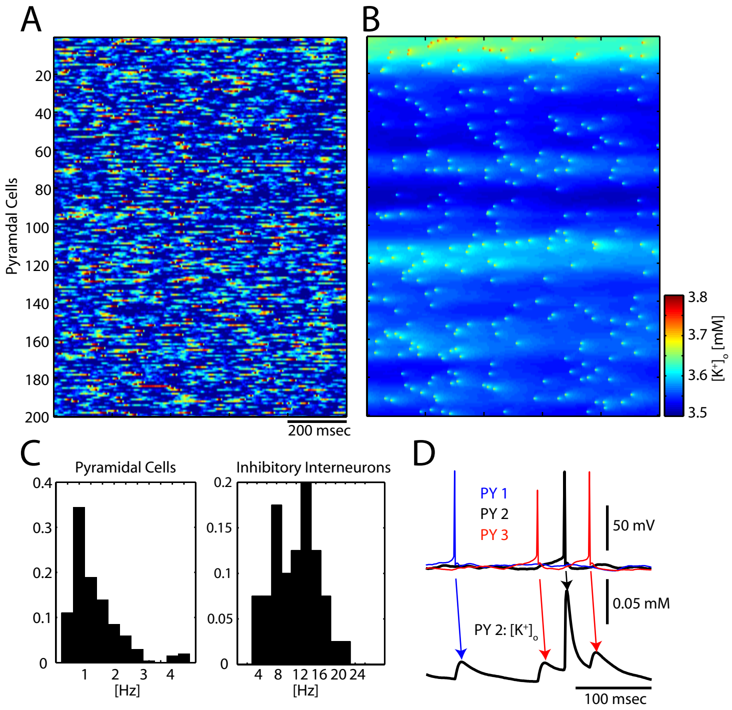

Figure 2-4 Physiological activity in network with $[K^+]_o$ dynamics. (A) Color-coded activity map of 200 PYs (cool and hot colors indicate hyperpolarization and depolarization, respectively). (B) Color-coded $[K^+]_o$ map corresponding to activity shown in Panel A. (C) Firing rate histograms for pyramidal cells and inhibitory interneurons. (D) Top: Overlaid membrane voltage traces of three neighboring pyramidal cells (PY 1, PY2, and PY 3 in blue, black, and red, respectively). Bottom: $[K^+]_o$ in extracellular compartment surrounding PY 2. Minor deflections stem from action potentials in neighboring cells PY 1 and PY 2 (diffusion), major deflection from action potentials in PY 2.

A transient increase (duration ΔT = 10 sec) in the afferent input ("perturbation") to the PY subpopulation resulted in an almost immediate increase in the average PY firing rate (histogram in Fig. 2-5A, duration of perturbation denoted by horizontal bar). Quite in contrast, $[K^+]_o$ (averaged over network, red line in Fig. 2-5A) gradually increased by activity-dependent accumulation of K^+ ions in the extracellular space over the entire interval of elevated afferent input. At the offset of the input perturbation, $[K^+]_o$ only slowly recovered back to its resting value (Fig. 2-5B, color-coded $[K^+]_o$ for entire network as a function of time). Thus, this perturbation of the PY firing did not elicit seizure-like activity since the network eventually returned to the stable physiological activity state. For such perturbations, $[K^+]_o$ alterations followed changes in the activity level due to the relatively slow rate of $[K^+]_o$ accumulation. In case of more prolonged perturbations (ΔT = 20 sec), however, sufficiently elevated $[K^+]_o$ prevented the network from returning to physiological state at the offset of the input perturbations (Fig. 2-5C, firing histogram and average $[K^+]_o$; Fig. 2-5D, color-coded $[K^+]_o$). Rather, both $[K^+]_o$ and activity levels further increased until sequences of tonic-clonic activity started to occur. In contrast to shorter perturbations, $[K^+]_o$ preceded the increase in neural activity after the perturbation offset in this case (Figure 2-5C).

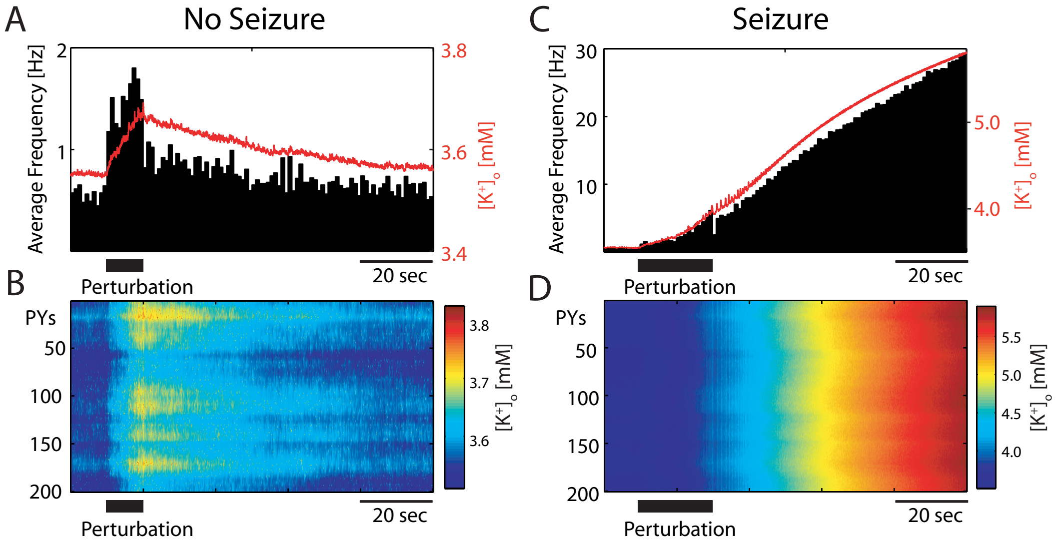

Figure 2-5 Transition from "physiological" to "pathological" activity. (A) Left Average PY firing frequency (black histogram) and average $[K^+]_o$ trace (red) for 10 second perturbation. Average frequency increased instantaneously while $[K^+]_o$ increased and decreased only gradually. (B) Color-coded $[K^+]_o$ map. (C) Same representation as in (A) but for 20 second perturbation. While $[K^+]_o$ increase initially lagged activity increase, $[K^+]_o$ became driving force in positive-feedback, "runaway" dynamics. (D) Color-coded $[K^+]_o$ map.

These results suggest that the duration of increased PY activity determined whether a seizure occurred. Since we found $[K^+]_o$ to increase during the input perturbation, we tested if there is indeed a corresponding elevation of $[K^+]_o$ above which seizure-like activity is elicited as previously predicted by the potassium accumulation hypothesis. We therefore systematically varied the duration ΔT of elevated afferent input to achieve different peak $[K^+]_o$ values at the offset of the perturbation (average $[K^+]_o$ traces in Fig. 2-6A). For $\Delta T \leq 15$ sec, the network returned back to physiological activity (traces labeled “no seizure” in Fig. 2-6A). For inputs longer than that, however, increased afferent synaptic input invariable initiated seizure-like discharge patterns (traces labeled “seizure” in Fig. 2-6A). Therefore, $[K^+]_o$ values indeed had to reach a critical value for the transition into the seizure state to occur (threshold indicated by dashed line in Fig. 2-6B). Interestingly, however, the average $[K^+]_o$ values at the offset of the elevated input (Fig. 2-6B, zoom in of region of interest from Fig. 2-6A) were initially very similar for values of ΔT that failed and succeeded in eliciting seizure-like discharge. We then considered the individual $[K^+]_o$ values in the extracellular compartments around individual cells instead of the average across the entire network. In agreement with the average traces (Fig. 2-6A and B), the histogram of these values (averaged over 1 second after offset of perturbation) for $\Delta T = 15$ (no seizure) and $\Delta T = 16$ (seizure) strongly overlapped (Fig 2-6C). This may explain the experimental difficulty to identify a threshold value from a single local $[K^+]_o$ measurement (Sypert and Ward, 1974). In order to further establish the causal role of $[K^+]_o$ in the seizure initiation process, we ran control simulations where we froze all $[K^+]_o$ values well in advance of the input perturbation. With $[K^+]_o$ dynamics absent, activity levels increased and decreased in close temporal alignment with the change in afferent input (Fig. 2-6D). Independent of the duration of the perturbation, the network always returned to the physiological state.

Therefore, the inclusion of $[K^+]_o$ dynamics had resulted in the existence of a second stable state. Input perturbations of sufficient length to increase $[K^+]_o$ above a critical value caused a transition from the physiological to the pathological network state. Above this $[K^+]_o$ threshold value, neural activity and $[K^+]_o$ were indeed linked in a positive feedback loop that caused this transition into a seizure.

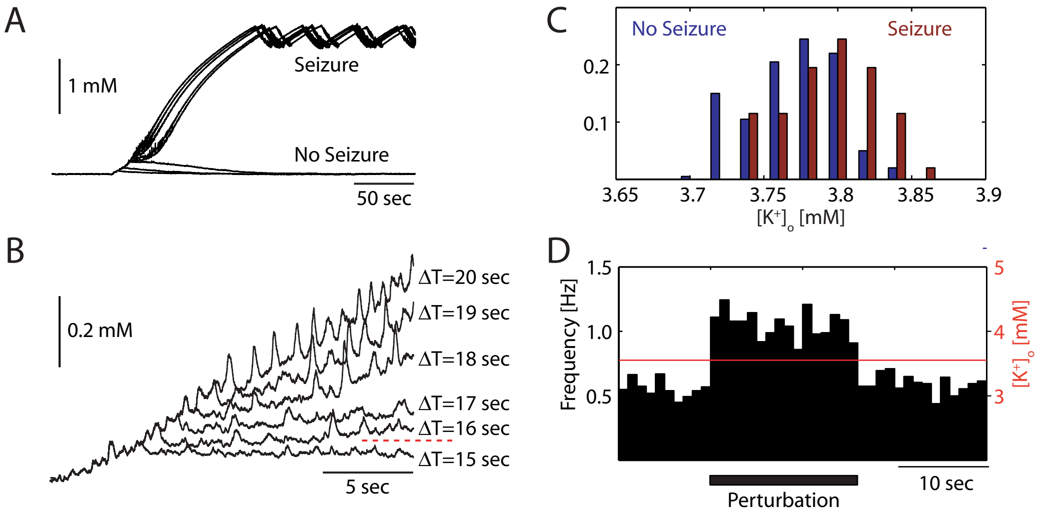

Figure 2-6 (A) Average $[K^+]_o$ traces for perturbation durations ΔT = 5, 10, and 15 seconds (no seizure-like activity induced) and ΔT = 16, 17, 18, 19, 20 seconds (runaway dynamics, transition into seizure-like activity). (B) Same as in (A) but with increased temporal resolution. (C) Histograms of $[K^+]_o$ at perturbation offset (averaged over 2 seconds) for ΔT = 15 and 16 seconds ("no seizure" and "seizure"). (D) Network with frozen $[K^+]_o$ exhibited constant activity level during perturbation. No runaway into seizure-like state due to absence of $[K^+]_o$ dynamics.

Together, the above discussed simulations provide evidence for an important role of $[K^+]_o$ dynamics in seizure initiation. When $[K^+]_o$ runaway dynamics were triggered, the network converged to slow state transition between tonic firing ("fast run") and slow "clonic" bursting (Fig.2-7A, before afferent input was reduced). These alternating epochs of two distinct oscillatory firing regimes were synchronized across the entire network and lasted several seconds each. We previously showed that a $[K^+]_o$ -mediated bistability between tonic firing and clonic bursting explains these transition dynamics in small networks without afferent input (Frohlich et al., 2006). As a consequence of this bistability with hysteresis, $[K^+]_o$ increased during tonic firing and decreased during bursting. We here now found the same mechanism in larger networks driven by afferent input. Importantly, these slow state transitions between tonic firing and bursting occurred for the same level of afferent input as the asynchronous activity state. Therefore, the network exhibited either of two stable activity modes: physiological activity or pathological tonic-clonic sequences. A sufficiently long perturbation in the afferent input was amplified by positive feedback dynamics between neural activity and $[K^+]_o$ that succeeded in switching the network from the physiological to the pathological state. We emphasize that also the pathological state is stable in the sense that without further perturbation the network remains in an infinite loop of alternating epochs of tonic firing and bursting. Thus, neither did $[K^+]_o$ monotonically increase nor did the seizure-like activity terminate by depolarization block.

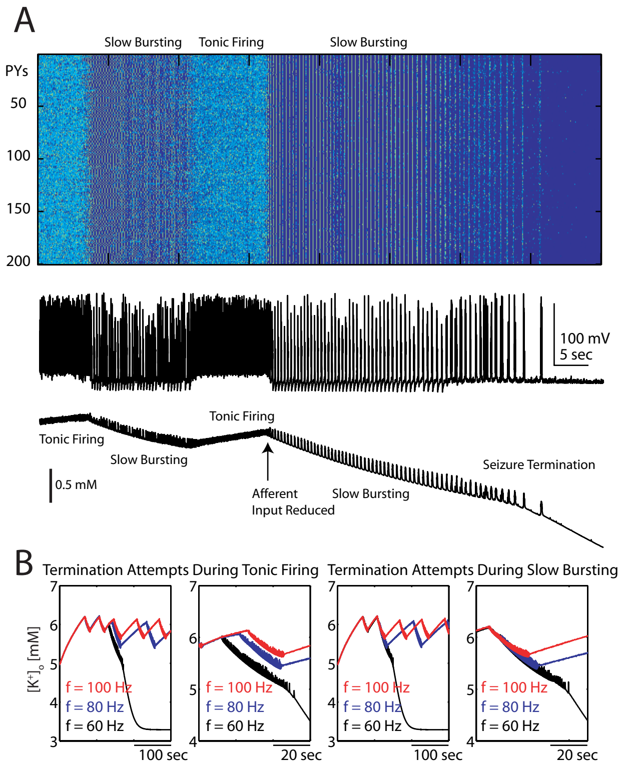

Figure 2-7 Termination of seizure-like activity by inducing switch back to physiological state. (A) Top: Color-coded PY activity map. Middle: Sample PY membrane voltage trace. Bottom: Corresponding $[K^+]_o$ trace. Plots show alternating epochs of tonic firing and slow bursting interrupted by reduction in afferent input (indicated by vertical arrow). At the onset of input reduction, the network switched to bursting and $[K^+]_o$ returned back to baseline. (B) Average $[K^+]_o$ traces for three different levels of input perturbations (reduction in frequency of afferent input to f = 100, 80, and 60 Hz, respectively, color-coded in red, blue, and black). Left: Perturbation applied during bursting. Right: Perturbation applied during tonic firing.

In order to induce seizure termination, the frequency of the afferent input had to be reduced to below baseline. Since the epileptiform activity was essentially mediated by elevated $[K^+]_o$, any perturbation that succeeded in seizure termination had to be sufficiently long such that no further positive feedback reaction was triggered at the offset (data not shown). At the moment when the input was reduced (labeled arrow in Fig. 2-7A), the network switched from tonic firing to bursting mode during which $[K^+]_o$ monotonically decreased. At $[K^+]_o = 4.85$ mM (network average), the network became silent and $[K^+]_o$ returned back to baseline with accelerated pace (PY activity map in Fig. 2-7A, top panel; sample membrane voltage and corresponding $[K^+]_o$ trace in middle and bottom panels, respectively). Seizure-like activity in our model therefore ended with an epoch of bursting. We next addressed the question whether seizure termination by input reduction preferably occurred during either slow bursting or tonic firing (average $[K^+]_o$ traces in Fig. 2-7B). For the values tested here (afferent input frequencies $f = 60, 80, 100$ Hz), we found no difference in degree of input reduction required for seizure termination. Rather, independent from whether the input decrease occurred during tonic firing (left panels) or bursting (right panels), the seizure-like activity exhibited the previously found stereotyped termination behavior (bursting followed by silence, black traces for $f = 60$ Hz in Fig. 2-7B). This finding is in agreement with the *in vivo* observation that spike-and-wave seizures in anesthetized cats always terminate in bursting mode (Igor Timofeev, personal communication). For input reductions that were not sufficient to terminate the seizure-like activity ($f = 80$

and 100 Hz in blue and red, respectively), the slow state transitions persisted but at slower frequency.

DISCUSSION

Key finding of our current study is that a cortical network driven by afferent input exhibited a bistability between a physiological and a pathological activity state when $[K^+]_o$ dynamics were included. In agreement with the potassium accumulation hypothesis (Fertziger and Ranck, 1970; Green, 1964), we found that positive feedback dynamics mediated the transition from the physiological to the pathological state. Importantly, however, we established several discrepancies to the predictions derived from the potassium accumulation hypothesis. First, we found that $[K^+]_o$ followed instead of preceded increases in activity at the onset of transient changes in the afferent input that elicited seizure-like activity. Second, the pathological state consisted of alternating epochs of tonic firing and bursting. As a result of this switching between these two meta-stable states, $[K^+]_o$ did not exhibit unstable runaway dynamics that would have led to depolarization block and seizure termination. Rather, reduction in afferent input mediated termination of the pathological activity.

In summary, our findings suggest that $[K^+]_o$ plays a crucial role in the pathophysiology of cortical seizures. Based on our result that including $[K^+]_o$ dynamics caused the emergence of two stable network states (physiological and pathological activity), we suggest a revised framework of seizure dynamics. We propose that seizures are not considered network instabilities (as for example in the original potassium accumulation hypothesis) but rather manifestations of a second stable network state. The basin of attraction of this “pathological” state may vary between healthy and epileptic brains. An increase of this basin in patients suffering from epilepsy would reduce the threshold for transitions from the physiological to the pathological state. The proposed model may explain the relatively random occurrence of most seizures. In the epileptic brain, fluctuations would more easily drive the network into the basin of attraction of the seizure state due to its increased size. In contrast, such transitions may never occur in the non-epileptic brain. In this framework, seizure initiation and termination are two possibly symmetric processes, namely the switching between two stable network states that coexist. This bistability mediated by $[K^+]_o$ dynamics may be a fundamental property of epileptic networks and deserves further research.

2.3 Slow State Transitions of Sustained Neural Oscillations by Activity-Dependent Modulation of Intrinsic Excitability

Little is known about the dynamics and mechanisms of transitions between tonic firing and bursting in cortical networks. Here, we use a computational model of a neocortical circuit with extracellular potassium dynamics to show that activity-dependent modulation of intrinsic excitability can lead to sustained oscillations with slow transitions between two distinct firing modes - fast run (tonic spiking or fast bursts with few spikes) and slow bursting. These transitions are caused by a bistability with hysteresis in a pyramidal cell model. Balanced excitation and inhibition stabilizes a network of pyramidal cells and inhibitory interneurons in the bistable region and causes sustained periodic alternations between distinct oscillatory states. During spike-wave seizures, neocortical paroxysmal activity exhibits qualitatively similar slow transitions between fast run and bursting. We therefore predict that extracellular potassium dynamics can cause alternating episodes of fast and slow oscillatory states in both normal and epileptic neocortical networks.

INTRODUCTION

Neural oscillations are a hallmark of cortical network dynamics (Buzsaki and Draguhn, 2004). Sustained oscillatory activity can be broadly classified as either tonic firing or bursting. Neurons in a number of brain structures including thalamus (Jahnsen and Llinas, 1984a, b) and neocortex (Connors and Gutnick, 1990; McCormick et al., 1985) exhibit either tonic firing or bursting in a state-dependent way. One of the most dramatic examples of global transitions between bursting and tonic spiking regimes is the transition from slow-wave sleep to REM sleep or waking in the thalamocortical system (McCormick, 1992; Steriade and McCarley, 2005; Steriade et al., 1993a; Steriade et al., 2001; Timofeev et al., 2001b). Slow transitions between a slow-wave state and a fast-wave state were also observed in olfactory cortex (Murakami et al., 2005). Coexistence of bursting and tonic spiking regimes is not limited to vertebrates (Lechner et al., 1996; Turrigiano et al., 1996); (Shilnikov et al., 2005). Different levels of synaptic excitatory drive, activation of intrinsic conductances by neuromodulation, and changes in the extracellular ionic environment control the state-dependent oscillatory regime (Gil et al., 1997; McCormick, 1992; Steriade and McCarley, 2005). Many of these mechanisms modulating neural excitability are activity-dependent themselves and therefore work in a feedback manner. However, the interaction between intrinsic or network oscillatory dynamics and activity-dependent feedback control mechanisms in cortical networks is poorly understood. In particular, little is known about how these mechanisms can lead to (1) sustained neural activity in the absence of external input and (2) slow transitions between different oscillatory regimes (Steriade, 2004b).

Intrinsic excitability depends on the reversal potential for potassium-mediated currents which is a function of extracellular potassium concentration $[K^+]_o$. Extracellular potassium accumulates during sustained neural activity (Amzica et al., 2002; Heinemann et al., 1977; Moody et al., 1974; Timofeev et al., 2002a). In turn, elevated $[K^+]_o$ increases intrinsic excitability, leading to spontaneous neural activity (Rutecki et al., 1985); (Traynelis and Dingledine, 1988). Thus, $[K^+]_o$ dynamics modulate intrinsic excitability in a positive feedback manner. It is well established that $[K^+]_o$ increases during paroxysmal activity (Heinemann et al., 1977; Moody et al., 1974); however, whether elevated $[K^+]_o$ is the primary factor eliciting seizures or is a byproduct of increased firing remains unknown. Glia cells play an important role in the regulation of $[K^+]_o$ by effectively acting as a potassium buffer (Kofuji and Newman, 2004; Kuffler et al., 1966; Orkand et al., 1966).

Here, in a realistic neocortical network model with potassium dynamics (Bazhenov et al., 2004), we investigate complex cellular and the network behavior caused by activity-dependent changes in extracellular potassium concentration. We show that a model of neocortical circuitry which includes the interaction between extracellular ion concentration and intrinsic excitability exhibits slow state transitions between two distinct oscillatory firing modes (tonic spiking and bursting) which have been observed *in vivo* but still lack theoretical explanations.

METHODS

COMPUTATIONAL MODELS

We used a mathematical model of a cortical network consisting of cortical pyramidal (PY) cells and inhibitory interneurons (INs) to study the effect of extracellular potassium dynamics on oscillatory firing regimes. Each model neuron (Bazhenov et al., 2004; Mainen and Sejnowski, 1996) incorporated both intrinsic and synaptic currents and was composed of an axo-somatic compartment with membrane voltage V_S governed by

$$g(V_S - V_D) = -I_S^{int}, \qquad (1)$$

and a dendritic compartment with membrane voltage V_D governed by:

$$C_m \, dV_D/dt = -g_L(V_D - E_L) - g(V_D - V_S) - I_D^{int} - I^{syn}, \qquad (2)$$

where g is the coupling conductance, I_S^{int} and I_D^{int} are the intrinsic currents in the two compartments, C_m is the membrane capacitance, g_L and E_L are the conductance and reversal potential of the leak current, respectively. As in previous studies (Mainen and Sejnowski, 1996), we have omitted the axo-somatic capacitance since axo-somatic currents are sufficiently strong to change the somatic membrane voltage almost immediately. Assuming these very fast dynamics to be instantaneous by setting the somatic conductance to zero permitted the use of a larger integration step size resulting in increased computational efficiency. The ratio of dendritic to axo-somatic area *r* was chosen to mimic regular spiking neuron (*r* = 165) for PY and fast spiking neuron (*r* = 50) for IN. Both active and passive biophysical mechanisms regulate potassium in the extracellular space. In the model, $[K^+]_o$ was continuously computed and the reversal potential for channels permeable to potassium accordingly updated. We studied the behavior of a single PY cell, a small globally connected network, and a larger one-dimensional two-layer (PY and IN) network. In order to investigate the effects of changes in $[K^+]_o$ on the firing behavior, we explicitly controlled and varied $[K^+]_o$ in a subset of simulations (bifurcation analysis).

INTRINSIC CURRENTS

Intrinsic ionic currents were mediated by a set of Hodgkin-Huxley type conductances. Fast inactivating Na^+ channels (high and low density in axo-somatic and dendritic compartment, respectively) and fast delayed rectifier K^+ channels (axo-somatic compartment) formed the basis of action potential generation. Further, persistent sodium conductance G_{NaP}, slow voltage-gated K^+ conductance G_{Km}, slow calcium-activated K^+ conductance G_{KCa}, high-threshold Ca^{2+} conductance G_{Ca}, hyperpolarization-activated depolarizing conductance G_{h} were included in the dendritic compartment and K^+ leak conductance G_{L} was introduced in both axo-somatic and dendritic compartments (Bazhenov et al., 2004; Timofeev et al., 2000). In a previous study (Bazhenov et al., 2004), many of these conductances were systematically varied to establish model robustness for parameter variations. The relative balance of intrinsic currents was altered by varying the maximal conductances. Here, we considered $G_{\mathrm{Ca}} = 0.012 - 0.018$ mS/cm^2, $G_{\mathrm{KCa}} = 1.5 - 3.5$ mS/cm^2, $G_{\mathrm{NaP}} = 3.0 - 4.0$ mS/cm^2, and $G_{\mathrm{h}} = 0.0 - 0.1$ mS/cm^2.

SYNAPTIC CURRENTS

Synaptic transmission was modeled by a first-order kinetic scheme of neurotransmitter binding and unbinding to postsynaptic receptors which was shown to well fit experimental data (Destexhe et al., 1994). We assumed neurotransmitter release time courses to be of rectangular shape, reducing the time-course of the fraction of open-receptors [O](t) after a presynaptic spike to a single exponential. All synaptic currents I_{syn} were governed by

$$I_{\mathrm{syn}} = g_{\mathrm{sy}n}[\mathrm{O}](V-E_{\mathrm{syn}}), \quad (3)$$

where g_{syn} is the maximal conductance ($g_{\mathrm{AMPA(PY\text{-}PY)}} = 0.20\ \mu\mathrm{S}$, $g_{\mathrm{NMDA(PY\text{-}PY)}} = 0.013\ \mu\mathrm{S}$, $g_{\mathrm{AMPA(PY\text{-}IN)}} = 0.010\ \mu\mathrm{S}$, $g_{\mathrm{NMDA(PY\text{-}IN)}} = 0.014\ \mu\mathrm{S}$, $g_{\mathrm{GABA(IN\text{-}PY)}} = 0.05\ \mu\mathrm{S}$) and E_{syn} the reversal potential ($E_{\mathrm{AMPA}} = 0$ mV, $E_{\mathrm{NMDA}} = 0$ mV, $E_{\mathrm{GABAA}} = -80$ mV). Dependence of NMDA receptors on postsynaptic membrane voltage V_{post} was modeled by $1/(1+\exp(-(V_{\mathrm{post}} - V_{\mathrm{th}})/\sigma))$ with $V_{\mathrm{th}} = -25$ mV and $\sigma = 12.5$ mV.

Synapses incorporated short-term depression described by a depression variable $D \leq 1$ which was multiplied with the maximal synaptic conductance (Markram et al., 1998; Tsodyks and Markram, 1997). D was adjusted with factor R =

0.93 (7% resources per action potential) from its previous value D_i after a presynaptic spike at time t_i with recovery time constant $\tau = 700$ ms:

$$D = 1-(1-D_i R)\exp(-(t-t_i)/\tau). \quad (4)$$

Depression D accounts for short-term use-dependent weakening of synaptic strength after subsequent stimulation and recovery thereof. To study the role of synaptic interaction, the balance of excitation and inhibition was altered in a subset of simulations by multiplying the maximal conductances of the corresponding synapses by the factors 0.8, 0.9, 1.1, and 1.2 (scaling factors PY-PY for excitatory coupling between pyramidal cells and IN-PY for inhibitory coupling, respectively).

POTASSIUM DYNAMICS

$[K^+]_o$ was computed for extracellular volumes surrounding each cell. Our model of extracellular potassium dynamics followed a previously developed model (Bazhenov et al., 2004) where parameters were systematically varied to study the robustness of the model. Processes affecting $[K^+]_o$ were channels permeable to K^+, K^+ pumps, and glial K^+ uptake (buffering) G:

$$d[K^+]_{o(D,S)}/dt = (k/Fd)\, I_{\Sigma K} + G, \qquad (5)$$

where $k = 10$ denotes a conversion factor, $F = 96489$ C/mol the Faraday constant, and d the ratio of the volume of the extracellular compartment to the surface area. The total potassium current $I_{\Sigma K}$ is the sum of all potassium currents (fast rectifying I_K, calcium-activated I_{KCa}, voltage-dependent non-inactivating I_{Km}, and leak current I_L) and the current I_{KPump} mediated by K^+ pumps:

$I_{\Sigma K} = I_K + I_{KCa} + I_{Km} + I_L + I_{KPump}$. (6)

The K^+ current I_{KPump} established by K^+ pumps was an inward current which had a sigmoidal dependence on the ratio of steady-state $[K^+]_{o(eq)} = 3.5$ mM to current $[K^+]_o$ and saturated at I_{max}, which was chosen to balance K^+ leak current (dendritic compartment $I_{max} = 5\text{mA/cm}^2$, somatic compartment $I_{max} = 40\ \text{mA/cm}^2$):

$I_{KPump} = I_{max} /(1+([K^+]_{o(eq)}/[K^+]_o))^2$. (7)

Glial K^+ uptake current G was modeled by a free buffer (total buffer $[B_{max}]$ = 500 mM) with concentration [B], which bound and unbound from K^+ with according on- and off-rates $k_1 = 0.008$ and $k_2 = k_1/(1+\exp(([K^+]_o-[K^+]_{o(th)})/-1.15))$ governed by first order kinetics:

$d[B]/dt = k_1([B]_{max}-[B])-k_2\ [K^+]_o\ [B]$, $G = k_1([B]_{max}-[B])/k_{1N}-k_2\ [K^+]_o\ [B]$. (8)

Threshold concentrations $[K^+]_{o(th)}$ (15 mM for somatic compartment, 9 mM for dendritic compartment) and $k_{1N} = 1.1$ were chosen such that K^+ concentration equilibrated both for silent and tonic firing mode (Bazhenov et al., 2004).

Changes in $[K^+]_o$ changed the reversal potential for all conductances modeling ion channels permeable to K^+. The Nernst equation described the reversal potential for pure K^+ conductances:

$E_K = 26.64\ \text{mV}\ \ln([K^+]_o/[K^+]_i)$. (9)

The reversal potential for G_h and G_L which are ion channels permeable to several ion types were updated according to the Goldman-Hodgkin-Katz equation taking into account the different ionic concentrations ($[\mathrm{Na}^+]_o$ = 130 mM, $[\mathrm{Na}^+]_i$ = 20 mM, $[\mathrm{Cl}^-]_o$ = 130 mM, $[\mathrm{Cl}^-]_i$ = 8 mM) and degrees of permeability:

$$E_\mathrm{h} = 26.64\ \mathrm{mV}\ \ln([\mathrm{K}^+]_o + 0.2\ [\mathrm{Na}^+]_o)/(\ [\mathrm{K}^+]_i + 0.2\ [\mathrm{Na}^+]_i) \quad (10)$$

$$E_\mathrm{L} = 26.64\ \mathrm{mV}\ \ln([\mathrm{K}^+]_o + 0.085\ [\mathrm{Na}^+]_o + 0.1\ [\mathrm{Cl}^-]_i)/$$

$$([\mathrm{K}^+]_i + 0.085\ [\mathrm{Na}^+]_i + 0.1\ [\mathrm{Cl}^-]_o). \qquad (11)$$

CALCIUM DYNAMICS

Intracellular calcium concentration $[\mathrm{Ca}^{2+}]_i$ was computed for the dendritic compartment where the calcium-activated potassium channels were located. Calcium influx through high-threshold calcium channels was counteracted by exponential return to baseline concentration $[\mathrm{Ca}^{2+}]_{i(eq)}$ modeling pumps extruding calcium from the cytosol:

$$d[\mathrm{Ca}^{2+}]_i/dt = k\ I_\mathrm{Ca}/(2\ F) + ([\mathrm{Ca}^{2+}]_{i(eq)} - [\mathrm{Ca}^{2+}]_i)/\tau_\mathrm{Ca}, \quad (12)$$

where k and F are constants as described above, $[\mathrm{Ca}^{2+}]_{i(eq)}$ = 0.0001 mM is the equilibrium concentration, and τ_Ca = 500 ms is the recovery time constant.

NETWORK TOPOLOGY

To dissociate the effect of synaptic coupling from the effect of intrinsic cellular responses to depolarized K^+ reversal potentials, we first studied the behavior of a single PY cell. Then, we used a small network of five PY cells and one IN with global connectivity where each PY cell was connected to every other PY cell by excitatory synapses (AMPA and NMDA). The IN received excitatory synapses from all PY cells

(AMPA and NMDA) and projected back to all PY cells ($GABA_A$). This compact network was a direct extension of the case of an isolated PY cell since no localized spatial patterns of activity arose and all neurons exhibited synchronous transitions in their firing regimes. We studied the effect of changes in excitatory and inhibitory coupling by systematically varying the maximal conductance for AMPA and NMDA or GABA mediated synaptic currents respectively. We further used a larger network model composed of two one-dimensional layers formed by 60 PY cells and 15 IN respectively. Each PY cell was connected to five neighboring PY cells on both sides, each PY cell connected to three neighboring INs, and each IN projected back to a total of eleven neighboring PY cells.

BIFURCATION ANALYSIS

In order to study how extracellular K^+ concentration, $[K^+]_o$, modulated neural activity, we held $[K^+]_o$ constant in a subset of the simulations to determine the firing behavior as a function of $[K^+]_o$. This corresponds to opening the positive feedback loop between neural activity and $[K^+]_o$. Such analysis provided useful predictions for the case where $[K^+]_o$ would freely evolve (i.e. closed feedback loop) because of the vastly different time-scales of the $[K^+]_o$ dynamics (slow) and the dynamics of the ion conductances mediating neural activity (fast). In other words, we used the slow/fast analysis technique for systems with widely differing time scales (geometric singular perturbation theory, (Jones, 1994; Osinga and England, 2005; Rinzel, 1985; Rinzel and Lee, 1987)). Extracellular K^+ concentration, $[K^+]_o$, which exhibited very slow dynamics with time-scale corresponding to entire epochs of oscillatory firing at a given frequency, was treated as a parameter for bifurcation analysis. We used a combination of direct integration for different parameter values, continuation analysis (MATCONT software (Dhooge et al., 2003)), and Poincare maps (Kuznetsov, 2004) to trace and analyze bifurcations.

IN VIVO EXPERIMENTS

Experiments were conducted on cats anesthetized with ketamine-xylazine anesthesia (10-15 and 2-3 mg/kg i.m., respectively). The animals were paralyzed with gallamine triethiodide (20 mg/kg) after the EEG showed typical signs of deep general anesthesia, essentially consisting of slow oscillation (0.5-1 Hz). Supplementary doses of the same anesthetics (5 and 1 mg/kg) or ketamine (5 mg/kg) were administered at the slightest changes toward diminished amplitudes of slow waves. The cats were artificially ventilated with the control of end-tidal CO_2 at 3.5-3.7%. Body temperature was maintained at 37-38^{o}C and the heart rate was ~90-100 beats/min. For intracellular recordings, stability was ensured by the drainage of cisterna magna, hip suspension, bilateral pneumothorax, and filling the hole made for recordings with a solution of 4% agar. At the end of experiments, the cats were given a lethal dose of pentobarbital (50 mg/kg i.v.). All experimental procedures were performed according to national guidelines and were approved by the committee for animal care of Laval University. Intracellular recordings from suprasylvian association areas 5 and 7 were performed using sharp glass micropipettes filled with a solution of 3 M potassium-acetate (KAc).

Field potentials were recorded in the vicinity of impaled neurons. All electrical signals were sampled at 20 kHz and digitally stored on Vision (Nicolet, Wisconsin, USA). Offline computer analysis of electrographic recordings was done with IgorPro software (Lake Oswego, Oregon, USA).

RESULTS

TRANSITION BETWEEN SLOW BURSTING AND TONIC FIRING IN A SINGLE CELL

A brief increase in $[K^+]_o$ was used to initiate activity in an otherwise silent pyramidal (PY) neuron. An isolated PY cell model (G_{Ca} = 0.015 mS/cm^2, G_h = 0.1 mS/cm^2) with a spatially limited extracellular compartment responded to a brief $[K^+]_o$ elevation with oscillatory firing before returning to rest. While $[K^+]_o$ decreased to its resting value (3.5 mM), the PY cell exhibited several oscillatory modes: first slow bursting oscillations and then tonic firing (Fig. 2-8A, transition in Fig. 2-8B). For significantly elevated $[K^+]_o > 5.6$ mM, bursts with spike inactivation, pronounced after-hyperpolarization, and strong calcium influx occurred (Fig. 2-8C, left panel, phase space plot of a single burst). Calcium influx during the depolarized state caused the calcium-activated potassium conductance to activate which in turn mediated burst termination and subsequent after-hyperpolarization (Fig. 2-10). For $[K^+]_o = 5.6$ mM, however, there was a transition to bursts with reduced after-hyperpolarization and with minor spike inactivation (Fig. 2-8C, middle panel). For $[K^+]_o = 5.5$ mM, the cell switched to tonic firing (spike doublets, Fig. 2-8C, right panel) before it eventually returned to rest. Both during slow bursting and tonic firing, potassium efflux occurred mainly through the fast delayed-rectifier (41% and 43% for bursting and tonic firing, respectively) and through the leak conductance (43% and 56%, respectively). This oscillatory firing patterns for elevated $[K^+]_o$ are not a mere consequence of the depolarization of the neuron since an injected depolarizing current step caused only tonic firing with spike adaptation (Fig. 2-9).

Since $[K^+]_o$ changed on a very slow time-scale, we next treated $[K^+]_o$ as a parameter to determine the cell's firing behavior as a function of $[K^+]_o$ Therefore, all the mechanisms controlling $[K^+]_o$ evolution in our model were blocked and the neuron behavior was analyzed for different fixed values of $[K^+]_o$ within the physiological range. Specifically, we focused on the occurrence of different stable firing modes as a function of parameter $[K^+]_o$ (Fig. 2-11). For low $[K^+]_o$, the neuron was at rest (Fig. 2-11A, left). For increasing $[K^+]_o$, the resting potential became more depolarized as the driving force for potassium decreased. For $[K^+]_o = 4.85$ mM, the neuron switched to tonic firing by means of a saddle-node bifurcation (Type I neural oscillator (Ermentrout, 1996; Rinzel and Ermentrout, 1989), fixed point bifurcations in Fig. 2-11C). Tonic firing and slow bursting coexisted for $[K^+]_o$ between 5.45 and 6.35 mM. Slow bursting was the only stable state for $[K^+]_o$ between 6.35 and 9.45 mM. At $[K^+]_o = 9.46$ mM, a new stable state corresponding to a depolarized state ($V_m = -26.3$ mV) appeared by means of a subcritical Hopf bifurcation (Fig. 2-11C). The depolarized state coexisted with the slow bursting regime in a narrow bistable region before it became the only stable state at $[K^+]_o = 10.05$ mM (Fig. 2-11A, right).

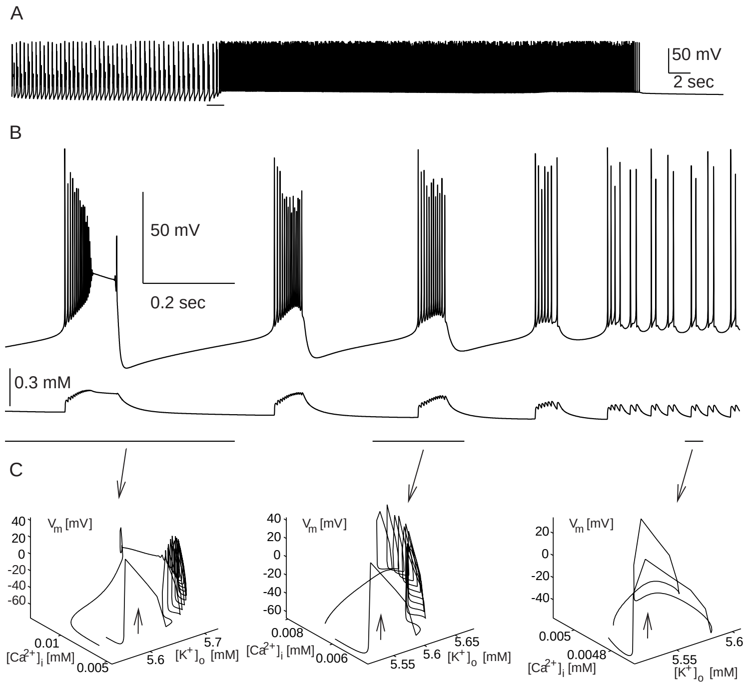

Figure 2-8 (A) A single PY neuron exhibits bursting and then tonic firing after a brief increase in extracellular potassium concentration ([K$^+$]$_o$) before returning to rest. (B) Membrane voltage (top) and [K$^+$]$_o$ (bottom) time courses for the time interval underlined in (A). Transition from bursting to tonic firing (spike doublets) at [K$^+$]$_o$ = 5.6 mM. (C) Phase space plots ([K$^+$]$_o$, intracellular calcium [Ca^{2+}]$_i$, and membrane voltage V_m) for the three intervals underlined in (A). Arrow indicates direction of time. Single burst with minor spike inactivation and after-hyperpolarization (left), single burst without spike inactivation and reduced after-hyperpolarization (middle), and spike doublet (right).

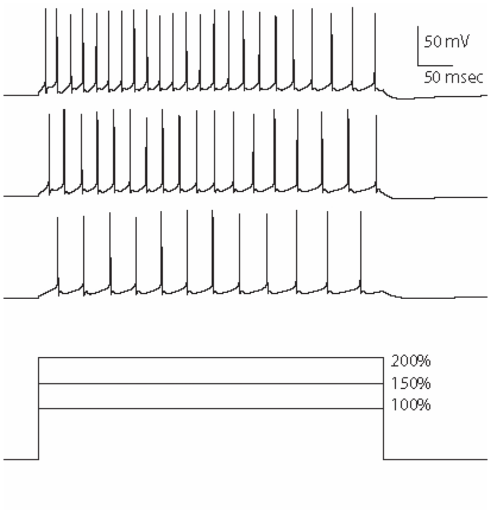

Figure 2-9 Membrane voltage traces for depolarizing current step injection into model PY cell for three different current intensities (200%, 150%, and 100%) from top to bottom.

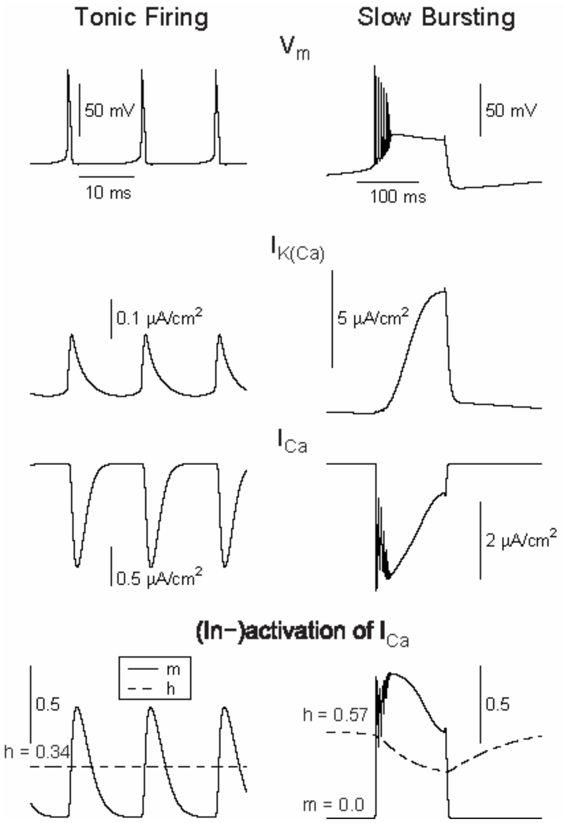

Figure 2-10 courses of membrane voltage V_m, calcium-activated potassium current I_{KCa}, high-threshold calcium current I_{Ca}, and (in-)activation of I_{Ca} for $[K^+]_o = 6.0$ mM. Tonic firing (left column) and slow bursting (right column). Note the different time-scales for the two columns. Bursts consisted of about 8 spikes at the onset, a sustained depolarization with spike inactivation lasting about 100 ms and a pronounced after-hyperpolarization at the end (top panels). Dynamic interplay of high-threshold calcium current I_{Ca} and calcium-activated potassium current I_{KCa} caused bursting (middle four panels). In comparison to the tonic firing mode, I_{KCa} was stronger by an order of magnitude and terminated the burst. Similarly, I_{Ca} was more pronounced during bursting. Activation variable *m* and inactivation variable *h* of the high-threshold calcium conductance G_{Ca} are shown in bottom panels. During tonic firing, high firing frequency and lack of pronounced after-hyperpolarization prevented G_{Ca} from fully deinactivating (inactivation variable $h \approx 0.34$, bottom left subpanel). This contrasted with the bursting regime where the lower burst frequency and the after-hyperpolarization caused more complete deinactivation of G_{Ca} between bursts ($h \approx 0.57$, bottom right subpanel). As a consequence, the depolarizing effect of I_{Ca} was stronger and prevented the membrane voltage from returning to rest after the first spike in the burst. The resulting gradual depolarization after each spike maintained the depolarized state of the burst. The different levels of deinactivation of the high-threshold calcium conductance G_{Ca} therefore mediate the bistability between tonic firing and bursting.

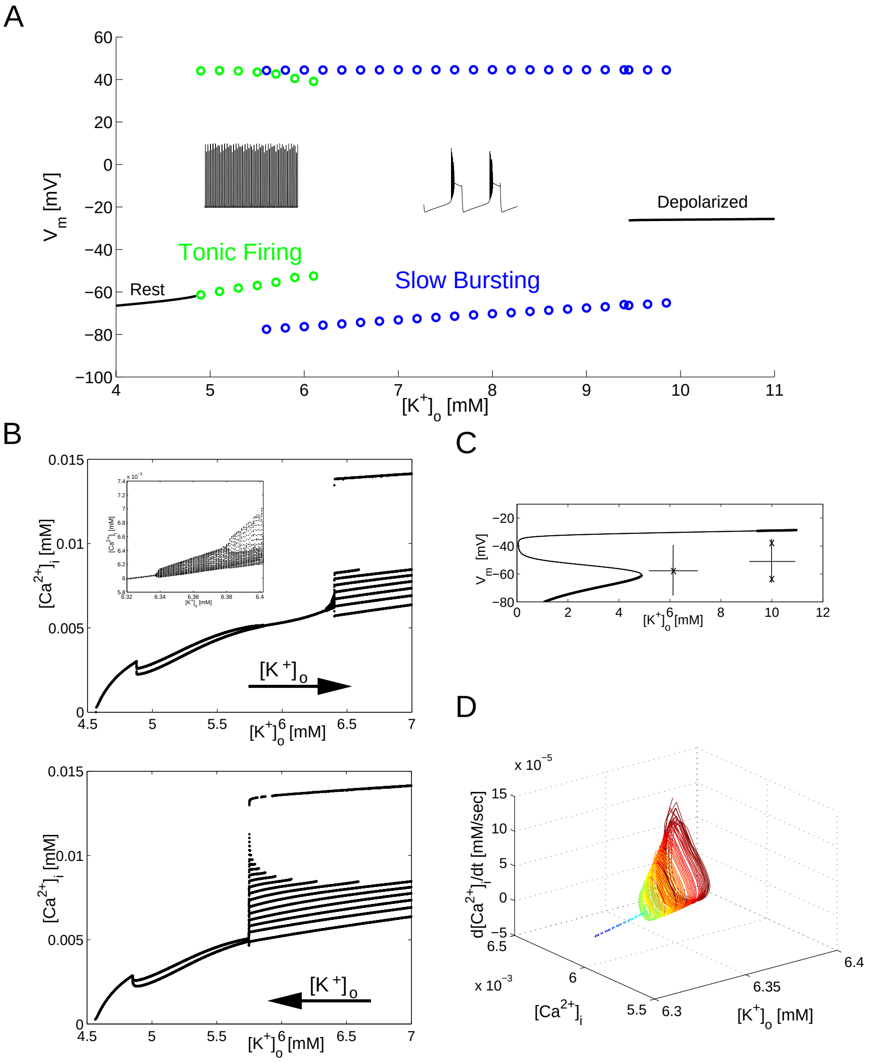

Figure 2-11 Bifurcation analysis of PY cell dynamics. (A) Maximum and minimum of membrane voltage as a function of $[K^+]_o$. Solid lines: stable fixed points. Circles: stable limit cycles. Four stable states are found - rest, tonic firing, slow bursting, and a depolarized state - with bistability occurring between tonic firing and slow bursting and between slow bursting and the depolarized state. (B) Poincare map. Intracellular calcium concentration for V_m = -20 mV as function of slowly increasing (top) and decreasing (bottom) $[K^+]_o$. Inset: Enlargement of transition from tonic firing to slow bursting. (C) Stable fixed points corresponding to rest and the depolarized state are connected via unstable fixed points. Transition from silent to tonic firing is a saddle-node bifurcation. Transition from slow bursting to depolarized is a Hopf bifurcation. Insets illustrate eigenvalues at bifurcation point. (D) Three dimensional representation of excerpt from (B) showing transition from tonic firing to frequency modulated fast firing. Neimark-Sacker bifurcation of limit cycle leads to slow spike modulation for $[K^+]_o > 6.33$ mM. Color scheme: From blue to red for low to high values of $[K^+]_o$.

In order to further characterize the transition between tonic firing and slow bursting, we computed a Poincare map by calculating the values of intracellular calcium concentration $[Ca^{2+}]_i$ each time the membrane potential crossed the threshold V_m = -20 mV; these values were plotted as a function of $[K^+]_o$ (Fig. 2-11, Poincare map). In such a representation, periodic oscillations (corresponding to limit cycles) are represented as points defined by a threshold crossing of a trajectory. This approach allows the graphical representation of changes in the nature of an oscillatory (firing) behavior as a function of a parameter. For a given value of $[K^+]_o$, a tonic spiking regime is represented on this Poincare plot by a single point since $[Ca^{2+}]_i$ assumes the same value at V_m = -20 mV for every spike. During a burst, however, $[Ca^{2+}]_i$ increases after each spike of a given burst. Therefore, a burst appears as a group of points each representing a single spike. In other words, a set of parallel lines in the Poincare plot (Fig. 2-11, Poincare map) illustrates a range of $[K^+]_o$ values for which bursting occurred. We gradually increased and decreased $[K^+]_o$ to reveal the complete tonic firing and slow bursting region, respectively. The bistability between tonic firing and slow bursting was associated with a hysteresis (compare top and bottom plots in Fig. 2-11B). For increasing $[K^+]_o$, the cell stayed in tonic firing until slow bursting with spike inactivation became the only stable state at $[K^+]_o$= 6.40 mM. Decreasing $[K^+]_o$ caused the cell to stay in slow bursting mode until tonic firing was the only stable state at $[K^+]_o$= 5.75 mM. For increasing $[K^+]_o$, the tonic firing region consisted of three subregions with single spikes, spike doublets, and single spikes, respectively (Fig. 2-11B, top). Time courses for single spikes ($[K^+]_o$ = 5.00 mM) and spike doublets ($[K^+]_o$

= 6.00 mM) are shown in Fig. 2-12A and B, respectively. Note that the left region with single spikes existed only in the case of a non-zero h-conductance (G_h = 0.05 mS/cm^2). At $[K^+]_o$ = 6.39 mM, tonic firing started to exhibit slow modulation of the membrane voltage and the spiking frequency (Fig. 2-12C; see, also, spectrogram in Fig. 2-12D). Detailed bifurcation analysis revealed that at $[K^+]_o$ = 6.39 mM, the limit cycle corresponding to the tonic spiking lost its stability by a supercritical Neimark-Sacker bifurcation (Kuznetsov, 2004) leading to a stable invariant torus in the phase space representation of the dynamical system (Fig. 2-11D). This type of behavior was not found for decreasing $[K^+]_o$ (Fig. 2-11B, bottom). Instead, two distinct bursting regimes - with and without spike inactivation - were found (see Fig. 2-12E and F). For these bursts, transition from silent state to spiking (burst onset) occurred through a saddle-node bifurcation of the fixed point corresponding to the silent (hyperpolarized) state. Return to the silent state (burst offset) occurred through a Hopf bifurcation of the fixed point corresponding to the depolarized (upper) state. Activation of $I_{K(Ca)}$ (slow variable) controlled the transitions between silent and oscillatory states during bursts (data not shown).

The biophysical mechanism for the bistability with hysteresis between tonic firing and slow bursting was examined by (1) comparing the ionic currents in both regimes for $[K^+]_o$ = 6.00 mM (Fig. 2-10) and (2) systematically varying the intrinsic conductances involved in burst generation (Fig. 2-12). We found that the different levels of deinactivation of the high-threshold calcium current I_{Ca} explain the hysteresis between tonic firing and bursting. I_{Ca} reinforced bursting and therefore increased the range of $[\mathrm{K}^+]_o$ values for which the neuron stayed in bursting mode. In contrast, when the neuron was in tonic firing mode, insufficient I_{Ca} deinactivation between spikes prevented switching to the bursting mode unless $[\mathrm{K}^+]_o$ was strongly elevated (Fig. 2-10, bottom panels). To confirm the role of I_{Ca} and to test the robustness of our model, we separately varied the three intrinsic conductances G_{Ca}, G_{NaP}, and G_{KCa}, involved in initiating, sustaining, and terminating bursts to study their impact on the bistability with hysteresis between tonic firing and bursting. Further, the effect of introducing a hyperpolarization-activated depolarizing conductance G_{h} was examined. As anticipated, the width of the hysteresis between tonic firing and bursting varied with G_{Ca}, whereas changes in the other conductances had minimal impact on the qualitative nature of the hysteresis (Fig. 2-12). These findings indicate the pivotal role of the high-threshold calcium conductance G_{Ca} in mediating bistability between the two oscillatory firing regimes.

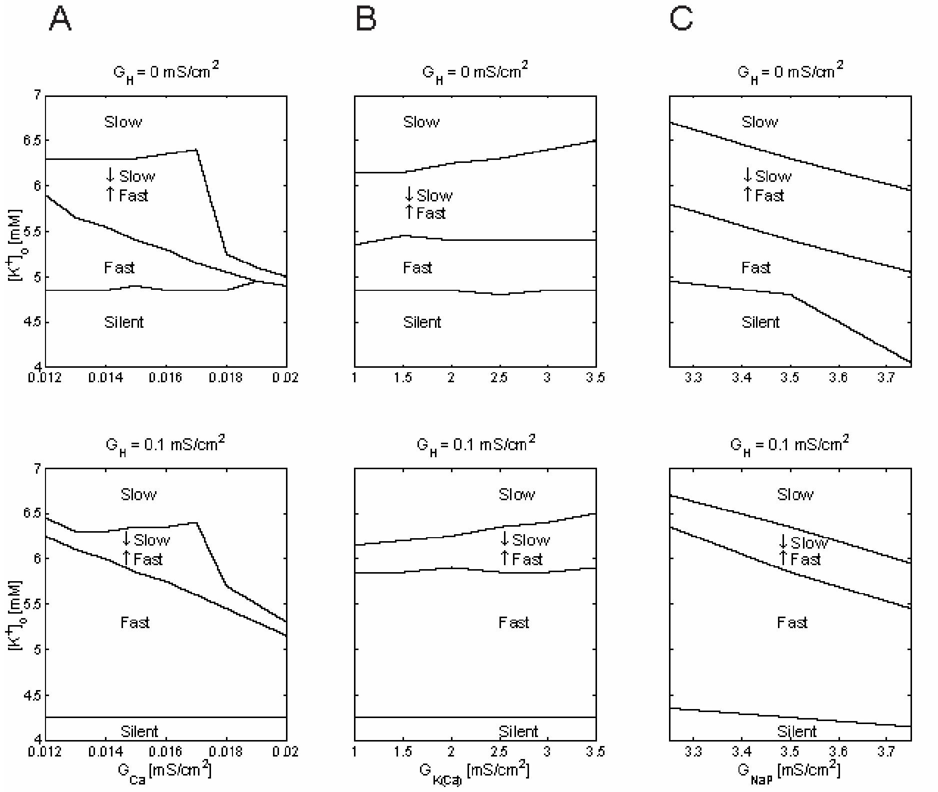

Figure 2-12 Robustness analysis to variation of intrinsic conductances (parameter sensitivity analysis). Dependence of single cell hysteresis for transition between slow bursting and fast run on G_{Ca} (A), $G_{K(Ca)}$ (B), and G_{NaP} (C) without (top row) and with (bottom row) hyperpolarization-activated depolarizing conductance G_h. The width of the hysteresis greatly depended on the choice of G_{Ca}. The hysteresis was robust to variations in $G_{K(Ca)}$. Increasing G_{NaP} shifted the hysteresis to lower values of $[K^+]_o$. In all three cases, introducing G_h = 0.1 mS/cm^2 decreased the value of $[K^+]_o$ for which the neuron became active and narrowed the width of the hysteresis.

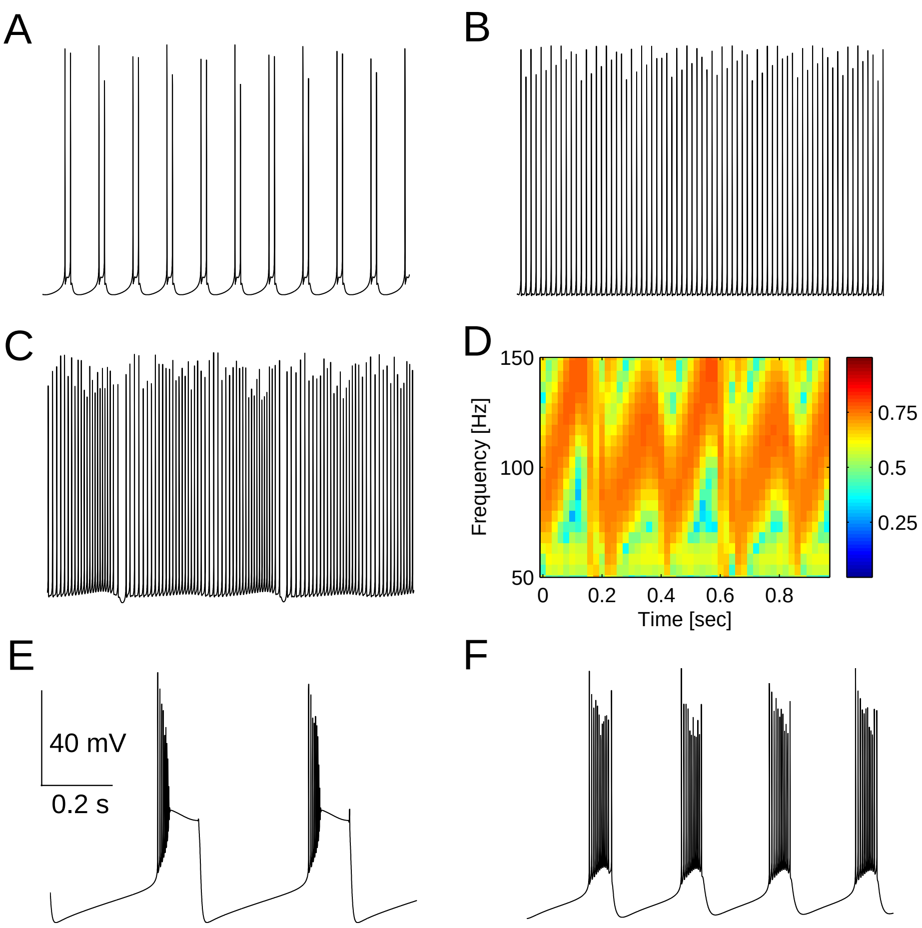

Figure 2-13 Time course of membrane voltage (1 sec duration) for different values of $[K^+]_o$. (A) Spike doublets for $[K^+]_o = 5.00$ mM. (B) Fast tonic firing for $[K^+]_o = 6.00$ mM (tonic firing branch, $[K^+]_o$ increasing). (C) Fast tonic firing modulated by slow oscillation corresponding to Neimark-Sacker bifurcation of limit cycle and consecutive torus bifurcation with period doubling for $[K^+]_o = 6.39$ mM (tonic firing branch, $[K^+]_o$ increasing). (D) Spectrogram of (C). Normalized arbitrary units. (E) Bursting with spike inactivation for $[K^+]_o = 6.00$ mM (slow bursting branch, $[K^+]_o$ decreasing). (F) Bursting without spike inactivation for $[K^+]_o = 5.75$ mM (slow bursting branch, $[K^+]_o$ decreasing).

SLOW TRANSITIONS BETWEEN OSCILLATORY STATES IN SMALL NETWORK

In order to determine whether the hysteresis between tonic firing and slow bursting was maintained in a network of neurons, we studied a network consisting of five PY cells with all-to-all excitatory coupling and one IN, which mediated global inhibition. When $[K^+]_o$ was held at various fixed values, four different states equivalent to those in the single cell model were found: silence, fast run, slow bursting, and a depolarized state (Fig. 2-14A, left, transition from fast run to slow bursting). Fast run (fast bursting with 2-4 spikes) corresponded to tonic firing found in the single cell model. Each of the three transitions between neighboring states was associated with a hysteresis, confirming that the hystereses found in the single cell model were indeed maintained in the small network.

When $[K^+]_o$ was released and continuously updated based on K^+ currents, K^+ pumps, and glial buffering (see Eq. 5), a major difference between the single cell model and the network model was found. For a single PY cell surrounded by an extracellular compartment, $[K^+]_o$ decreased steadily during both tonic spiking and bursting. Thus, the hysteresis between tonic firing and slow bursting had no effect on neural dynamics triggered by elevated $[K^+]_o$ since the cell never switched back from tonic firing to bursting. In the small network, however, the cells did not return to rest after the initial $[K^+]_o$ injection but instead displayed self-sustained oscillations with periodic alternations between fast run and slow bursting (Fig. 2-14B, activity of all 5 PY cells as a function of time for 40 seconds). $[K^+]_o$ increased during fast run, which caused a transition of the network to the slow bursting regime as predicted by the upper endpoint of the hysteresis found by bifurcation analysis (Arrow 1 in Fig. 2-14A, top right). If there were no hysteresis, this would lead to an immediate return to fast run since $[K^+]_o$ decreased during slow bursting. Due to the hysteresis, however, slow bursting mode was maintained until the lower transition point for $[K^+]_o$ back to fast run was reached where the cycle restarted (Arrow 2 in Fig. 2-14A, top right). By averaging over many periods during fast run and a single period during slow bursting, we determined the time derivative of extracellular potassium concentration as a function of $[K^+]_o$ if it were free to change. This further illustrates the fact that $[K^+]_o$ increased during fast run and decreases during slow bursting (Fig. 2-14A, bottom right, dashed line represents $d[K^+]_o/dt = 0$ “nullcline”). The dependence of the lower and upper transition points on whether $[K^+]_o$ was increasing or decreasing matched the prediction from bifurcation analysis (Fig. 2-14A, end points of hysteresis). Thus, synaptic interaction stabilized the network in the hysteresis region between fast run and slow bursting ($[K^+]_o$ between 5.0 and 5. 4 mM). Synchrony is not required for this mechanism to work as long as the time derivatives of potassium follow this general rule. Rather, overall excitation mediated by network interaction needs to provide sufficient excitatory drive for firing frequencies which enable potassium to increase during tonic firing (fast run) without causing a switch to the bursting regime. Note that a single PY cell with a self-excitatory synapse did not exhibit these transitions (data not shown): it either displayed bursting (for strong coupling) or tonic firing (for weak coupling). Because the inhibitory interneuron was active during epochs of fast run, the spike structure of the fast run was different between the single cell and small network models. PY neurons from the network displayed fast oscillations with groups of spikes separated by short hyperpolarizing events mediated by IPSPs. When excitatory input to the inhibitory interneurons was reduced such that they became silent during fast run, PY neurons displayed tonic spiking activity similar to the single cell model (see Fig. 2-15).

Single cell model analysis revealed that high-threshold calcium current I_{Ca} inactivation was critical for determining the oscillatory mode (tonic spiking or bursting). In a further set of simulations, we extended this finding to the network model by perturbing inactivation variable, h, of I_{Ca} for all neurons in the network to induce switching between the two oscillatory states (Fig. 2-16). The network switched from fast run to slow bursting when enforcing a value of $h = 0.53$ (mean value between bursts) for 0.25 sec. Similarly, imposing a value of $h = 0.36$ (mean value during fast run) for 1 sec during slow bursting caused the network to switch to fast run.

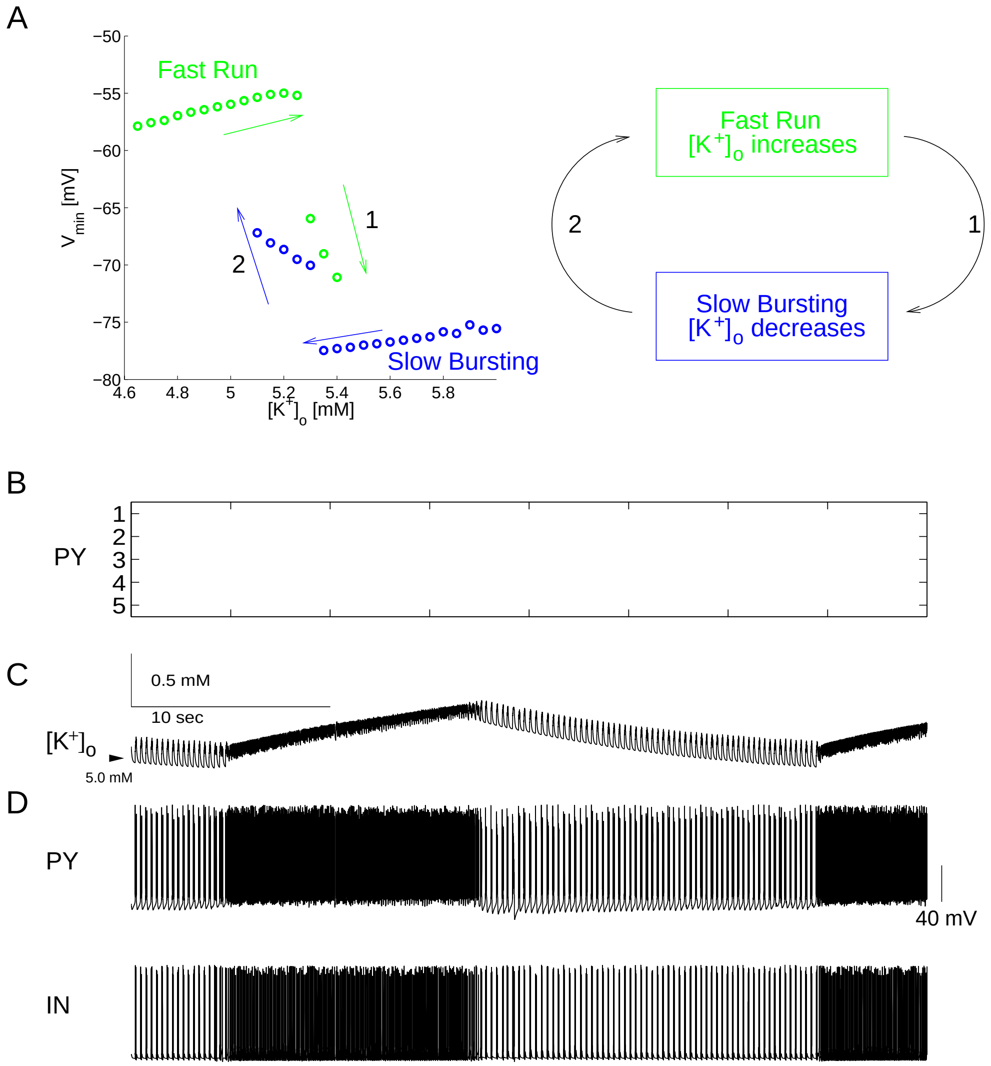

Figure 2-14 Globally connected network with five PY cells and one IN. (A) Left: Bifurcation analysis (minimum of membrane voltage): Hysteresis between fast run and slow bursting for $[K^+]_o$ between 5.0 and 5.4 mM. Circles denote stable limit cycle oscillations. Top right: Schematic of slow periodic network dynamics. Bottom right: Averaged $[K^+]_o$ change rate as a function of $[K^+]_{o.}$ (B-D) Slow transitions after initial brief increase in $[K^+]_o$ (B) Network activity of PY cells (40 seconds duration) shows alternating epochs of fast run and slow bursting. (C) $[K^+]_o$ increased during fast run and decreased during slow bursting. Upper switching point for transition from fast run to slow bursting and lower switching point for transition from slow bursting to fast run correspond to hysteresis endpoints in (A). (D) Membrane voltage time course of PY cell (top trace) and of IN (bottom trace).

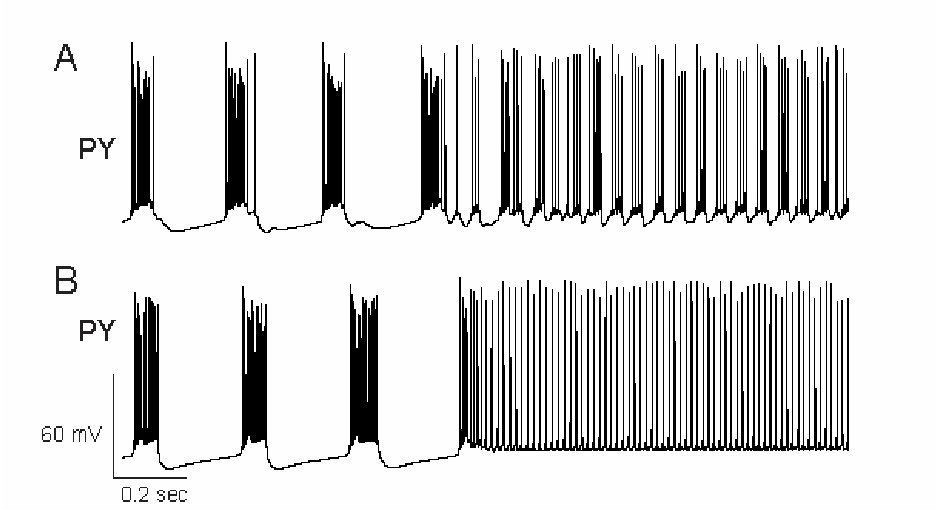

Figure 2-15 Transition from slow bursting to fast run in a PY cell for weak and strong excitatory drive of IN. (A) The inhibitory interneuron follows firing in the PY cell for $g_{AMPA(PY\text{-}IN)} = 0.010$ mS and $g_{NMDA(PY\text{-}IN)} = 0.014$ mS. PY firing is interrupted by IPSCs. PY cells fire in groups of spikes (fast bursts). (B) The IN interneuron is silent during fast run for $g_{AMPA(PY\text{-}IN)} = 0.007$ mS and $g_{NMDA(PY\text{-}IN)} = 0.008$ mS. Fast run in the PY cell is tonic firing at high frequency.

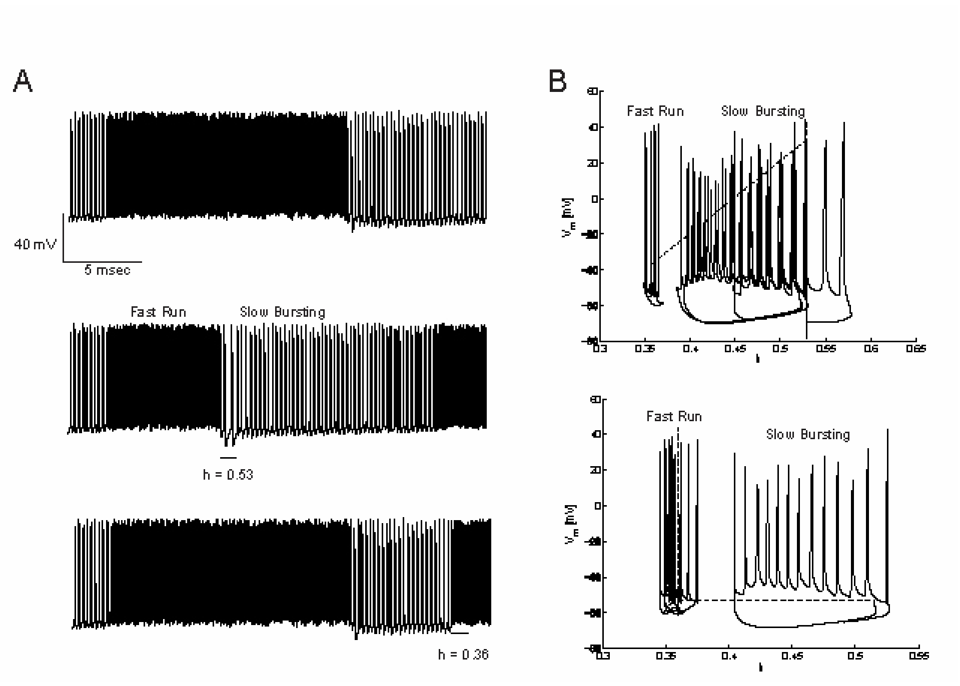

Figure 2-16 Controlling inactivation, *h*, of high-threshold calcium conductance GCa induced switching between slow bursting and fast run. (A) An unperturbed time-course of a PY cell in a model of small cortical network (top panel). Enforcing inactivation *h* = 0.53 for 1 sec caused the network to switch to slow bursting (middle panel). Similarly, a transition from slow bursting to fast run was induced by setting *h* = 0.36 for 1 sec (bottom panel). Horizontal bars delimit intervals where h was held constant. (B) Phase plane plots of switching between fast run and slow bursting (top panel) and vice versa (bottom panel) by controlling inactivation *h*.

ROLE OF SYNAPTIC CONDUCTANCES

Network interaction was critical for the occurrence of alternating epochs of fast run and slows bursting. Therefore, we systematically varied the synaptic strength to uncover its specific effect on the network dynamics. Increasing excitation (PY-PY coupling) without changing inhibition (IN-PY = 1.1) widened the $[K^+]_o$ hysteresis (from 0.24 to 0.62 mM for PY-PY = 0.8 and 1.2, respectively, Fig. 5A, left, dashed line) and prolonged the episodes of slow bursting at the expense of fast run (solid lines). The increase in hysteresis width was mainly caused by a lower value of $[K^+]_o$ for which the network switched from slow bursting to fast run (from 5.38 to 4.77 mM for PY-PY = 0.8 and 1.2, respectively, Fig. 2-17A, right). In contrast, increasing inhibition (IN-PY coupling) without changing excitation (PY-PY = 0.9) shortened epochs of slow bursting and prolonged epochs of fast run, respectively (Fig. 2-17B, left, solid lines). The $[K^+]_o$ hysteresis was narrowed (from 0.75 mM to 0.28 mM for IN-PY = 0.8 and 1.2, respectively, Fig. 2-17B, left, dashed line), mostly by an increase in the range of $[K^+]_o$ for which fast run was the only stable state (from 4.86 to 5.36 mM for IN-PY = 0.8 and 1.2, respectively). Thus, during fast run, $[K^+]_o$ increased more slowly due to the reduced firing frequency. Additionally, increased inhibition forced the network back to fast run for higher $[K^+]_o$. (Fig. 2-17B, right). Examples of non-alternating regimes resulted from major changes in the balance between excitation and inhibition (areas in dark blue in Fig. 2-17C right). For strong excitation and weak inhibition, the network returned to the silent state after a single epoch of bursting. Conversely, strong inhibition and weak excitation led to sustained fast run (time-courses in Fig. 2-18). Combinatorial variation of both excitatory (PY-PY) and inhibitory (IN-PY) synaptic coupling strength showed that the existence of the transitions between fast run and slow bursting is robust to changes in synaptic connectivity as long as the balance between excitatory and inhibitory coupling was maintained. Both the logarithmic ratio of the duration of fast run and slow bursting episodes and the width of the hysteresis were only slightly affected by changes in synaptic connectivity strength as long as excitation and inhibition was scaled accordingly (diagonal structure in Fig. 2-17C).

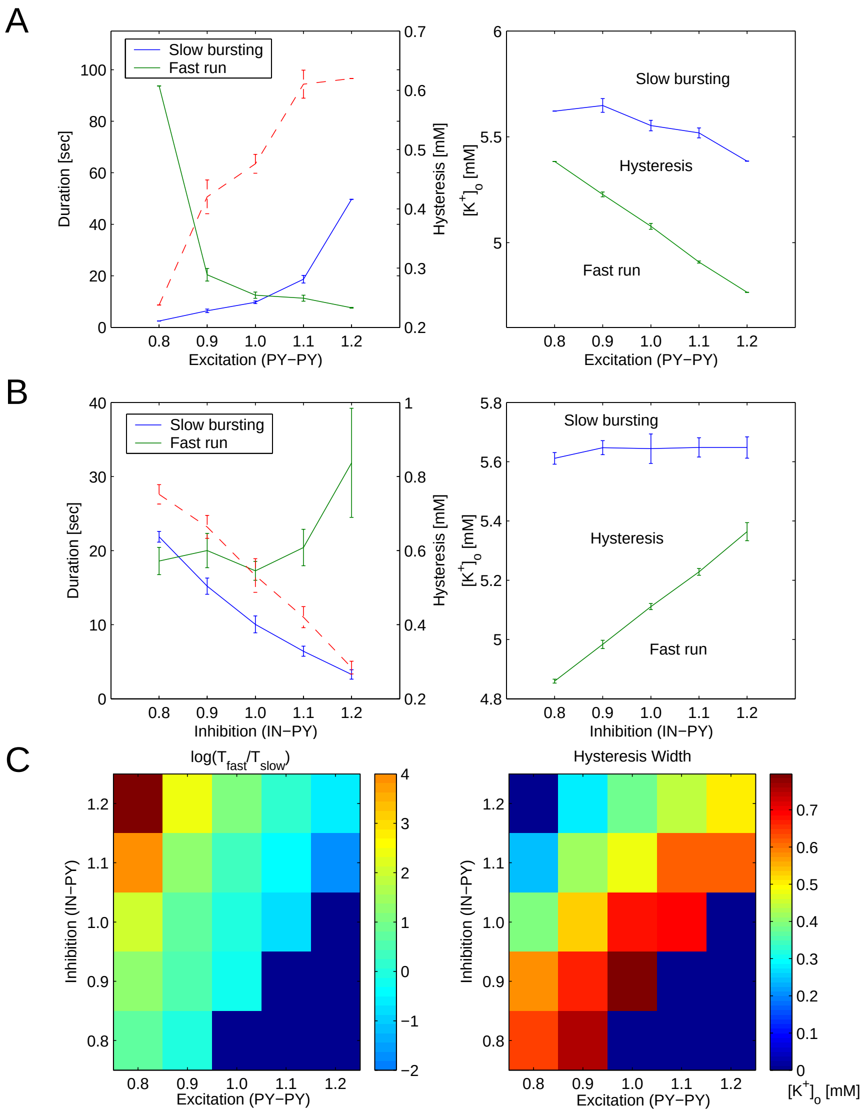

Figure 2-17 Quantification of periodic slow transitions between slow bursting and fast run as a function of excitatory and inhibitory coupling. Balanced excitation and inhibition causes alternating epochs of slow bursting and fast run. Left: Duration of epochs of slow bursting and fast run (blue and green solid line, respectively) and width of hysteresis (dashed red line) and upper and lower endpoint of hysteresis (right) for changing (A) excitatory coupling (PY-PY) and (B) inhibitory coupling (IN-PY). Values determined from simulation of 400 sec of activity. Error bars, s.e.m. (C) Overview plot showing logarithmic ratio of duration of fast run and slow bursting (left) and width of hysteresis (right) as a function of synaptic excitation and inhibition. Top left corner corresponds to regime with exclusive fast run, whereas bottom right corner denotes the regime with exclusive slow bursting.

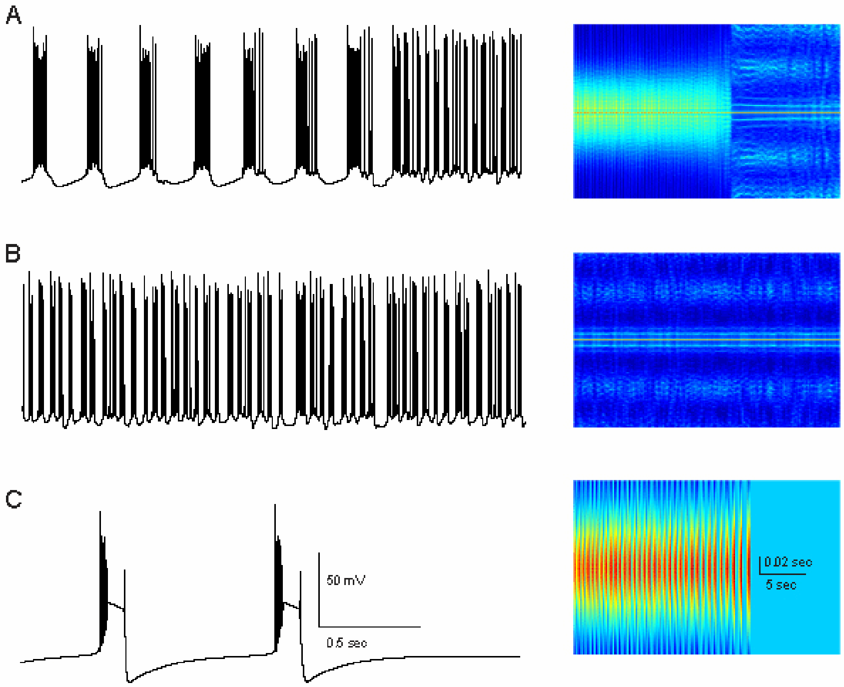

Figure 2-18 Effect of synaptic coupling. PY membrane voltage time course (left column) and time-dependent autocorrelation computed every 100 msec for a window of 400 msec (right column). (A) Transition between slow bursting and fast run for $g_{AMPA(PY\text{-}PY)} = 0.20$ mS, $g_{NMDA(PY\text{-}PY)} = 0.013$ mS, $g_{AMPA(PY\text{-}IN)} = 0.010$ mS, $g_{NMDA(PY\text{-}IN)} = 0.014$ mS, $g_{GABA(IN\text{-}PY)} = 0.05$ mS. (B) Weak excitation and strong inhibition (scaling: PY-PY = 0.8 and IN-PY = 1.2). PY cells remained in fast run. No transition to slow bursting due to decreased excitatory drive. (C) Strong excitation and weak inhibition (scaling: PY-PY = 1.2 and IN-PY = 0.8). Network directly returned to silence after a single epoch of bursting.

Bursts differed in their characteristics depending on the balance between excitation and inhibition (Fig. 2-19). In the case of reduced excitation (PY-PY = 0.9) and inhibition (IN-PY = 0.8), bursts exhibited a gradual decline in spike amplitude, spike inactivation, and a pronounced after-hyperpolarization (Fig. 2-19A, first row). Excitatory AMPAergic input to PY cells built up during spiking at the onset of the burst. NMDA current was active until burst termination (Fig. 2-19A, second row). For increased inhibition (IN-PY = 1.2, Fig. 2-19B), bursts showed decreased spiking frequency and lacked both spike inactivation and after-hyperpolarization. Excitatory synaptic currents mediated by AMPA and NMDA receptors were of similar amplitude and duration. Balancing increased inhibition (IN-PY = 1.2) by strengthening excitation (PY-PY = 1.2) increased both firing frequency within the burst and the total number of spikes per burst (Fig. 2-19C). Fast run spiking structure was less sensitive to moderate changes in the balance between excitation and inhibition as long as the inhibitory interneuron remained active during periods of fast runs (see above).

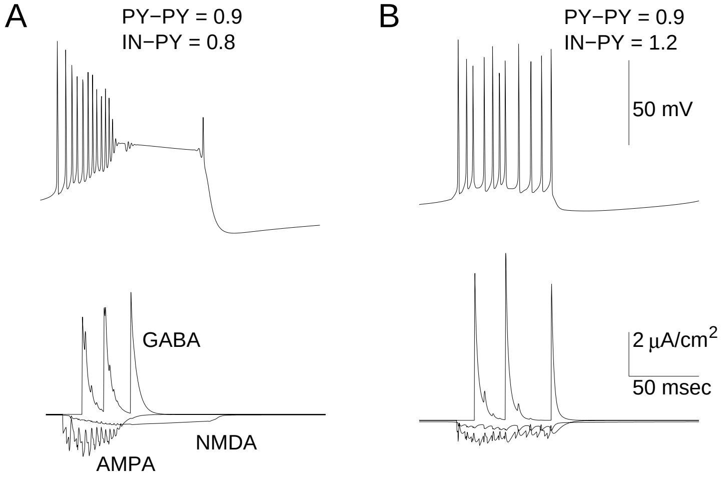

Figure 2-19 Time course of burst and underlying synaptic currents for three different synaptic configurations. First row: Membrane voltage time course. Second row: Total synaptic current on PY cell. (A) Weak excitation and weak inhibition (scaling factors: PY-PY = 0.9 and IN-PY = 0.8). (B) Weak excitation and strong inhibition (scaling factors: PY-PY = 0.9 and IN-PY = 1.2). (C) Strong excitation and strong inhibition (scaling factors: PY-PY = 1.2 and IN-PY = 1.2).

SLOW TRANSITIONS OF OSCILLATORY STATES IN LARGE NETWORK

In a larger network consisting of 60 PY cells and 15 INs with local synaptic connectivity, each PY neuron switched between fast run and slow bursting at a similar time-scale as in the case of the small, compact network (Fig. 2-20A, Top panel: network activity as a function of time. Bottom panel: single membrane voltage trace). In contrast to the small network, however, state transitions did not occur synchronously across the network. Rather, a given PY cell reached the $[K^+]_o$ required for a state transition first, switched its oscillatory firing mode and induced an according transition in the neighboring PY cells by synaptic coupling. Epochs of slow bursting or fast run therefore spread in neighboring cells. In other words, state transitions were induced according to the hysteresis in the leading neurons which were the cells with highest $[K^+]_o$ (Fig. 2-20B, top panel). Transitions in the neighboring cells were then promoted by the synaptic coupling. This resulted in a multitude of switching points for each neuron (Fig. 2-20B, bottom panel). The behavior of the neurons initiating network transitions was governed according to the bistability described before. Intracellular calcium $[Ca^{2+}]_i$ was highly elevated during paroxysmal activity (>0.004 mM), in comparison to the equilibrium value at the resting potential (0.0001 mM). $[Ca^{2+}]_i$ remained more or less constant during epochs of fast run and oscillated during bursting (Fig. 2-20C, top panel) since I_{Ca} was the major contributor to the burst depolarization. In any given PY neuron, peak value of $[Ca^{2+}]_i$ almost doubled during each burst (Fig. 2-20C, bottom panel). Including lateral K^+ diffusion did not change the global structure of alternating epochs of fast run and slow bursting (data not shown).

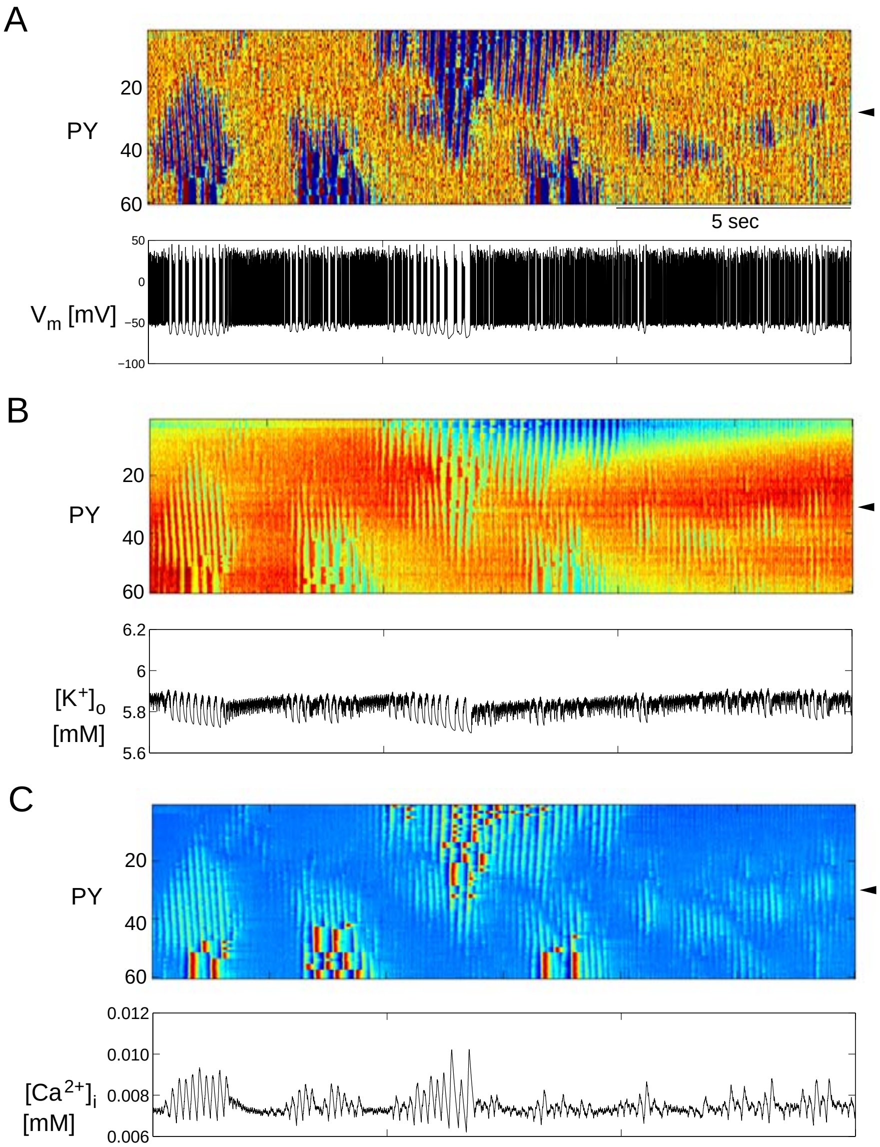

Figure 2-20 Large network (60 PY cells and 15 INs) with local synaptic connectivity. (A) PY cell activity as a function of time (top panel). Time-course of V_m for PY 30 (bottom panel, arrow in top panel). Cells switched between bursting and fast run as in the case of the small network. Due to the local synaptic connectivity, the activity pattern exhibited complex spatial structure. (B) $[K^+]_o$ in extracellular compartments surrounding PY cells as a function of time (top panel). Time-course of $[K^+]_o$ for PY 30 (bottom panel, arrow in top panel). (C) Intracellular calcium $[Ca^{2+}]_i$ in PY cells as a function of time. Time-course of $[Ca^{2+}]_i$ for PY 30 (bottom panel, arrow in top panel). Color scheme in (B) and (C): From blue to red for low to high values of ionic concentration.

SLOW TRANSITIONS OF OSCILLATORY STATES IN VIVO

We recorded paroxysmal activity with similar patterns of sustained transitions between fast run and slow bursting from association areas 5 and 7 in anesthetized cats (Fig. 2-21). Cats under ketamine-xylazine anesthesia reveal sleep-like slow oscillatory pattern with frequency 0.8-0.9 Hz (Steriade et al., 1998). In 31 cats (N = 45), we found spontaneous paroxysmal discharges consisting of spike-wave (polyspike-wave) complexes (slow bursting, 1.5-3 Hz) and epochs of fast run (fast spiking, 8-15 Hz). In average, 2.4 (std 1.4) episodes of fast run occurred during a seizure. Episodes of slow bursting and fast run lasted 37.2 sec (std 22.2) and 4.9 sec (std 5.7), respectively. The mechanism of these slow transitions is unknown. Our modeling work reproduces the qualitative features of these transitions between slow bursting and fast run and therefore suggests activity-dependent modulation of excitability (e.g. extracellular potassium dynamics) as a candidate mechanism.

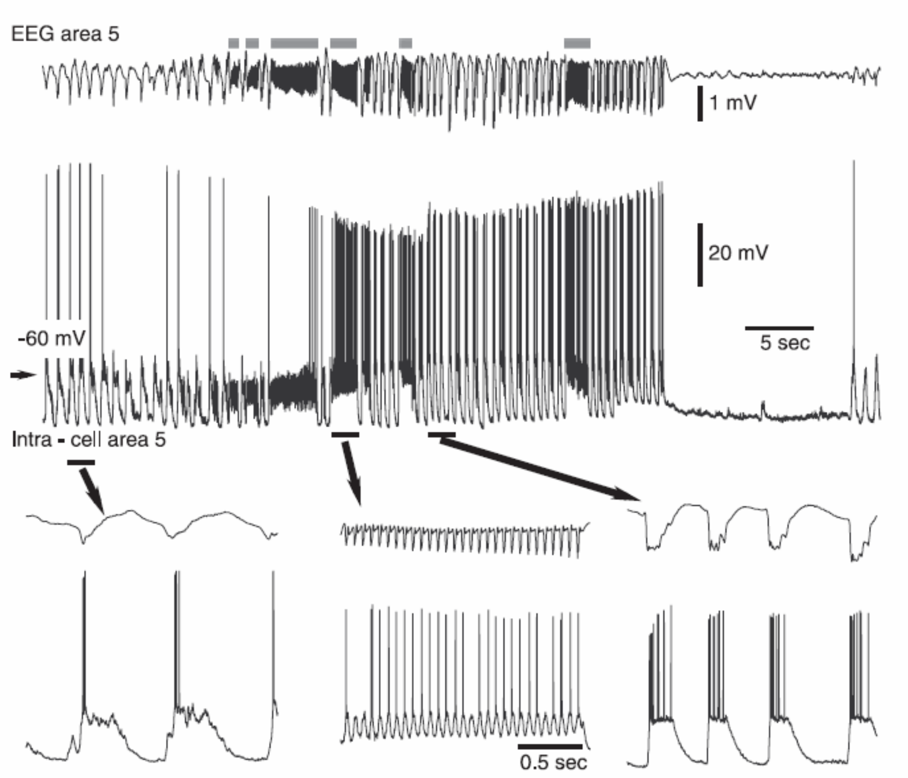

Figure 2-21 Sample trace of electrographic seizure composed of alternating epochs of spike-wave complexes (slow bursting) and fast run. Upper panel shows depth EEG and intracellular activity during normal slow oscillation and its transformation to paroxysmal activity composed of fast runs and spike-wave complexes. The electrographic seizure is indicated by the rectangle in the upper panel. Thick gray lines indicate periods of fast runs. The other periods of the seizure are spike-wave complexes. Three expanded fragments indicated by horizontal bars and arrows show (from left to right) a period of slow oscillation, a paroxysmal fast run, and a period of spike-wave discharges (slow bursting).

DISCUSSION

Extracellular potassium concentration, $[K^+]_o$, reflects past firing activity. In turn, elevated $[K^+]_o$ increases the intrinsic excitability of neurons. Yet, very little is known about the dynamics of such activity-dependent modulation of intrinsic excitability. K^+-dependent regulation of neuronal activity essentially provides a positive feedback mechanism that can lead to tonic depolarization and to instability exhibited through high frequency sustained firing. Here we found, however, that dynamic interplay of fast processes (mediated by intrinsic and synaptic conductances) and $[K^+]_o$ dynamics can mediate very slow transitions between two different oscillatory states in conditions of balanced excitation and inhibition for elevated $[K^+]_o$. Thus, the inherently positive feedback mechanism of extracellular potassium dynamics stabilizes cortical network oscillations and causes sustained neural firing structured into alternating periods of fast run and slow bursting.

BISTABILITY AND HYSTERESIS

In our neocortical network models, we found a bistability with hysteresis between tonic firing and slow bursting under conditions of balanced excitation and inhibition. Thus, the hysteresis causes a sustained pattern of alternating episodes of fast and slow oscillations in the absence of external input. Network connectivity was critical to maintain oscillations. While the hysteresis between several oscillatory states was found already in a single cell model, those states appeared only transiently following initial stimulation. Balanced excitatory and inhibitory connections between pyramidal cells and interneurons were essential to stabilize the network in the regime of alternating modes. After an initial increase in $[K^+]_o$, a small globally connected PY-IN network exhibits periodic transitions between fast run and slow bursting every few seconds. During fast run, the spiking frequency is sufficiently high for extracellular K^+ to accumulate. When $[K^+]_o$ reaches the upper endpoint of the hysteresis, the network switches back to slow bursting, during which $[K^+]_o$ decreases until it reaches the lower endpoint of the hysteresis for transition to fast run. We showed that a similar mechanism also occurs in larger networks with more realistic synaptic connectivity where oscillatory regimes are initiated and driven by $[K^+]_o$ dynamics.

Various types of potassium mediated bistabilities have been described in both experimental and theoretical studies. Elevated $[K^+]_o$ led to a bistability between tonic firing and quiescence in a model of a hippocampal pyramidal cell (Hahn and Durand, 2001). Exposing cardiac Purkinje fibers to changing K^+ concentration revealed two stable levels of resting potentials; switching between these two stable states was associated with a hysteresis (Gadsby and Cranefield, 1977). A simplified model of cerebellar Purkinje cells comprised of high-threshold calcium and delayed-rectifier potassium channels reproduced an experimentally observed bistability between resting potential and a depolarized state (Yuen et al., 1995). Myocardial cells exhibited two stable levels of diastolic potential when exposed to 4 mM K^+ *in vitro* (McCullough et al., 1990).

In contrast to these studies, we investigated here a novel bistability between two different oscillatory firing regimes. In our model, $[K^+]_o$ dynamics not only created bistability but also forced periodic transitions between two metastable oscillatory states. The rate of $[K^+]_o$ change depends on the balance between neuronal K^+ currents, K^+ pumps and glial buffering and, therefore, can be arbitrary slow. Because of this, the time scale of slow transitions between oscillatory states in the model was not explicitly restricted by the time constants of any intrinsic or synaptic conductances. The relative duration of the different oscillatory modes depended on the width of hysteresis that was controlled by the combination of intrinsic and synaptic currents. Thus, mechanisms proposed in this work can potentially explain a wide range of oscillatory phenomena different by the time scale of oscillations and duration of alternating modes.

Other mechanisms may create multistability in synaptically coupled networks. Synaptic depression mediated bistability between two modes of oscillations in networks with recurrent inhibitory connectivity (Manor and Nadim, 2001). Bistability between silence and firing mediated by nonlinear firing characteristics of neurons and by feedback between the two neurons was found in small biological circuits *in vitro* (Kleinfeld et al., 1990). While all these mechanisms may potentially explain periodic transitions between different network states, an explicit assumption about the time constant of plasticity that should match the time constant of the slow transitions between modes is required. Our model is free from this limitation. As we showed here, interaction in a population of neurons (or neuronal circuits) mediated by extracellular ionic concentrations may lead to complex oscillatory regimes with continuous and arbitrarily slow transitions between individual stable modes.

BALANCED EXCITATION AND INHIBITION

In our model, extracellular potassium dynamics caused sustained neural oscillations with alternating epochs of slow bursting and fast run provided synaptic excitation and inhibition was balanced. Substantial change of the excitatory PY-PY or inhibitory IN-PY coupling away from the balanced state created regimes with exclusive fast tonic oscillations or slow bursting. The concept of balanced synaptic excitation and inhibition plays a central role in many neurobiological processes. Experimental *in vivo*, *in vitro* and modeling studies of transitions between cortical UP and DOWN states showed that periods of high activity are accompanied by a decrease in input resistance mediated by a simultaneous increase in both excitation and inhibition (Bazhenov et al., 2002; Compte et al., 2003; Steriade et al., 2001). Self-sustained activity mediated by balanced synaptic inputs might underlie short-term memory (Durstewitz et al., 2000) and the modulation of neuronal excitability with attention (Mehta et al., 2000). We find it notable that potentially similar conditions for the balance between excitation and inhibition can allow different forms of self-sustained activity and state-dependent transitions between different activity regimes.

Our model sheds a new light on the interaction between excitatory and inhibitory synaptic coupling during cortical oscillations. Traditionally, the role of inhibitory interneurons is to maintain reasonable firing frequency levels, and a shift in the balance between excitation and inhibition towards excitation is often associated with epileptic states (Dichter and Ayala, 1987; Galarreta and Hestrin, 1998; Nelson and Turrigiano, 1998; Tasker and Dudek, 1991). A number of studies conclude, however, that synaptic inhibition remains functional in many forms of paroxysmal activities (Cohen et al., 2002; Davenport et al., 1990; Engel et al., 2003; Esclapez et al., 1997; Higashima, 1988; Prince et al., 1997; Timofeev et al., 2002a; Topolnik et al., 2003a; Traub et al., 1996). In agreement with these findings, the role of inhibition is rather subtle in our model. If the balance of excitation and inhibition is shifted towards excitation, the PY cells were sufficiently active to stay in the bursting mode and fast run never occurred. Since $[K^+]_o$ decreased progressively during bursting, the network switched to the silent state. Thus, contrary to what was expected, decrease of inhibition in the model terminated oscillations since a single epoch of slow bursting was followed by silence (Fig. 2-18).

Synaptic plasticity can change the balance between excitation and inhibition and therefore move the network away from the region of sustained oscillations. These dynamic changes in synaptic weights could be especially prominent during high frequency synchronized paroxysmal oscillations. Therefore, the mechanism described in our model may potentially explain termination of the paroxysmal activity after seizures.

CONCLUSION

We describe a novel biophysical mechanism for slow periodic transitions between different oscillatory states of cortical networks. A positive feedback mechanism modulating intrinsic excitability caused metastable slow state transitions rather than unstable "run-away" dynamics as intuition might suggest. Such slow transitions between different oscillatory regimes have been observed in a number of *in vivo* recordings from different cortical structures. We expect the dynamics observed in our modeling work to be potentially valid for various brain states characterized by a (transient) increase in cellular excitability. Neocortical paroxysmal activity mediated by elevated extracellular K^+ concentration represents one "extreme" example of such a change in excitability. Other potential mechanisms include upregulation of some intrinsic depolarizing currents, increase of input resistance or decrease in extracellular Ca^{2+} concentration. Specifically, our model predicts that (1) dynamic interaction of fast processes (such as intrinsic and synaptic conductances) in the system with positive feedback mechanism controlling excitability (extracellular potassium dynamics) can introduce dynamics on a much slower time scale, (2) the slow patterning of sustained neuronal firing behavior into alternating epochs of tonic firing and bursting can be mediated by extracellular potassium dynamics, (3) balanced synaptic excitation and inhibition is required for maintaining the slow transition dynamics, and (4) the high-threshold calcium conductance plays an important role in creating sustained neural oscillations.

ACKNOWLEDGEMENT

Section 2.3, in full, is a reprint of the material as it appeared in the Journal of Neuroscience, 2006, Frohlich, Flavio; Bazhenov, Maxim, Timofeev, Igor; Steriade, Mircea; Sejnowski, Terrence. The dissertation author was the prime investigator and author of this paper. Reprinted with permission from (Frohlich et al., 2006). Copyright Society for Neuroscience, 2006.

2.4 Coexistence of Tonic Firing and Bursting in Cortical Neurons

Sustained neuronal activity can be broadly classified as either tonic firing or bursting. These two major patterns of neuronal oscillations are state-dependent and may coexist. The dynamics and intracellular mechanisms of transitions between tonic firing and bursting in cortical networks remain poorly understood. Here we describe a detailed two-compartment conductance-based cortical neuron model which exhibits bistability with hysteresis between tonic firing and bursting for elevated extracellular potassium concentration. The study explains the ionic and dynamical mechanisms of burst generation and reveals the conditions underlying coexistence of two different oscillatory modes as a function of neuronal excitability.

INTRODUCTION

Oscillatory activity is an emerging property of many biological systems. In the brain, neuronal oscillations modulate cortical excitability and are critically involved in almost every cognitive task including information coding, memory formation, and perception (Gray et al., 1989; Maquet, 2001; Stickgold et al., 2000; Womelsdorf et al., 2006). Neuronal oscillations result from the activity of individual neurons that can be broadly classified as tonic spiking (unimodal distribution of interspike intervals) and bursting (multimodal distribution with distinct peaks for intraburst intervals). Many neuron classes display transitions between tonic spiking and bursting as a function of the brain state (e.g. sleep vs. wakefulness) (Sherman, 2001; Shilnikov and Cymbalyuk, 2005; Steriade et al., 1993a; Steriade et al., 2001; Turrigiano et al., 1996); these transitions can modify the information transfer mode of neuronal networks. Understanding the dynamical mechanisms underlying the existence of tonic spiking and bursting oscillations and conditions that trigger transitions between these patterns of neuronal activity is critical for understanding processing of sensory information in the brain.

An increase in intrinsic excitability can cause bursting in cells which usually fire single action potentials. Extracellular potassium concentration $[K^+]_o$ has been shown to modulate intrinsic excitability (Jensen and Yaari, 1997; Leschinger et al., 1993; Pan and Stringer, 1997). It is well established that $[K^+]_o$ increases during epileptogenesis (Dietzel et al., 1989; Moody et al., 1974; Somjen, 2004) and may be critically involved in synchronized burst oscillations during several seizure types (Traynelis and Dingledine, 1988). Little, however, is known about the underlying dynamics of these state-dependent transitions between different oscillatory modes. Here, we show that non-synaptic, spontaneous activity in hippocampal region CA3 *in vitro* switches from single spikes to bursting when $[K^+]_o$ is increased. We then build a conductance-based model of a cortical neuron which we show to exhibit bistability with hysteresis between tonic firing and bursting for elevated $[K^+]_o$. Using fast-slow analysis, we explain the mechanism of bursting and reveal the source of bistability in this system for a range of $[K^+]_o$.

CONDUCTANCE-BASED MODEL

The conductance-based model used in our study includes a dendritic and an axo-somatic compartment reflecting the functional morphology of cortical neurons (Mainen and Sejnowski, 1996). Motivation for the choice of a two-compartmental model is that different firing patterns (e.g. different levels of spike frequency adaptation for regular spiking neuron versus fast spiking interneuron) can be easily modeled by varying the electrical coupling between the two compartments (Mainen and Sejnowski, 1996). Here, we model a pyramidal cell with spike frequency adaptation for injection of a depolarizing step current:

$$C_m \, dV_D/dt = -g_L(V_D-E_L) - g_{KL,D}(V_D-E_K) - g(V_D-V_S)S_D - I_{D,ionic} \quad (1)$$

$$g(V_S-V_D)/S_S = -g_{KL,S}(V_S-E_K) - I_{S,ionic},$$

where V_D and V_S are dendritic and somatic membrane voltages respectively, $g = 0.1$ mS is the coupling conductance between the two compartments, $I_{D,ionic}$ and $I_{S,ionic}$ are the ionic currents in the two compartments, $C_m = 0.75$ μF/cm^2 is the membrane capacitance, and $g_L = 0.03$ mS/cm^2, $g_{KL,D} = 0.01$ mS/cm^2, $g_{KL,S} = 0.1$ mS/cm^2, E_L, and E_K are the conductances and equilibrium potentials of the mixed and potassium-mediated dendritic and somatic leak currents, respectively. The surface areas of the dendritic and somatic compartments are $S_D = 1.65\ 10^{-4}$ cm^2 and $S_S = 10^{-6}$ cm^2, respectively. All ionic currents are of the form $I_j = g_j(V_{D,S}-E_j)$ with conductance g_j and equilibrium potential E_j. The conductance g_j is written as: $g_j = G_j m^M h^H$, with maximal conductance Gj and voltage-dependent activation and inactivation variables m and h. The activation and inactivation dynamics are described by first-order kinetics of the form $\tau\ dx/dt = -(x-x_\infty)$ where $x \in m,h$. Specifically, the dendritic compartment is endowed with voltage-gated transient and persistent sodium ($I_{Na,D}$ and $I_{Nap,D}$), slow voltage-dependent and calcium-dependent non-inactivating potassium (I_{Km} and I_{KCa}), high-threshold calcium I_{Ca}, and hyperpolarization-activated depolarizing I_h currents:

$I_{D,ionic} = I_{Na,D}+I_{Nap,D}+I_{Km}+I_{KCa}+I_{Ca}+I_h$.

The $I_{Na,D}$ current has M = 3, H = 1,

$A_m = 0.182(V_D+25)/(1-\exp(-(V_D+25)/9))$,

$B_m = 0.124(-V_D-25)/(1-\exp(-(-V_D-25)/9))$,

$A_h = 0.024(V_D+40)/(1-\exp(-(V_D+40)/5))$,

$B_h = 0.0091(-V_D-65)/(1-\exp(-(-V_D-65)/5))$,

$m = 1/(\alpha(A_m+B_m))$,

$\tau_h = 1/(\alpha(A_h+B_h))$,

$m_\infty = A_m/(A_m+B_m)$,

$h_\infty = 1/(1+\exp((V_D+55)/6.2))$.

The $I_{Nap,D}$ current has M = 1, H = 0,

$m_\infty = 0.02/(1 + \exp(-(V_D+42)/5))$,

$\tau_m = 0.1992$.

The I_{Km} current has M = 1, H = 0,

$A_m = 0.001(V_D + 30) / (1 - \exp(-(V_D + 30)/9))$,

$B_m = -0.001(V_D + 30) / (1 - \exp((V_D + 30)/9))$,

$\tau m = 1/(\alpha(A_m + B_m))$,

$m_\infty = A_m/(A_m+B_m)$.

The I_{KCa} current has M = 2, H = 0,

$m_\infty = (48\ [Ca^{2+}]_i^2/0.03)/(48\ [Ca^{2+}]_i^2/0.03 + 1)$,

$\tau_m = (1/(0.03(48\ [Ca^{2+}]_i/0.03 + 1)))/4.6555$.

The I_{Ca} current has M = 2, H =1,

$A_m = 0.055(-27 - V_D)/(\exp((-27-V_D)/3.8) - 1)$,

$B_m = 0.94 \exp((-75-V_D)/17)$,

$\tau_m = 1/(\alpha\ (A_m+B_m))$,

$m_\infty= A_m/(A_m+B_m)$,

$A_h = 0.000457 \exp((-13-V_D)/50)$,

$B_h = 0.0065/(\exp((-V_D-15)/28) + 1)$,

$\tau_h = 1/(\text{alpha}(A_h+ B_h))$,

$h_\infty = A_h/(A_h+B_h)$.

The I_h current has M = 1, H = 0,

$m_\infty = 1/(1 + \exp((V_D + 82)/7))$,

$\tau_m = 38$.

The axo-somatic compartment exhibits a transient and persistent sodium current ($I_{Na,S}$ and $I_{Nap,S}$) and a delayed-rectifier potassium I_{Kv} current:

$I_{S,ionic} = I_{Na,S}+I_{Nap,S}+I_{Kv}$.

The sodium currents are of identical form as for the dendritic compartment except for the maximal conductances. The current I_{Kv} has M = 4, H = 0,

$A_m = 0.02(V_S-25)/(1-\exp(-(V_S-25)/9))$

$B_m = -0.002(V_S-25)/(1-\exp((V_S-25)/9))$,

$\tau_m = 1/(2.9529(A_m+B_m))$,

$m_\infty = A_m/(A_m+B_m)$.

The maximal conductances are $G_{Na,D} = 1$, $G_{Nap,D} = 3.5$, $G_{Km} = 0.01$, $G_{KCa} = 2.5$, $G_{Ca} = 0.015$, $_{Gh} = 0.05$, $G_{Na,S} = 3000$, $G_{Nap,S} = 3.5$, and $G_{Kv} = 200$ (all conductances in mS/cm^2, voltage-dependent conductances scaled with temperature adjustment factor $\alpha = 2.95$). The equilibrium potentials were $E_{Na} = 50$ mV and $E_{Ca} = 140$ mV. The equilibrium potential E_K for potassium conductances is determined by the Nernst equation. The voltage-independent leak conductance g_L, with equilibrium potential E_L given by the Goldman-Hodgkin-Katz equation, defines the resting potential (Bazhenov et al., 2004; Kager et al., 2000):

$$E_K = 26.64 \ln([K^+]_o/[K^+]_i)$$

$$E_L = 26.64 \ln([K^+]_o + 0.085\,[Na^+]_o + 0.1\,[Cl^-]_i)/$$

$$([K^+]_i + 0.085\,[Na^+]_i + 0.1\,[Cl^-]_o), \qquad (5)$$

where the ion concentrations are set to $[Na^+]_o = 130$ mM, $[Na^+]_i = 20$ mM, $[Cl^-]_o = 130$ mM, $[Cl^-]_i = 8$ mM. Intracellular calcium dynamics are described by

$$d[Ca^{2+}]_i/dt = -5.18\ 10\text{-}5I_{Ca} + ([Ca^{2+}]_{i(eq)}-[Ca^{2+}]_i)/\tau_{Ca},$$

where $[Ca^{2+}]_{i(eq)} = 240$ nM is the equilibrium concentration and $\tau_{Ca} = 300$ ms is the time constant for intracellular Ca^{2+} removal. All bifurcation diagrams are built using XPP-AUTO (http://www.pitt.edu/~phase).

Transverse hippocampal slices (400 µm) from a male Wistar rat (p18) were cut in ice cold standard artificial cerebrospinal fluid (ACSF) equilibrated with 95% O$_2$ and 5% CO$_2$ (119 mM NaCl, 2.5 mM KCl, 1.3 mM NaHPO$_4$, 1.3 mM MgCl$_2$, 2.5 mM CaCl$_2$, 26 mM NaHCO$_3$, and 11 mM glucose) and then transferred into an interface chamber where they were incubated at 34°C for 45 minutes. A multiwire electrode (ALA Scientific, Westbury, NY) was used for recording spontaneous spiking activity in CA3. Fast synaptic transmission was blocked by bath application of 10 µM NBQX and 2.5 µM Gabazine (Tocris Bioscience, Ellisville, MO). Slices were submerged in standard ACSF (32°C); the high potassium condition corresponded to an increase of KCl concentration to 6.5 mM. Extracellular traces were bandpass filtered (300 Hz, 5000 kHz) and sampled at 20 kHz. Potential spikes were detected by threshold crossing. A spike from a given unit was typically picked up by 3-4 recording sites (tetrode-like recordings). Spikes were then sorted by first overclustering the waveforms into subclusters with the k-means clustering algorithm. As a result, spikes corresponding to a single unit were represented by several neighboring subclusters. These subclusters were then manually combined to clusters representing individual units (Fee et al., 1996). All experiments were carried out in accordance with the guidelines set forth by the University of California.

RESULTS

Potassium-mediated currents essentially define the resting state of the membrane voltage and act against any depolarizing ion currents. Therefore, an increase in $[K^+]_o$, which weakens potassium currents, causes an increase in intrinsic excitability. Here, we show how a change in $[K^+]_o$ modulates the spontaneous activity patterns mediated by intrinsic conductances in the absence of any current injection; we recorded non-synaptic, spontaneous activity in hippocampal region CA3 *in vitro* for $[K^+]_o$ = 2.5 mM and $[K^+]_o$ = 6.5 mM (extracellular single unit recordings). For low $[K^+]_o$, all units which we recorded from fired single action potentials most of the time. Increasing $[K^+]_o$ caused bursting to become the prevalent firing pattern (representative units in Fig. 2-22). Bottom panel of Fig. 2-22 displays the probability distribution of instantaneous frequencies (inverse of interspike intervals) for two cells and two $[K^+]_o$ concentrations. It shows that the cells recorded in high potassium ($[K^+]_o$ = 6.5 mM) clearly exhibit bimodal distribution of instantaneous frequencies with one peak corresponding to frequencies higher than 130 Hz (interspike intervals < 7.7 msec) and another one corresponding to frequencies less than 4.8 Hz (interspike intervals > 208 msec). Only the latter peak corresponding to interspike intervals larger than 208 msec was found for neurons recorded in low potassium ($[K^+]_o$ = 2.5 mM).

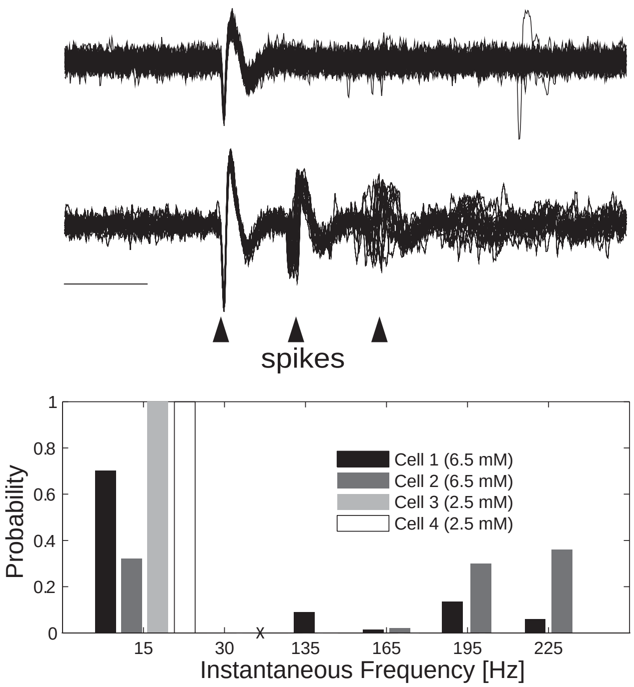

Figure 2-22 Top panels: Representative single unit activity for $[K^+]_o$ = 2.5 mM (top) and $[K^+]_o$ = 6.5 mM (bottom) in hippocampal region CA3. Ten traces are aligned by the first spike in a sequence. In high $[K^+]_o$ solution, the neurons fired bursts with several spikes. Scale bar: 5 ms. Bottom panel: Probability distribution of instantaneous frequencies (calculated as inverse of interspike intervals, N = 204) for two cells for each $[K^+]_o$ concentration. Cell 1 and 2 ($[K^+]_o$ = 6.5 mM) exhibit nonzero probabilities for instantaneous frequencies higher than 130 Hz, corresponding to spiking during bursts. Cell 3 and 4 ($[K^+]_o$ = 2.5 mM) never show instantaneous frequencies exceeding 4.8 Hz (that corresponds to interspike intervals > 208 msec).

To explain these data and to understand the dynamical mechanisms of the transition between different oscillatory modes, we used the two-compartmental neuron model (1)-(6). In the following, we treat $[K^+]_o$ in Eq. (5) as a constant parameter to determine the stable oscillatory states as a function thereof. We plot the Poincare cross-section, where the intracellular calcium level is plotted at the intersection of the membrane voltage of the axo-somatic compartment with the manifold V = -25 mV, for a range of $[K^+]_o \in [4.5, 7]$ mM. In such a plot, limit cycles are represented as points defined by a threshold crossing of a trajectory for different values of $[K^+]_o$. This method allows the graphical representation of changes in the nature of oscillatory behavior as a function of a parameter, in our case $[K^+]_o$. For a given value, tonic firing is represented as a single point, whereas bursting corresponds to a group of points. Hence, parallel lines indicate a parameter range for which bursting occurs. Here, the Poincare cross-section reveals tonic firing, coexistence of tonic firing and bursting, and only bursting for increasing levels of $[K^+]_o$ (Fig. 2-23). Below, we investigate the dynamics of this model neuron for different values of $[K^+]_o$ to explain the bistability between tonic firing and bursting in terms of the attractor landscape mediating the two different oscillatory states. At this point, we broadly classify the temporal activity patterns into tonic firing (which includes other non-bursting, fast activity, such as spike doublets with similar frequency) and bursting, which is characterized by prolonged depolarization, quickly occasioning several spikes, before incurring in spike inactivation, followed by a pronounced after-hyperpolarization. Our bifurcation analysis presented below reveals two separate dynamical mechanisms responsible for the two different activity types defined above.

To study the dynamics of bursting, we used fast-slow analysis by choosing a state variable with dynamics on the time-scale of individual bursts and treating it as a parameter of the resulting reduced system. Here, the calcium-activated potassium conductance g_{KCa}, with a time scale at least as slow as the already very slow $[Ca^{2+}]_i$ dynamics, was chosen as the slow variable. As we show below, this conductance is responsible for burst termination after sufficient calcium influx via the high-threshold calcium conductance activated during the depolarized membrane state.

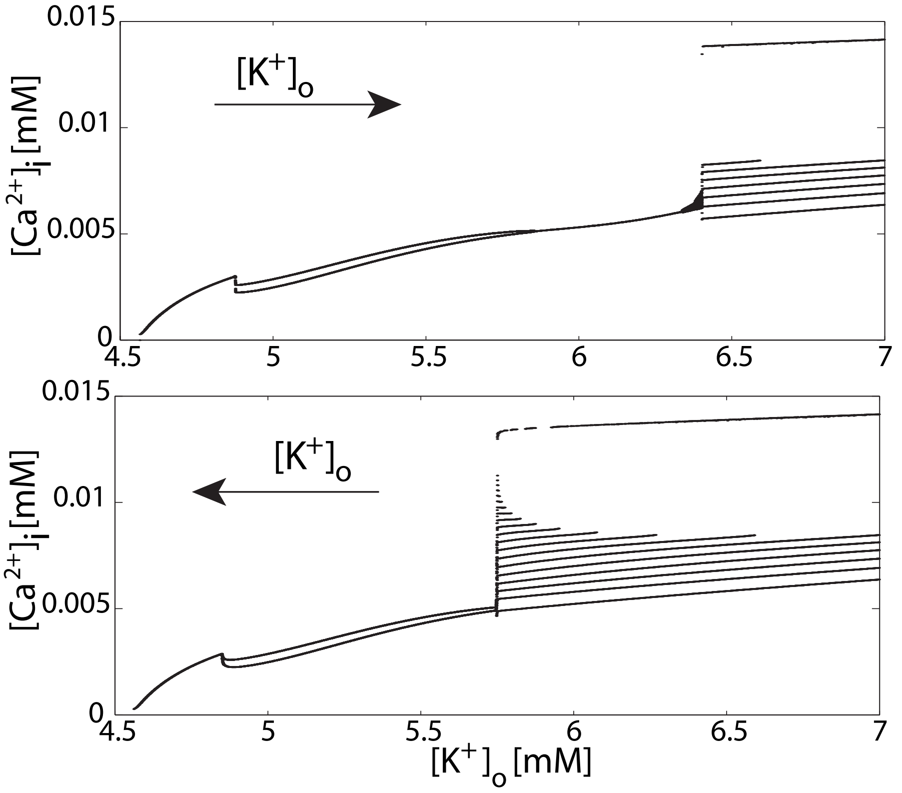

Figure 2-23 Poincare cross-section for gradually increasing (top) and decreasing (bottom) $[K^+]_o$. Tonic firing corresponds to a single point, spike doublets to two points, and bursting to a series of points in the Poincare cross-section for a given value of $[K^+]_o$. Bistability between tonic firing and bursting for $[K^+]_o \in [5.75, 6.4]$ mM.

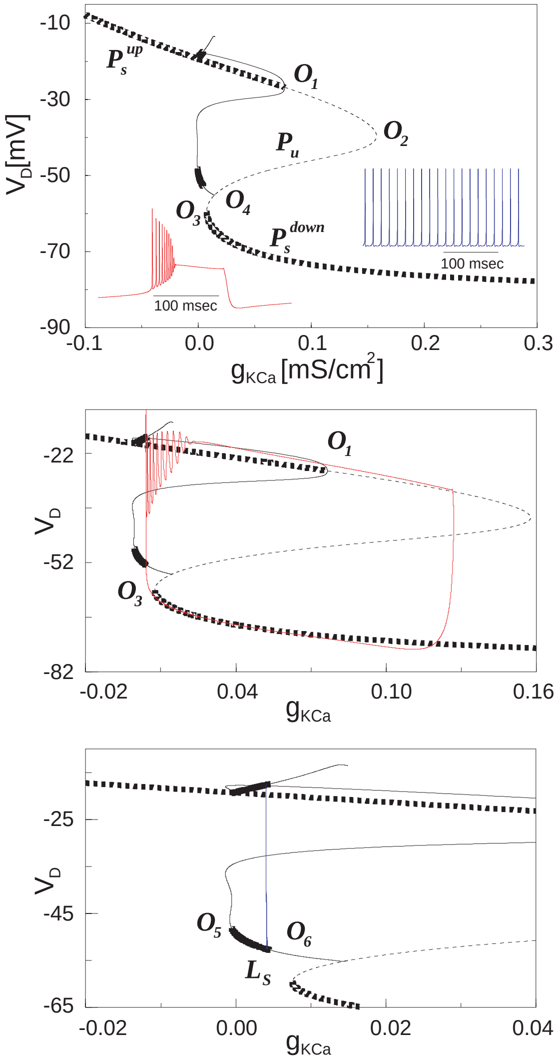

Figure 2-24 Bifurcation diagram for $[K^+]_o$ = 5.9 mM. Stable fixed points P^{up}_s and P^{down}_s (thick dashed line) are connected by the branch of unstable fixed points P_u (thin dashed line). Solid lines indicate stable (thick) and unstable (thin) limit cycles. O_1 - Andronov-Hopf, O_2 and O_3 - fold, O_4 - saddle homoclinic orbit bifurcation points. Insets show bursting and tonic spiking patterns in the complete system with freely-running g_{KCa}. Middle and bottom panels - enlarged region of interest. O_5 - Neimark-Sacker and O_6 - period doubling bifurcation points. Ls indicates stable limit cycles. Projection of the phase trajectory for the complete system during bursting mode (solid red line, middle panel) and tonic firing (solid vertical blue line, bottom panel).

We first consider the case for $[K^+]_o$ = 5.9 mM which is within the bistable region (see Fig. 2-23). Although in the full system $g_{KCa} \geq 0$ by definition, we included $g_{KCa} < 0$ in our analysis to reveal the entire bifurcation structure of the system. For all limit cycles, we show both maximum and minimum dendritic membrane voltage of the oscillatory trajectory on the ordinate of the bifurcation plots. The fixed points of the reduced system follow a z-shaped line as a function of g_{KCa} (Fig. 2-24, top panel). Two stable fixed points, P^{down}_s and P^{up}_s, are connected by a branch of unstable fixed points P_u. For g_{KCa} in {0.007,0.076} mS/cm^2, both stable states co-exist. P^{up}_s loses stability by a sub-critical Andronov-Hopf bifurcation at O_1. P^{down}_s coalesces with the unstable fixed point in a saddle-node bifurcation at O_3. The following mechanism underlies burst generation in this system (Fig. 2-24, middle panel). Conductance g_{KCa} decreases while the system tracks P^{down}_s because of the calcium pump's efforts to remove intracellular Ca^{2+}. As a consequence, P^{down}_s eventually loses stability in the saddle-node bifurcation point O_3 and a transition to P^{up}_s occurs. The trajectory rotates several times around P^{up}_s, which is a stable focus, but never quite reaches it in the complete system with freely running g_{KCa}. These rotations correspond to the rapid sequence of action potentials at the onset of the burst. The decaying amplitude of the transient oscillations is reflected in the decreasing spike amplitude in the membrane voltage time-course during a burst. As the system approaches this fixed point, no more action potentials occur and the membrane voltage remains depolarized. In the meantime, the intracellular Ca^{2+} concentration increases since the cell is sufficiently depolarized to activate the high-threshold Ca^{2+} conductance which mediates calcium influx. In turn, this causes an increase in g_{KCa} which eventually leads to a loss of stability of $P^{up}{}_{s}$ at O_1. The trajectory then falls back to $P^{down}{}_{s}$. In short, burst generation in the complete system is mediated by periodic transitions between two fixed points of the reduced system. These transitions form a periodic orbit corresponding to the bursting dynamics.

The small-amplitude unstable limit cycle which originates at O_1 wraps around at g_{KCa} = -0.001 mS/cm^2 leading to the coexistence of a small- and a large-amplitude unstable limit cycle (Fig. 2-24). Before coalescing with the unstable fixed point P_u in a saddle homoclinic orbit bifurcation point O_4, the unstable limit cycle with larger amplitude in the V_D dimension becomes stable in a narrow range for $g_{KCa} \in [-0.0005, 0.0045]$ mS/cm^2 (indicated by L_s in Fig. 2-24, bottom panel). At the left bifurcation point O_5, the large-amplitude cycle gains stability through a subcritical Neimark-Sacker bifurcation.

At the right point O_6 the limit cycle loses stability again through a period-doubling bifurcation. Between these two points, the limit cycle L_s remains stable, mediating tonic firing. If this regime is present in the complete system with freely-running g_{KCa} depends on whether g_{KCa} stays in the range where the cycle L_s is stable in the reduced system. In the complete system, g_{KCa} remains very low during tonic firing since g_{Ca} mediating calcium influx is in average only weakly activated. Also, g_{KCa} is bounded by zero on the left side since an ionic conductance cannot become negative.

Therefore it is critical for the existence of tonic firing in the full system that the corresponding limit cycle L_s is stable for arbitrarily small positive values of g_{KCa}. This is indeed the case for selected value of $[K^+]_o = 5.9$ mM since the left bifurcation point O_5, where the limit cycle loses stability, corresponds to a negative value of g_{KCa} and therefore permits stable tonic oscillations in the complete system. In short, the stable limit cycle of the reduced system L_s remains a stable periodic orbit in the complete system. This limit cycle mediating tonic spiking dynamics co-exists with the periodic orbit mediating bursting (see above).

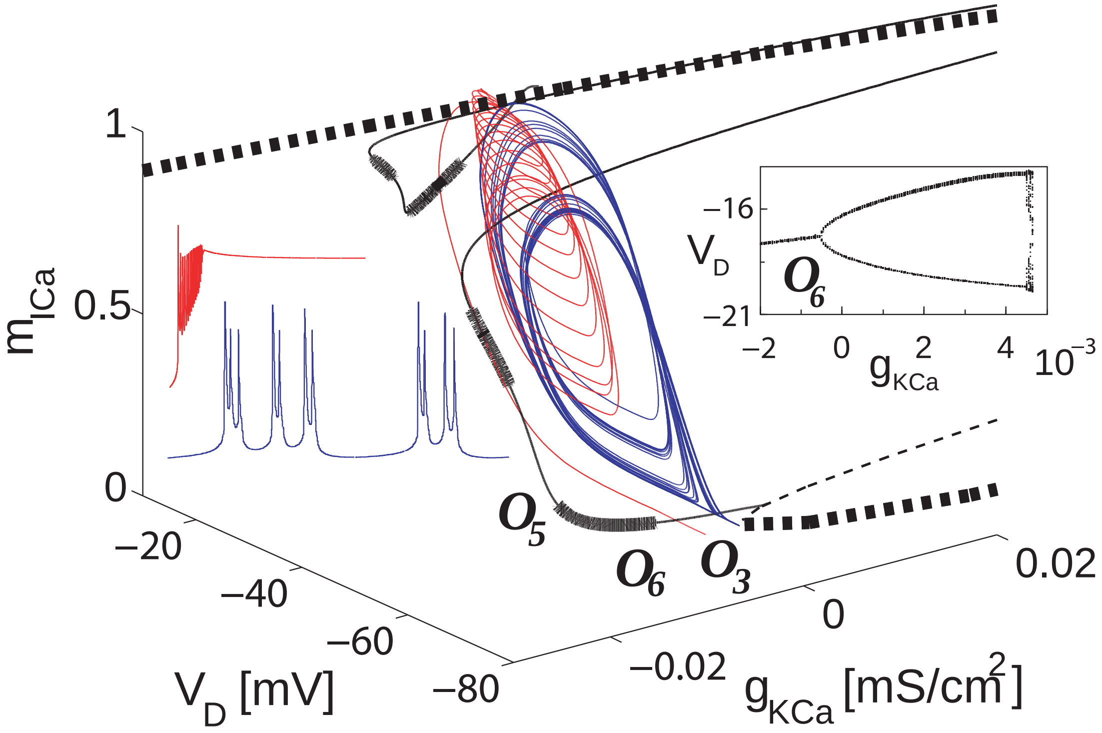

Figure 2-25 Three-dimensional bifurcation diagram for $[K^+]_o$ = 5.5 mM. The Z-axis shows the activation variable of the high-threshold Ca^{2+} current, m_{ICa}. A small perturbation (g_{KCa} = 0.0045 mS/cm^2) left from O_3 (g_{KCa} = 0.005 mS/cm^2) leads to convergence to the limit cycle (blue line starting close to O_3). A larger perturbation (g_{KCa} = 0.001 mS/cm^2) triggers convergence to the stable fixed point P^{up}_s (red line starting further away from O_3). Left insets show time courses of convergence to the stable fixed point (top, red) and limit cycle (bottom, blue). Right inset - sequence of period doubling bifurcations in Poincare cross-section: m_{ICa} = 0.4.

We next consider $[K^+]_o$ = 5.5 mM. In the complete system, we only observed firing with spike doublets (Fig. 2-25). The bifurcation diagram of the reduced system (Fig. 2-25) looks similar to the previous case. In contrast to $[K^+]_o$ = 5.9 mM, however, the limit cycle corresponding to tonic firing is unstable for $g_{KCa} > 0$ mS/cm^2 (Fig. 2-25, right inset). Instead, a cycle of period 2 is stable within a range of g_{KCa} fluctuations occurring during non-bursting activity in the complete system with freely-running g_{KCa}.

To determine why bursting does not occur in this system, we applied a set of perturbations of different amplitudes in the vicinity of saddle-node bifurcation point O_3 (Fig. 2-25). A small deflection off the saddle-node bifurcation point caused nearly periodic firing with period 4. A larger deflection left from O_3 triggered convergence to the stable upstate fixed point Pups. Therefore, for low values of $[K^+]_o$ the vicinity of the saddle-node point O_3 no longer belongs to the basin of attraction of the upper stable fixed point $P^{up}{}_s$. For initial conditions from the low stable branch of fixed points $P^{down}{}_s$, the system reaches the saddle-node bifurcation point and then immediately jumps to the stable limit cycle with period 2, mediating firing with spike doublets.

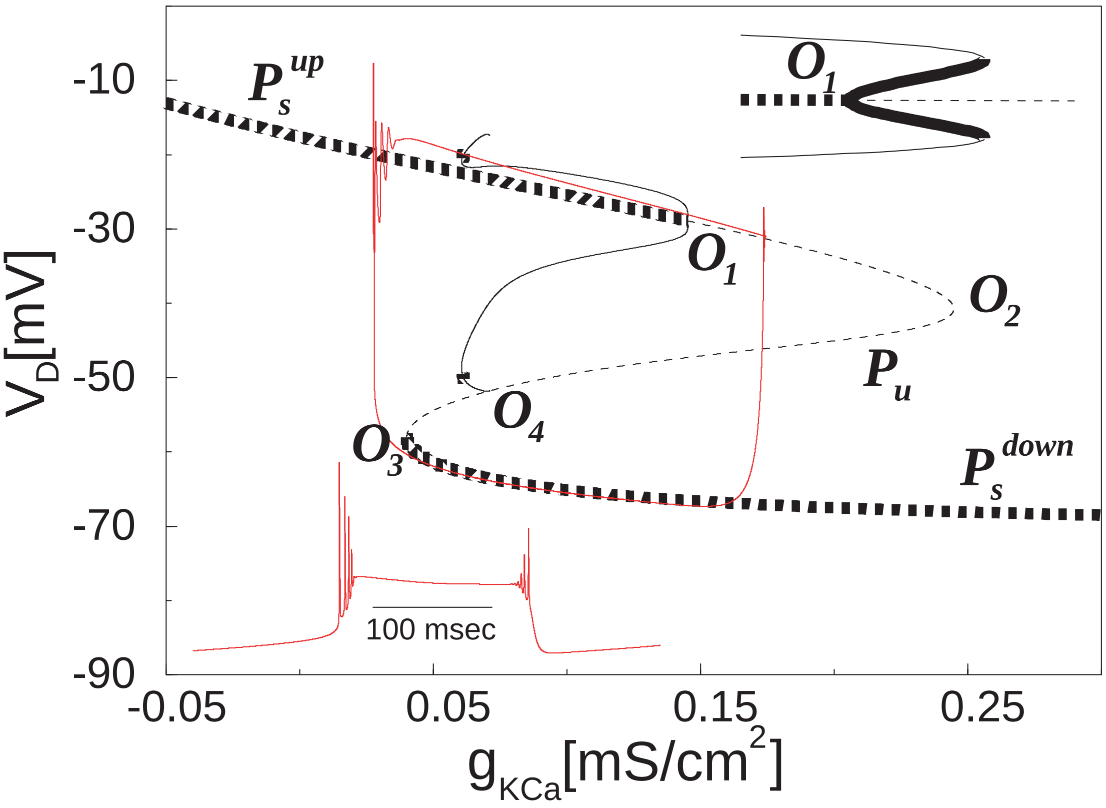

Figure 2-26 Bifurcation diagram for $[K^+]_o$ = 9.0 mM. Projected trajectory of full system (thin solid line, red) shows transient oscillation at the end of the burst before switching to P^{down}_s. Top inset, supercritical Andronov-Hopf bifurcation at O_1. Bottom inset, membrane (soma, V_S) voltage time-course during burst.

Conversely, for $[K^+]_o$ = 6.5 mM (not shown), we only observed bursting in the complete system. The bifurcation plot distinguishes itself from the previous two cases by the fact that for low values of g_{KCa} there is only a very narrow region of $g_{KCa} \in [0.01, 0.014]$ mS/cm^2 for which a stable limit cycle L_s exists. The left bifurcation point O_5 occurs at a positive value of g_{KCa}. In the complete system, starting from the initial conditions belonging to the limit cycle, the value of g_{KCa} decreases toward its equilibrium, corresponding to a very low value of g_{KCa}. Before reaching this point, however, the limit cycle loses its stability at the Neimark-Sacker bifurcation point O_5 and the system moves to the Pups branch, starting a burst. Hence, non-bursting firing does not exist as a stable state for sufficiently elevated $[K^+]_o$. Further elevation of $[K^+]_o$ (e.g. $[K^+]_o$ = 9 mM) changes the type of bifurcation point O_1 (Fig. 2-26). The stable up state $P^{up}{}_s$ now loses stability via a supercritical Andronov-Hopf bifurcation for g_{KCa} = 0.145 mS/cm^2 (Fig. 2-26, top inset). It changes the burst pattern displayed by the complete system. Rather than displaying a "smooth" transition to the low branch of fixed points $P^{down}{}_s$, the system produces a series of spikelets with increasing amplitude at the end of each depolarization state (burst offset). This particular pattern was previously described *in vivo* (Steriade et al., 1998).

DISCUSSION

Extracellular potassium concentration has been shown to vary as a function of neural activity (Bazhenov et al., 2004; Kager et al., 2000). Specifically, potassium currents tend to increase $[K^+]_o$, whereas pumps, glial buffering, and diffusion contribute to stabilize $[K^+]_o$. When any of these mechanisms fails to operate normally, $[K^+]_o$ rises and a neuron starts to burst spontaneously (Bazhenov et al., 2004), as frequently observed during paroxysmal seizures *in vivo* (Perreault and Avoli, 1989; Steriade and Contreras, 1995; Ziburkus et al., 2006). Here, we showed that non-synaptic, spontaneous activity changes from single action potentials to bursts in conditions of increased $[K^+]_o$ in hippocampal region CA3. Our experimental approach of extracellular single unit recordings in acute hippocampal slice does not perturb the intracellular milieu (including $[Ca^{2+}]_i$, which we showed to be essential for burst termination) and is therefore free from this limitation of intracellular recordings.

Using a detailed mathematical model, we have discussed the dynamic landscape underlying the coexistence of tonic firing and bursting in a cortical pyramidal cell for elevated extracellular potassium concentration. A common mechanism of burst generation involves a transition between two attractors: a stable fixed point corresponding to a hyperpolarized state, and a limit cycle corresponding to spiking (Izhikevich, 2007). In our model, the fast subsystem does not have such a limit cycle attractor, and therefore spike generation depends on fast rotations around the upper fixed point with relatively weak convergence (point-point mechanisms of bursting). When the trajectory reaches this stable fixed point, this corresponds to spike inactivation (depolarization block) frequently observed during seizures *in vivo* and in slices treated with high potassium and/or 4-aminopyridine (4-AP) (Ziburkus et al., 2006). The bursting mechanism which we described here is essentially mediated by the dynamic interaction of the high-threshold calcium conductance g_{Ca}, intracellular calcium concentration $[Ca^{2+}]_i$, and the calcium-activated potassium conductance g_{KCa}. During tonic firing, g_{Ca} is minimally activated and therefore $[Ca^{2+}]_i$ stays near its equilibrium value. This allows the spiking to continue indefinitely. In contrast, in bursting mode, substantial calcium influx mediated by g_{Ca} during the depolarized state causes g_{KCa} to activate. This in turn mediates burst termination and subsequent after-hyperpolarization. The different levels of deinactivation of g_{Ca} explain the bistability between tonic firing and bursting. In the bursting mode, g_{Ca} becomes significantly deinactivated during the hyperpolarized phase therefore enabling a rapid sequence of spikes initiating the onset of a further burst when the hyperpolarized phase is over. In contrast, when the neuron is in tonic firing mode, insufficient g_{Ca} deinactivation between spikes reduces the effect of this conductance and prevents switching to the bursting mode. The persistent sodium conductance g_{NaP} enables the existence of the bursting mode by providing additional depolarizing force to sufficiently activate g_{Ca} during the bursts. Accordingly, an increase in g_{NaP} shifts the bistable region to lower values of $[K^+]_o$. A significant decrease in g_{NaP} abolishes the bursting regime. Introducing g_h decreases the value of [K+]o for which the neuron became active and narrowed the width of the hysteresis (data not shown).

Our model predicts the existence of a bistable regime for elevated $[K^+]_o$ where tonic firing and bursting co-exist. Direct experimental verification would require a tight control of $[K^+]_o$ in the extracellular environment which is probably easier to achieve in case of isolated neurons (e.g. in dissociated culture). Additionally, fluid dynamics of the perfusion system would need to be constrained such that $[K^+]_o$ could be rapidly increased and decreased by changing K^+ concentration at the source. Furthermore, activity-dependent changes in $[K^+]_o$ would need to be suppressed to ensure constant $[K^+]_o$.

Other potassium-mediated bistabilities between a silent and active state or between two membrane voltage values have been found both in models and experiments (Gadsby and Cranefield, 1977; Hahn and Durand, 2001; McCullough et al., 1990; Yuen et al., 1995). Bistability between tonic spiking and bursting was described in a model of a leech heart interneuron under specific pharmacological conditions (Shilnikov et al., 2005). Burst generation in this model was mediated by transitions between a fixed point and a periodic orbit of the fast subsystem and included bursting regimes with arbitrary long oscillatory depolarized states.

Existence of bistability between tonic spiking and bursting for an intermediate range of $[K^+]_o$ predicts that in a neuronal system with dynamically updated $[K^+]_o$, K^+-dependent regulation of neuronal activity may lead to complex oscillatory behavior (Frohlich et al., 2006). In an isolated neuron model where $[K^+]_o$ was continuously computed based on neuronal K+ currents, K+ pumps and glial buffering, $[K^+]_o$ decreased faster during periodic bursting and slower during tonic firing (Bazhenov et al., 2004). Since the $[K^+]_o$ gradient depends on the frequency of firing, excitation mediated by lateral synaptic connections between neurons may increase the frequency of tonic spiking sufficiently to provide $[K^+]_o$ elevation during tonic spiking throughout the network of neurons. On the other hand, frequency of bursting is mainly mediated by intrinsic cell properties - rate of deactivation of the calcium-dependent potassium conductance during the intraburst interval - and, therefore, the $[K^+]_o$ gradient during bursting can stay negative even in the presence of excitatory synaptic connections. This suggests that activity-dependent modulation of intrinsic excitability can lead to sustained oscillations in a cortical network with slow transitions between two distinct firing modes - tonic spiking and bursting - mediated by slow $[K^+]_o$ oscillations. Examples from *in vivo* experiments where such transitions were observed include the transition between fast runs and slow bursting during spike-wave seizures (Timofeev et al., 1998) and periodic transitions between slow-wave and fast-wave oscillations in olfactory cortex (Murakami et al., 2005).

ACKNOWLEDGEMENT

Section 2.4, in full, is a reprint of the material as it appeared in Physical Review E, 2006, Frohlich, Flavio; Bazhenov, Maxim. The dissertation author was the prime investigator and author of this paper. The authors are grateful to N.F. Rulkov for insightful suggestions and critical reading of the manuscript and to T.J. Sejnowski and M. Scanziani for stimulating discussions. This research was supported by NIDCD (grant R01 DC006306). Reprinted with permission from (Frohlich and Bazhenov, 2006). Copyright American Physical Society 2006.

2.5 Maintenance and Termination of Neocortical Oscillations by Dynamic Modulation of Intrinsic and Synaptic Excitability

Mechanisms underlying seizure cessation remain elusive. The Lennox-Gastaut syndrome, a severe childhood epileptic disorder, is characterized by episodes of seizure with alternating epochs of spike-wave and fast run discharges. In a detailed computational model incorporating extracellular potassium dynamics, we studied the dynamics of these state transitions between slow and fast oscillations. We show that dynamic modulation of synaptic transmission can cause termination of paroxysmal activity. An activity-dependent shift in the balance between synaptic excitation and inhibition towards more excitation caused seizure termination by favoring the slow oscillatory state which permits recovery of baseline extracellular potassium concentration. We found that slow synaptic depression and change in chloride reversal potential can have similar effects on the seizure dynamics. Our results suggest a novel role for synaptic dynamics during epileptic neural activity patterns.

INTRODUCTION

A prominent feature of cortical circuits is their propensity for rhythmic activity (Buzsaki and Draguhn, 2004; Steriade, 2006). This oscillatory activity might exist in either normal forms, such as during sleep (Bazhenov et al., 2002; Contreras et al., 1997a; Contreras et al., 1997b; Destexhe et al., 1998; Nita et al., 2003; Steriade, 2004a, 2003a, 2006; Steriade, 2003b; Steriade and Amzica, 2003, 1998; Steriade et al., 1986; Steriade and McCarley, 2005; Steriade et al., 1993a; Steriade et al., 1993b;

Steriade et al., 2001; Timofeev et al., 2001a), or paroxysmal forms, such as during epilepsy (Amzica and Steriade, 2000; Neckelmann et al., 1998; Steriade, 2003b; Steriade and Amzica, 1998; Steriade et al., 1998; Steriade and Contreras, 1995, 1998; Timofeev et al., 2002a; Timofeev et al., 2004, 1998; Timofeev and Steriade, 2004). Epileptic seizures are characterized by epochs of hypersynchronized neural oscillations that are accompanied by firing. Experimental animals exhibit electrographic seizures that closely mimic the dynamics of clinical seizures. Here, we focus on the paroxysmal activity that closely resembles Lennox-Gastaut seizures (Markand, 2003; Niedermeyer, 2002), which are characterized by slow bursting (spike-wave or polyspike-wave complexes) intermixed with epochs of fast runs (Frohlich et al., 2006; Neckelmann et al., 1998; Timofeev et al., 1998).

Recently, we proposed a mechanism for the slow state transitions between two different oscillatory regimes using a computational model of a cortical network with extracellular potassium dynamics (Frohlich et al., 2006). Pyramidal cells exhibited bistability with hysteresis between tonic firing and slow bursting for elevated extracellular potassium concentration $[K^+]_o$ (Frohlich and Bazhenov, 2006). In a model that included $[K^+]_o$ as a dynamic variable, this bistability caused persistent oscillations with slow transitions between slow bursting and fast run. We concluded that activity-dependent modulation of intrinsic excitability can mediate slow patterning of sustained neural oscillations. Activity-dependent changes of synaptic and intrinsic properties can modulate excitability through positive- and negative-feedback mechanisms. Thus, an increase in $[K^+]_o$ during sustained neural activity (Amzica and Steriade, 2000; Heinemann et al., 1977) upregulates excitability by decreasing the driving force on potassium currents and, hence, forms a positive-feedback (Yaari et al., 1986). By contrast, expression of excitatory recurrent coupling between pyramidal cells mediates negative feedback, whereas depression of inhibition constitutes positive feedback. Little is known about the combined effect of different dynamic mechanisms that modulate excitability. Here, we study network oscillatory states in the presence of dynamic mechanisms that shift the balance between excitation and inhibition towards more excitation. The positive-feedback nature of activity-dependent increase in excitability would indicate the occurrence of some form of self-amplifying 'runaway dynamics' by a global loss of stability. We found the opposite, namely that a dynamic shift in balance towards more excitation can force the network back to its silent state after a period of patterned oscillator activity. We discuss the resulting dynamics as a model for seizure cessation.

OBJECTIVES

Key objective of this study was to investigate how slow activity-dependent changes of synaptic transmission modulate paroxysmal network activity. Specifically, we studied the effect of slow synaptic depression and of change in GABAergic reversal potential mediated by chloride accumulation on the oscillatory network dynamics.

METHODS

COMPUTATIONAL MODEL

The model neocortical network with extracellular potassium dynamics has been described in detail elsewhere (Bazhenov et al., 2004; Frohlich and Bazhenov, 2006; Frohlich et al., 2006). In short, individual neurons were modeled with an axo–somatic and a dendritic compartment, each endowed with Hodgkin–Huxley type conductances including fast transient sodium, delayed-rectifier potassium, persistent sodium, high-threshold calcium, calcium-activated potassium, and a mixed cationic leak conductance. Passive and active ion-transport mechanisms and glial buffering regulated the extracellular potassium concentration. The two-layered network consisted of a line of 80 pyramidal cells (PYs) and 16 inhibitory interneurons (INs). PYs were recurrently coupled through excitatory synapses (both AMPA and NMDA) to their local neighbors (five PYs on each side). Each PY excited three neighboring INs, which, in turn, inhibited 11 neighboring PYs through GABA(A) synapses. Synaptic transmission was modeled with first-order gating kinetics (Destexhe *et al*., 1994). Maximal conductances denoting the total excitation and inhibition received by a given cell were set to G(AMPA)(PY-PY) = 200 nS, G(NMDA)(PY-PY) = 13 nS, G(AMPA)(PY-IN) = 100 nS, G(NMDA)(PY-IN) = 14 nS, and G(IN-PY) = 50 nS. All synapses included spontaneous release of neurotransmitter resulting in miniature postsynaptic potentials (Bazhenov et al., 2002). All synapses included short-term depression (STD) modeled with depression factor (D = 0.07) denoting the fraction of synaptic resources lost per presynaptic action potential and with first-order-recovery dynamics with time-constant of 700 msec (Markram *et al.*, 1998). Slow, activity-dependent synaptic depression ('slow depression') was modeled similarly to STD but with different parameters. Depression factor D was set to a low value (D = 0.001) and recovery time constant was very slow (τ = 1000 sec). In some simulations, intracellular chloride concentration was computed for each cell by integration of the inhibitory currents mediated by GABA(A) receptors. The reversal potential for chloride was dynamically updated using Nernst equation with extracellular concentration $[Cl^-]_o = 130$ mM: $E_{Cl} = 26.64$ mV $\ln([Cl^-]_i/[Cl^-]_o)$.

IN VIVO EXPERIMENTS

The details of *in vivo* electrophysiological experiments involving intracellular recordings during paroxysmal activities has been described in detail (Timofeev et al., 2002a; Timofeev et al., 2004). Briefly, intracellular recordings from neocortical neurons were performed in 15 cats anesthetized with ketamine−xylazine (10−15 mg kg^{-1} and 2−3 mg kg^{-1}; i.m.) Following ketamine-xylazine anesthesia ~30% of cats (*n* = 6) displayed spontaneous electrographic seizures consisting of SW/PSW complexes at 1.5−3 Hz, often associated with fast runs at about 10−15 Hz. In cats that did not display spontaneous electrographic seizures, the electrographic seizures were elicited by 3−4 pulse-trains (10−20 stimuli at 100 Hz) applied to cortical areas in the vicinity of the intracellular recording pipette.

Field-potential recordings and stimulation were obtained by using bipolar coaxial macroelectrodes inserted into the cortex. The outer pole of the electrode was placed at the cortical surface or 0.1 mm deeper, whereas the inner pole was placed at 0.8−1 mm in the cortical depth.

Intracellular recordings were obtained with sharp glass micropipettes filled in the majority of cases with a solution of 2.5−3.0 M potassium acetate (KAc). Electrophysiological identification of recorded neurons was achieved by intracellular application of depolarizing current pulses of 0.2−1.0 nA lasting for 200−300 msec. Because the intrinsic firing patterns of neurons are influenced by the network state (Steriade, 2004b; Steriade et al., 1998), formal identification was performed during active phases of slow oscillation in seizure-free periods. In this study, we only report data on regular-spiking neurons that revealed spike-frequency adaptation and on fast-spiking neurons that exhibited both thin spikes and high-frequency tonic discharge without spike-frequency adaptation upon direct depolarization. In some experiments with dual intracellular recordings, one pipette was filled with KAc and the other with potassium chloride (KCl, 2.0−3.0 M). Intracellular pipettes had a DC resistance of 30−80 MΩ. A high-impedance amplifier (bandpass, 10 kHz) with an active-bridge circuitry was used to record and inject current into the neurons. All electrical signals were sampled at 20 kHz and digitally stored on Vision (Nicolet). To simplify data processing, occasionally the data were downsampled to 2 kHz. All experimental procedures were performed in accordance with the guidelines of the Canadian Council on Animal Care and were approved by the Committee for Animal Care of Laval University.

RESULTS

PERSISTENT OSCILLATORY ACTIVITY IN THE CORTICAL NETWORK MODEL

Step depolarization of all 80 pyramidal cells in the network induced high-frequency firing that resulted in a gradual increase in $[K^+]_o$ (Fig. 2-27A). At the end of the stimulation $[K^+]_o = 5.5$ mM, for which activity-dependent potassium outflow was approximately balanced by mechanisms for removal of excess extracellular potassium. Therefore, $[K^+]_o$ remained elevated, causing sustained oscillations in absence of stimulation. The persistent activity was structured into epochs of tonic firing (fast runs) and slow bursting (sample epochs labeled in Fig. 2-27A, top panel). Both the pyramidal cells (Fig. 2-27A, top panel) and the inhibitory interneurons (Fig. 2-27A, middle panel) were subject to this slow patterning. Previously, we showed that these slow state transitions between the two oscillatory regimes are mediated by a bistability with hysteresis of the two modes for elevated $[K^+]_o$ (Frohlich et al., 2006). At the offset of external stimulation, the network started slow bursting during which $[K^+]_o$ decreased (Fig. 2-27A, bottom panel) to a level at which only fast run is a stable mode. At this point the network switched to fast run and $[K^+]_o$ started to increase because of the higher overall activity during fast run compared with slow bursting (Fig. 2-27A, bottom panel). Eventually, the system reached $[K^+]_o$ at which fast run becomes unstable and the system switched to slow bursting again.

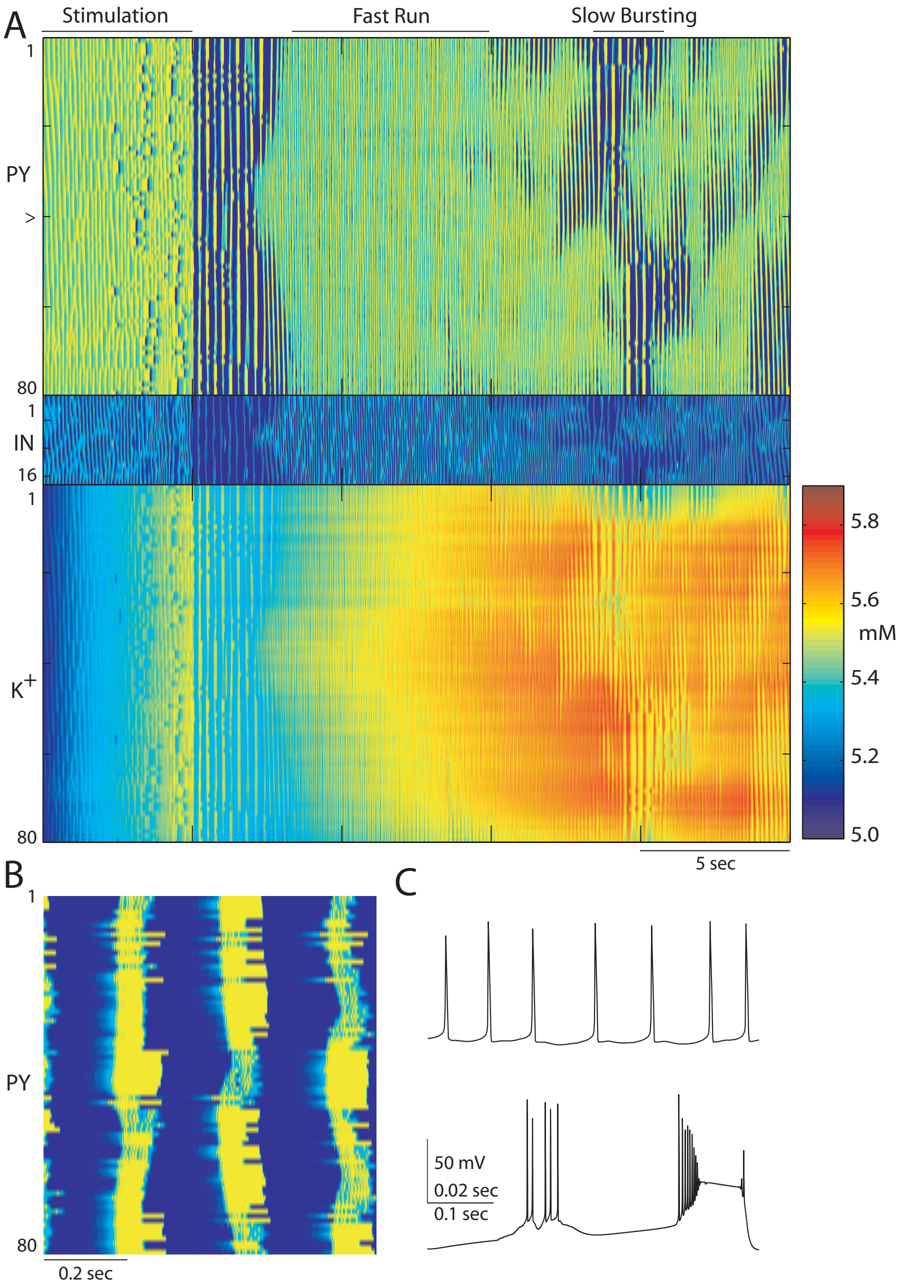

Figure 2-27 Cortical network oscillation patterned into alternating epochs of slow bursting and fast run following stimulation of PYs. (A) Top: Activity of all 80 PYs as a function of time. Middle: INs. Bottom: $[K^+]_o$ time-course. After an initial transient increase, $[K^+]_o$ increases and decreases during fast run and slow bursting, respectively. (B) Activity of all 80 PYs during slow bursting. (C) Membrane voltage-time course during fast run (top) and slow bursting (bottom). Scale bars: top, 20 msec; bottom, 100 msec.

Slow bursting was synchronized throughout the network and occurred at frequencies of few bursts per second (Fig. 2-27B). In individual neurons, fast run denotes firing patterns similar to tonic firing (Fig. 2-27C top panel shows sample epoch of fast run in PY 40, marked in Fig. 2-27A, top panel). During slow bursting, pyramidal cells exhibited both burst with and without spike inactivation (Fig. 2-27C bottom panel shows sample epoch of slow bursting in PY 40).

Here, we investigate possible mechanisms for the termination of the persistent oscillatory firing. In the model, transitions between fast run and slow bursting last indefinitely in presence of balanced synaptic excitation and inhibition. In case of strong recurrent excitation and weak inhibition, however, the network exhibited only bursting followed by silence (Frohlich et al., 2006). In other words, if the excitatory coupling is sufficient to prevent the network from switching to fast run, the network is bound to return to the silent state because $[K^+]_o$ only decreases during slow bursting. Therefore we asked if a dynamic mechanism can shift the balance between excitation and inhibition such that a network that initially exhibits transition dynamics eventually reaches the regime where only bursting is stable and the persistent activity eventually terminates. In the following, we discuss two alternative dynamic mechanisms mediating an activity-dependent shift in the balance of excitation and inhibition towards more excitation. As we show below, both differential synaptic depression of excitation and inhibition with slow-recovery time constant (‘slow depression’) and increase in intracellular chloride concentration terminated the oscillatory activity.

EFFECT OF SYNAPTIC DEPRESSION ON SEIZURE CESSATION

First, we consider depression of both excitatory coupling between pyramidal cells and inhibitory coupling between interneurons and pyramidal cells. We used a generic model of synaptic depression with a low depression rate and a long recovery-time constant causing activity-dependent depression for synaptic coupling without recovery on the time-scale of a seizure. In presence of such slow depression, a transient increase in $[K^+]_o$ initiated a series of alternating epochs of fast run and slow bursting with eventual return to the silent state in a network with 80 PYs and 16 INs (Fig. 2-28A, activity map of pyramidal cells). As in the case without slow depression (Fig. 2-27), $[K^+]_o$ decreased during slow bursting and increased during epochs of fast run (Fig. 2-28B); this regime would persist in the network with balanced excitation and inhibition. However, depression rates of excitatory and inhibitory synaptic conductances were chosen such that inhibition decreased faster than excitation [D(PY-PY) = 0.00005 and D(IN-PY) = 0.001]. This resulted in a net shift of the balance between excitation and inhibition towards more excitation. The phase plane representing the normalized synaptic-coupling strengths (Fig. 2-28C) shows that during the development of the seizure both excitation and inhibition decreased. However, because of the different depression rates, the trajectory moved away from the diagonal band (blue lines) corresponding to persistent oscillations mediated by balanced excitation and inhibition (red arrow in Fig. 2-28C). The persistent oscillations ended with an epoch of slow bursting during which $[K^+]_o$ decreased to a value where all cells eventually became silent (membrane voltage time-course in Fig. 2-28D).

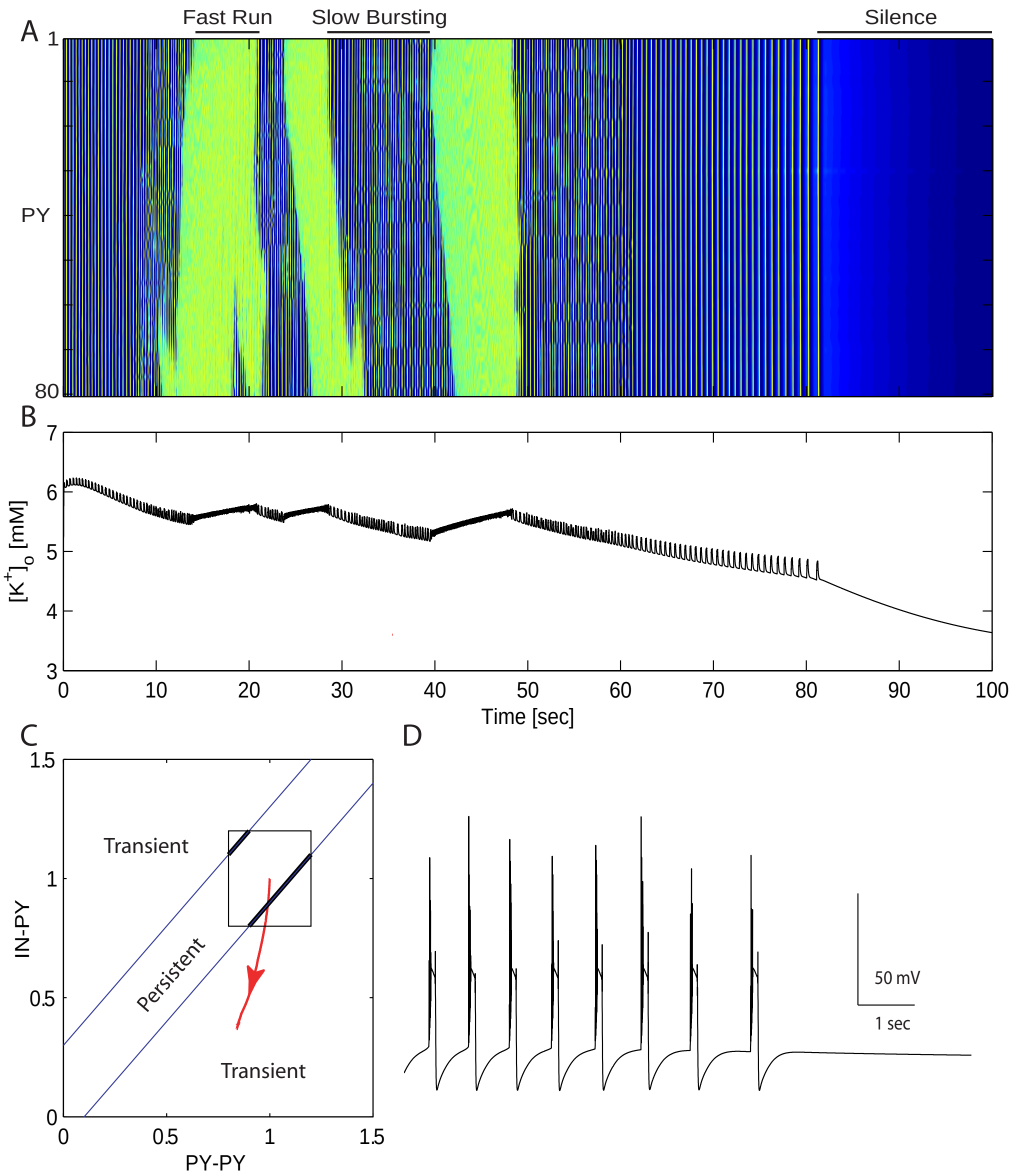

Figure 2-28 Patterned cortical network oscillations of finite length for slow depression of synaptic transmission. (A) Activity of all 80 PYs as a function of time. (B) Time-course of changes in $[K^+]_o$. (C) Phase–space representation of normalized synaptic-coupling strength. Dynamic change in balance between excitation and inhibition (red line). Arrowhead indicates direction of time. Blue diagonal lines delimit the region for which alternating epochs of fast run and slow bursting might occur infinitely. The box corresponds to the values of synaptic coupling strengths for which we found persistent oscillations in a small network with the same dynamics (Frohlich et al., 2006). (D) Time-course of membrane voltage before termination of oscillations shows slow bursting.

We next analyzed 10 seizures triggered by a transient increase in [K+]o for two values of the slow-depression rate for the inhibitory coupling [Fig. 2-29A for D(IN-PY) = 0.001 and Fig. 2-29B for D(IN-PY) = 0.0011, all activity maps aligned on onset of oscillatory firing]. Slow bursting is shown in black, fast run in gray, and silence in white. The difference between the firing patterns for a given value of D(IN-PY) was mediated by the random modulation of the membrane voltages by miniature postsynaptic potentials evoked by spontaneous release of neurotransmitter vesicles. For D(IN-PY) = 0.001, three out of 10 seizures did not terminate within the time window simulated (150 sec). All cases exhibited a series of transitions between fast run and slow bursting. In case of D(IN-PY) = 0.0011 (Fig. 2-29B), only one out of 10 seizures did not terminate within 150 sec. In one case, the seizure consisted only of slow bursting with no epoch of fast run. In all cases for which the network returned to the silent state, the oscillatory pattern ended with an epoch of slow bursting. In phase space, the normalized synaptic conductances diverged from the diagonal band that corresponds to persistent activity. We found a statistically significant difference in seizure duration for the two values of D(IN-PY) (Fig. 2-29D, left panel, $P = 0.02$). Accordingly, the number of epochs of fast run decreased for increased D(IN-PY) (Fig. 2-29D, right panel). All this can be explained by faster depression for D(IN-PY) = 0.0011 that moved the system further away from the region of balanced excitation and inhibition where oscillation could persist infinitely (Fig. 2-28C). Our results also indicate that the same network might produce a different pattern of paroxysmal oscillations as a result of random fluctuations of the membrane voltages.

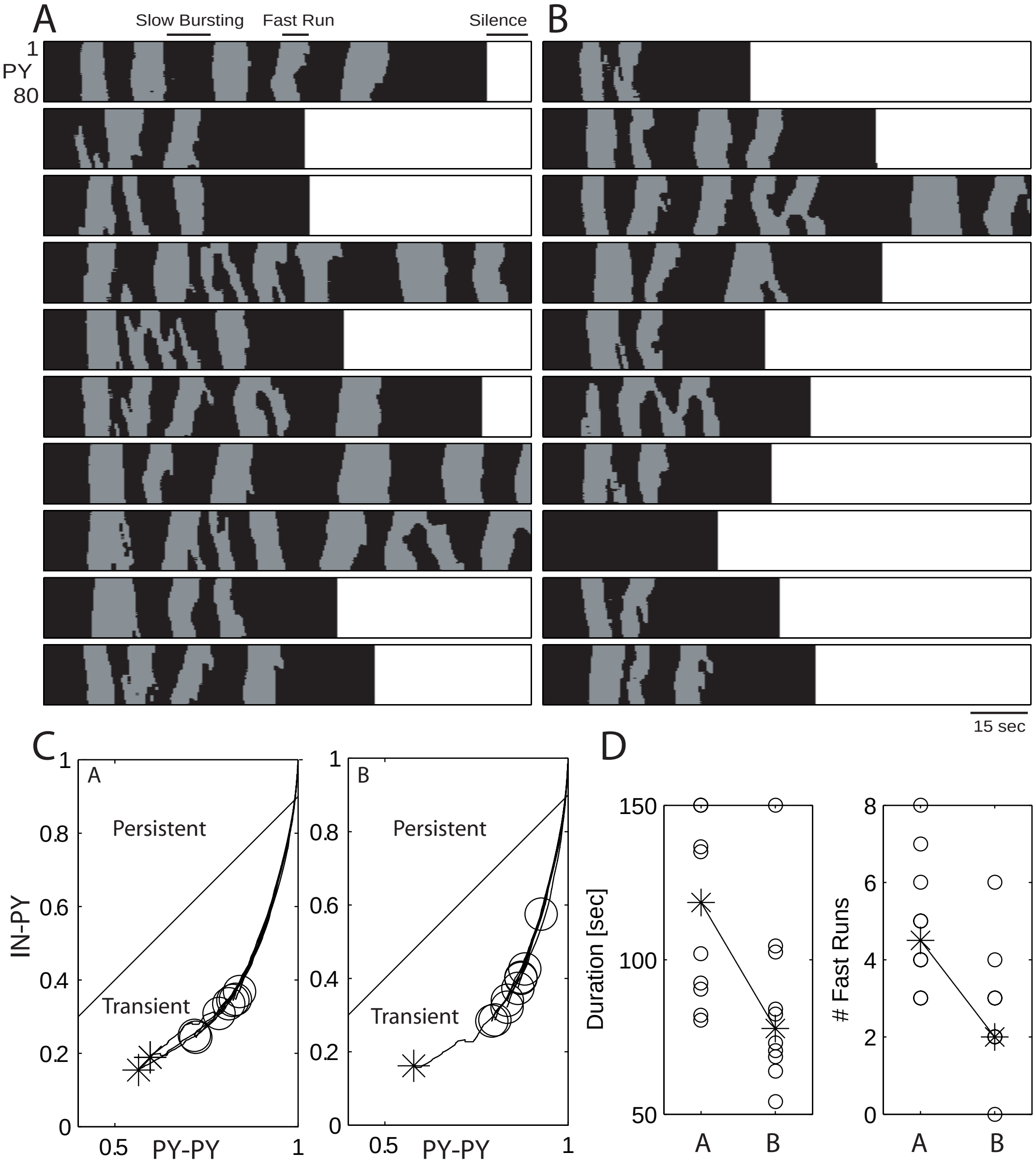

Figure 2-29 (A,B) Ten instances of patterned oscillatory firing for slow synaptic depression rate D = 0.001 (A) and D = 0.0011 (B). Black, gray, and white denote slow bursting, fast run and silence, respectively. (C) Phase–space representation of normalized excitation and inhibition (Left, D = 0.001; right, D = 0.0011). Circles, endpoints with termination of oscillations; stars, endpoint with no termination of oscillations within 150 sec. (D) Left, duration of seizures. Right, number of epochs of fast runs. Stars, median values.

EFFECT OF CHLORIDE REVERSAL POTENTIAL ON SEIZURE CESSATION

Our simple model of slow depression with differential scaling of synaptic excitation and inhibition represents a general principle of activity-dependent shift in the balance between excitation and inhibition. Next, we focused on a specific experimentally determined physiological mechanism, which can mediate such a shift in balance of excitation and inhibition. We previously found that the reversal potential for fast GABAergic synaptic currents mediated by chloride ions changes over the time course of an electrographic seizure (Timofeev et al., 2002b). Specifically, chloride influx caused a depolarization of the chloride reversal potential from -69.7 mV before seizure onset to - 46.7 mV at the end of the seizure. The resulting decrease in inhibitory currents is, therefore, a potential candidate mechanism for a slow, activity-dependent shift in the balance between synaptic excitation and inhibition during a seizure. We included these data in our model by adding simplified intracellular chloride dynamics in the form of a simple, activity-dependent accumulation mechanism that integrates the inhibitory currents targeting a cell. When using the dynamically updated chloride concentration to compute the reversal potential for the currents mediated by GABA receptors, the persistent neural oscillations terminated (Fig. 2-30A). Over the duration of the patterned oscillatory activity, the chloride concentration increased from 8.0 mM (corresponding to a reversal potential E_{Cl} = -74.3 mV) to 16.4 mM (E_{Cl} = -55.1 Mv) (Fig. 2-30B). This led to a weakening of inhibition without affecting synaptic excitation (Fig. 2-30C). As in the case of slow depression, the seizure ended with an epoch of slow bursting (Fig. 2-30D).

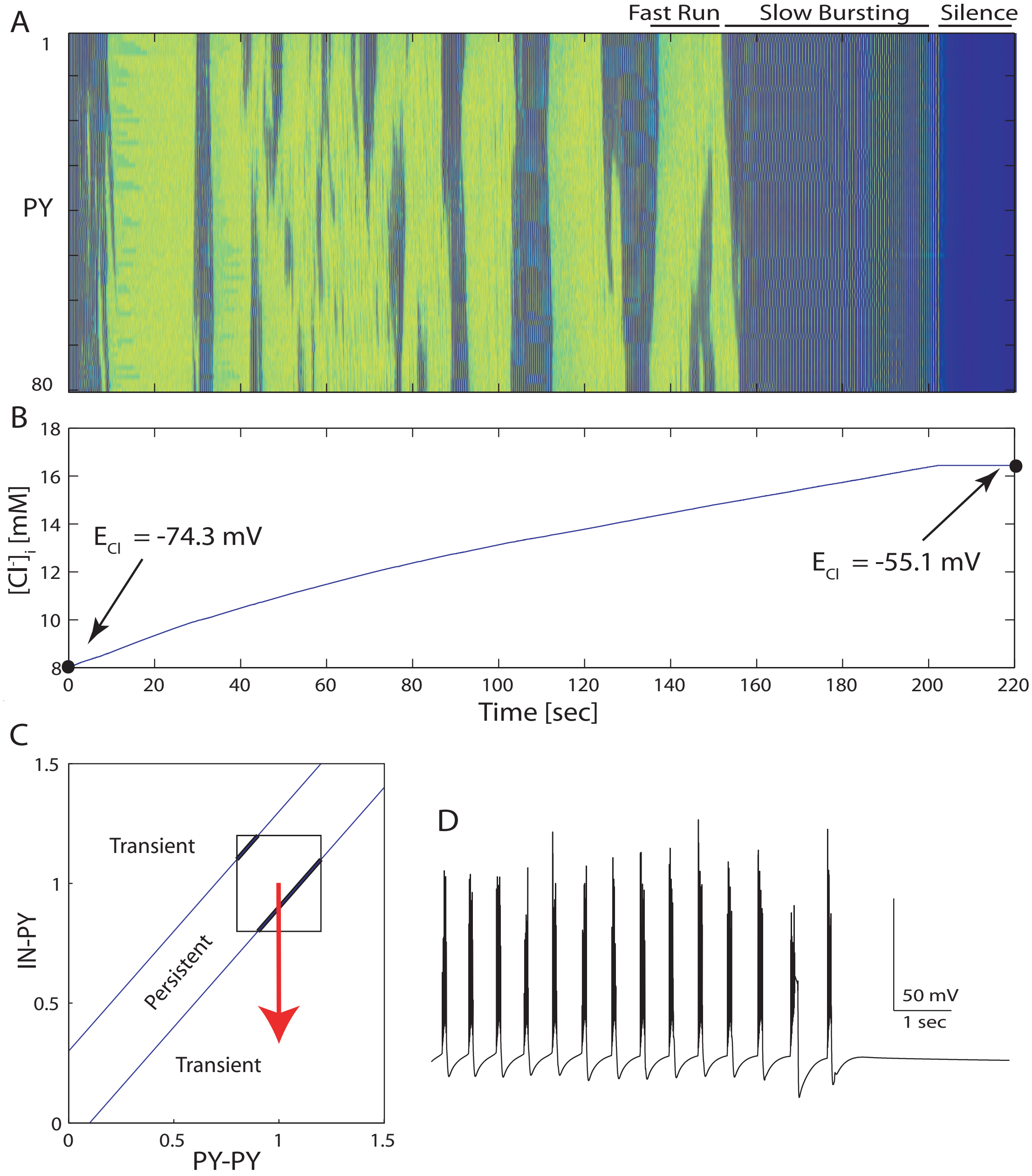

Figure 2-30 Patterned cortical network oscillations of finite length for dynamically updated intracellular chloride concentration. (A) Activity of all 80 PYs as a function of time. (B) Time-course of changes in intracellular chloride concentration ($[Cl^-]_i$). Corresponding reversal potentials are shown for the onset and the end of oscillations. (C) Symbolic phase–space representation of dynamic change in balance between excitation and inhibition (red line). Arrowhead indicates direction of time. Blue diagonal lines delimit the region for which alternating epochs of fast run and slow bursting might occur infinitely. (D) Time-course of membrane voltage before termination of oscillations.

DIFFERENCES IN ACTIVITIES OF REGULAR-SPIKING NEURONS AND FAST-SPIKING INTERNEURONS DURING SEIZURES *IN VIVO*

For the depolarization of the chloride reversal potential to have an effect on the seizure dynamics, inhibitory interneurons need to be active throughout the seizure. Fast-spiking neurons constitute an important class of inhibitory interneurons in the CNS. For this study, we recorded from 120 regular-spiking and 15 fast-spiking neurons (cell-type classification based on electrophysiological properties). In five, simultaneous, dual intracellular registrations, at least one regular-spiking and one fast-spiking neuron was recorded during electrographic seizures (Fig. 2-31). The observed seizures evolve from the slow oscillation and consist of spike-wave complexes with frequency 1−3 Hz (mainly 1.5−2.5 Hz) interrupted with periods of fast runs (8−20 Hz). On all occasions, the first 3−5 initial paroxysmal discharges were characterized by high-frequency firing of fast-spiking neurons (50−300 Hz, with some time reaching 500 Hz). Regular-spiking neurons also increased their firing frequency (Fig. 2-31B). During later stages of seizure spike-wave components, the fast-spiking inhibitory interneurons continued to maintain high-frequency firing during each burst, often reaching 500 Hz (Fig. 2-31C). However, despite large depolarization, the regular-spiking neurons displayed mainly one or two action potentials per paroxysmal spike (Fig. 2-31C). The loss of ability to fire spikes by regular-spiking neurons is probably caused by depolarizing block. Thus, in these experiments, the fast-spiking neurons maintained high-firing rate and, therefore, were in a position to exhibit a strong influence on their postsynaptic target neurons during both initial and spike-wave components of seizure. Combined with our earlier findings that chloride reversal potential increases over the duration of the seizure to an extent that chloride mediated synaptic currents mediate depolarizing postsynaptic potentials (Timofeev *et al*., 2002), our experiments imply – in agreement with our modeling results – a crucial shift in the balance between inhibition and excitation towards excitation over the time-course of the seizure. The relative increase in firing for the fast-spiking interneurons over the time-course of the seizure can be explained by depolarizing GABAergic postsynaptic potential from synaptic connectivity between fast-spiking interneurons and further amplifies the divergence from balanced excitation and inhibition towards more excitation in the case of elevated intracellular chloride concentration.

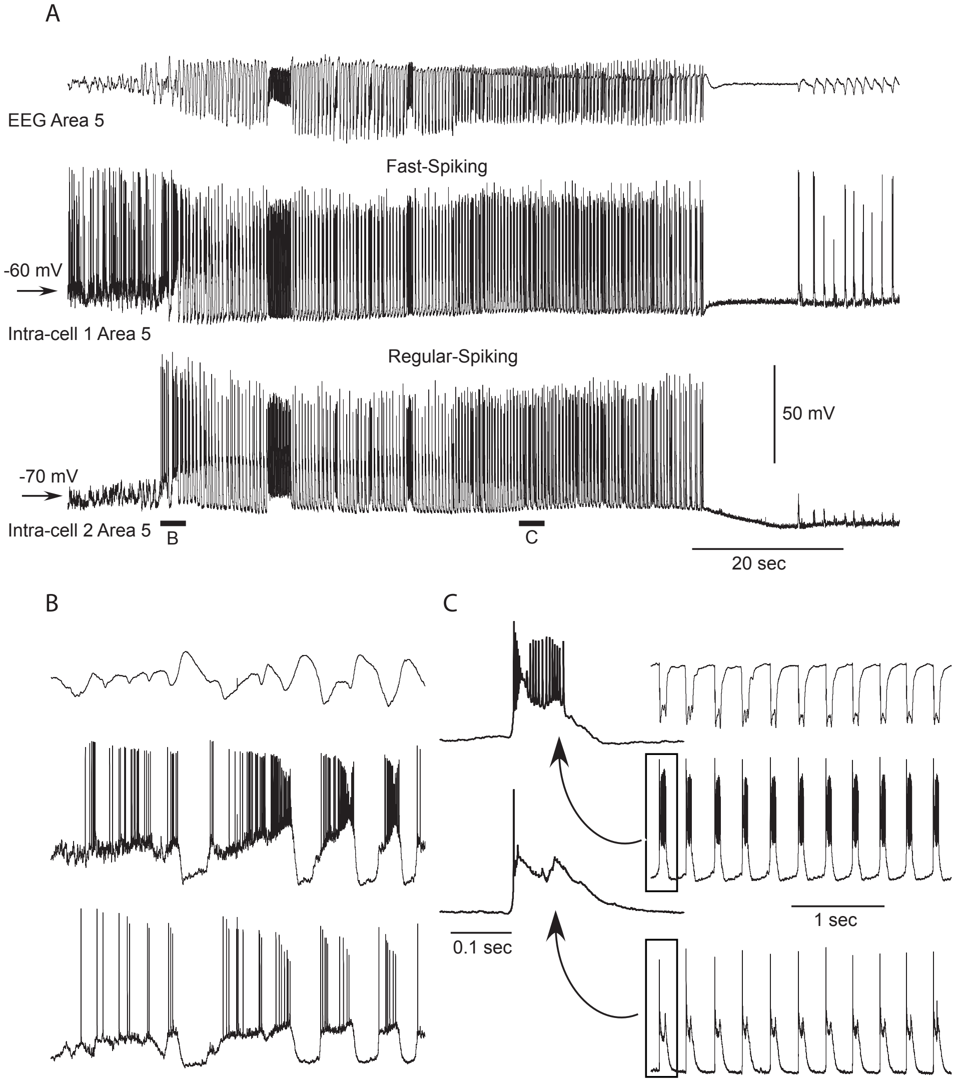

Figure 2-31 Spontaneous firing patterns of regular-spiking and fast-spiking cortical neurons during electrographic seizure *in vivo*. (A) Simultaneous, dual intracellular recording of EEG, regular-spiking and fast-spiking neurons (indicated) during seizure that is composed of spike-wave components and fast runs. The seizure evolves from slow oscillation. The fast-spiking inhibitory interneuron is active throughout the seizure. (B,C) Expansions of underlined fragments. (B) Intracellular activities during transition from slow oscillation to seizure. The fast-spiking neuron fires much more spikes than the regular-spiking neuron. (C) During spike-wave complexes the regular-spiking neuron displays one spike, whereas the fast-spiking neuron maintains ability to fire high-frequency trains of spikes.

CONCLUSIONS

We have shown that a cortical-network model that includes ion-concentration dynamics exhibits both seizure maintenance and termination dynamics in qualitative agreement with experimental results on electrographic seizures in experimental animals (Timofeev and Steriade, 2004) and human clinical EEG recordings (Niedermeyer, 2002). We suggest that the same shift towards more excitation that initiates and maintains a seizure will eventually also permit seizure cessation.

DISCUSSION

Little is known about the mechanisms underlying seizure cessation (Timofeev and Steriade, 2004). Here, we found in the model of neocortical seizures with epochs of slow bursting and fast run mediated by extracellular K^+ dynamics that an activity-dependent shift towards more excitation can mediate seizure cessation. For both activity-dependent scaling of synaptic conductances (slow depression) and change in chloride reversal potential, the transition dynamics was followed by silence that is similar qualitatively to *in vivo* intracellular recordings in anesthetized cats (Timofeev et al., 1998). Using a computational model, we first identified the general mechanism of a relative increase in excitation as a potential cause of seizure cessation. Then, based on experimentally established chloride-concentration dynamics (Timofeev et al., 2002b) as a physiological candidate mechanism for differential weakening of inhibition, we verified the hypothesis that a collapse in the chloride gradient can mediate seizure cessation. Synaptic inhibition is a highly efficient mechanism for cortical synchronization and therefore we suggest that a decrease in inhibitory efficiency (more depolarizing reversal potential for inhibitory postsynaptic potentials, IPSPs) would terminate hypersynchronous activities such as seizures.

It is widely accepted that the development of epileptiform activity results from a shift in the balance between excitation and inhibition towards excitation (Dichter and Ayala, 1987; Galarreta and Hestrin, 1998; Nelson and Turrigiano, 1998). The easiest way to elicit acute seizures is to block inhibition (Chagnac-Amitai and Connors, 1989a, b; Gutnick et al., 1982; Matsumoto and Ajmonemarsan, 1964; Prince, 1978), which is a well known approach to elicit experimental seizures (McNamara, 1994; Steriade and Amzica, 1998; Timofeev and Steriade, 2004; Traub et al., 1996). Chloride concentration has been implicated previously in seizure dynamics because it directly affects synaptic inhibitory currents mediated by GABA(A) receptors (Cohen et al., 2002). Contrary to expectation, the model implementing activity-dependent increase of $[\mathrm{Cl}^{-}]_{\mathrm{I}}$ showed that seizure cessation was mediated by a relative increase in excitation over the course of paroxysmal oscillations. This provides a new interpretation for the changes in intracellular chloride concentration that occur during a seizure. Although a decrease in inhibition can promote seizure initiation in normal cortex, we propose here that an actual increase in excitability during paroxysmal run itself can lead to seizure cessation.

Importantly, our model predicts that the termination of a seizure is preceded by an epoch of slow bursting. This finding is confirmed by experimental recordings (I. Timofeev, unpublished observations).

Our model of chloride dynamics is relatively simple, and other mechanisms that we have not included in our model also affect intracellular chloride concentration (Kaila et al., 1997; Thompson and Gahwiler, 1989). For example, an increase in $[K^+]_o$ in mature neocortical PYs would result in further increase in $[Cl^-]_i$ via activation of the neuron-specific protein K^+Cl^- (KCC2) co-transporter (DeFazio et al., 2000). Although we have not included this mechanism in our model, our results indicates that adding another activity-dependent mechanism of intracellular chloride dynamics might affect the duration of a seizure and contribute further to seizure cessation. Chloride concentration dynamics have also been implicated in the field of pain research where a change from inhibitory to excitatory GABAergic transmission has been associated with neuropathic pain (Coull et al., 2003).

ACKNOWLEDGEMENT

Section 2.5, in full, is a reprint of the material as it appeared in Thalamus and Related Systems, 2006, Frohlich, Flavio; Bazhenov, Maxim, Timofeev, Igor; Sejnowski, Terrence. The dissertation author was the prime investigator and author of this paper. This research was supported by National Institute of Health, the Canadian Institutes of Health Research and Natural Science and Engineering Research Council of Canada. I.T. is scholar of Canadian Institutes of Health Research. The authors thank Steven Prescott for valuable scientific discussion. We dedicate this paper to the memory of Mircea Steriade, whom we thank for many stimulating discussions and continuous support. Reprinted from (Frohlich et al., 2007a) with permission. Copyright Cambridge University Press 2007.

3 Conclusions

Computational neuroscience has become a mature discipline that has successfully contributed to a better understanding of many aspects of the functioning of the nervous system. Nevertheless, the study of neurological disorders by means of computer models has yet to develop into a fully recognized interdisciplinary scientific discipline. With our work, we hope to contribute to this emerging field by fostering an increased understanding of dynamic principles that govern pathological oscillatory cortical activity. We believe that we may find in the future that the clinical complexity and diversity of pathological brain activity can be conceptually reduced to a limited set of dynamic principles. The identification of these principles - if they exist - would certainly greatly aid the development of improved clinical modalities to prevent, treat, and cure disorders with neurological manifestations.

In the first part of this dissertation, we studied how cortical networks reorganize in response to loss of afferent synaptic input and showed that homeostatic plasticity may paradoxically cause hypersynchronous periodic network facilitation. Importantly, the model we used is free of any specific assumptions about particular pathologies and may therefore indeed manifest a general principle of brain reorganization dynamics that occurs in a broad variety of CNS disorders associated with reduced synaptic input due to synapse or presynaptic cell loss. In fact, we showed that the same principle (given a more structured pattern of deafferentation) may also explain epileptogenesis in the posttraumatic brain.

In the second part, we studied the dynamics of cortical seizures with computational models that included potassium concentration ($[K^+]_o$) homeostasis mechanisms. In essence, we found that $[K^+]_o$ dynamics can indeed explain initiation, maintenance, and termination of cortical seizures. Of particular interest in this context is the fact that our work revisited an old hypothesis that had been prematurely abandoned for other hypotheses on the pathophysiology of cortical seizures. In fact, the results from our modeling work reveal the underlying dynamics and explain the previously ununderstood experimental findings. We therefore believe that our work illustrates the importance of computer models for advancing our understanding of physiological and pathological brain activity.

Of course, all our findings are limited by the sophistication and robustness of the models used. Our goal was to build models that were sufficiently general without being too unspecific. The final answer to the question whether we have achieved a good balance in that regard will only be available once the according *in vivo* and human clinical studies are going to be performed. In fact, only time will show how useful efforts of our kind will be for improving the human condition. In the mean time it remains for us to hope that they in fact will.

4 Appendix

4.1 Extracellular single-unit recordings of spontaneous and evoked population activity in the acute cortical slice preparation

The acute brain slice preparation represents an important experimental system for the study of spatio-temporal dynamics in cortical networks. Multi-electrode arrays for extracellular recordings of action potentials have matured into an essential tool for the study of network dynamics *in vivo*. In acute cortical slices *in vitro*, however, extracellular recordings with single-cell resolution from a population of neurons have remained an elusive goal. Here, we present a robust and relatively simple method for single-unit recordings based on extracellular multiunit recordings with penetrating metal microelectrodes and consequent isolation of putative single units by spike sorting. Combined intracellular whole-cell patch-clamp and extracellular recordings in hippocampal slices provided the opportunity to directly assess the accuracy of the spike sorting and to describe the cell-type dependence of the extracellular action potential waveforms. We demonstrate the application of the technique to the study of network dynamics in acute hippocampal slices. First, we found slow patterning of spontaneous activity in hippocampus CA3 under standard ionic conditions. Second, we probed the dynamic input-output mapping in the CA3 - CA1 network in hippocampus by combining single-unit recordings with extracellular stimulation of afferent fibers. We conclude by discussing opportunities and limitations of extracellular single unit recordings *in vitro*.

INTRODUCTION

Information processing and storage in the central nervous system relies on both spatial and temporal coding strategies. Thus, understanding the functional dynamics of neuronal networks requires techniques that permit the simultaneous recording of the activity of many neurons with high temporal resolution. Extracellular recordings of action potentials with arrays of electrodes serve this exact purpose and have become an established technique *in vivo* (Buzsaki, 2004; Hubel, 1957). With this technique, extracellular signatures of action potentials from a population of cells are recorded with a set of electrodes and subsequently sorted into individual units corresponding to different neurons. However, similar techniques have so far not prevailed in the acute cortical slice preparation *in vitro*. Yet, recording from a population of neurons from acute brain slices *in vitro* with high temporal resolution represents an essential technique to bridge the gap between multi-electrode recordings *in vivo* and whole-cell patch-clamp recordings *in vitro*. Here we describe a relatively simple and robust experimental approach for extracellular single-unit recordings of spontaneous and evoked population activity in the acute cortical slice preparation. We show that this technique permits the study of temporal dynamics of small populations of neurons in combination with whole-cell patch-clamp recordings.

Network behavior strongly depends on the local ionic and neurochemical environment which can only be controlled to a very limited extent in an *in vivo* experiment. Quite in contrast, the slice preparation provides a unique experimental set-up with the necessary stability and controllability for studying the state-dependence of spatio-temporal network dynamics. However, such studies have been hampered by the constraints of the currently available recording techniques *in vitro*. Fluorometric measurements of neural activity with calcium-sensitive indicators achieve single unit resolution but are currently restricted to relatively low temporal resolution. While the whole-cell patch-clamp method provides the required temporal resolution, the method is limited to simultaneous recordings from at most few cells. Thus, the lack of a tool to study network dynamics of populations of neurons with millisecond time resolution at the single-cell level represents a major hurdle to overcome for the study of network dynamics *in vitro*.

While simultaneous multielectrode recordings from hundreds of ganglion cells *in vitro* have become feasible (Shlens et al., 2006), achieving reliable recordings with single unit resolution in acute cortical slice of both spontaneous and evoked activity has remained an elusive goal. Previous studies of network dynamics in the acute cortical slice have used multiunit recordings without single-unit resolution (Cohen and Miles, 2000; Sanchez-Vives and McCormick, 2000). Electrical stimulation and extracellular recordings have been combined in cultured neurons (Wagenaar and Potter, 2002). Substantial research has been dedicated to the development of commercial multielectrode arrays that require dedicated set-ups (Egert et al., 2002; Heuschkel et al., 2002). Also, custom-made silicon probes have been used to record action potentials that were evoked by glutamate application *in vitro* (Hempel et al., 2002). Here, we focused on the development of a relatively simple method to record from a population of neurons with single-unit and high temporal resolution which can be integrated into an existing whole-cell patch-clamp setup. Specifically, we recorded extracellular action potentials with penetrating metal electrodes designed for *in vivo* extracellular microelectrode recordings. We then used a spike sorting algorithm to extract individual putative single units from the multiunit data. Importantly, we made use of simultaneous whole-cell recordings to directly determine the quality of the achieved single-unit isolation. Here we describe the method and provide first results that illustrate its usefulness for the study of network dynamics in cortical circuits *in vitro*.

METHODS

Transverse hippocampal slices (400 μm thick) from Wistar rats (age: p16 - p38) were cut in ice cold standard artificial cerebrospinal fluid ACSF (119 mM NaCl, 2.5 mM KCl, 1.3 mM $NaHPO_4$, 1.3 mM $MgCl_2$, 2.5 mM $CaCl_2$, 26 mM $NaHCO_3$, and 11 mM glucose) equilibrated with 95% O_2 and 5% CO_2. Slices were immediately transferred into an interface chamber where they were incubated at 34°C for 45 minutes and afterwards maintained at room temperature. For all recordings, slices were submerged in standard ACSF and maintained at 32-34°C. All experiments were carried out in accordance with the guidelines by the University of California.

Extracellular recordings in acute cortical slice submerged in ACSF were achieved with commercial *in vivo* metal microelectrodes that were mounted on a micromanipulator (Luigs & Neumann Feinmechanik und Elektrotechnik GmbH, Ratingen, Germany) as typically used for whole-cell patch-clamp recordings. Electrodes were inserted into the tissue at depths between 10 and 200 microns and at an angle comparable to the one for whole-cell recordings with glass micropipettes. In some cases, a transient increase in spontaneous discharge was observed that disappeared within few seconds. Electrodes resistance, material, and tip geometry were found to be crucial parameters for successful recordings. Most reliable recordings were achieved with tungsten electrodes with nominal impedance at 1 kHz between 500 kOhm and 2 MOhm (FHC Inc., Bowdoin, ME). Electrodes with sharp tips (final taper angle less than 15°) did not pick up action potentials. Too blunt tips (final taper angle more than 25°) caused macroscopic tissue damage upon insertion which often resulted in absence of detected spiking activity. While we successfully tested these single electrodes in preliminary experiments, we eventually settled on a commercially available electrode with 8 recording sites (impedance 500-800 kOhms as reported by the manufacturer) with close spacing of the recording pads (estimated 20 μm) which are positioned 360° around the tip of the electrode (ALA Scientific, Westbury, NY). This high density of recording sites permitted spike sorting with high accuracy (Harris et al., 2000) since action potentials were typically picked up from several recording sites [“tetrode effect”, (McNaughton et al., 1983)]. The electrodes were connected to an eight channel preamplifier MPA8I with gain 10 (Multi Channel Systems MCS GmbH, Reutlingen, Germany) which was mounted on the micromanipulator and connected to the stimulation artifact suppression unit (Multi Channel Systems MCS GmbH, Reutlingen, Germany) which leaded into to a sixteen channel amplifier Model 3500 (A-M Systems, Inc., Carlsborg, WA). Data was filtered (bandpass filter with cut-off frequencies 0.1 Hz and 5 kHz, respectively) and amplified with gain 100. Data was digitized with a Digidata 1440A A/D converter (Molecular Devices Corporation, Sunnyvale, CA) at 20-50 kHz sampling rate and recorded on a hard drive with the pClamp software (Molecular Devices Corporation, Sunnyvale, CA). Whole-cell patch-clamp recordings and extracellular stimulation were performed as previously described (Glickfeld and Scanziani, 2006; Pouille and Scanziani, 2001, 2004).

Our recording set-up permitted the extracellular stimulation of afferent fibers and the simultaneous extracellular recording of evoked spiking with monosynaptic latencies. Since metal electrodes record changes in electrical field by means of capacitative coupling, electrical stimulation in the submerged chamber filled with conducting ACSF caused an electrical artifact which outlasted the time window of interest for spikes in response to the activation of afferent synapses. While we experimented with several different possible solutions (not reported her), we achieved by far the best results with a stimulus blanking device (Multi Channel Systems MCS GmbH, Reutlingen, Germany) which was integrated between preamplifier and amplifier. This blanking device contained a rapid electronic switch for disconnecting the preamplifier from the amplifier. The TTL pulse triggering the stimulus isolation unit for extracellular stimulation also triggered the blanking device which transiently grounded the preamplifier such that no charge reached the amplifier during stimulation. Blanking duration was chosen to be as short as possible. Typical duration of the TTL pulse for blanking was between 100 and 800 microseconds and depended on the geometry of stimulation and recording electrode positioning and the stimulation amplitude.

Data analysis was performed offline by custom written software in MATLAB (The MathWorks, Inc., Natick, MA). Low frequency components in the signal which consisted of local field potential mediated by synaptic currents (abolished by 10 μM NBQX, data not shown) was removed by subtraction of a locally fitted low-order polynomial [SALPA algorithm, (Wagenaar and Potter, 2002)]. The spike sorting process consisted of two consecutive steps: (1) spike extraction and (2) spike clustering into single units. First, the pre-processed signal was subjected to a threshold (manually chosen, usually with a negative threshold of minus five standard deviations of the extracellular trace) to extract presumed spikes. Each time the threshold was crossed a corresponding 2 msec waveform snippet was extracted from all recording sites and concatenated to form a composite waveform vector. Second, spikes were assigned to putative single units with a spike sorting algorithm adapted from Fee et al (1998). Specifically, waveform vectors were grouped into clusters using the k-means clustering algorithm. The number of these "subclusters" was manually set to a value around ten times as high as the number of expected single units to be found. These subclusters were then iteratively merged to form clusters that eventually represented individual single units. Linkage analysis of the subcluster centroids was used as a guide for this manual merging of subclusters. Finally, spike clustering results were assessed by testing for refractory period violations and by visual inspection of resulting waveform clusters in a reduced two-dimensional space determined by principal component analysis. Waveform stability was evaluated by plotting the first two principal components of all spikes as a function of time.

RESULTS

We recorded the extracellular signatures of action potentials in acute hippocampal slices with a single shank metal electrode with eight recording sites. In order to reveal the network dynamics with single-cell resolution, we separated the extracellular waveforms into individual clusters that corresponded to putative single units. While such spike sorting procedures are routinely applied to multiunit recordings *in vivo* (Buzsaki, 2004), the application of these algorithms to *in vitro* recordings has not yet been established. Therefore, we first determined the accuracy of spike sorting of *in vitro* multiunit data by making use of the advantage that we readily achieved simultaneous whole-cell intracellular recordings. Specifically, we simultaneously recorded whole-cell from a neuron close to the tip of the multisite electrode. This experimental paradigm permitted us to trigger action potentials in this identified neuron by brief intracellular current injections (“control unit”). In such experiments, the extracellular recording sites picked up action potentials from both spontaneously active cells in the vicinity and the control unit (Fig. 4-1A, intracellular recording and extracellular traces from four recording sites). We then sorted the spikes blind to which spikes originated from the control unit. This procedure enabled an explicit quantification of the accuracy of the spike sorting by determining how many spikes were erroneously associated with the control unit (false positives) and how many spikes from the control unit were missed (false negatives) in the spike sorting process (Harris et al., 2000; Henze et al., 2000). In the sample experiment shown in Figure 4-1, we extracted eight putative single units (Fig. 4-1B; raw waveforms on six recoding sites; units are color-coded). Unit 4 represented the control unit that had fired 707 action potentials during the experiment according to the results from spike sorting. In reality, the intracellular recording of the control unit showed 701 spikes. Also, 10 spikes were wrongly assigned to the control unit by the spike sorting algorithm. Thus, we found a false positive rate of 1.41% and a false negative rate 0.45%. All eight units determined by spike-sorting formed clusters when plotted in two-dimensional PCA space (Fig. 4-1C, same color code as in Fig. 4-1B). Importantly, the waveforms remained stable over the duration of the experiment (Fig. 4-1D, first two principal components plotted as a function of time) Thus, this experiment shows that spike sorting with very high reliability is achievable with the methods presented here.

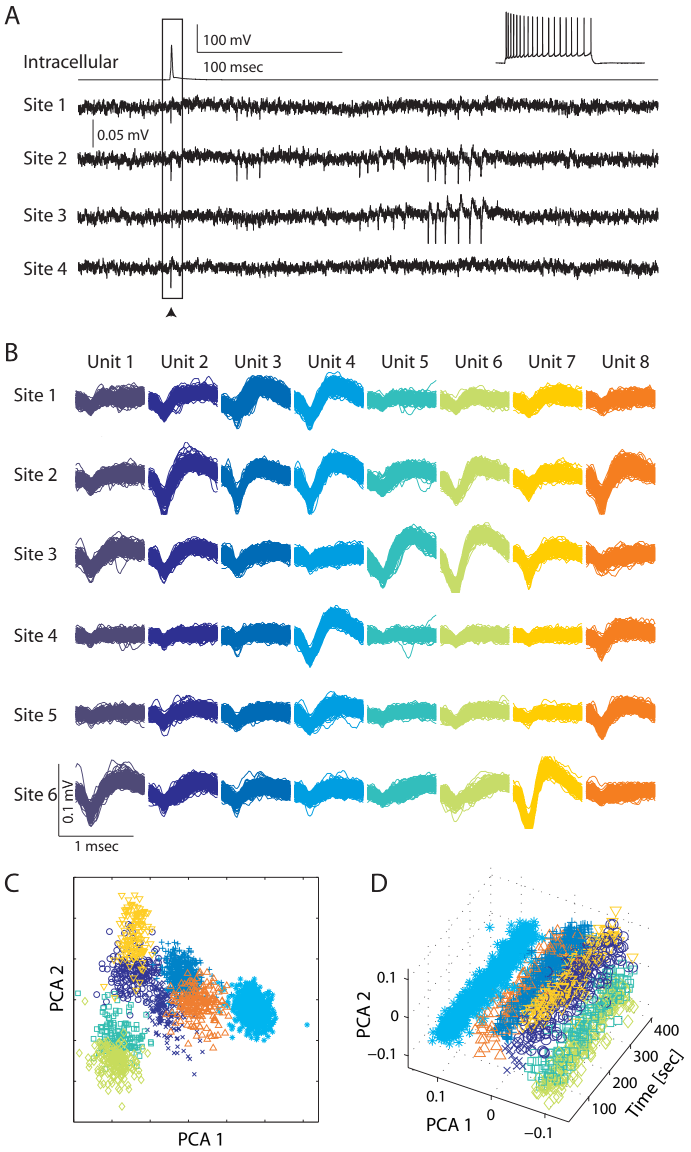

Figure 4-1 *Spike sorting* in vitro. (A) Combined intracellular (top trace; pyramidal cell; inset: spike pattern in response to depolarizing current step) and extracellular recording (bottom four traces for recording sites 1-4) in hippocampus *in vitro*. Arrow head points to action potential in control unit elicited by brief intracellular current injection. (B) Raw extracellular waveforms of all eight single units extracted by spike sorting algorithm (columns, units are color-coded). Rows correspond to six of the eight extracellular recording sites. Note that the distinction of different units only based on a single recording site would be exceedingly difficult. Unit 4 in light blue was the control unit. (C) All action potentials plotted in reduced two-dimensional PCA space. Units form distinct clusters. (D) First two principal components of all action potentials plotted as a function of time. Clusters remained stable over duration of experiment.

We next considered the nature of the extracellular action potential waveform in more detail by simultaneous extracellular and intracellular recordings from visually identified cells (Fig. 4-2A). Since the extracellular waveform is presumed to be mostly mediated by a capacitative current (Gold et al., 2006), we investigated whether the first derivative of the intracellular waveform corresponded to the extracellular waveform. Specifically, we triggered a series of action potentials in current clamp mode and simultaneously recorded the extracellular spike train. Using these data, we then determined the impulse response of the linear transfer function that mapped the intracellular to the extracellular action potential waveform (Fig. 4-2D). Most prominently, the resulting impulse response had two consecutive non-zero samples of opposite sign. Thus, the value of the extracellular waveform at any time-point was indeed approximately determined by the arithmetic difference between two consecutive time-samples of the intracellular membrane voltage (“differentiator”).

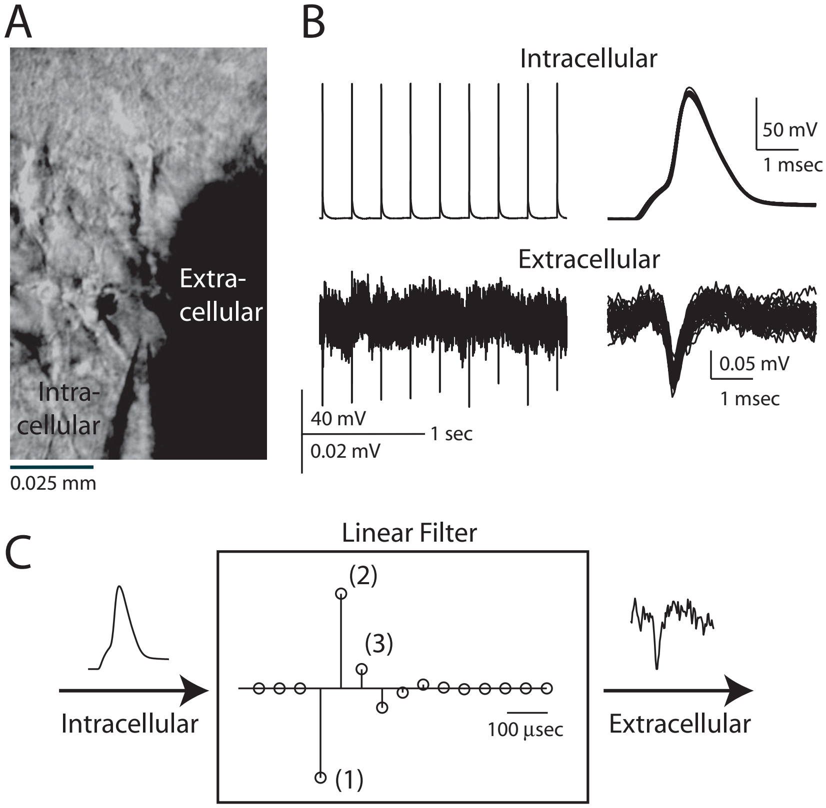

Figure 4-2 *Intracellular and extracellular waveforms*. (A) Pyramidal cell layer in hippocampus CA1 with intracellular (left) and extracellular (right) recording electrode. (B) Intracellular (top) and extracellular (bottom) raw action potential waveforms. (C) Impulse response of linear filter that transformed intracellular into extracellular waveform.

Different cell types exhibit different intracellular waveforms depending on their specific ion channel complement. For example, fast spiking inhibitory interneuron are characterized by “fast” spikes when recorded intracellularly (McCormick et al., 1985). Consequently, extracellular waveforms with short duration have been associated with inhibitory interneurons (Bartho et al., 2004; Henze et al., 2002). We performed simultaneous extra- and intracellular recordings from pyramidal cells (sample in Fig. 4-3A) and fast-spiking inhibitory interneurons (sample in Fig. 4-3B) to confirm this suggested relationship between cell type and extracellular waveform. We determined two parameters from the extracellular waveforms: (1) the duration defined as the time from the negative to the positive peak and (2) the ratio of the positive and the negative peak amplitudes. We found significant differences between pyramidal cells and fast-spiking inhibitory interneurons for both of these parameters (Fig. 4-3C and D). In fact, the distribution of both parameters did not overlap and therefore permitted us to define a separation criterion by determining a straight line that maximally separated the two cell types (Fig. 4-3E, equation of classification boundary: slope: 1.30; y-axis intercept: 0.44).

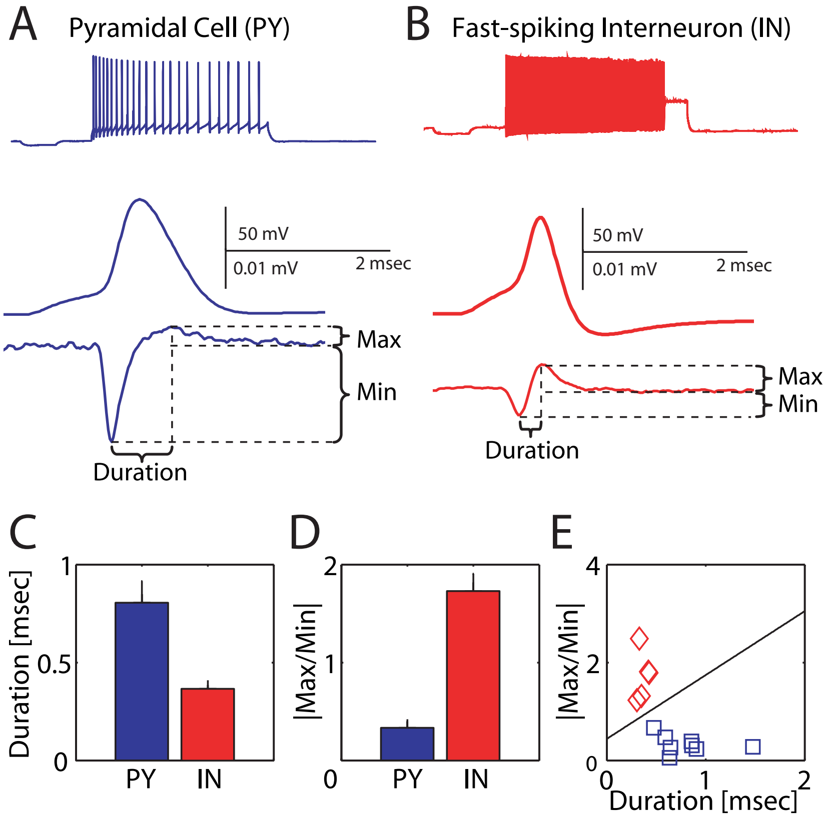

Figure 4-3 *Pyramidal cells and fast-spiking interneurons have different extracellular action potential waveforms.* (A) Pyramidal cell (PY, blue). Top: Intracellular recording. Response to depolarizing current step and average action potential waveform. Bottom: Average extracellular waveform. Dashed lines delimit duration and peak values. (B) Fast-spiking inhibitory interneuron (IN, red). Same plots as in (A). (C) Duration from negative to positive peak of extracellular waveform for PYs (N = 9) and INs (N=5). Error bars denote S.E.M. Difference is significant ($p<0.05$, t-test). (D) Ratio of negative and positive peak amplitudes for PYs (N = 9) and INs (N = 5). Error bars denote S.E.M. Difference is significant ($p<0.05$, t-test). (E) Group data from panels (C) and (D). INs: red diamonds. PYs: blue squares. Black diagonal line denotes classification boundary (slope: 1.30; y-axis intercept: 0.44).

Hippocampus field CA3 represents an interesting network to study due to its presumed attractor network like dynamics (Guzowski et al., 2004; Hopfield, 1982; Leutgeb et al., 2007; Leutgeb et al., 2005). Under standard *in vitro* conditions, we found spontaneous action potential firing in the pyramidal cell layer of CA3 (Fig. 4-4). In a typical experiment, the rastergram (Fig. 4-4A) and firing frequency histogram (Fig. 4-4B) exhibited periods of stable activity and periods where individual cells exhibited strong fluctuation of activity levels. Importantly, this modulation of activity levels was not synchronized across cells. Thus, these fluctuations were cell specific and did not simply reflect a change in overall excitability of the entire network. We then calculated an activity trajectory (Mazor and Laurent, 2005) that represented the evolution of the network activity as a function of time (1 sec bin width). For each time bin, we determined the activity vector that represented the number of action potentials for each cell (e.g. if "Cell 1" fired four action potentials in a given one second time interval, the first entry in the activity vector would be "4").

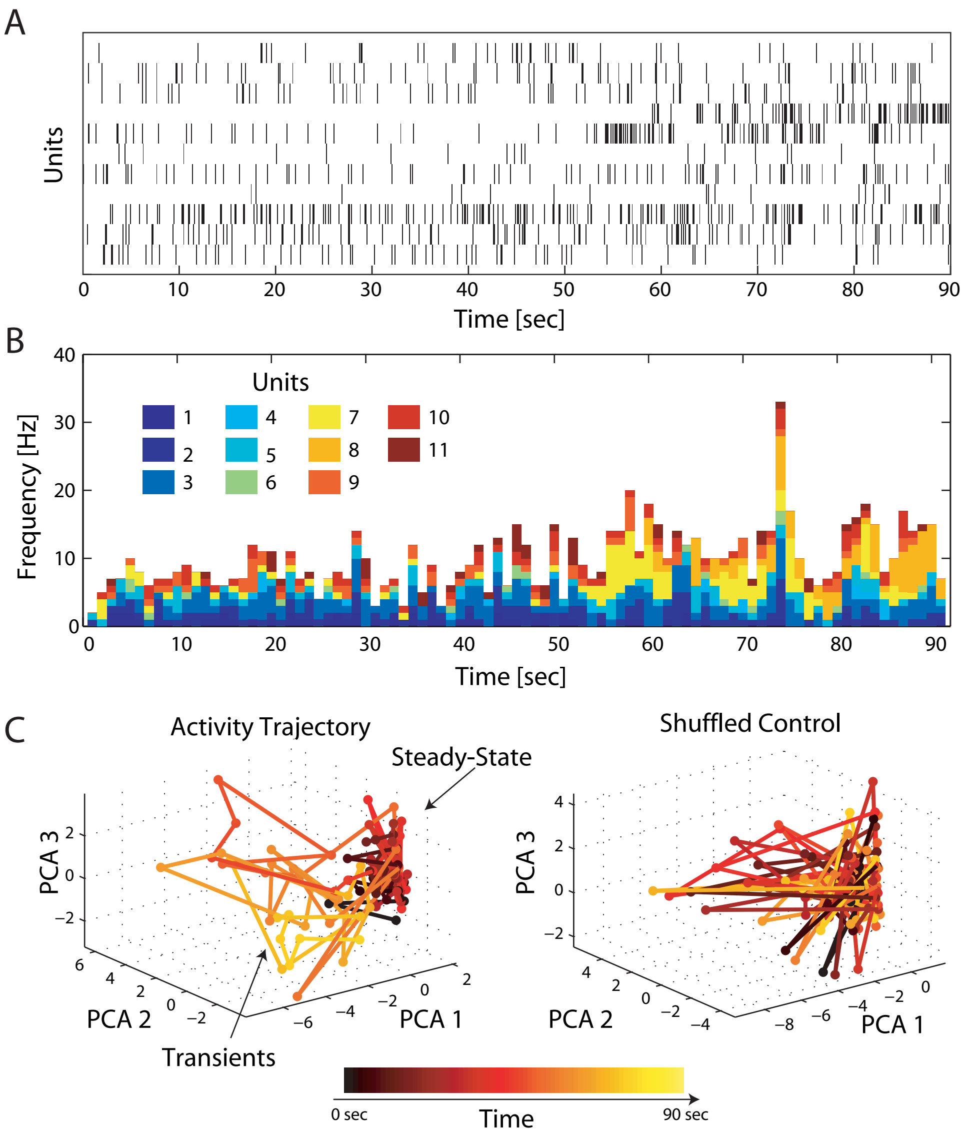

Figure 4-4 *Spontaneous activity in hippocampus CA3*. (A) Spike rastergram of eleven isolated units. (B) Spike histogram determined from spike histogram (bin width: 1 second). Units are color-coded. (C) Activity trajectory in reduced three dimensional principal component space (time color-coded). Trajectory initially remained in steady-state location (dark red) but then exhibited several transients away from the steady-state location (yellow). (D) Control trajectory for shuffled spike identities. No structure as in (C).

We then plotted the activity vector in a reduced three-dimensional space determined by PCA (Fig. 4-4C, left, time is color-coded). The plotted activity trajectory exhibited (1) a “steady-state location” where most of the trajectory resided and (2) several “transients” where the trajectory traveled away from the steady-state location and returned back within few seconds. As a simple control, we scrambled the spike identities such that the overall firing histogram remained the same but the cell identities were randomly mixed up. The corresponding activity trajectory did not exhibit the previously found structure (Fig. 4-4C, right). Therefore, the observed dynamics did indeed not merely reflect fluctuations in overall activity levels. While these trajectories are suggestive of attractor-type network dynamics, we emphasize that the underlying mechanism of these network dynamics were not the subject of this study and deserve more detailed separate investigations.

Key advantage of the slice preparation for the study of network dynamics is the controllability of the afferent inputs. In particular, the hippocampus provides the opportunity to study input-output dynamics of networks of neurons through its simple layered structure with segregated afferent pathways. Here, we use our experimental set-up to study how simulated bursts in CA3 neurons are represented by CA1 neurons. To that end, we disconnected CA3 from CA1 by a microsurgical cut in the slice and stimulated the Schaffer collaterals stemming from CA3 by means of extracellular current stimulation through a metal microelectrode. The stimulation amplitude was chosen to be sufficiently low such that only few postsynaptic neurons in CA1 were activated. Such low stimulation amplitudes imitated the sparse activation patterns in the behaving animal (Henze et al., 2000). Also, we were limited to low stimulation amplitudes by an important inherent constraint of extracellular single-unit recordings. Synchrony in action-potential firing in a local group of cells consistently resulted in the appearance of a single population spike instead of a group of separate spikes from individual cells (data not shown). As a consequence, our method to record and extract spikes from individual units failed.

Stimulation of the Schaffer collaterals with five pulses at 100 Hz elicited a positive going field potential envelop with superimposed individual spikes in the pyramidal cell layer of CA1 (Fig. 4-5A, top panel). The slow field potential was removed with SALPA, essentially an adaptive subtraction of the estimated underlying waveform by piecewise fitting with low-order polynomials (Wagenaar and Potter, 2002) without distortion of the spike waveforms (Fig. 4-5A, bottom panel). Individual trials were separated by a 10 second interval to prevent short-term synaptic dynamics to pollute the responses. In a typical experiment, we isolated about 10 neurons from one single shank electrode with eight recording sites (11 units in experiment shown in Fig. 4-5B). Spike-timing histograms of two sample units revealed two different response types (Fig. 4-5C). One cell exhibited very little spike jitter and short response delay (top panel), whereas the other one had more jitter and longer latencies (bottom panel).

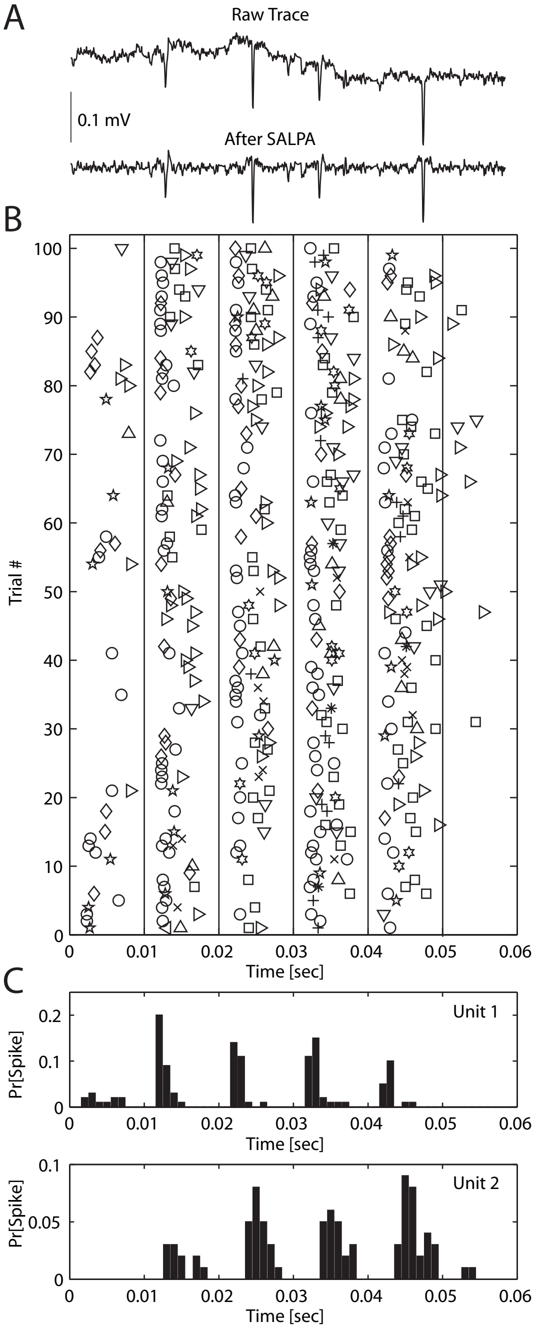

Figure 4-5 *Input-output map in the hippocampal CA3 – CA1 circuit*. Evoked action potentials in pyramidal cell layer of hippocampus CA1 by extracellular stimulation of afferent Schaffer collaterals. (A) Raw trace consists of synaptic field potential and individual spikes (top). Same trace after application of the SALPA algorithm to remove slow synaptic field potential (bottom). (B) Raster plot for 100 consecutive sweeps; each symbol denotes a different unit. (C) Spike histograms for two sample units.

A further application of a similar set-up but with stimulation of two independent pathways is illustrated in Fig. 4-6, where we studied the input discrimination ability of the CA3 - CA1 circuit. Goal of this type of experiment was to determine how similar the postsynaptic spiking response patterns for activation of two independent afferent pathways were. We positioned two extracellular stimulation electrodes ("Input A" and "Input B") at two closely spaced locations within the Schaffer collaterals and established the independence of the two pathways activated by testing for linearity of the postsynaptic field (data not shown). Action potentials were extracted and assigned to individual units as described above. In this specific case, we isolated 7 units (Figure 4-6A; units coded by symbols). The two panels show the responses to the two inputs on a trial-by-trial basis (blue and red, for response to Input A and Input B, respectively). While some units had a strong preference for one of the two inputs (unit denoted by square, firing histogram in Fig. 4-6B, left panel), other units exhibited less of a response preference (unit denoted by star, firing histogram in Fig. 4-6B, right panel). Also, we noted variability on a trial-to-trial basis due to the fact that our stimulation protocol operated in a near threshold regime where any unit responded only on a fraction of trials.

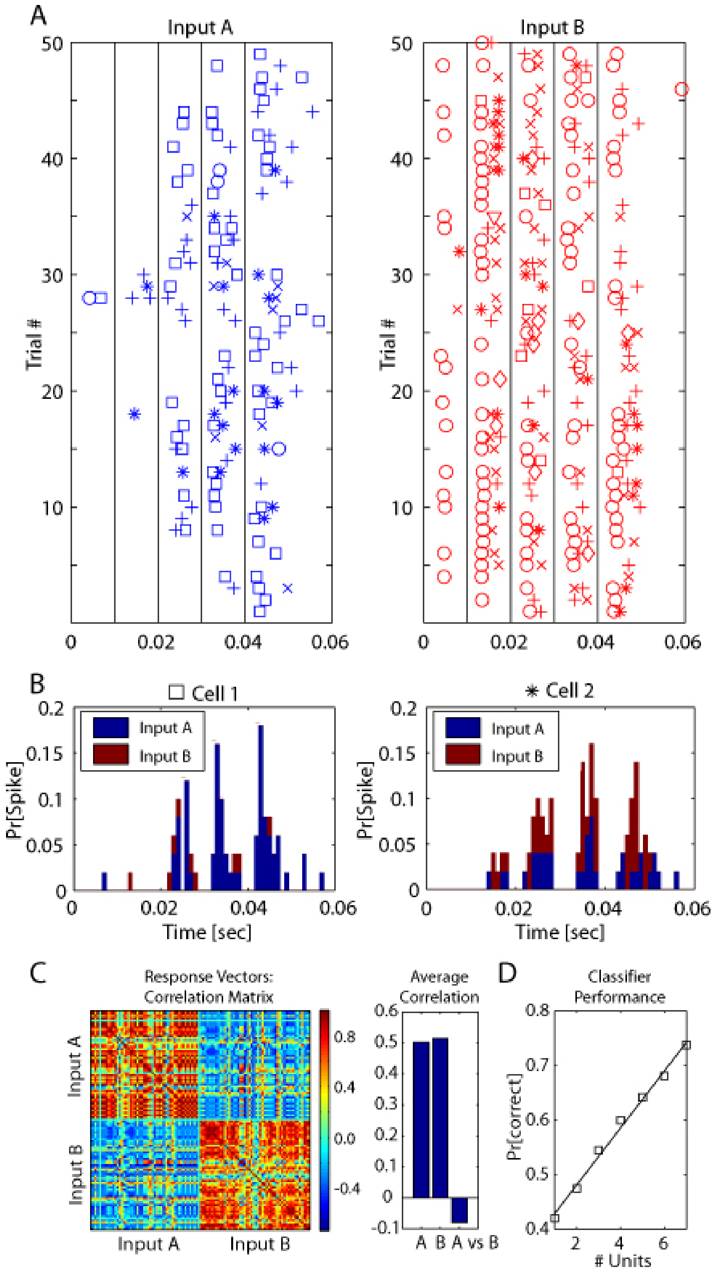

Figure 4-6 *Input discrimination ability of a small population of neurons in hippocampus CA1.* (A) Spike rastergram for two independent inputs A and B (blue and red, respectively). Symbols represent units. (B) Spike response histograms of two sample units. Response to Input A and B are shown in blue and red, respectively. (C) Left: Correlation matrix for all response vectors. Right: Average correlation for [Input A, Input A], [Input B, Input B], and [Input A, Input B] response-vector pairs. (D) Average performance of linear classifier as a function of number of neurons considered. Classifier performance linearly increased with the number of neurons included.

To quantify the ability of the monitored population of neurons to discriminate between the two inputs, we determined the response vectors for each trial for both inputs. These response vectors had as many entries as units found by spike sorting. Each entry in a response vector consisted of the number of spikes of a given unit on a given trial. In order to quantify how strongly and robustly the postsynaptic network of CA1 cells discriminated between the two inputs, we computed the correlation of response-vector pairs. We expected that pairs of response vectors for the same input were stronger correlated than pairs of response vectors from two different inputs. For presentation purposes, we reordered all trials such that trials for inputs A and B formed two neighboring contiguous blocks and plotted the correlation of all possible response-vector pairs (Fig. 4-6C, color-coded correlation matrix). In agreement with our hypothesis, the average correlation of all response vectors pairs from the same inputs equaled 0.505 (Input A) and 0.510 (Input B) respectively, whereas the average correlation for pairs of vectors from two different inputs equaled -0.07. This finding shows that pooling the response from a small population of cells may be beneficial for decoding inputs. To more directly test the ability to correctly decode which input was activated for a given response vector, we built a linear classifier (support vector machine). Indeed, we found that classification performance of all non-zero response vectors linearly increased with the number of neurons included. In conclusion, this experiment illustrates how our method can be used to study functional properties of circuits *in vitro*.

DISCUSSION

We have here introduced a technique which is aimed at empowering the study of network dynamics *in vitro*. By adapting and combining extracellular recording strategies, we found a way to combine extracellular recordings with whole-cell patch-clamp measurements. Importantly, we avoided the use of a cost intensive commercial multi-electrode array solution. To our knowledge, we are the first to describe a simple and feasible method for reliable extracellular recordings of both spontaneous and evoked activity with single-unit resolution in acute cortical slices.

Extracellular single unit recordings in acute cortical slices may provide the basis for advances in two key fields of neurophysiology. First, the ease with which extracellular recordings of spontaneous activity can be combined with whole-cell patch-clamp recordings enables the efficient collection of comprehensive data sets for the development and evaluation of spike sorting algorithms. Recent progress in method developments in this field [e.g. (Schmitzer-Torbert et al., 2005)] have heavily relied on a single data set of combined intracellular and extracellular recordings *in vivo* (Harris et al., 2000). Additional data sets, possibly from different brain regions, may thus be crucial for further developments. Second, small neural circuits represent an important spatial scale for the study of functional dynamics. Single-unit resolution extracellular recordings from neural populations appear to well serve the purpose of studying neural circuits. Our first results indicate that both spontaneous and evoked spiking activity reveal interesting network properties when probed with extracellular recordings.

As any technique, the method described here has some limitations. First, by the nature of extracellular recordings, where essentially every spike from any neuron within a certain neighborhood of the electrode is recorded, only sparse activation levels can be monitored with single-unit resolution. This limitation is of particular relevance in the case of recording action potentials with monosynaptic latencies after extracellular stimulation of afferent fibers. The experiments shown in Figures 3-5 and 3-6 had to be based on very low stimulation intensities to avoid synchronous action potential firing in the postsynaptic population. Practically spoken, only a narrow window of stimulation amplitudes provided recordings from which we were able to extract single-unit activity. In our hands, this precluded us from varying the stimulation amplitude to study the response behavior of the CA1 network as a function of number of afferent fibers activated. Yet, our stimulation amplitude regime is most likely more physiological than the strong stimulation amplitudes commonly used when recording synaptic currents *in vitro*. Second, wile the described methods were robust in our hands, we noted that not all metal microelectrodes used *in vivo* do actually work *in vitro*. Most likely, this can be explained by the fact that the submerged acute slice preparation imposes more severe challenges for extracellular recordings than brain tissue *in vivo* due to the higher conductivity of the environment around the electrodes.

In summary, we introduced a method which can be used to monitor the spiking of a population of neurons in acute cortical slices *in vitro*. By combining technology used for *in vivo* and *in vitro* culture experiments, we built a set-up with which we were able to record both spontaneous and evoked action potentials from a population of neurons with high temporal resolution. We described sample experiments which illustrate the potential of extracellular recordings combined with stimulation of afferent fibers to probe the input-output transformation mediated by cortical circuits in slice. From our viewpoint, key advantage of this method is that it can be easily integrated in a standard whole-cell patch clamp rig for acute slice experiments. This provides the opportunity to address questions which truly integrate single cell behavior with network level dynamics recorded with single-unit and high temporal resolution.

5 REFERENCES

Amiry-Moghaddam M, Ottersen OP. The molecular basis of water transport in the brain. Nat Rev Neurosci, 2003; 4: 991-1001.

Amiry-Moghaddam M, Williamson A, Palomba M, Eid T, de Lanerolle NC, Nagelhus EA, Adams ME, Froehner SC, Agre P, Ottersen OP. Delayed K+ clearance associated with aquaporin-4 mislocalization: phenotypic defects in brains of alpha-syntrophin-null mice. Proc Natl Acad Sci U S A, 2003; 100: 13615-20.

Amzica F, Massimini M, Manfridi A. Spatial buffering during slow and paroxysmal sleep oscillations in cortical networks of glial cells in vivo. J Neurosci, 2002; 22: 1042-53.

Amzica F, Steriade M. Neuronal and glial membrane potentials during sleep and paroxysmal oscillations in the neocortex. J Neurosci, 2000; 20: 6648-65.

Ballanyi K, Grafe P, ten Bruggencate G. Ion activities and potassium uptake mechanisms of glial cells in guinea-pig olfactory cortex slices. J Physiol, 1987; 382: 159-74.

Bartho P, Hirase H, Monconduit L, Zugaro M, Harris KD, Buzsaki G. Characterization of neocortical principal cells and interneurons by network interactions and extracellular features. J Neurophysiol, 2004; 92: 600-8.

Bauer G, Pieber R. Ueber periodische Komplexe im EEG. Z. EEG-EMG, 1974; 5: 75-86.

Bazhenov M, Houweling AR, Timofeev I, Sejnowski TJ. Homeostatic plasticity and post-traumatic epileptogenesis. In Soltesz I, Staley KJ, editors. Computational Neuroscience in Epilepsy. Academic Press, 2007.

Bazhenov M, Timofeev I, Steriade M, Sejnowski TJ. Model of thalamocortical slow-wave sleep oscillations and transitions to activated states. J Neurosci, 2002; 22: 8691-704.

Bazhenov M, Timofeev I, Steriade M, Sejnowski TJ. Potassium model for slow (2-3 Hz) in vivo neocortical paroxysmal oscillations. J Neurophysiol, 2004; 92: 1116-32.

Binder DK, Steinhauser C. Functional changes in astroglial cells in epilepsy. Glia, 2006; 54: 358-68.

Binder DK, Yao X, Verkman AS, Manley GT. Increased seizure duration in mice lacking aquaporin-4 water channels. Acta Neurochir Suppl, 2006; 96: 389-92.

Brenner RP, Schaul N. Periodic EEG patterns: classification, clinical correlation, and pathophysiology. J Clin Neurophysiol, 1990; 7: 249-67.

Butt AM, Kalsi A. Inwardly rectifying potassium channels (Kir) in central nervous system glia: a special role for Kir4.1 in glial functions. J Cell Mol Med, 2006; 10: 33-44.

Buzsaki G. Large-scale recording of neuronal ensembles. Nat Neurosci, 2004; 7: 446-51.

Buzsaki G, Draguhn A. Neuronal oscillations in cortical networks. Science, 2004; 304: 1926-9.

Chagnac-Amitai Y, Connors BW. Horizontal spread of synchronized activity in neocortex and its control by GABA-mediated inhibition. J Neurophysiol, 1989a; 61: 747-58.

Chagnac-Amitai Y, Connors BW. Synchronized excitation and inhibition driven by intrinsically bursting neurons in neocortex. J Neurophysiol, 1989b; 62: 1149-62.

Chong DJ, Hirsch LJ. Which EEG patterns warrant treatment in the critically ill? Reviewing the evidence for treatment of periodic epileptiform discharges and related patterns. J Clin Neurophysiol, 2005; 22: 79-91.

Cohen I, Miles R. Contributions of intrinsic and synaptic activities to the generation of neuronal discharges in in vitro hippocampus. J Physiol, 2000; 524 Pt 2: 485-502.

Cohen I, Navarro V, Clemenceau S, Baulac M, Miles R. On the origin of interictal activity in human temporal lobe epilepsy in vitro. Science, 2002; 298: 1418-21.

Compte A, Sanchez-Vives MV, McCormick DA, Wang XJ. Cellular and network mechanisms of slow oscillatory activity (<1 Hz) and wave propagations in a cortical network model. J Neurophysiol, 2003; 89: 2707-25.

Connors B, Dray A, Fox P, Hilmy M, Somjen G. LSD's effect on neuron populations in visual cortex gauged by transient responses of extracellular potassium evoked by optical stimuli. Neurosci Lett, 1979; 13: 147-50.

Connors BW, Gutnick MJ. Intrinsic firing patterns of diverse neocortical neurons. Trends Neurosci, 1990; 13: 99-104.

Contreras D, Destexhe A, Sejnowski TJ, Steriade M. Spatiotemporal patterns of spindle oscillations in cortex and thalamus. J Neurosci, 1997a; 17: 1179-96.

Contreras D, Destexhe A, Steriade M. Spindle oscillations during cortical spreading depression in naturally sleeping cats. Neuroscience, 1997b; 77: 933-6.

Coull JA, Boudreau D, Bachand K, Prescott SA, Nault F, Sik A, De Koninck P, De Koninck Y. Trans-synaptic shift in anion gradient in spinal lamina I neurons as a mechanism of neuropathic pain. Nature, 2003; 424: 938-42.

D'Ambrosio R, Gordon DS, Winn HR. Differential role of KIR channel and Na(+)/K(+)-pump in the regulation of extracellular K(+) in rat hippocampus. J Neurophysiol, 2002; 87: 87-102.

D'Ambrosio R, Maris DO, Grady MS, Winn HR, Janigro D. Impaired K(+) homeostasis and altered electrophysiological properties of post-traumatic hippocampal glia. J Neurosci, 1999; 19: 8152-62.

D'Ambrosio R, Perucca E. Epilepsy after head injury. Curr Opin Neurol, 2004; 17: 731-5.

Davenport CJ, Brown WJ, Babb TL. Sprouting of GABAergic and mossy fiber axons in dentate gyrus following intrahippocampal kainate in the rat. Exp Neurol, 1990; 109: 180-90.

DeFazio RA, Keros S, Quick MW, Hablitz JJ. Potassium-coupled chloride cotransport controls intracellular chloride in rat neocortical pyramidal neurons. J Neurosci, 2000; 20: 8069-76.

Desai NS. Homeostatic plasticity in the CNS: synaptic and intrinsic forms. J Physiol Paris, 2003; 97: 391-402.

Destexhe A, Contreras D, Steriade M. Mechanisms underlying the synchronizing action of corticothalamic feedback through inhibition of thalamic relay cells. J Neurophysiol, 1998; 79: 999-1016.

Destexhe A, Mainen ZF, Sejnowski TJ. Synthesis of models for excitable membranes, synaptic transmission and neuromodulation using a common kinetic formalism. J Comput Neurosci, 1994; 1: 195-230.

Dhooge A, Govaerts W, Kuznetsov YA. MATCONT: A MATLAB package for numerical bifurcation analysis of ODEs ACM Trans. Math. Softw. , 2003; 29: 141-64.

Dichter MA, Ayala GF. Cellular mechanisms of epilepsy: a status report. Science, 1987; 237: 157-64.

Dietzel I, Heinemann U, Lux HD. Relations between slow extracellular potential changes, glial potassium buffering, and electrolyte and cellular volume changes during neuronal hyperactivity in cat brain. Glia, 1989; 2: 25-44.

Dominguez M, Becker S, Bruce I, Read H. A spiking neuron model of cortical correlates of sensorineural hearing loss: Spontaneous firing, synchrony, and tinnitus. Neural Comput, 2006; 18: 2942-58.

Duncan JS, Sander JW, Sisodiya SM, Walker MC. Adult epilepsy. Lancet, 2006; 367: 1087-100.

Durstewitz D, Seamans JK, Sejnowski TJ. Neurocomputational models of working memory. Nat Neurosci, 2000; 3 Suppl: 1184-91.

Echegoyen J, Neu A, Graber KD, Soltesz I. Homeostatic plasticity studied using in vivo hippocampal activity-blockade: synaptic scaling, intrinsic plasticity and age-dependence. PLoS ONE, 2007; 2: e700.

Echlin FA, Battista A. Epileptiform Seizures from Chronic Isolated Cortex. Arch Neurol, 1963; 9: 154-70.

Egert U, Heck D, Aertsen A. Two-dimensional monitoring of spiking networks in acute brain slices. Exp Brain Res, 2002; 142: 268-74.

Engel J, Jr., Wilson C, Bragin A. Advances in understanding the process of epileptogenesis based on patient material: what can the patient tell us? Epilepsia, 2003; 44 Suppl 12: 60-71.

Ermentrout B. Type I membranes, phase resetting curves, and synchrony. Neural Comput, 1996; 8: 979-1001.

Esclapez M, Hirsch JC, Khazipov R, Ben-Ari Y, Bernard C. Operative GABAergic inhibition in hippocampal CA1 pyramidal neurons in experimental epilepsy. Proc Natl Acad Sci U S A, 1997; 94: 12151-6.

Fee MS, Mitra PP, Kleinfeld D. Automatic sorting of multiple unit neuronal signals in the presence of anisotropic and non-Gaussian variability. J Neurosci Methods, 1996; 69: 175-88.

Fertziger AP, Ranck JB, Jr. Potassium accumulation in interstitial space during epileptiform seizures. Exp Neurol, 1970; 26: 571-85.

Fisch BJ. Fisch and Spehlmann's EEG primer: basic principles of digital and analog EGG. Elsevier: Amsterdam, 1999.

Fisher RS, Pedley TA, Prince DA. Kinetics of potassium movement in norman cortex. Brain Res, 1976; 101: 223-37.

Frohlich F, Bazhenov M. Coexistence of tonic firing and bursting in cortical neurons. Phys Rev E Stat Nonlin Soft Matter Phys, 2006; 74: 031922.

Frohlich F, Bazhenov M, Timofeev I, Sejnoski T. Maintenance and Termination of Neocortical Oscillations by Dynamic Modulation of Intrinsic and Synaptic Excitability. Thalamus and Related Systems, 2007a; 3.

Frohlich F, Bazhenov M, Timofeev I, Steriade M, Sejnowski TJ. Slow state transitions of sustained neural oscillations by activity-dependent modulation of intrinsic excitability. J Neurosci, 2006; 26: 6153-62.

Frohlich F, Timofeev I, Sejnowski T, Bazhenov M. Extracellular potassium dynamics and epileptogenesis. In Soltesz I, Staley KJ, editors. Computational Neuroscience in Epilepsy. Elsevier, 2007b.

Gabriel S, Eilers A, Kivi A, Kovacs R, Schulze K, Lehmann TN, Heinemann U. Effects of barium on stimulus induced changes in extracellular potassium concentration in area CA1 of hippocampal slices from normal and pilocarpine-treated epileptic rats. Neurosci Lett, 1998; 242: 9-12.

Gadsby DC, Cranefield PF. Two levels of resting potential in cardiac Purkinje fibers. J Gen Physiol, 1977; 70: 725-46.

Galarreta M, Hestrin S. Frequency-dependent synaptic depression and the balance of excitation and inhibition in the neocortex. Nat Neurosci, 1998; 1: 587-94.

Gardner-Medwin AR. Analysis of potassium dynamics in mammalian brain tissue. J Physiol, 1983; 335: 393-426.

Garga N, Lowenstein DH. Posttraumatic epilepsy: a major problem in desperate need of major advances. Epilepsy Curr, 2006; 6: 1-5.

Gil Z, Connors BW, Amitai Y. Differential regulation of neocortical synapses by neuromodulators and activity. Neuron, 1997; 19: 679-86.

Glickfeld LL, Scanziani M. Distinct timing in the activity of cannabinoid-sensitive and cannabinoid-insensitive basket cells. Nat Neurosci, 2006; 9: 807-15.

Gold C, Henze DA, Koch C, Buzsaki G. On the origin of the extracellular action potential waveform: A modeling study. J Neurophysiol, 2006; 95: 3113-28.

Gray CM, Konig P, Engel AK, Singer W. Oscillatory responses in cat visual cortex exhibit inter-columnar synchronization which reflects global stimulus properties. Nature, 1989; 338: 334-7.

Green JD. The Hippocampus. Physiol Rev, 1964; 44: 561-608.

Grisar T, Guillaume D, Delgado-Escueta AV. Contribution of Na+,K(+)-ATPase to focal epilepsy: a brief review. Epilepsy Res, 1992; 12: 141-9.

Gurer G, Yemisci M, Saygi S, Ciger A. Structural lesions in periodic lateralized epileptiform discharges (PLEDs). Clin EEG Neurosci, 2004; 35: 88-93.

Gutnick MJ, Connors BW, Prince DA. Mechanisms of neocortical epileptogenesis in vitro. J Neurophysiol, 1982; 48: 1321-35.

Guzowski JF, Knierim JJ, Moser EI. Ensemble dynamics of hippocampal regions CA3 and CA1. Neuron, 2004; 44: 581-4.

Hablitz JJ, Lundervold A. Hippocampal excitability and changes in extracellular potassium. Exp Neurol, 1981; 71: 410-20.

Hahn PJ, Durand DM. Bistability dynamics in simulations of neural activity in high-extracellular-potassium conditions. J Comput Neurosci, 2001; 11: 5-18.

Harris KD, Henze DA, Csicsvari J, Hirase H, Buzsaki G. Accuracy of tetrode spike separation as determined by simultaneous intracellular and extracellular measurements. J Neurophysiol, 2000; 84: 401-14.

Heinemann U, Dietzel I. Extracellular potassium concentration in chronic alumina cream foci of cats. J Neurophysiol, 1984; 52: 421-34.

Heinemann U, Lux HD. Ceiling of stimulus induced rises in extracellular potassium concentration in the cerebral cortex of cat. Brain Res, 1977; 120: 231-49.

Heinemann U, Lux HD. Undershoots following stimulus-induced rises of extracellular potassium concentration in cerebral cortex of cat. Brain Res, 1975; 93: 63-76.

Heinemann U, Lux HD, Gutnick MJ. Extracellular free calcium and potassium during paroxsmal activity in the cerebral cortex of the cat. Exp Brain Res, 1977; 27: 237-43.

Hempel CM, Sugino K, Nelson SB. Multi-unit spike-triggered averaging: a method for probing the physiology of central synapses. J Neurosci Methods, 2002; 120: 121-9.

Henze DA, Borhegyi Z, Csicsvari J, Mamiya A, Harris KD, Buzsaki G. Intracellular features predicted by extracellular recordings in the hippocampus in vivo. J Neurophysiol, 2000; 84: 390-400.

Henze DA, Wittner L, Buzsaki G. Single granule cells reliably discharge targets in the hippocampal CA3 network in vivo. Nat Neurosci, 2002; 5: 790-5.

Heuschkel MO, Fejtl M, Raggenbass M, Bertrand D, Renaud P. A three-dimensional multi-electrode array for multi-site stimulation and recording in acute brain slices. J Neurosci Methods, 2002; 114: 135-48.

Higashima M. Inhibitory processes in development of seizure activity in hippocampal slices. Exp Brain Res, 1988; 72: 37-44.

Hille B. Ion channels of excitable membranes, 3rd ed. Sinauer: Sunderland, Mass., 2001.

Hinterkeuser S, Schroder W, Hager G, Seifert G, Blumcke I, Elger CE, Schramm J, Steinhauser C. Astrocytes in the hippocampus of patients with temporal lobe epilepsy display changes in potassium conductances. Eur J Neurosci, 2000; 12: 2087-96.

Hirsch LJ, Brenner RP, Drislane FW, So E, Kaplan PW, Jordan KG, Herman ST, LaRoche SM, Young B, Bleck TP, Scheuer ML, Emerson RG. The ACNS subcommittee on research terminology for continuous EEG monitoring: proposed standardized terminology for rhythmic and periodic EEG patterns encountered in critically ill patients. J Clin Neurophysiol, 2005; 22: 128-35.

Hodgkin AL, Huxley AF. A quantitative description of membrane current and its application to conduction and excitation in nerve. J Physiol, 1952; 117: 500-44.

Hoffman SN, Salin PA, Prince DA. Chronic neocortical epileptogenesis in vitro. J Neurophysiol, 1994; 71: 1762-73.

Hopfield JJ. Neural networks and physical systems with emergent collective computational abilities. Proc Natl Acad Sci U S A, 1982; 79: 2554-8.

Houweling AR, Bazhenov M, Timofeev I, Steriade M, Sejnowski TJ. Homeostatic synaptic plasticity can explain post-traumatic epileptogenesis in chronically isolated neocortex. Cereb Cortex, 2005; 15: 834-45.

Houweling AR, Bazhenov M, Timofeev I, Steriade M, Sejnowski TJ. Homeostatic Synaptic Plasticity Can Explain Post-traumatic Epileptogenesis in Chronically Isolated Neocortex. Cereb Cortex, 2004.

Hubel D. Tungsten Microelectrode for Recording from Single Units. Science, 1957; 125: 549-50.

Huberfeld G, Wittner L, Clemenceau S, Baulac M, Kaila K, Miles R, Rivera C. Perturbed chloride homeostasis and GABAergic signaling in human temporal lobe epilepsy. J Neurosci, 2007; 27: 9866-73.

Illis LS, Taylor FM. The electroencephalogram in herpes-simplex encephalitis. Lancet, 1972; 1: 718-21.

Ivens S, Kaufer D, Flores LP, Bechmann I, Zumsteg D, Tomkins O, Seiffert E, Heinemann U, Friedman A. TGF-beta receptor-mediated albumin uptake into astrocytes is involved in neocortical epileptogenesis. Brain, 2007; 130: 535-47.

Izhikevich EM. Dynamical systems in neuroscience : the geometry of excitability and bursting. MIT Press: Cambridge, MA, 2007.

Jahnsen H, Llinas R. Electrophysiological properties of guinea-pig thalamic neurones: an in vitro study. J Physiol, 1984a; 349: 205-26.

Jahnsen H, Llinas R. Voltage-dependent burst-to-tonic switching of thalamic cell activity: an in vitro study. Arch Ital Biol, 1984b; 122: 73-82.

Jansen LA, Uhlmann EJ, Crino PB, Gutmann DH, Wong M. Epileptogenesis and reduced inward rectifier potassium current in tuberous sclerosis complex-1-deficient astrocytes. Epilepsia, 2005; 46: 1871-80.

Jarolimek W, Lewen A, Misgeld U. A furosemide-sensitive K+-Cl- cotransporter counteracts intracellular Cl- accumulation and depletion in cultured rat midbrain neurons. J Neurosci, 1999; 19: 4695-704.

Jauch R, Windmuller O, Lehmann TN, Heinemann U, Gabriel S. Effects of barium, furosemide, ouabaine and 4,4'-diisothiocyanatostilbene-2,2'-disulfonic acid (DIDS) on ionophoretically-induced changes in extracellular potassium concentration in hippocampal slices from rats and from patients with epilepsy. Brain Res, 2002; 925: 18-27.

Jensen MS, Azouz R, Yaari Y. Variant firing patterns in rat hippocampal pyramidal cells modulated by extracellular potassium. J Neurophysiol, 1994; 71: 831-9.

Jensen MS, Cherubini E, Yaari Y. Opponent effects of potassium on GABAA-mediated postsynaptic inhibition in the rat hippocampus. J Neurophysiol, 1993; 69: 764-71.

Jensen MS, Yaari Y. Role of intrinsic burst firing, potassium accumulation, and electrical coupling in the elevated potassium model of hippocampal epilepsy. J Neurophysiol, 1997; 77: 1224-33.

Jin X, Huguenard JR, Prince DA. Impaired Cl- extrusion in layer V pyramidal neurons of chronically injured epileptogenic neocortex. J Neurophysiol, 2005; 93: 2117-26.

Jin X, Prince DA, Huguenard JR. Enhanced excitatory synaptic connectivity in layer v pyramidal neurons of chronically injured epileptogenic neocortex in rats. J Neurosci, 2006; 26: 4891-900.

Jirsch J, Hirsch LJ. Nonconvulsive seizures: Developing a rational approach to the diagnosis and management in the critically ill population. Clin Neurophysiol, 2007.

Jones CKRT. Geometric Singular Perturbation Theory. C.I.M.E. Lectures: Montecatini Terme, 1994.

Kager H, Wadman WJ, Somjen GG. Conditions for the triggering of spreading depression studied with computer simulations. J Neurophysiol, 2002; 88: 2700-12.

Kager H, Wadman WJ, Somjen GG. Simulated seizures and spreading depression in a neuron model incorporating interstitial space and ion concentrations. J Neurophysiol, 2000; 84: 495-512.

Kaila K, Lamsa K, Smirnov S, Taira T, Voipio J. Long-lasting GABA-mediated depolarization evoked by high-frequency stimulation in pyramidal neurons of rat hippocampal slice is attributable to a network-driven, bicarbonate-dependent K+ transient. J Neurosci, 1997; 17: 7662-72.

Kalamangalam GP, Diehl B, Burgess RC. Neuroimaging and Neurophysiology of Periodic Lateralized Epileptiform Discharges: Observations and Hypotheses. Epilepsia, 2007.

Kilman V, van Rossum MC, Turrigiano GG. Activity deprivation reduces miniature IPSC amplitude by decreasing the number of postsynaptic GABA(A) receptors clustered at neocortical synapses. J Neurosci, 2002; 22: 1328-37.

Kivi A, Lehmann TN, Kovacs R, Eilers A, Jauch R, Meencke HJ, von Deimling A, Heinemann U, Gabriel S. Effects of barium on stimulus-induced rises of [K+]o in human epileptic non-sclerotic and sclerotic hippocampal area CA1. Eur J Neurosci, 2000; 12: 2039-48.

Kleinfeld D, Raccuia-Behling F, Chiel HJ. Circuits constructed from identified Aplysia neurons exhibit multiple patterns of persistent activity. Biophys J, 1990; 57: 697-715.

Kocsis JD, Malenka RC, Waxman SG. Effects of extracellular potassium concentration on the excitability of the parallel fibres of the rat cerebellum. J Physiol, 1983; 334: 225-44.

Kofuji P, Newman EA. Potassium buffering in the central nervous system. Neuroscience, 2004; 129: 1045-56.

Konnerth A, Heinemann U, Yaari Y. Nonsynaptic epileptogenesis in the mammalian hippocampus in vitro. I. Development of seizurelike activity in low extracellular calcium. J Neurophysiol, 1986; 56: 409-23.

Korn SJ, Giacchino JL, Chamberlin NL, Dingledine R. Epileptiform burst activity induced by potassium in the hippocampus and its regulation by GABA-mediated inhibition. J Neurophysiol, 1987; 57: 325-40.

Kuffler SW, Nicholls JG, Orkand RK. Physiological properties of glial cells in the central nervous system of amphibia. J Neurophysiol, 1966; 29: 768-87.

Kuramoto T, Haber B. The K+ liquid ion exchange electrode system: responses to drugs and neurotransmitters. J Neurosci Res, 1981; 6: 37-48.

Kuroiwa Y, Celesia GG. Clinical significance of periodic EEG patterns. Arch Neurol, 1980; 37: 15-20.

Kuznetsov YA. Elements of Applied Bifurcation Theory, Third ed. Springer: New York, 2004.

Lazar A, Pipa G, Triesch J. Fading memory and time series prediction in recurrent networks with different forms of plasticity. Neural Netw, 2007; 20: 312-22.

LeBeau FE, Towers SK, Traub RD, Whittington MA, Buhl EH. Fast network oscillations induced by potassium transients in the rat hippocampus in vitro. J Physiol, 2002; 542: 167-79.

Lebovitz RM. Quantitative examination of dynamic interneuronal coupling via single-spike extracellular potassium ion transients. J Theor Biol, 1996; 180: 11-25.

Lechner HA, Baxter DA, Clark JW, Byrne JH. Bistability and its regulation by serotonin in the endogenously bursting neuron R15 in Aplysia. J Neurophysiol, 1996; 75: 957-62.

Leschinger A, Stabel J, Igelmund P, Heinemann U. Pharmacological and electrographic properties of epileptiform activity induced by elevated K+ and lowered Ca2+ and Mg2+ concentration in rat hippocampal slices. Exp Brain Res, 1993; 96: 230-40.

Leutgeb JK, Leutgeb S, Moser MB, Moser EI. Pattern separation in the dentate gyrus and CA3 of the hippocampus. Science, 2007; 315: 961-6.

Leutgeb JK, Leutgeb S, Treves A, Meyer R, Barnes CA, McNaughton BL, Moser MB, Moser EI. Progressive transformation of hippocampal neuronal representations in "morphed" environments. Neuron, 2005; 48: 345-58.

Li H, Bandrowski AE, Prince DA. Cortical injury affects short-term plasticity of evoked excitatory synaptic currents. J Neurophysiol, 2005; 93: 146-56.

Li H, Prince DA. Synaptic activity in chronically injured, epileptogenic sensory-motor neocortex. J Neurophysiol, 2002; 88: 2-12.

Lian J, Bikson M, Shuai J, Durand DM. Propagation of non-synaptic epileptiform activity across a lesion in rat hippocampal slices. J Physiol, 2001; 537: 191-9.

Lux HD, Neher E. The equilibration time course of (K +) 0 in cat cortex. Exp Brain Res, 1973; 17: 190-205.

Mainen ZF, Sejnowski TJ. Influence of dendritic structure on firing pattern in model neocortical neurons. Nature, 1996; 382: 363-6.

Malenka RC, Kocsis JD, Ransom BR, Waxman SG. Modulation of parallel fiber excitability by postsynaptically mediated changes in extracellular potassium. Science, 1981; 214: 339-41.

Manor Y, Nadim F. Synaptic depression mediates bistability in neuronal networks with recurrent inhibitory connectivity. J Neurosci, 2001; 21: 9460-70.

Maquet P. The role of sleep in learning and memory. Science, 2001; 294: 1048-52.

Markand ON. Lennox-Gastaut syndrome (childhood epileptic encephalopathy). J Clin Neurophysiol, 2003; 20: 426-41.

Markram H, Pikus D, Gupta A, Tsodyks M. Potential for multiple mechanisms, phenomena and algorithms for synaptic plasticity at single synapses. Neuropharmacology, 1998; 37: 489-500.

Matsumoto H, Ajmonemarsan C. Cellular Mechanisms in Experimental Epileptic Seizures. Science, 1964; 144: 193-4.

Mazor O, Laurent G. Transient dynamics versus fixed points in odor representations by locust antennal lobe projection neurons. Neuron, 2005; 48: 661-73.

McBain CJ. Hippocampal inhibitory neuron activity in the elevated potassium model of epilepsy. J Neurophysiol, 1994; 72: 2853-63.

McCormick DA. Neurotransmitter actions in the thalamus and cerebral cortex and their role in neuromodulation of thalamocortical activity. Prog Neurobiol, 1992; 39: 337-88.

McCormick DA, Connors BW, Lighthall JW, Prince DA. Comparative electrophysiology of pyramidal and sparsely spiny stellate neurons of the neocortex. J Neurophysiol, 1985; 54: 782-806.

McCullough JR, Chua WT, Rasmussen HH, Ten Eick RE, Singer DH. Two stable levels of diastolic potential at physiological K+ concentrations in human ventricular myocardial cells. Circ Res, 1990; 66: 191-201.

McNamara JO. Cellular and molecular basis of epilepsy. J Neurosci, 1994; 14: 3413-25.

McNaughton BL, O'Keefe J, Barnes CA. The stereotrode: a new technique for simultaneous isolation of several single units in the central nervous system from multiple unit records. J Neurosci Methods, 1983; 8: 391-7.

Meeks JP, Mennerick S. Selective effects of potassium elevations on glutamate signaling and action potential conduction in hippocampus. J Neurosci, 2004; 24: 197-206.

Mehta AD, Ulbert I, Schroeder CE. Intermodal selective attention in monkeys. I: distribution and timing of effects across visual areas. Cereb Cortex, 2000; 10: 343-58.

Mody I. Aspects of the homeostaic plasticity of GABAA receptor-mediated inhibition. J Physiol, 2005; 562: 37-46.

Moody WJ, Futamachi KJ, Prince DA. Extracellular potassium activity during epileptogenesis. Exp Neurol, 1974; 42: 248-63.

Munoz A, Mendez P, DeFelipe J, Alvarez-Leefmans FJ. Cation-chloride cotransporters and GABA-ergic innervation in the human epileptic hippocampus. Epilepsia, 2007; 48: 663-73.

Murakami M, Kashiwadani H, Kirino Y, Mori K. State-dependent sensory gating in olfactory cortex. Neuron, 2005; 46: 285-96.

Neckelmann D, Amzica F, Steriade M. Spike-wave complexes and fast components of cortically generated seizures. III. Synchronizing mechanisms. J Neurophysiol, 1998; 80: 1480-94.

Neher E, Lux HD. Rapid changes of potassium concentration at the outer surface of exposed single neurons during membrane current flow. J Gen Physiol, 1973; 61: 385-99.

Nelson SB, Turrigiano GG. Synaptic depression: a key player in the cortical balancing act. Nat Neurosci, 1998; 1: 539-41.

Nicholson C, Chen KC, Hrabetova S, Tao L. Diffusion of molecules in brain extracellular space: theory and experiment. Prog Brain Res, 2000; 125: 129-54.

Niedermeyer E. Abnormal EEG Patters: Epileptic and Paroxysmal. In Niedermeyer E, Lopes da Silva F, editors. Electroencephalography: basic principles, clinical applications, and related fields. Lippincott Williams & Wilkins: Philadelphia, 2005: 255-80.

Niedermeyer E. Lennox-Gastaut syndrome. Clinical description and diagnosis. Adv Exp Med Biol, 2002; 497: 61-75.

Niermann H, Amiry-Moghaddam M, Holthoff K, Witte OW, Ottersen OP. A novel role of vasopressin in the brain: modulation of activity-dependent water flux in the neocortex. J Neurosci, 2001; 21: 3045-51.

Nita DA, Cisse Y, Timofeev I, Steriade M. Increased propensity to seizures after chronic cortical deafferentation in vivo. J Neurophysiol, 2006; 95: 902-13.

Nita DA, Cisse Y, Timofeev I, Steriade M. Waking-sleep modulation of paroxysmal activities induced by partial cortical deafferentation. Cereb Cortex, 2007; 17: 272-83.

Nita DA, Steriade M, Amzica F. Hyperpolarisation rectification in cat lateral geniculate neurons modulated by intact corticothalamic projections. J Physiol, 2003; 552: 325-32.

Odette LL, Newman EA. Model of potassium dynamics in the central nervous system. Glia, 1988; 1: 198-210.

Orkand RK, Nicholls JG, Kuffler SW. Effect of nerve impulses on the membrane potential of glial cells in the central nervous system of amphibia. J Neurophysiol, 1966; 29: 788-806.

Osinga HM, England JP. Separating manifolds in slow-fast systems. ENOC-2005: Eindhoven, Netherlands, 2005.

Padmawar P, Yao X, Bloch O, Manley GT, Verkman AS. K+ waves in brain cortex visualized using a long-wavelength K+-sensing fluorescent indicator. Nat Methods, 2005; 2: 825-7.

Palma E, Amici M, Sobrero F, Spinelli G, Di Angelantonio S, Ragozzino D, Mascia A, Scoppetta C, Esposito V, Miledi R, Eusebi F. Anomalous levels of Cl- transporters in the hippocampal subiculum from temporal lobe epilepsy patients make GABA excitatory. Proc Natl Acad Sci U S A, 2006; 103: 8465-8.

Pan E, Stringer JL. Role of potassium and calcium in the generation of cellular bursts in the dentate gyrus. J Neurophysiol, 1997; 77: 2293-9.

Park EH, Durand DM. Role of potassium lateral diffusion in non-synaptic epilepsy: a computational study. J Theor Biol, 2006; 238: 666-82.

Payne JA. Functional characterization of the neuronal-specific K-Cl cotransporter: implications for [K+]o regulation. Am J Physiol, 1997; 273: C1516-25.

Payne JA, Rivera C, Voipio J, Kaila K. Cation-chloride co-transporters in neuronal communication, development and trauma. Trends Neurosci, 2003; 26: 199-206.

Perreault P, Avoli M. Effects of low concentrations of 4-aminopyridine on CA1 pyramidal cells of the hippocampus. J Neurophysiol, 1989; 61: 953-70.

Pollen DA, Trachtenberg MC. Neuroglia: gliosis and focal epilepsy. Science, 1970; 167: 1252-3.

Poolos NP, Mauk MD, Kocsis JD. Activity-evoked increases in extracellular potassium modulate presynaptic excitability in the CA1 region of the hippocampus. J Neurophysiol, 1987; 58: 404-16.

Pouille F, Scanziani M. Enforcement of temporal fidelity in pyramidal cells by somatic feed-forward inhibition. Science, 2001; 293: 1159-63.

Pouille F, Scanziani M. Routing of spike series by dynamic circuits in the hippocampus. Nature, 2004; 429: 717-23.

Prince DA. Neurophysiology of epilepsy. Annu Rev Neurosci, 1978; 1: 395-415.

Prince DA, Jacobs KM, Salin PA, Hoffman S, Parada I. Chronic focal neocortical epileptogenesis: does disinhibition play a role? Can J Physiol Pharmacol, 1997; 75: 500-7.

Prince DA, Lux HD, Neher E. Measurement of extracellular potassium activity in cat cortex. Brain Res, 1973; 50: 489-95.

Prince DA, Tseng GF. Epileptogenesis in chronically injured cortex: in vitro studies. J Neurophysiol, 1993; 69: 1276-91.

Qian N, Sejnowski TJ. When is an inhibitory synapse effective? Proc Natl Acad Sci U S A, 1990; 87: 8145-9.

Rabinowitch I, Segev I. The endurance and selectivity of spatial patterns of long-term potentiation/depression in dendrites under homeostatic synaptic plasticity. J Neurosci, 2006a; 26: 13474-84.

Rabinowitch I, Segev I. The interplay between homeostatic synaptic plasticity and functional dendritic compartments. J Neurophysiol, 2006b; 96: 276-83.

Rich MM, Wenner P. Sensing and expressing homeostatic synaptic plasticity. Trends Neurosci, 2007; 30: 119-25.

Rinzel J. Bursting oscillations in an excitable membrane model. In Sleeman BD, Jones D, editors. Ordinary and Partial Differential Equations. Springer Verlag: Berlin, 1985.

Rinzel J, Ermentrout B. Analysis of neural excitability and oscillations. In Koch C, Segev I, editors. Methods in Neuronal Modeling. MIT Press: Cambridge MA, 1989.

Rinzel J, Lee YS. Dissection of a model for neuronal parabolic bursting. J Math Biol, 1987; 25: 653-75.

Rivera C, Voipio J, Thomas-Crusells J, Li H, Emri Z, Sipila S, Payne JA, Minichiello L, Saarma M, Kaila K. Mechanism of activity-dependent downregulation of the neuron-specific K-Cl cotransporter KCC2. J Neurosci, 2004; 24: 4683-91.

Rutecki PA, Lebeda FJ, Johnston D. Epileptiform activity induced by changes in extracellular potassium in hippocampus. J Neurophysiol, 1985; 54: 1363-74.

Salin P, Tseng GF, Hoffman S, Parada I, Prince DA. Axonal sprouting in layer V pyramidal neurons of chronically injured cerebral cortex. J Neurosci, 1995; 15: 8234-45.

Sanchez-Vives MV, McCormick DA. Cellular and network mechanisms of rhythmic recurrent activity in neocortex. Nat Neurosci, 2000; 3: 1027-34.

Santhakumar V, Voipio J, Kaila K, Soltesz I. Post-traumatic hyperexcitability is not caused by impaired buffering of extracellular potassium. J Neurosci, 2003; 23: 5865-76.

Schaette R, Kempter R. Development of tinnitus-related neuronal hyperactivity through homeostatic plasticity after hearing loss: a computational model. Eur J Neurosci, 2006; 23: 3124-38.

Schmitzer-Torbert N, Jackson J, Henze D, Harris K, Redish AD. Quantitative measures of cluster quality for use in extracellular recordings. Neuroscience, 2005; 131: 1-11.

Schroder W, Hinterkeuser S, Seifert G, Schramm J, Jabs R, Wilkin GP, Steinhauser C. Functional and molecular properties of human astrocytes in acute hippocampal slices obtained from patients with temporal lobe epilepsy. Epilepsia, 2000; 41 Suppl 6: S181-4.

Sharpless SK, Halpern LM. The electrical excitability of chronically isolated cortex studied by means of permanently implanted electrodes. Electroencephalogr Clin Neurophysiol, 1962; 14: 244-55.

Sherman SM. Tonic and burst firing: dual modes of thalamocortical relay. Trends Neurosci, 2001; 24: 122-6.

Shilnikov A, Calabrese RL, Cymbalyuk G. Mechanism of bistability: tonic spiking and bursting in a neuron model. Phys Rev E Stat Nonlin Soft Matter Phys, 2005; 71: 056214.

Shilnikov A, Cymbalyuk G. Transition between tonic spiking and bursting in a neuron model via the blue-sky catastrophe. Phys Rev Lett, 2005; 94: 048101.

Shlens J, Field GD, Gauthier JL, Grivich MI, Petrusca D, Sher A, Litke AM, Chichilnisky EJ. The structure of multi-neuron firing patterns in primate retina. J Neurosci, 2006; 26: 8254-66.

Singer W, Lux HD. Extracellular potassium gradients and visual receptive fields in the cat striate cortex. Brain Res, 1975; 96: 378-83.

Skinner JE, Molnar M. Event-related extracellular potassium ion activity changes in frontal cortex of the conscious cat. J Neurophysiol, 1983; 49: 204-15.

Somjen GG. Extracellular potassium in the mammalian central nervous system. Annu Rev Physiol, 1979; 41: 159-77.

Somjen GG. Ion regulation in the brain: implications for pathophysiology. Neuroscientist, 2002; 8: 254-67.

Somjen GG. Ions in the brain : normal function, seizures, and stroke. Oxford University Press: New York, 2004.

Staley KJ, Dudek FE. Interictal spikes and epileptogenesis. Epilepsy Curr, 2006; 6: 199-202.

Staley KJ, Proctor WR. Modulation of mammalian dendritic GABA(A) receptor function by the kinetics of Cl- and HCO3- transport. J Physiol, 1999; 519 Pt 3: 693-712.

Stellwagen D, Malenka RC. Synaptic scaling mediated by glial TNF-alpha. Nature, 2006; 440: 1054-9.

Steriade M. Acetylcholine systems and rhythmic activities during the waking--sleep cycle. Prog Brain Res, 2004a; 145: 179-96.

Steriade M. The corticothalamic system in sleep. Front Biosci, 2003a; 8: d878-99.

Steriade M. Grouping of brain rhythms in corticothalamic systems. Neuroscience, 2006; 137: 1087-106.

Steriade M. Neocortical cell classes are flexible entities. Nat Rev Neurosci, 2004b; 5: 121-34.

Steriade M. Neuronal substrates of sleep and epilepsy. Cambridge University Press: Cambridge ; New York, 2003b.

Steriade M, Amzica F. Sleep oscillations developing into seizures in corticothalamic systems. Epilepsia, 2003; 44 Suppl 12: 9-20.

Steriade M, Amzica F. Slow sleep oscillation, rhythmic K-complexes, and their paroxysmal developments. J Sleep Res, 1998; 7 Suppl 1: 30-5.

Steriade M, Amzica F, Neckelmann D, Timofeev I. Spike-wave complexes and fast components of cortically generated seizures. II. Extra- and intracellular patterns. J Neurophysiol, 1998; 80: 1456-79.

Steriade M, Contreras D. Relations between cortical and thalamic cellular events during transition from sleep patterns to paroxysmal activity. J Neurosci, 1995; 15: 623-42.

Steriade M, Contreras D. Spike-wave complexes and fast components of cortically generated seizures. I. Role of neocortex and thalamus. J Neurophysiol, 1998; 80: 1439-55.

Steriade M, Domich L, Oakson G. Reticularis thalami neurons revisited: activity changes during shifts in states of vigilance. J Neurosci, 1986; 6: 68-81.

Steriade M, McCarley R. Brain control of wakefulness and sleep. Kluwer-Springer: New York, 2005.

Steriade M, McCormick DA, Sejnowski TJ. Thalamocortical oscillations in the sleeping and aroused brain. Science, 1993a; 262: 679-85.

Steriade M, Nunez A, Amzica F. Intracellular analysis of relations between the slow (< 1 Hz) neocortical oscillation and other sleep rhythms of the electroencephalogram. J Neurosci, 1993b; 13: 3266-83.

Steriade M, Timofeev I, Grenier F. Natural waking and sleep states: a view from inside neocortical neurons. J Neurophysiol, 2001; 85: 1969-85.

Stickgold R, James L, Hobson JA. Visual discrimination learning requires sleep after training. Nat Neurosci, 2000; 3: 1237-8.

Sykova E, Rothenberg S, Krekule I. Changes of extracellular potassium concentration during spontaneous activity in the mesencephalic reticular formation of the rat. Brain Res, 1974; 79: 333-7.

Sypert GW, Ward AA, Jr. Changes in extracellular potassium activity during neocortical propagated seizures. Exp Neurol, 1974; 45: 19-41.

Tasker JG, Dudek FE. Electrophysiology of GABA-mediated synaptic transmission and possible roles in epilepsy. Neurochem Res, 1991; 16: 251-62.

Thompson SM, Gahwiler BH. Activity-dependent disinhibition. II. Effects of extracellular potassium, furosemide, and membrane potential on ECl- in hippocampal CA3 neurons. J Neurophysiol, 1989; 61: 512-23.

Timofeev I, Bazhenov M, Sejnowski T, Steriade M. Cortical hyperpolarization-activated depolarizing current takes part in the generation of focal paroxysmal activities. Proc Natl Acad Sci U S A, 2002a; 99: 9533-7.

Timofeev I, Grenier F, Bazhenov M, Sejnowski TJ, Steriade M. Origin of slow cortical oscillations in deafferented cortical slabs. Cereb Cortex, 2000; 10: 1185-99.

Timofeev I, Grenier F, Steriade M. Contribution of intrinsic neuronal factors in the generation of cortically driven electrographic seizures. J Neurophysiol, 2004; 92: 1133-43.

Timofeev I, Grenier F, Steriade M. Disfacilitation and active inhibition in the neocortex during the natural sleep-wake cycle: an intracellular study. Proc Natl Acad Sci U S A, 2001a; 98: 1924-9.

Timofeev I, Grenier F, Steriade M. Disfacilitation and active inhibition in the neocortex during the natural sleep-wake cycle: an intracellular study. Proc Natl Acad Sci U S A, 2001b; 98: 1924-9.

Timofeev I, Grenier F, Steriade M. The role of chloride-dependent inhibition and the activity of fast-spiking neurons during cortical spike-wave electrographic seizures. Neuroscience, 2002b; 114: 1115-32.

Timofeev I, Grenier F, Steriade M. Spike-wave complexes and fast components of cortically generated seizures. IV. Paroxysmal fast runs in cortical and thalamic neurons. J Neurophysiol, 1998; 80: 1495-513.

Timofeev I, Steriade M. Neocortical seizures: initiation, development and cessation. Neuroscience, 2004; 123: 299-336.

Topolnik L, Steriade M, Timofeev I. Hyperexcitability of intact neurons underlies acute development of trauma-related electrographic seizures in cats in vivo. Eur J Neurosci, 2003a; 18: 486-96.

Topolnik L, Steriade M, Timofeev I. Partial cortical deafferentation promotes development of paroxysmal activity. Cereb Cortex, 2003b; 13: 883-93.

Toyoizumi T, Pfister JP, Aihara K, Gerstner W. Optimality model of unsupervised spike-timing-dependent plasticity: synaptic memory and weight distribution. Neural Comput, 2007; 19: 639-71.

Trasande CA, Ramirez JM. Activity deprivation leads to seizures in hippocampal slice cultures: is epilepsy the consequence of homeostatic plasticity? J Clin Neurophysiol, 2007; 24: 154-64.

Traub RD, Borck C, Colling SB, Jefferys JG. On the structure of ictal events in vitro. Epilepsia, 1996; 37: 879-91.

Traynelis SF, Dingledine R. Potassium-induced spontaneous electrographic seizures in the rat hippocampal slice. J Neurophysiol, 1988; 59: 259-76.

Triesch J. Synergies between intrinsic and synaptic plasticity mechanisms. Neural Comput, 2007; 19: 885-909.

Tsodyks MV, Markram H. The neural code between neocortical pyramidal neurons depends on neurotransmitter release probability. Proc Natl Acad Sci U S A, 1997; 94: 719-23.

Turrigiano G. Homeostatic signaling: the positive side of negative feedback. Curr Opin Neurobiol, 2007; 17: 318-24.

Turrigiano GG, Leslie KR, Desai NS, Rutherford LC, Nelson SB. Activity-dependent scaling of quantal amplitude in neocortical neurons. Nature, 1998; 391: 892-6.

Turrigiano GG, Marder E, Abbott LF. Cellular short-term memory from a slow potassium conductance. J Neurophysiol, 1996; 75: 963-6.

Turrigiano GG, Nelson SB. Homeostatic plasticity in the developing nervous system. Nat Rev Neurosci, 2004; 5: 97-107.

Upton A, Gumpert J. Electroencephalography in diagnosis of herpes-simplex encephalitis. Lancet, 1970; 1: 650-2.

Vanmolkot KR, Kors EE, Hottenga JJ, Terwindt GM, Haan J, Hoefnagels WA, Black DF, Sandkuijl LA, Frants RR, Ferrari MD, van den Maagdenberg AM. Novel mutations in the Na+, K+-ATPase pump gene ATP1A2 associated with familial hemiplegic migraine and benign familial infantile convulsions. Ann Neurol, 2003; 54: 360-6.

Vern BA, Schuette WH, Thibault LE. [K+]o clearance in cortex: a new analytical model. J Neurophysiol, 1977; 40: 1015-23.

Vyskocil F, Kriz N. Modifications of single and double-barrel potassium specific microelectrodes for physiological experiments. Pflugers Arch, 1972; 337: 365-76.

Wagenaar DA, Potter SM. Real-time multi-channel stimulus artifact suppression by local curve fitting. J Neurosci Methods, 2002; 120: 113-20.

Walker JL. ION SPECIFIC LIQUID ION EXCHANGER MICROELECTRODES. Analytical Chemistry, 1971; 43: A89-&.

Whisler JW, Johnston D. Epileptogenesis: a model for the involvement of slow membrane events and extracellular potassium. J Theor Biol, 1978; 75: 271-8.

Womelsdorf T, Fries P, Mitra PP, Desimone R. Gamma-band synchronization in visual cortex predicts speed of change detection. Nature, 2006; 439: 733-6.

Yaari Y, Konnerth A, Heinemann U. Nonsynaptic epileptogenesis in the mammalian hippocampus in vitro. II. Role of extracellular potassium. J Neurophysiol, 1986; 56: 424-38.

Yemisci M, Gurer G, Saygi S, Ciger A. Generalised periodic epileptiform discharges: clinical features, neuroradiological evaluation and prognosis in 37 adult patients. Seizure, 2003; 12: 465-72.

Yuen GL, Hockberger PE, Houk JC. Bistability in cerebellar Purkinje cell dendrites modelled with high-threshold calcium and delayed-rectifier potassium channels. Biol Cybern, 1995; 73: 375-88.

Ziburkus J, Cressman JR, Barreto E, Schiff SJ. Interneuron and pyramidal cell interplay during in vitro seizure-like events. J Neurophysiol, 2006; 95: 3948-54.